Nanostructured materials for sensor applications

Martin Jendrlin

Thesis submitted for the degree of Doctor of Philosophy

June 2022

Keele University

E bok baka, prošel sam

Supervised by: Dr Vladimir Zholobenko

Dr Aleksandar Radu

Research institute: Faculty of Natural Sciences, School of Chemical and Physical Sciences, Birchall Centre

The project was funded by the Royal Society, Keele University and Newton fund.

Abstract

The utilisation of zeolites as infrared spectroscopy-based gas sensors and as potentiometric sensors in zeolite-modified electrodes is reported in this thesis.

Commercial zeolites (NaX, NaY, MOR, FER, BEA-12, BEA-19 and ZSM-5) and prepared Sn-BEA zeolite have been modified by $CuSO_4$, $Cu(NO_3)_2$ and $Cu(CH_3COO)_2$ as copper sources to obtain room-temperature CO sensors. Cu^+ forms stable complexes with CO at room temperature that can be observed by IR spectroscopy. In preliminary screening, MOR impregnated by $Cu(NO_3)_2$ showed the highest response to 1mbar of CO in a vacuum and from ~10 ppm to 5000 ppm under flow conditions. After further testing, water interference presented a significant problem to sensor performance. Therefore, hydrophobic Sn-BEA (Si/Al >1500, Si/Sn = 64) was prepared. $Cu(NO_3)_2$ – impregnated Sn-BEA demonstrated resistance to water interference in a humid environment (~1500 ppm of H_2O) while maintaining the sensing properties.

Hydrophobic Sn-BEA and dealuminated BEA zeolite were prepared from a commercial BEA-19 precursor to obtain a room-temperature infrared spectroscopy-based exhaust gas fumes sensor. Due to fluoride-assisted synthesis, Sn-BEA has high hydrophobicity and a nearly defect-free structure. Both materials have been subjected to CO, CO_2, NO and NO_2 in Ar flow containing 100 ppm of H_2O. Dealuminated BEA showed a response to CO_2 and NO_2, while Sn-BEA showed selective response only to NO_2. Also, Sn-BEA demonstrated two types of response that could be used for determining both the current and the cumulative concentration of NO_2.

The new concept of zeolite-modified electrodes called “Ion-Sensitive Pencil” has been established. Zeolite and graphite were combined in a uniform mixture (40:60 wt.% ratio) and pressed by a hydraulic press (4 tonnes) to form a pellet, which was subsequently used to draw

electrodes. Heulandite zeolites from three natural deposits and 11 commercial zeolites (NaX, KX, NaY, KY, NaA, KA, BEA-12, BEA-19, ZSM-5, MOR, FER, LTL) have been used to detect 9 cations (Na^+, K^+, NH_4^+, Ca^{2+}, Mg^{2+}, Mn^{2+}, Zn^{2+}, Ni^{2+}, Cu^{2+}). Most sensors exhibited near-Nernstian responses to alkali and alkaline-earth cations, while the responses to transition-metal cations were relatively low. Zeolites demonstrated inferior selectivities and sensitivities as compared to classical ion-selective electrodes, although the production is simpler and less expensive. Therefore, the zeolite-containing electrodes were used in a multisensor array to quantify Mg^{2+} content in a model plant fertilizer solution (Na^+, K^+, NH_4^+, Mg^{2+}). The relationship between the responses was determined using the partial least squares method. The R^2 coefficient in cross-validation was 0.83 and the root mean square error of cross-validation was 0.34 log[Mg^{2+}].

The structure-performance relationship of ion-sensitive pencils has been determined using chemometrics. Principal component analysis has been used to visualise the variation of selected zeolite properties (*Si/Al; Al/(Si+Al); Pore Size (Å); Largest Channel, MR; Channel Network; Extraframework Cations (Na^+, K^+, NH_4^+, Ca^{2+}, Mg^{2+} or Fe^{3+}); Crystallite Size (XRD); Particle Size (SEM-TEM); SiOH Intensity*). Partial least squares regression was used to relate zeolite properties with sensor responses to Na^+, K^+, NH_4^+, Ca^{2+} and Mg^{2+}. *Pore size*, *largest channel* and *Si/Al ratio* affect the sensor performance the most. Additionally, it was found that the presence of K^+ and Na^+ as extraframework cations affect the sensitivity towards Ca^{2+}. The R^2 coefficients in calibration models were 0.81-0.96 and root mean square errors of cross-validation for the presented models were 4.1-12.4 mV/dec.

Acknowledgements

I would like to start by saying thank you to everyone who contributed to my education and ultimately writing this thesis.

I would like to thank the Royal Society, Keele University, and the Newton Fund for funding this project.

I would like to thank my mom, dad, sister, aunt and grandma (*in memoriam*) for their limitless support, love and trust throughout my life, both during this PhD journey, as well as before and after it. I would also like to thank my amazing girlfriend Raquel for her love, support and patience throughout this time we have been together.

I am most grateful to my supervisors Dr Vladimir Zholobenko and Dr Aleksandar Radu for providing me with an opportunity to do this research project. Your ideas, mentorship and support have been invaluable and I would never manage to reach the submission phase without your help. Also, I am ultimately grateful for teaching me how enriching could scientific collaborations be, both by providing me with a chance to visit the laboratory at ENSICAEN and by hosting international students at Keele. If I ever get a chance to supervise someone, I wish could be at least partially as good to them as you were to me.

I would like to thank prof Svetlana Mintova for the opportunity of collaboration, for hosting me at her laboratory at ENSICAEN, all the practical pieces of advice and helping me to improve my research skills. I would also like to thank prof Dmitry Kirsanov for the opportunity of collaboration, for introducing me to the world of chemometrics and all the great possibilities it provides.

I would like to thank my master project supervisor prof. Mirta Rubčić for introducing me to scientific research, giving me confidence in my research skills and preparing me for this PhD project.

I would like to thank Catia, Aqeel, Alessandro, Matt, Emma, Isabel, Ernesto, Salma and Sarah for being an amazing group of friends. I am grateful for all the fun, positivity and wonderful moments spent together both in the LJ and out of it.

I would like to thank Viktorija, Luz, Kamila, Anastasia, Dusan, Julien, Maxime, Peng, Rafa, Florent, Weitao, Radek, Ivan, Bruno, Nikolaj and Abdelhafid from the ENSICAEN lab for a warm welcome and feeling as a part of the group from the very first day.

I would like to thank all the visiting students: Goncalo, Jittima, Suntisak (Fluke), Ivana, Vladimir, Sergio, Ivan, Miguel, Vullnet, Erjona, Arijeta and Nikola for the shared knowledge, their great friendship and delicious international meals.

I would like to thank Alexandra Elbakyan for always sharing inaccessible research papers with me.

I would like to thank all my Birmingham friends and all my flatmates at Keele for the great time spent together, you have made my time in England much more fun.

I would like to thank all my friends in Croatia for their support, great time spent together and understanding for the absence during this journey.

I would also like to thank all the Keele University and ENSICAEN staff for creating a pleasant and inspiring work environment.

Personal Statement

During this PhD project my skills and knowledge were improved by taking part in the following workshops and training courses:

"Academic English for Postgraduate Science Students" – module organised by Keele University

"Introduction to teaching and demonstrating" – module organised by Keele University

"Instrument operation and radiation safety training"- module organised by Keele University

"Microsoft Office workshops" - module organised by Keele University

"Spectrocat Workshop: Spectroscopies for the characterization of adsorption, diffusion and separation phenomena: state of the art, current limits and challenges" – module organised by University of Normandie, Caen, France

"IZC'19 Pre-conference school" - module organised by International Zeolite Association

"ICDD X-ray diffraction clinic" - module organised by International Centre for Diffraction Data

"ICDD In Session" - module organised by International Centre for Diffraction Data

"FEZA 21 Pre-conference school" - module organised by Federation of European Zeolite Associations

The research conducted during this PhD course was presented at the following scientific conferences, symposia and meetings:

"BZA Annual meeting", 2018, Ambleside, UK - Poster presentation

"The Faculty of Natural Sciences' Postgraduate Research Symposium", 2018, Keele, UK - Poster presentation

"Conference on Sensors in Precision Agriculture", 2018, Keele, UK - Poster presentation

"Emerging Analytical Professionals Conference", 2019, Leeds, UK - Oral presentation

"21st DKMT Conference on Environment and Health", 2019, Novi Sad, Serbia - Oral presentation

"19th International Zeolite Conference", 2019, Perth, Australia - Poster presentation

"Emerging Analytical Professionals Conference", 2020, Leeds, UK - Oral presentation (Awarded, but not presented due to conference cancellation)

"The Faculty of Natural Sciences' Postgraduate Virtual Research Symposium", 2021, Oral presentation

"FEZA 2021 Virtual Conference", 2021 - Oral presentation, poster presentation

Papers prepared during the PhD project:

M. Jendrlin, S. Khumngern, A. Numnuam, P. Thavarungkul, P. Kanatharana, D. Kirsanov, V. L. Zholobenko, L. Mendecki, A. Radu, *Ion sensing pencil: Draw your own sensor*, Sensors and Actuators B: Chemical, 2021, **337**, 129751

M. Jendrlin, A. Radu, V. Zholobenko, D. Kirsanov, *Performance modelling of zeolite-based potentiometric sensors*, Sensors and Actuators B: Chemical, 2022, **356**, 131343

M. Jendrlin, J. Grand, L. Lakiss, F. Dubray, P. Bazin, J. El Fallah, S. Mintova, V. Zholobenko, *Hydrophobic Sn-BEA as a selective gas sensor for exhaust fumes*, in peer review

M. Jendrlin, J. Grand, L. Lakiss, F. Dubray, P. Bazin, J. El Fallah, S. Mintova, V. Zholobenko, *Preparation and screening of Cu-modified zeolites utilised as potential environmental CO sensors*, in peer review

V. Zholobenko, C. Freitas, M. Jendrlin, P. Bazin, A. Travert, F. Thibault-Starzyk, *Probing the acid sites of zeolites with pyridine: Quantitative AGIR measurements of the molar absorption coefficients*, Journal of Catalysis, 2020, **385**, 52-60

L. Mendecki, S. Granados-Focil, M. Jendrlin, M. Mold, A. Radu, *Self-plasticized, lumogallion-based fluorescent optical sensor for the determination of aluminium (III) with ultra-low detection limits*, Analytica Chimica Acta, 2020, **1101**, 141-148

D. Kirsanov, S. Mukherjee, S. Pal, K. Ghosh, N. Bhattacharyya, R. Bandyopadhyay, M. Jendrlin, A. Radu, V. Zholobenko, M. Dehabadi, A. Legin, *A Pencil-Drawn Electronic Tongue for Environmental Applications*, Sensors 2021, **21(13)**, 4471

Table of contents

Abbreviations

Abbreviation	Explanation
ATR	Attenuated total reflectance
BAS	Brønsted acid sites
BEA	Zeolite Beta
BET	Brunauer–Emmett–Teller
CAN	Cancrinite
CHA	Chabazite
CNT	Carbon nanotubes
CP MAS NMR	Cross-polarisation magic angle spinning nuclear magnetic resonance
CS	Citizen Science
CTL	Cataluminescence
D4R	Double four ring
D6R	Double six ring
DBP	Dibutyl phthalate
deAl-BEA	Dealuminated BEA zeolite
DR-UV	Diffuse reflectance ultraviolet spectroscopy
DSC	Differential scanning calorimetry
DTACL	Dodecyltrimethylammonium chloride
DTGS	Deuterated Triglycine sulphate
EDX	Electron dispersion X-ray spectroscopy
EMT	Ecole Supérieure Mulhouse Chimie - two
ENFET	Enzyme-linked field-effect transistor
FAU	Faujasite
FER	Ferrierite
FTIR	Fourier-transform infrared spectroscopy
HDPCL	Hexadecylpyridinium chloride
HEU	Heulandite
ICDD	International Centre for Diffraction Data
ICSD	Inorganic Crystal Structure Database
IoT	Internet of Things
ISE	Ion-selective electrode
ISFET	Ion-selective field-effect transistor
ISP	Ion-sensitive pencil
KFI	Kerr zeolite five
LAS	Lewis acid sites
LOD	Limit of detection
LTL	Linde type L
MAP	Maximum aluminium P
MAS NMR	Magic-angle spinning nuclear magnetic resonance
MB	Methylene blue
MCT	Mercury cadmium telluride
MEI	Mobil Eighteen

MFI	Mobil Five
MOF	Metal-organic framework
MOR	Mordenite
MSO	Metal oxide semiconductor
NaX	Sodium X zeolite
NaY	Sodium Y zeolite
NDIR	Nondispersive infrared
NMR	Nuclear magnetic resonance
o-NPOE	2-Nitrophenyl octyl ether
PCA	Principal component analysis
PET	polyethylene terephthalate
PEVA	poly(ethylene vinyl alcohol
PLA	Polylactic acid
PLS	Partial least squares
ppm	Parts per million
PTEV	Poly(tetrafluoroethylene-co-ethylene-co-vinyl acetate)
PVC	Polyvinyl chloride
RB	Rhodamine B
RB6G	Rhodamine
REP	Reference electrode pencil
RMSEC	Root mean square errors of calibration
RMSECV	Root mean square errors of cross-validation
SDA	Structure-directing agent
SEM	Scanning electron microscopy
TBA-TBB	Tetra-n-butylammonium tetrafluoroborate
TEA^+	Tetraethylammonium cation
TEM	Transmission electron microscope
TEOS	Tetraethyl orthosilicate
TGA	Thermogravimetric analysis
TMPO	Trimethyl phosphate
XRD	X-ray diffraction
ZME	Zeolite-modified electrode
ZSM-5	Zeolite Socony Mobil five

Chapter 1

Introduction

1.1 Zeolites – brief historical overview

Zeolites are crystalline aluminosilicates that comprise uniformly sized pores of molecular dimensions. Geologically they are present in the earth's crust in places where volcanic rocks and ash layers react with alkaline groundwater. Zeolites also crystallize in post-depositional environments over periods ranging from thousands to millions of years in shallow marine basins.[1] From the other rocks, they were distinguished by Swedish mineralogist Axel Frederik Cronstedt. In 1756 he was studying minerals from a Svappavari copper mine (Sweden) when he stumbled upon a mineral of unusual and to that date uncharacterised properties. When the mineral was heated with a blow-pipe flame it looked like it was boiling. Based on this property, Cronstedt named it "zeolite". This term was coined from the Greek words "*zeo*" (boiling) and "*lithos*" (stone),[2] which has later been adopted by researchers who studied these minerals after him. For the following two centuries, zeolites were mainly studied by mineralogists[3] who tried to elucidate their crystallisation conditions, structure stability upon reversible dehydration,[4,5] and adsorption of small molecules such as ammonia, carbon dioxide, hydrogen sulphide, etc. after initial water desorption.[6,7] At that time, zeolites were not of much interest because no practical application was observed.[8] The interest in the field was regained after O. Weigel and E. Steinhof's,[9] and J.C. McBain's papers,[10] where they reported that chabazite adsorbs water, methanol, ethanol and formic acid, but not diethyl-ether, acetone or benzene. Based on this observation of partial exclusion of certain molecule types, McBain establishes the term "molecular sieve". In 1944 Barrer reported that linear alkanes such as propane, *n*-butane, *n*-pentane, can be separated from their branched isomers using chabazite.[11] The molecular sieving property raised interest in the field, but there were only limited amounts of natural zeolites present. Another drawback is that they were rarely pure and usually contaminated with other minerals, metals and quartz.

R. M. Barrer and R. Milton revolutionised the field in the 1940s by preparing synthetic zeolites in their laboratories, as an alternative to the use of natural zeolites.[12,13] Although, they were not the first researchers that attempted to synthesize a zeolite. In 1862 H. Saint-Claire-Deville reported the hydrothermal synthesis of a zeolite from potassium silicate and sodium aluminate.[14] In years to follow, many other scientists synthesised analogues of naturally occurring zeolites.[15] Barrer's and Milton's work was revolutionary because they produced synthetic zeolites, which had no natural counterparts. To grasp the importance of this discovery, it should be stressed that from ~260 different zeolite types known today only 67 occur naturally, so almost 200 are synthetic.[16] For the following 10 years, zeolites were synthesised from only inorganic systems (Barrer synthesized zeolites P and Q (KFI network),[17] while Milton prepared zeolites A, B and C).[13] That has limited Si/Al ratio to low values. Another important factor that contributed to the progress in the field was characterisation techniques development, most importantly XRD powder diffraction.[18] Without it, there was almost no possibility to identify and confirm structural differences and uniformity. In 1961 Barrer[19] achieved another milestone, he introduced organic molecules as structure-directing agents (SDA) in the synthesis of a zeolite. SDAs are used to direct zeolite's pore size and volume. In the beginning, it was tetramethylammonium hydroxide (TMA-OH), but in the years to follow, other researchers used many types of organic molecules, but mainly quaternary ammonium salts. Using of SDAs allowed the synthesis of high silica zeolites (e.g. BEA ranging from Si/Al= 5 to 100) and even pure-silica ZSM-5 (Silicalite 1).[20]

In 1997 a definition of zeolites was presented by IZA, and it stated: *a crystalline substance with a structure characterized by a framework of linked tetrahedra, each consisting of four O atoms surrounding a cation. This framework contains open cavities in the form of channels and cages. These are usually occupied by H_2O molecules and extraframework cations that are commonly exchangeable. The channels are large enough to allow the passage of guest*

species. In the hydrated phases, dehydration occurs at a temperature mostly below about 400 °C and is largely reversible. The framework may be interrupted by (OH, F) groups; these occupy a tetrahedron apex that is not shared with adjacent tetrahedra''.[21] From this definition, it can be seen that the zeolite family is not restricted only to classical silicon and aluminium zeolites, but also it comprises (aluminophosphates) AlPOs, (silico-alumino-phosphates) SAPOs, (metal-containing AlPO) MeAPOs and (metal-containing SAPO) MeAPSOs. A distinction of zeolites among other crystalline oxide materials stems from the unique properties of zeolites: uniform microporosity, ion exchange capacity, framework acidity, and thermal stability.

1.2 Zeolite structure

The structure of a zeolite consists of TO_4 tetrahedra (primary building unit), where T atom (Si, Al) is surrounded by four oxygen atoms in the corners of tetrahedra. Those tetrahedra are interconnected only by corner-sharing. Two T atoms cannot be connected directly, they have to be connected via bridging oxygen atom (Figure 1.1). T-O-T bond angles can vary from 130° to 180°, and thus produce various structure patterns (secondary building units, SBUs). SBUs are made from up to 16 T atoms containing tetrahedra interconnected in 23 possible ways. [16,22,23] The most common SBUs are visualised in Figure 1.2.

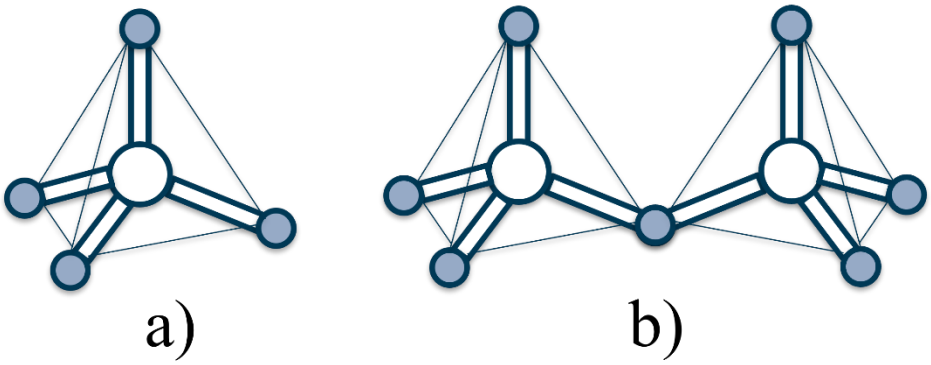

Figure 1.1. a) TO_4 tetrahedra, b) Corner-sharing TO_4 tetrahedra, (White circles represent T atoms (Si, Al), blue circles represent O atoms), adapted according to ref.[8]

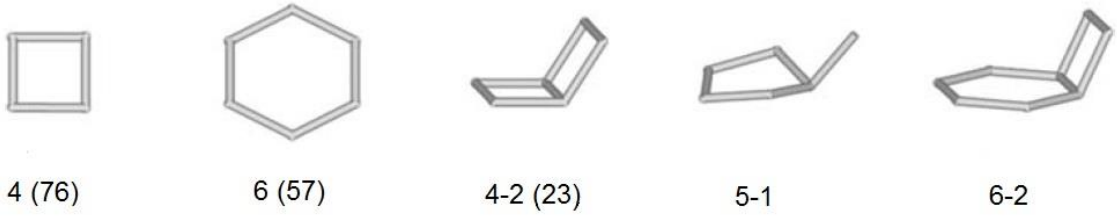

Figure 1.2. Selection of most common SBUs.[8]

Each specific zeolite structure can be made from one or more different types of SBUs (e.g. LTA contains 5). They are not chiral and in a unit cell, there has to be an integral number of SBUs. With a variety of combinations, SBUs can produce a range of chains and 2-D networks which are then mutually interconnected while forming a distinct structure. Depending on the structure type, differently sized and shaped channels and cavities can be made.[24] Based on a specific framework, characteristic units made from several SBUs are present in sodalite, zeolite A (LTA), faujasite and zeolite L (LTL), which are depicted in Figure 1.3.[16] These rings form a number of different composite building units, which are characteristic of each type of zeolite.

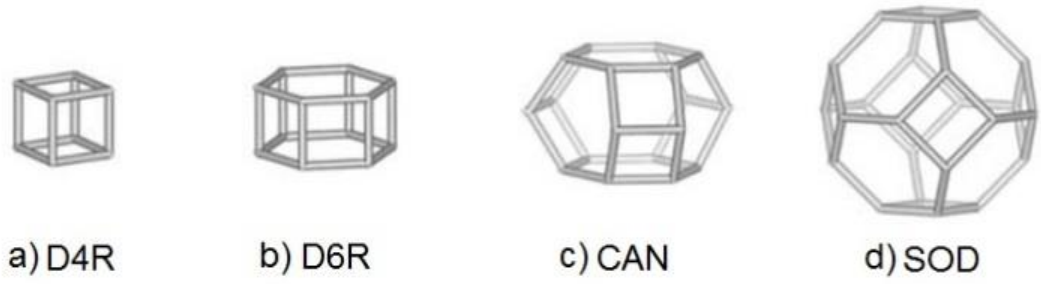

Figure 1.3. The composite building units for sodalite, zeolite A, faujasite and zeolite L; a) double four-ring, b) double six-ring, c) cancrinite cage (CAN), d) β-cage (sodalite cage). [8]

The nature of their links gives rise to different structures. For example, sodalite or *β*-cages connected through single four rings make a sodalite structure, whilst connecting them via double four rings (D4R) yields LTA and if they are linked through double six rings (D6R) the structure of faujasite (FAU) or EMT is obtained (Figure 1.4).[25]

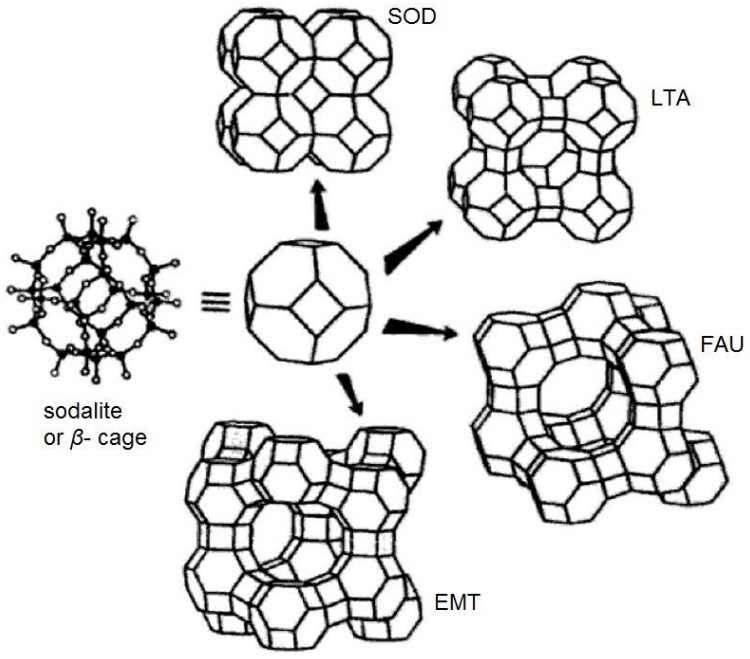

Figure 1.4. Sodalite or *β*-cage in different zeolite structures. [25]

So far ~260 zeolite structure types are known. Each structure type is labelled with a 3 letter symbol provided by the Structure Commission of International Zeolite Association (IZA-SC).[16] Zeolite framework is negatively charged. The negative charge stems from the isomorphous substitution of silicon ions (Si^{4+}) with trivalent ions (Al^{3+}, Fe^{3+}, Ga^{3+}, In^{3+}, B^{3+}), of which aluminium is the most common. Consequently, that negative charge has to be compensated with extra-framework cations. Zeolite framework cannot have more aluminium than silicon in the framework due to the "Löwenstein's rule".[26] It states that Al-O-Al connections are not possible. In other words, each aluminium atom has to be surrounded by oxygen bridges to four silicon atoms, which means that Si/Al ratio has to be at least one or greater than one. This leads to the chemical composition of a zeolite:

$$(M^{+})_a(M^{2+})_b\left[Al_{(a+2b)}Si_{n-(a+2b)}O_{2n}\right] * mH_2O$$

In this formula, M, represents extra-framework ions, that most commonly are alkaline (K^+, Na^+) or alkaline earth (Ca^{2+}, Mg^{2+}) ions. Extra-framework ions are not bonded to the framework, they only have weak interactions, and therefore can be easily exchanged for other ions that are present in zeolite's proximity.[8] Contemporary zeolite synthesis depends on organic SDAs. Since organic molecules are bulkier than the inorganic ions of the same charge, fewer ions are needed to fill the channel or a cavity void and less aluminium atoms are required in the structure to compensate for the charge imbalance. Therefore, SDAs can facilitate the synthesis of zeolites with higher Si/Al ratios.

1.3 Acid and basic properties

Besides structural characteristics of zeolites, another important feature is the presence of very strong acid sites. The acid sites that can be found in the zeolite framework, and solids in general, are Brønsted or Lewis in nature (Figure 1.5). As mentioned previously, the introduction of trivalent aluminium atoms in the tetrahedral framework brings negative charges that have to be

balanced by extra-framework cations. In cases when the exchange is performed with ammonium cations which can be later decomposed (to gaseous ammonia and a proton), protons act as compensating cations near aluminium centres, considering their formal charge.

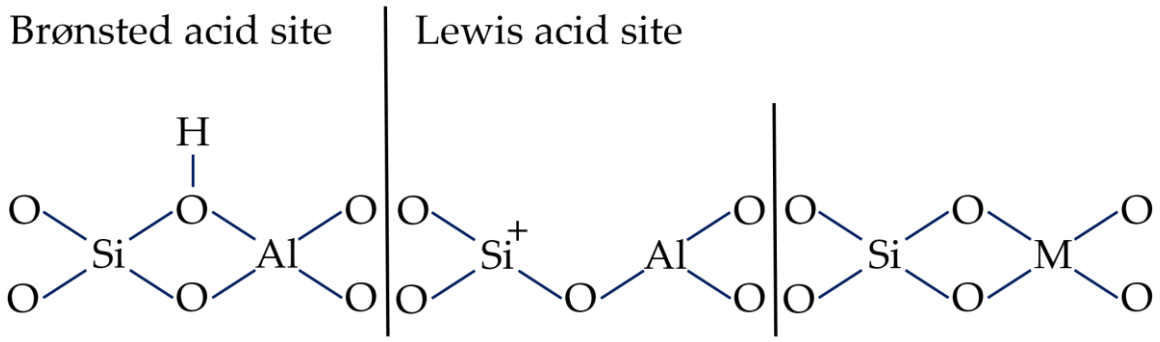

Figure 1.5. Visualisation of Brønsted and Lewis acid site,

M = tetravalent metal atom (e.g. Sn, Ti, Zr), adapted according to ref.[27]

Those protons contribute to forming of bridging OH-groups with a polar covalent O-H bond, (Figure 1.5) which can easily donate H^+ and hence behave as Brønsted acid sites (BASs). Therefore, a number of possible BASs strongly depends on Si/Al ratio.[28] Nowadays, protonic or H-forms of zeolites are mostly synthesized directly, by using SDA molecules. In this case, the protons may be residual from the combustion or decomposition of the templating agents. That allows various synthesis paths to produce the so-called H-forms of zeolites, which are very strong solid Brønsted acids.[29] The idea that zeolite acidity originates from aluminium tetrahedral bonding was first suggested by Thomas.[30] Milliken et al.[31] conceived different structures of the acid sites, with tricoordinated silicon atoms located on small structure defects acting as electron-acceptor sites, i.e., as Lewis centres. Other Lewis sites can be created by local charge imbalances originating from defect sites, extra-framework aluminium cations, thermal dehydroxylation, the presence of coordinately unsaturated metals (Sn, Ti, Hf, …), surface defects. Some Lewis acid sites are important in catalytic reactions with transition metals that involve reduction or oxidation steps. To measure solid acidity, the experiments have

to convey information on the chemical nature of the acid sites (Brønsted or Lewis), site concentration, acid strength distribution, and accessibility to acid sites. The amount of framework aluminium controls the highest possible number of BASs. However, the concentration of aluminium and the amount of acid sites rarely match because zeolites tend to release aluminium as a result of thermal or chemical treatments. This is a characteristic of Y zeolite, one of the most important commercial zeolites. Additionally, the ion exchange is an equilibrium process that may be incomplete. Also, BASs can be lost via dehydroxylation at high temperatures. It can be realized that the holistic description of acidity requires the characterization of several factors so that in general multiple techniques must be used.

1.4 Ion-exchange

Of the total annual zeolite consumption, 73% is used as detergent builders, hence the ion-exchange ability of zeolites is widely exploited.[8] Following the discovery that soils undergo ion exchange when contacted with solutions of ammonium salts[32] and that ammonium or potassium were exchanged for calcium in 1858,[33] H. Eichhorn first reported that this phenomenon reversibly occurs also in natrolite and chabazite.[34] That was successful and provided great possibilities for the industrial use of zeolites. To this date, it is thoroughly studied by many scientists for various applications from gas adsorption to catalysis and fuel conversion. In comparison to other ion-exchangers such as organic resins that swell in water, zeolite structure remains almost intact in aqueous solutions with a wide pH range (pH < 2 cause dealumination, and pH > 10 cause desilication).[35] For the research presented in this thesis, ion-exchange process is one of the most important ones, because it allows entering of the ions that are interacting with species of interest in the zeolite channels or cavities. Therefore, this process is described in a more detail way. In general, ion-exchange process can be thermodynamically defined by two statements:

(a) the system is in a true state of equilibrium;

(b) the exchange process is fully reversible. If the system is not reversible then there will be two different reactions (one representing the forward exchange and another the reverse exchange) that need to be examined separately. These processes must have different standard Gibbs energies also, in the reversible case, the forward and reverse reactions have different Gibbs energies although the difference is only in sign.

Those definitions are not solely for zeolites, but all solids in general. Since they are uniform, definitions provide a possibility to compare the cation selectivity of a zeolite with different types of compounds. Ion exchange as a process can be defined as the exchange of ion A^{q_A} , which is in the beginning only in the solution, and ion B^{q_B} that is present only in the zeolite.

$$q_B A_S^{q_A} + q_A B_Z^{q_B} \leftrightarrow q_B A_Z^{q_A} + q_A B_S^{q_B}$$

In the equation above, q_A and q_B are the charges of the ions, A_S and B_S solution cations, while $A_Z$and B_Z are cations inside the zeolite structure. Ion exchange isotherm at a standard condition of temperature and pressure can be constructed to yield the distribution of cations between the zeolite and solution phases when equilibrium has been reached. Detailed experimental methodology for the construction of an isotherm is described by Dyer et al.[36] and by Townsend.[37] Idealised isotherm shapes are shown in Figure 1.6. They give a visual indication of the relative preferences of the cations for the zeolite and solution phases.

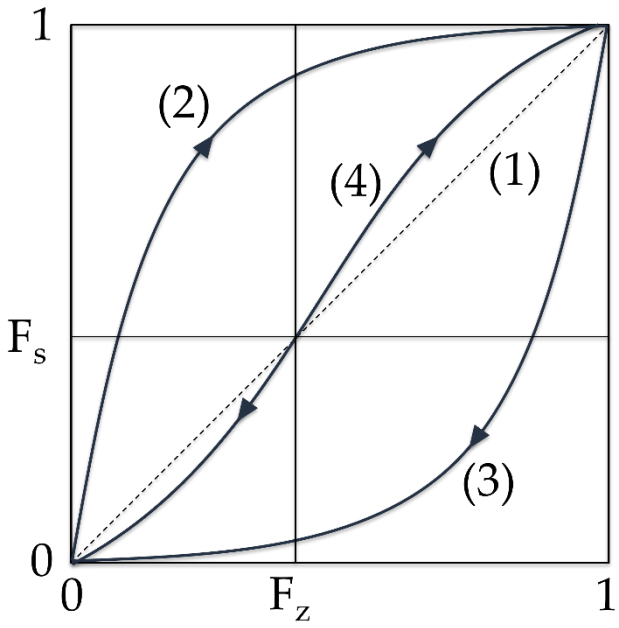

Figure 1.6. Theoretical ion-exchange isotherms, adapted from ref[35],

F_S- equivalent fraction of cation in a solution, F_S- equivalent fraction of cation in a zeolite

When there is no difference in affinity for cations in the zeolite phase the isotherm is a straight line – the dotted line (1) in Figure 1.6. Isotherm (2) is the shape adopted when A remains in solution, it does not readily substitute B from the zeolite phase, under defined experimental conditions. Isotherm (3) occurs when A replaces B from the zeolite. The sigmoidal shape of (4) arises when there is a change in selectivity, in the concentration range that is studied, and it could indicate that more than one exchange sites in the structure are available for the competing cations. This must be viewed in the light of the conclusions of Barrer and Klinowski[38] who provided a fundamental approach to the effect of electrolyte concentration on selectivity. They concluded that when competing cations have different valencies, selectivity increases for the cation with the higher valency as dilution increases. Changes in isotherm shape can occur, with both the loss and gain of a sigmoidal shape being possible, so the presence of inflexions in an isotherm may not be taken as evidence that there is more than one possible exchange site in the zeolite. This enables an isotherm to be plotted

recording the equivalent fraction (F_S) of the ingoing cation in solution against its equivalent fraction in the zeolite (F_Z). When ions have the same valency, changes in isotherms with dilution are very small. These quantities can be defined as,

$$F_S(A) = q_A c_S(A)/(q_A c_S(A) + q_B c_S(B)) \qquad F_Z(A) = q_A c_Z(A)/(q_A c_Z(A) + q_B c_Z(B))$$

where q_A and q_B are the charges of the ions, $c_S(A)$, $c_S(B)$, $c_Z(A)$ and $c_Z(B)$ are the cation concentrations in solution and solid phases, respectively.

The selectivity of a zeolite for ion A can be expressed quantitatively as a separation factor,

$$\alpha = F_Z(A)c_S(B)/F_Z(B)c_S(A)$$

A fuller consideration of the normalisation and its theoretical justification can be found in Barrer et al.[39] As it was mentioned in the definitions, to apply thermodynamic analyses to isotherm data it is imperative that the process be demonstrably reversible. In a majority of real zeolite-cation systems, the path of the reverse isotherm deviates markedly from that of the forward exchange (Figure 1.7).

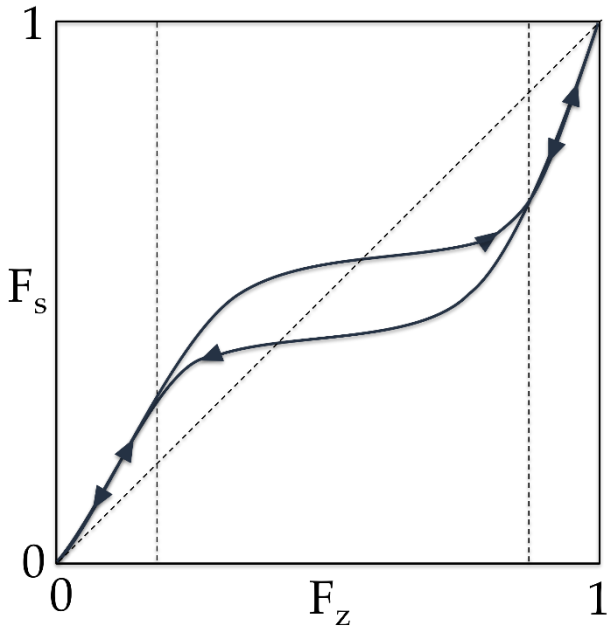

Figure 1.7. Ion-exchange isotherm hysteresis, adapted from ref.[35]

This phenomenon is known as “hysteresis” and can arise from the presence of phase separation and the coexistence of two phases over the composition range studied. It can also

be a consequence of changes in occupancy of heteroenergetic cation sites created by drying the zeolite samples prior to their use to generate the reverse curve. Other causes are the incidence of unsuspected ternary exchanges, small errors in analysis or even the precipitation of metal oxide or hydroxides on the zeolite external surface. Not all isotherms in the literature have been constructed in the formal ways described above. Often they arise from contacting the zeolite with solutions containing only the in-coming cation, analysis for only one ion is carried out in one phase (solid or aqueous) and various units of concentration are used.[40] For most applications, the full thermodynamical analysis is not necessary, so only the distribution coefficient at one point is used. It is used in cases when the only important fact is the final amount of the desired cation that is going to be present in the exchanged zeolite. At each point a distribution coefficient (K_D) can be defined for ion A:

$$K_D(A) = c_Z(A)/c_S(A)$$

where $c_Z(A)$ is the concentration of ion A per unit mass of anhydrous zeolite and $c_S(A)$ is the concentration of A per unit volume of external solution. Distribution coefficients are widely used as convenient checks of practical selectivities under fixed experimental conditions, provided equilibrium has been reached. These equations are suitable only for binary systems, which means that there is one ion entering and one leaving the zeolite. For commercial utilisation in real-life samples where multiple ions are present, zeolites should be able to exchange at least two or more different types of cations. However, then thermodynamic calculations become more complicated. Since those conditions were not studied during this project, they will not be covered.

As mentioned above, commercially zeolites are mostly used in detergents, as a detergent builder. That is zeolites are used to soften hard water as well as to enhance the overall detergent performance. During the water softening process Ca^{2+} and Mg^{2+} ions from water are exchanged for Na^{+} ions from the zeolite. In the past, that process was utilising phosphates, but since the

excess amount of phosphates in wastewater caused the proliferation of algae that created a disturbance in the ecosystem, a better solution had to be found. Nowadays, zeolites are used as eco-friendly compounds. Since the water hardness, as well as the washing customs, are not the same throughout the world, not only one zeolite type is suitable to cover all the market demands. Several zeolites are used, of which LTA,[41] FAU[42] and MAP[43] are most common. Those zeolites are used because they have a low Si/Al ratio and therefore high ion-exchange capacity and selectivity towards small and highly charged cations such as Ca^{2+} and Mg^{2+}. Apart from the detergent industry, zeolites are also used in wastewater and nuclear waste treatment. From the wastewater, the most important ion to be removed is the ammonium ion, while the nuclear waste can have a wide variety of ions such as Cs^{+}, U^{2+}, Sr^{2+}, Th^{4+}, etc. Zeolites MOR, CHA and ANA were tested, but clinoptilolite showed the best efficiency in both fields. Another great advantage of clinoptilolite is its availability as a naturally occurring zeolite in vast quantities.[35] In addition to these large-scale processes, ion-exchange properties of zeolites are important in other areas, e.g. catalyst preparation and sensor applications.

As this project is going to be focused on zeolite applications as environmental pollutant gas sensors and as electrode-based cation sensors in water solution, the alternative approaches to sensing those species are explored in the following two sections (their sensitivity range, cost, durability and ease of use).

1.5 Gas sensors: state of the art

IUPAC defined a chemical sensor as "A device that transforms chemical information, ranging from the concentration of a specific sample component to total composition analysis, into a useful analytical signal."[44] Gas sensors for environmental pollutant gases (CO_x, NO_x, SO_x) present on the market can be divided into two main types: optical and electronic sensors (Figure

1.8). The main principles of these sensors will be explained in the example of CO sensors since they are the most common in UK households.

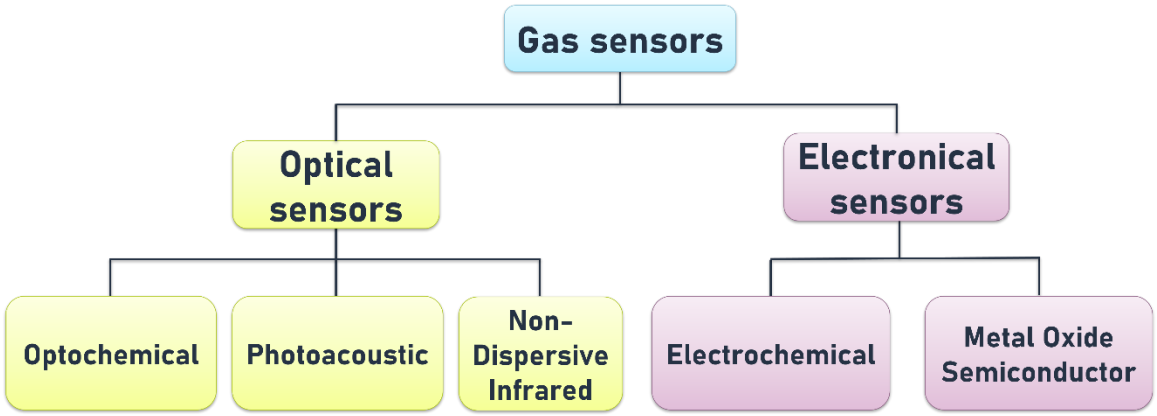

Figure 1.8. Classification of state-of-the-art CO gas sensors.

1.5.1 Optical sensors

Optical sensors can be further divided into optochemical, photoacoustic and non-dispersive infrared (NDIR) sensors. The optochemical sensors are metal salts (e.g $PdCl_2$) that are reduced upon interaction with carbon monoxide. The salt changes colour when reduced and this is the feature alerting the observer. Even though they are inexpensive, a big drawback is that the alerting system requires the vigilance of the observer to recognise the change in concentration.[45] If it is considered that at high concentration carbon monoxide causes dizziness and confusion,[46,47] an average person may be in no condition to readily observe this change and get away from the danger.

The second type of optical sensors gas sensors depends on photoacoustic spectroscopy. Photoacoustic spectroscopy observes sounds formed by the interaction of EM waves with the detector. [48] Upon contact with EM waves, a thermal expansion is generated, which produces a pressure wave (sound). For CO sensing, a 4.55 μm (~2200 cm^{-1}) laser was pointed to a gas chamber [49–51]. Upon interaction with CO, the signal attenuation was proportional to the CO

concentration. The technique has been tested with both low and high CO concentrations, but the long signal response (~35s) and the bulky design prevent it from widespread use.

The third major type of gas sensor is an NDIR gas analyser. It shows great responses to high concentrations of CO (200-1000ppm), but the response at lower concentrations is worse than with metal oxides[52], Figure 1.9. Therefore, it is not suitable for commercial use, because a home gas sensor is supposed to warn the homeowners about the leakage while their life is still not in danger. Combined with NDIR technology, biomimetic sensors are in use as well.

1.5.2 Electronic sensors

Electronic sensors come in two main types: thermistor type metal-oxide-semiconductor (MOS) detectors that detect a change in heat when target gas reacts with the oxide layer (the change in temperature raising the alarm), and an electrochemical detector that works by sensing the change in charge carriers in an electrolyte solution when target gas interacts with an electrode of the device. Sensors have been utilised by researchers to actively measure the varying concentration of CO in the environment. Wiegleb and Heitbaum reported the use of metal oxide gas sensors as detectors for monitoring NO and CO gas concentrations in cars, studying the variation in concentration over an extended period. SnO_2 was used to detect the change in concentration of CO and In_2O to detect the concentration of NO.[52] The sensor was used to measure the concentration of CO and NO at varying stages of the journey; metal oxides were used due to their fast response to the change in concentration. These responses were compared with an infrared gas analyser (Figure 1.9). The responses are comparable although the NDIR analyser has a greater dynamic range, the MOS device had a better response at low concentrations.[45]

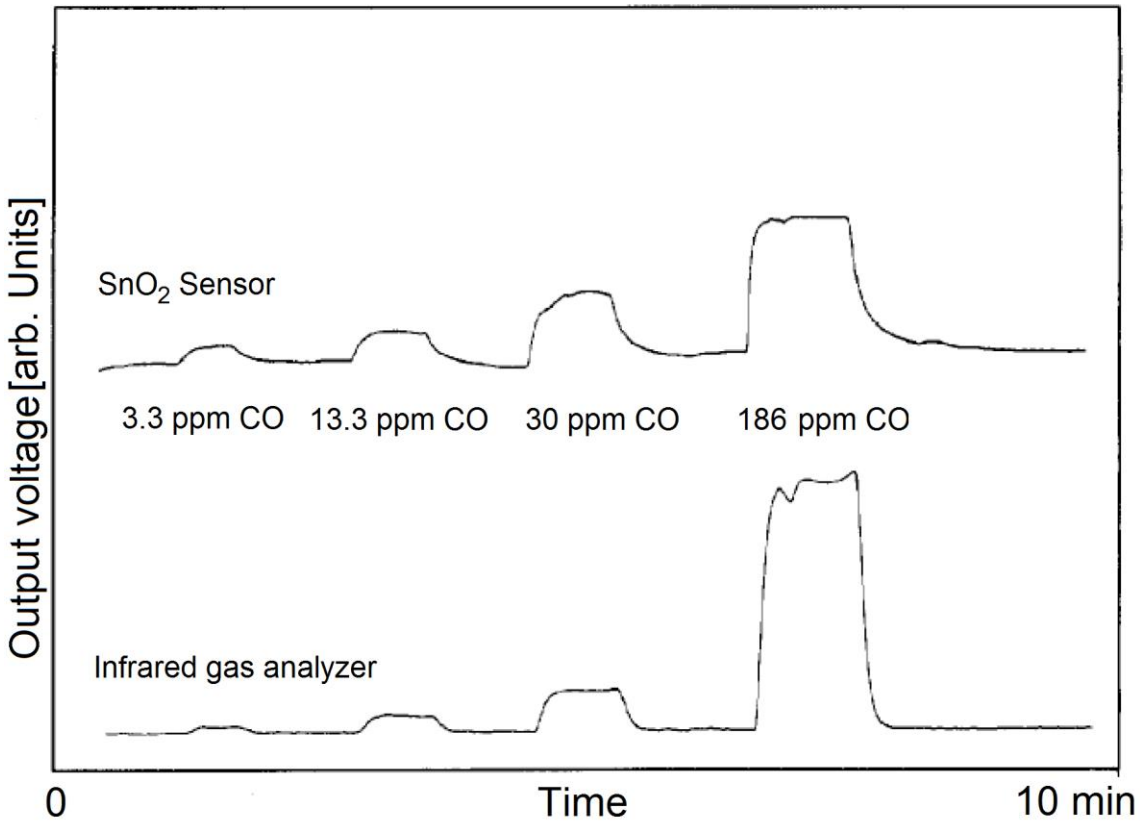

Figure 1.9. SnO_2 based sensor and infrared gas analyser intensities comparison at various concentrations of CO.[52]

According to recent studies, the best metal oxide semiconductor (MOS) material for the detection of carbon monoxide is SnO_2. Others, such as CeO_2 and TiO_2, have been investigated but are yet to match the performance of SnO_2 systems having poor responses at low CO concentrations. Such sensors have been demonstrated to have higher responses to carbon monoxide at low concentrations than an infrared gas analyser and as a result, show great promise for cheaper air quality measurement.[52] The operating temperatures around 250 °C help to lower power requirements, although it is still desirable to minimise these further, as this remains the largest obstacle to the use of MOS technology. The small particle size, around 2 nm, has been shown to increase gas response, although material processing in device fabrication has yet to be optimised in this instance. The investigation of nanomaterials provides

a potential way forward for future research into lowering device power consumption and increasing gas response.

Currently, most of the CO sensors on the market are based on electrochemical technology. [[53]] The electrochemical cell consists of the working electrode, counter electrode and electrolyte. At working electrodes that are usually made from noble metals (e.g. Pt for CO), the target gases are oxidised and at counter electrodes, the oxygen from the air is reduced.

Working electrode $2CO + 2H_2O \rightarrow 2CO_2 + 4H^+ + 4e^-$

Counter electrode $O_2 + 4H^+ + 4e^- \rightarrow 2H_2O$

Electrolytes could be either liquid (acid or salt solution) or solid (yttria-stabilised zirconia or "NASICON" ($Na_3Zr_2Si_2PO_{12}$)) [54,55]. The former are less common since there is a risk of leaking and drying out.

The electric current produced upon oxidation of the gas on the working electrode is related to the CO concentration. The sensors show almost no response to H_2, CH_4 and NH_3, but ethanol is a significant interference since its reducing potential is similar to CO. [55] This is compensated by utilisation of chemical filter membranes on top of the working electrode. At lower concentrations the response to CO is quick, but at higher concentrations, the response depends on CO permeability through the membrane.

The main advantages of this technology over the others can be attributed to a nearly linear response to CO concentration, compact design, long lifespan and ability to operate at room temperature. Since no heating of the sensing substrate is required, the sensors can also be battery-operated, which facilitates their mobility. On the other hand, the disadvantages are a limited long-term temperature range (0-50 °C), the need for stable oxygen supply and potential handling hazards when acids are utilised as electrolytes[56].

1.6 Zeolites as sensors

Due to their unique properties, zeolites are of high interest in the field of gas sensing. Their adsorptivity, porosity, high surface area, the presence of mobile ions, and catalytic activity make them potential candidates as chemical sensors in numerous applications. Zeolite-based gas sensors can be divided into two main groups. Zeolites can serve as a main functional element of a sensor, or as an auxiliary element (Figure 1.10).

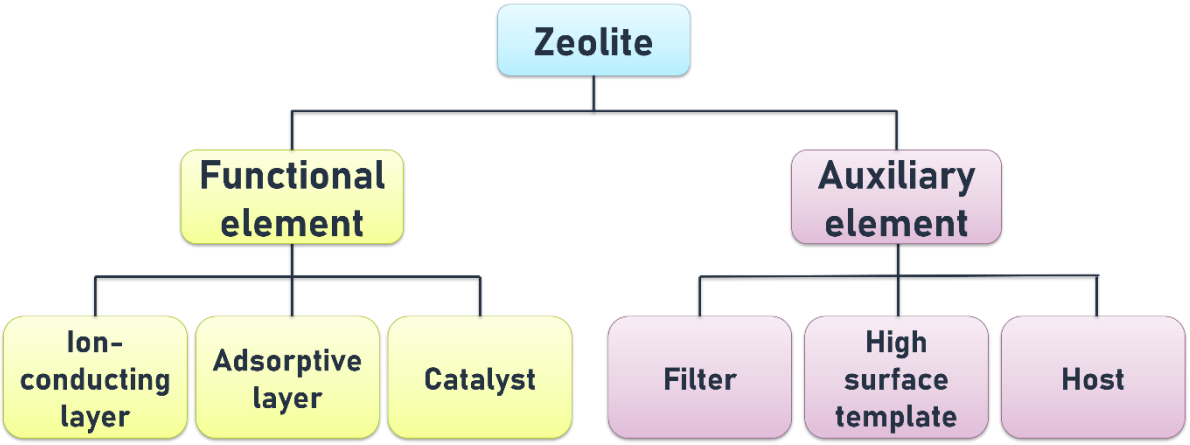

Figure 1.10. Classification of zeolite-based sensors. [57]

1.6.1 Zeolite as a main functional element

Sensors that have zeolites as main functional elements rely on conductive, adsorptive, or catalytic properties of one specific zeolite and its interaction with the target species, i.e. their chemical features are exploited (Figure 1.10). General aspects of ionic conductivity in zeolites have been studied extensively.[57] Due to the band gap of several eV between the valence and conduction bands, no electronic conductivity (direct current) is observed with zeolites in general.[58] However, as extra-framework cations present within the zeolite can move from one binding site to the next, the zeolite exhibits ionic conductivity.[59] In the dehydrated state, ions

move within the zeolite according to ion-hopping mechanism, while in the hydrated state, protons in zeolites move via the "vehicle" or Grotthus mechanism.[60] The thermal activation energy of conduction and the specific conductivity varies for every specific cation. Na^+ -containing zeolites (e.g. $2.9x10^{-3}$ Ω cm^{-1} in LTA at 600 °C) have the highest conductivity values and lowest activation energies in the dehydrated state, as determined by impedance spectroscopy.[61] By increasing the cation diameter, electrostatic interactions decrease from Li^+ to Na^+, which results in lower activation energies and higher conductivity, but with K^+ and Rb^+, an increase in activation energy is observed due to steric effects. Compared to other solid electrolytes, zeolites are in the middle range. For example, conductivities are 2 orders of magnitude lower than in Na^+-β-alumina, and 3 orders of magnitude higher than in CaF_2.

Sensors that use conductivity to measure the analyte concentration can be grouped depending on the localisation of the effect. The interaction involves either the entire bulk of the zeolite, i.e., it takes place within the channels and cages, or it is confined mostly to the interface between the zeolite surface and an adjacent phase (gas, liquid or solid). Apart from ionic conductivity, zeolite-containing sensors can change their visual properties. In this case, cataluminescence (CTL) is utilised. This term describes chemiluminescence produced during the heterogeneous catalytic oxidation of organic vapours on the surface of a solid catalyst,[62] for example, a zeolite. Recently, this radiation was used by Yang et al. to prepare CTL optical sensor devices based on Na-FAU or Na-Cs-FAU for the selective detection of acetaldehyde and n-hexane. .[57,63]

1.6.2 Zeolites as an auxiliary phase

When zeolites are auxiliary phases, sensors utilise physical aspects more, so that other materials could benefit from them. Zeolites as an auxiliary phase in gas sensing are divided into three major subgroups (Figure 1.10). They can act as filter layers (either catalytic or size-restrictive

to enhance the selectivity of a sensitive film), high-surface templates, and host structures to immobilize gas-sensitive species. Zeolite filters are of particular interest for conventional n- or p-type semiconducting sensor materials. One major drawback of the latter is lack of selectivity. If a zeolite film is deposited on the top of the actual sensor element, it may act as a barrier for interfering gases, thus preventing their interaction with the sensor. This method of selectivity enhancement has been reported in the literature for a large variety of semiconductor–zeolite pairs, e.g., LTA zeolite on Pd-doped SnO_2,[64] Pt-loaded MFI on $SrTi_{(1-x)}Fe_xO_3$,[65] MOR on SnO_2.[66] Due to their characteristic framework structure, zeolites also serve as templates for the synthesis of sensor materials with an exceptionally high surface area. This is of particular interest in the case of conventional n-type semiconducting sensor devices, e.g. tin oxide, where the sensing mechanism is closely connected to the interactions between the analytes and oxygen species adsorbed on the surface.[67] The zeolite framework structure also serves as a host for the immobilization of gas-sensitive agents.[35] Due to its comparatively large cages, the so-called “super cages”, zeolite FAU is suitable to encapsulate bulky dye molecules or complexes.[35]

1.7 Ion-selective electrodes

The second part of this project is dedicated to utilising zeolites in systems analogous to ionophore doped ion-selective electrodes (ISE). ISE, also known as a specific ion electrode, is a sensor that converts the activity of a specific ion dissolved in a solution into an electrical potential. The voltage is dependent on the ionic activity, according to the Nernst equation.[68] ISE measures the potentiometric response of a phase boundary potential between the aqueous phase and water-immiscible (sensing) phase.

$$EMF = E° + \frac{RT}{z_i F} lna_i = E° + \frac{2.303RT}{z_i F} loga_i$$

where *EMF* represents the measured value, $E°$ is a constant and in the case of the phase boundary potential it depends on solvation of ion *i* in two adjacent phases, *R* is the universal gas constant (8.314 J mol^{-1} K^{-1}), *T* is the absolute temperature in K, *F* is Faraday constant (96485 C), z_i is the charge and a_i is the activity of an ion. The origin of the potentiometric response is discussed later in this chapter.

The research on ion-selective electrodes started in 1906 when Cremer reported that a rise of potential occurred when two solutions with the different activity of hydrogen ions (H^+) were separated by a glass membrane.[69] Those findings have become the main principles of the pH electrode, which is the most used ISE. Glass ISE were later optimised to detect other ions other than H^+, but the biggest breakthrough occurred when ionophore-based polymeric membrane ISEs were introduced.[68,70] One of the most important ionophores to this date is valinomycin which specifically binds K^+ ions (Figure 1.11).[71] Benefits of valinomycin use as ionophore originate from the structure that allows interaction with K^+ ion in stoichiometric ratio 1:1, and also K^+ fits snuggly in the ring, while other ions like Na^+ or Rb^+ are either too big or too small to interact in the desired way. In contemporary designs of ISEs, ionophores are dispersed in

the porous polymer matrices (PVC, polyurethanes, acrylates, perfluoropolymers, etc.) that work as a membrane in the sensing phase. [68,70,72,73]

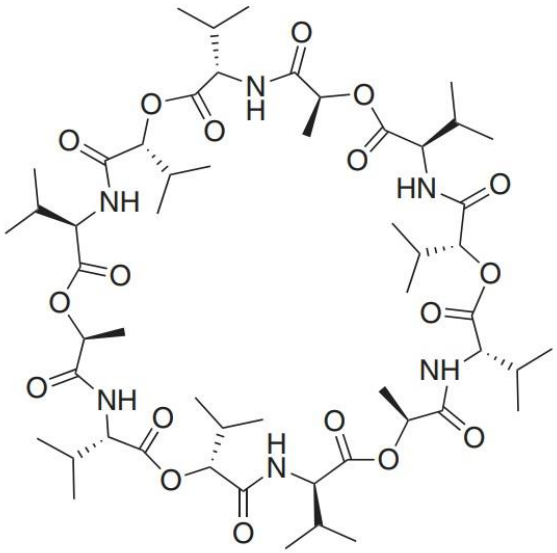

Figure 1.11. Structure of valinomycin.[70]

In the field of ISEs zeolites are for their structural characteristics used as ionophores, too. The first report on zeolites as elements in electrochemical electrodes was published by Marshal in 1939, where the potentiometric response of zeolites in a cement matrix was reported.[74] In 1970, Barrer and James exploited the pore size of zeolite A to detect sodium ions in a mixture with tetraethylammonium species based on the size exclusion from the channels.[75] In addition, the selectivity for dopamine and epinephrine over ascorbic acid was reported based on a difference in the charge of these species.[76] A significant amount of research effort was put into conducting-polymer-zeolite membranes[77–80] and zeolite-modified carbon paste electrodes[81–83] but so far the selectivity and the Nernstian response obtained with valinomycin have not been matched.[84] That fact should not be discouraging for the further study of this type of electrode, because the development of new zeolite structures and matrix types provides a great opportunity to design a highly selective and commercially usable sensor. Also, as

demonstrated in chapter 4, the lack of selectivity could be overcome by using the chemometric methods.

1.8 Chemometric methods

Chemometrics encompasses a number of mathematical, statistical and computational methods that are used to interpret or predict the data in experimental natural sciences. They are most commonly used in experimental design modelling, pattern recognition and multivariate calibration. The latter two method types were used during this thesis.[85,86]

Principal component analysis (PCA) is a pattern recognition method aiming to represent the samples characterized by multiple variables in a series of 2D plots (scores and loadings plots). The PCA scores plots could be used to assess the similarity or dissimilarity of the studied samples and the PCA loadings plots to evaluate the impact of specific sample variables on these differences.[85,86]

Partial least squares (PLS) is a multivariate calibration method that aims to find the linear regression model using the dependent variables (e.g. spectra, chromatograms) and correlate them with the independent variables (sample properties). The calibration process requires an initial data set with values that are of interest for prediction (e.g. spectrum, chromatogram), and the system features that are believed to contribute to the response. Using the data from the training set, the model predicts the response of new samples. In chemistry, PLS is used to determine the influence of sample properties to the observed signal response.[85,86]

1.9 Characterisation techniques

Apart from the evaluation of sensor response towards an analyte, it is necessary to characterise all the constituent materials to determine the physical and chemical properties of the sensor.

Thus, the source of the analytical signal can be identified and the overall sensor performance optimised. The main principles of characterisation techniques are described below.

1.10 Infrared Spectroscopy

Infrared (IR) spectroscopy utilises electromagnetic radiation in the infrared region (~30 to ~12000 cm^{-1}) of the spectrum to characterise the molecular structure based on their bond vibration properties.[87–90] The IR part of the EM spectrum could be further separated into three regions based on the observed vibration types:

- Far-IR (400-30 cm^{-1}): molecular skeleton and crystal lattice vibrations; molecules containing heavy atoms,
- Mid-IR (4000-400 cm^{-1}): lighter element bonds and functional group vibrations; organic compounds, metal-organic complexes and lighter inorganic sample analysis
- Near IR (12820-4000 cm^{-1}): overtones and combination frequencies; mainly used for quantitative analysis

To be IR active, the vibration must be accompanied by a change of the dipole moment upon interaction with IR radiation. For example, molecules with a permanent dipole moment (CO and NO) can be observed using IR spectroscopy. On the other hand, molecules like H_2 and N_2, without a permanent dipole moment are not infrared active. For molecules with N number of atoms, 3N-6 number of vibration modes are possible (3N-5 in case of linear molecules). The IR active vibration modes involve bond stretching or bending (Figure 1.12). Stretching modes can exist as symmetric or asymmetric while bending modes can be classified into four different types. Rocking and scissoring are in-plane modes, twisting and wagging are out-of-plane modes. [87–90]

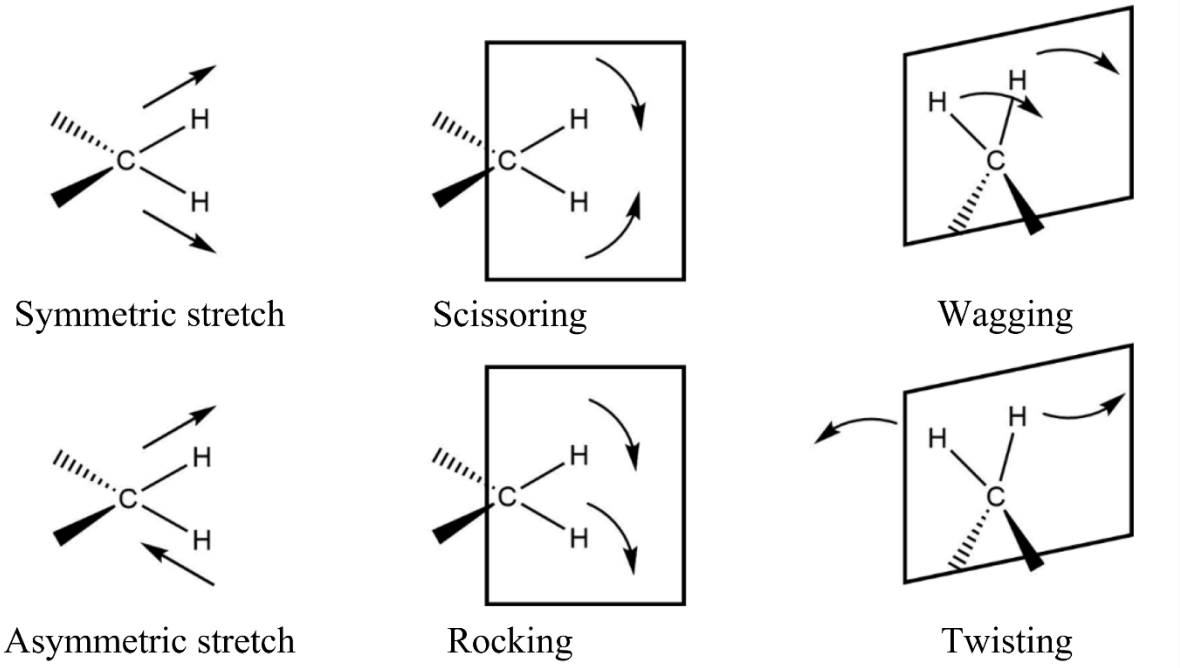

Figure 1.12 Molecular vibration modes, adapted according to the ref.[90]

1.10.1 Instrument components:

Infrared spectrometers can utilise dispersive or Fourier transform (FT) setup. The latter is most common in contemporary laboratories, and it was used during this work, as well, so it is described in more detail. The main components of an FTIR spectrometer are an IR source, interferometer, sample cell and detector (Figure 1.13).

Common IR sources are silicon carbide ("Globar") or ceramic ("Nernst glower") rods which are electrically heated to ~1500 °C. No monochromators or dispersive elements are present in the FTIR instruments, but all the wavelengths are collected simultaneously. The interferometer is used to produce an interference pattern which could be later transformed to a spectrum by using Fourier-transform mathematical operation.

The main parts of an interferometer are a beam-splitter, a fixed mirror, and a moving mirror. The beam-splitter is a semi-transparent mirror positioned at a 45° angle to the incident beam.

The incoming radiation is separated by the beam-splitter and into two beams. One part is transmitted to the fixed mirror while the other one to the moving mirror. The moving mirror is controlled by a special mechanism that changes its position by several millimetres. When both reflected beams reach the beam-splitter, they are recombined and produce an interferogram. The amplitudes of the interferogram are registered by a detector and using Fourier transform mathematical operations extracted from the time domain to the frequency domain. [87–90]

The photonic and thermal detectors are the two most common types of IR detectors. In the former ones (e.g. MCT – mercury cadmium telluride) incident IR radiation causes electron excitations from the ground and first excited states of the semiconductors. Photonic detectors have faster response times and higher sensitivity but require to be cooled down by liquid nitrogen to avoid the thermally induced electron excitation. Thermal detectors are pyroelectric crystals like DTGS (deuterium triglycerine sulphate). They produce a temperature-dependent potential difference when exposed to IR radiation. [87–90]

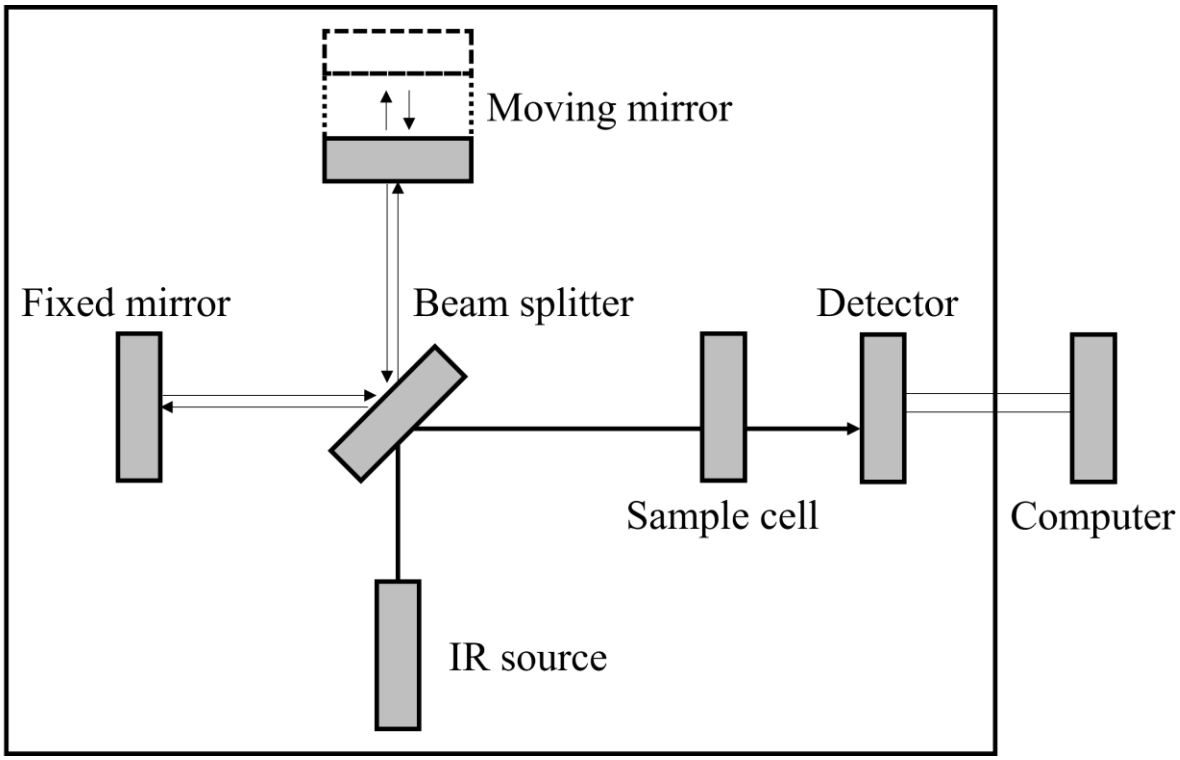

Figure 1.13. FTIR instrument scheme, adapted according to the ref.[90]

1.10.2 Non-dispersive IR spectroscopy

Non-dispersive IR (NDIR) spectroscopy setup does not contain any optical dispersing components (e.g. prisms) that separate the incident light. Rather, the light is filtered after the interaction with the sample and before reaching the detector. Also, the use of microelectromechanical systems enables the instrument miniaturisation viable for gas sensing applications. The three main types of NDIR-based setup are the total absorption, negative filter and positive filter. The latter one is the most common, so the working principle will be further explained. The NDIR system could have either one or two IR sources, where the emitted light is directed to the sample and the reference cell. The reference cell is sealed and contains a non-absorbing gas (e.g. N_2), while the target gas can flow through the sample cell. Since the absorption region of gaseous molecules (CO_x, NO_x, SO_x) overlap with the water adsorption, the optical filters are used to increase the sensitivity of the detectors to the specific gas.[91,92] Usually, the optical width of a filter is from 50 to 300 nm, which would be ~100 cm^{-1} in the mid-IR region. Additionally, the gas adsorbing sensor materials usually shift the adsorption wavelengths, thus further increasing the selectivity of the recorded signal.

1.11 Powder X-ray diffraction

Powder X-ray diffraction is a characterisation technique primarily used for phase identification of polycrystalline samples. It could also be used for semiquantitative analysis, unit cell and crystalline structure determination. The X-ray of the EM spectrum is the most suitable for the diffraction of crystals since the wavelengths (~10^{-10} m) are the same order of magnitude as the interatomic distances. [88,89] X-rays produce constructive interference when interacting with the crystal lattice when the conditions by Bragg's Law are satisfied.

$$n\lambda = 2d\ sin\theta$$

n (integer) represents the order of reflection, θ [°] is the incoming angle of X-rays of a specific wavelength (λ, [m]) and *d* [m] stands for the interplanar spacing (Figure 1.14).

Standard laboratory powder X-ray instrument uses a cathode tube as an X-ray source. In this type of X-ray source, a tungsten filament is heated with high voltage to produce electrons that then bombard the anode.[88,89] If the excited electrons have the energy sufficient to displace the inner shell electrons, the X-rays with wavelengths characteristic to that anode material are produced. During this work, Cu-anode ($K\alpha_1$=1.5406 Å) was used. After passing through several optical components (e.g. monochromatic filter and collimator) the X-rays diffracted from the sample are recorded by the detector and further processed to obtain the powder diffraction pattern.[88,89]

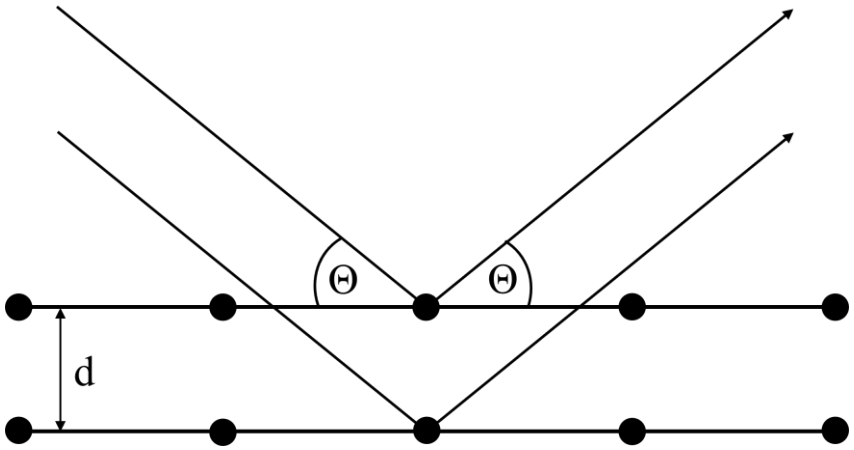

Figure 1.14. Scheme of Bragg's diffraction law.

1.12 Thermogravimetric analysis, differential scanning calorimetry

Thermogravimetric analysis (TGA) and differential scanning calorimetry (DSC) are methods for thermal analysis of the samples. In TGA experiments, the mass of a sample is monitored as a function of temperature. Experiments could be dynamic (temperature ramp), isothermal

(stable temperature over a certain period) or quasistatic (sample is heated stepwise).[88,89] DSC measures the changes in the temperature between the studied sample and a reference. There are two types of DSC setup. In a heat-flux experiment, where the change in heat flow is monitored by temperature sensors and both the sample and a reference crucible are positioned in the same furnace close to each other. The other type is power differential DSC where the reference and the sample are placed in separate furnaces and the change in temperature flow is measured as the amount of electrical power required to match the temperature in both systems. TGA and DSC experiments are usually performed simultaneously and can provide information on sample composition, thermal stability and phase transition.[88,89]

TGA-DSC used in this work had a heat-flux DSC setup. The instrument consists of a furnace with a microbalance. Depending on the required information, thermal experiments could be conducted under an inert atmosphere (N_2, Ar) or using a gas of choice (air, O_2, CO_2, …). Additionally, FTIR or mass spectroscopy instruments can be coupled with a TGA-DSC setup to analyse the thermal decomposition products.[88,89]

1.13 Scanning electron microscopy, energy-dispersive X-ray spectroscopy

Scanning electron microscopy (SEM) is an imaging technique that uses a focused beam of electrons to produce high-magnification (up to 100,000x) sample micrographs.[93–96] In zeolite characterisation it is mainly used for the morphology characterisation and potential impurities detection. The image is produced by scanning the surface of a sample in a raster scan way, i.e. the observed image is a collection of a number of scanned lines. In a laboratory SEM instrument, electrons are produced by heating a tungsten filament using a high voltage (up to 40 kV). The produced electrons are focused on the sample by several electromagnetic lenses.

The micrograph is obtained by the detection of backscattered and secondary electrons. The former are produced by elastic scattering and are used to form elemental composition contrast. The latter are produced by inelastic scattering of the primary electron beam and are used for producing the topographic contrast of the samples. [93–96] The secondary electrons are formed when the incident electrons transfer the energy to the electrons in the sample atoms and then electrons from the sample atoms with sufficient energy leave their orbitals to become the secondary electrons. Both types of electrons are detected by Everhart-Thornley detectors that are based on scintillators. Scintillators transform electron signals into photons which are then amplified by a photomultiplier. To produce a micrograph, samples have to be conductive to prevent charge build-up when exposed to the electron beam. Since zeolites are insulators, it is required to coat them with a conductive layer (~2-20 nm). Usually, carbon, gold or platinum-palladium alloy are used to coat the samples.[93–96] The modern SEM setups are coupled with an energy-dispersive X-ray spectroscopy (EDX) system. EDS is used for elemental characterisation of the samples based on characteristic X-rays produced by the sample atoms.[94,96] Characteristic X-rays are formed when the primary electrons remove the inner shell electrons of an atom. Subsequently, the electron from an outer shell is moved to the vacated spot and an X-ray photon with a wavelength that matched the energy difference is emitted. Since all the elements have unique energy differences, this can be used for element identification. Additionally, since the SEM micrograph is collected by raster-scanning, it is also possible to map the element distribution. [94,96]

Throughout the thesis characterisation techniques such as N_2 adsorption-desorption, solid-state nuclear magnetic resonance, solid-state UV-vis spectroscopy and inductively coupled plasma optical emission spectrometry have been utilised as well. However, since they were not used extensively, their working principles will not be described.

1.14 Potentiometry

Potentiometry is an electrochemical technique that enables the determination of the activity of dissolved charged species based on a difference in potential between two electrodes. The analytical equipment for potentiometric measurement includes a reference electrode, an indicator electrode, a salt bridge and a potential-measuring device. [70,88] A reference electrode has a known electrode potential that is independent of the analyte concentration and remains constant at a constant temperature. Most commonly in an experimental setup, Ag/AgCl or calomel (Hg_2Cl_2) electrodes are used. The indicator electrode develops a potential, E_{ind}, that depends on the activity of the analyte in a predictable way. The third component of a potentiometric cell is a salt bridge that prevents the components of the analyte solution from mixing with those of the reference electrode. The most common salt bridge is a saturated solution of KCl, but saturated solutions of NH_4NO_3 or LiOAc are used as well. As potential-measuring devices voltmeters with high input impedance are used. For optimal performance, the impedance has to be at least three orders of magnitude higher than the electrodes to minimise the current flow.[70,88]

The total measured potential or electromotive force is a sum of the potential differences at all interfaces in an electrochemical cell. However, only the liquid junction potential and the membrane interface potential are sample-dependent. Therefore, the equation describing the potentiometric response can be written as:

$$EMF = E_{const} + E_{mem} + E_{ref}$$

where *EMF* [mV] presents the total response of the electrochemical cell, E_{const} is the non-sample-dependent potential differences, E_{mem} is the potential difference developed at the indicator membrane interface and E_{ref} is the liquid junction potential at the reference electrode. The latter potential difference occurs at the sample solution-salt bridge phase boundary due to

the difference in ion mobility. Generally, using KCl, NH_4NO_3 or LiOAc salt bridges of high concentration (1M) this contribution can be minimised because the mobility of both ions in a pair is similar. Therefore, E_{ref} can be considered as a constant, and the only sample-dependent potential difference is E_{mem}. [70,88]

$$EMF = E_{const} + E_{mem}$$

The potential difference at indicator electrode-sample solution interface can have three contributions: membrane – inner electrode solution (if there is any), transmembrane potential and membrane-sample solution interface potential. The transmembrane potential occurs due to the diffusion of ions from areas of higher to areas of lower concentration within the membrane. However, if there is a uniform distribution within the membrane, the contribution of transmembrane potential is minimal and can be neglected. The indicator electrode membrane-sample solution interface potential difference arises due to charge separation at the phase boundary. [70,88]

$$E_{mem} = \frac{RT}{z_i F} \ln k_i + \frac{RT}{z_i F} \ln \frac{a_i(aq)}{a_i(mem)}$$

R is the universal gas constant (8.314 $JK^{-1}mol^{-1}$), F is the Faraday constant (96485 C mol^{-1}), T [K] represents the temperature, z_i is the charge of the ion, k_i is the measure of lipophilicity of an ion, while a_i(aq) and a_i(mem) are the activity of the uncomplexed ion in both aqueous and membrane phase. Since the k_i factor is related to the energy of phase transfer from aqueous to membrane phase, it is a feature of a single type of ions and it is kept constant. Also, using the assumption that the ion activity in the membrane phase is constant, the equation can be re-written to look as a well-known Nernstian equation,

$$EMF = E° + \frac{RT}{z_i F} \ln a_i$$

where $E°$ represents the constant terms under standard conditions (273 K, 10^5 Pa). For a singly charged ion, the response should be 59.2 mV/dec. [70,88]

1.15 Objectives and thesis outline

This project aimed to develop and characterise novel zeolite-based sensors for environmental applications. The first part of the research work presented in this thesis is focused on the preparation of gas sensors for exhaust fume gases (CO_x, NO_x), while the emphasis in the second part is on the preparation of zeolite-based electrochemical sensors.

The thesis includes six chapters and an appendix:

I. The introductory chapter is focused on providing a brief historical and theoretical background of zeolites, sensors in general and used characterisation techniques.
II. In the 2nd chapter, the preparation, characterisation and screening of Cu-containing zeolites as potential CO environmental sensors is presented.
III. The 3rd chapter describes the preparation and characterisation of selective NO_2 sensors based on hydrophobic Sn-BEA zeolite.
IV. The concept of an ion-sensitive pencil is introduced in chapter 4, and the first zeolite-based multi-sensor array is also demonstrated.
V. In chapter 5, the potentiometric performance of ISP-drawn electrodes is related to the physical and chemical properties of zeolites using chemometric techniques.
VI. In the final chapter, the reported findings are summarised, and future work recommendations are presented.

1.16 References

1. Barrer, R. M. *Hydrothermal Chemistry of Zeolites*. (Academic Press, 1983).

2. Cronstedt, A. F. Natural zeolite and minerals. *K. Sven. Vetenskapsakad. Handl.* **19**, 363 (1756).

3. Damour, A. Comparative examination and analysis of eudialite and eukolite. *C. R. Acad. Sci.* **44**, 975 (1857).

4. Friedel, G. Sur quelques propriétés nouvelles des zéolithes. *Bull. Soc. Fr. Miner. Cristal.* **21**, 5 (1896).

5. Friedel, G. Sur un nouveau silicate artificiel. *Bull. Soc. Fr. Miner. Cristal.* **19**, 363 (1896).

6. Grandjean, F. Coloration des argiles par les couleurs d'aniline. *C. R. Acad. Sci.* **149**, 866 (1909).

7. Seeliger, R. & Lapkamp, K. No Title. *Phys. Z.* **22**, 563 (1921).

8. *Zeolites in Catalysis - Properties and Applications*. (eds. Čejka, J., Morris, R. E. & Nachtigall, P.) (The Royal Society of Chemistry, 2017).

9. Weigel, O. & Steinhoff, E. Adsorption of organic liquid vapors by chabazite. *Z. Krist.* **61**, 125 (1925).

10. McBain, J. W. *The sorption of gases and vapours by solids*. (G. Routledge & Sons, 1932).

11. Barrer, R. M. & Ibbitson, D. A. Occlusion of hydrocarbons by chabazite and analcite. *Trans. Farraday Soc.* **40**, 206 (1944).

12. Barrer, R. M. Syntheses and Reactions of Mordenite. *Treatise Inorg. Gen. Chem.* **6**, 2158 (1944).

13. Milton, R. M. Molecular Sieve Science and Technology A Historical Perspective. *ACS Symp. Ser.* **398**, 1 (1989).

14. Saint-Claire-Deville, H. No Title. *C. R. Acad. Sci.* **54**, 324 (1862).

15. Morey, G. W. & Ingerson, F. E. The pneumatolytic and hydrothermal alteration and

synthesis of silicates. *Econ. Geol.* **32**, 607–761 (1937).

16. Baerlocher, C., Mccusker, L. B. & Olson, D. H. *Atlas of Zeolite Framework types*. (Elsevier, 2007).

17. Barrer, R. M. & Marcilly, C. Hydrothermal chemistry of silicates. Part XV. Synthesis and nature of some salt-bearing aluminosilicates. *J. Chem. Soc. A Inorganic, Phys. Theor.* 2735–2745 (1970).

18. Taylor, W. H. I. The structure of analcite. *Zeitschrift für Krist. - Cryst. Mater.* **74**, 1–19 (1930).

19. Barrer, R. M. & Denny, P. J. Nitrogenous aluminosilicates. in *Hydrothermal chemistry of silicates* 971–982 (1961).

20. Flanigen, E. M., Bennett, J. M., Grose, R. W., Cohen, J. P., Patton, R. L., Kirchner, R. M. & Smith, J. V. Silicalite, a new hydrophobic crystalline silica molecular sieve. *Nature* **271**, 512–516 (1978).

21. Coombs, D. S. *et al.* Recommended nomenclature for zeolite minerals: report of the subcommittee on zeolites of the International Mineralogical Association, Commission on new Minerals and Mineral names. *Can. Mineral.* **35**, 1571–1606 (1997).

22. Meier, W. M. Zeolite structure, and Molecular sieves. *Soc. Chem. Ind.* **10**, 27 (1968).

23. Smith, J. V. Topochemistry of Zeolites and Related Materials. 1. Topology and Geometry. *Chem. Rev* **88**, 149–182 (1988).

24. Xu, R., Pang, W., Yu, J., Huo, Q. & Chen, J. *Chemistry of Zeolites and Related Porous Materials: Synthesis and Structure*. (John Wiley & Sons, 2007).

25. Auerbach, S. M., Carrado, Kathleen, A. & Dutta, P. K. *Handbook of Zeolite Science And Techonology*. *Science* (2003).

26. Löwenstein, W. The distribution of aluminum in the tetrahedra of silicates and aluminates. *Am. Mineral.* **39**, 92–96 (1954).

27. Gary, J. H., Handwerk, G. E. & Kaiser, M. J. Crude Oil Properties. *Pet. Refining. Technol. Econ.* 57–58 (2007).

28. Sandoval-Díaz, L. E., González-Amaya, J. A. & Trujillo, C. A. General aspects of zeolite acidity characterization. *Microporous Mesoporous Mater.* **215**, 229–243 (2015).

29. Busca, G. Acidity and basicity of zeolites: A fundamental approach. *Microporous Mesoporous Mater.* **254**, 3–16 (2017).

30. Thomas, C. L. Chemistry of cracking catalysts. *Ing. Eng. Chem* 25–64 (1949).

31. Milliken, T., Mills, G. & Oblad, D. The Chemical Characteristics and Structure od Cracking Catalysts. *Disc. Farraday Soc.* **8**, 279–302 (1950).

32. Thompson, H. S. On the absorbent power of soils. *J. R. Soc. Engl.* **11**, 68–74 (1850).

33. Way, J. T. On the Power of Soils to absorb Manure. *J. R. Soc. Engl.* **11**, 313 (1850).

34. Eichhorn, H. Ueber die Einwirkung verdünnter Salzlösungen auf Silicate. *Ann. Phys.* **181**, 126–133 (1858).

35. *Introduction to Zeolite Science and Practice*. (eds. Cejka, J., van Bekkum, H., Corma, A. & Schuth, F.) (Elsevier Science, 2007).

36. Dyer, A., Enamy, H. & Townsend, R. P. The Plotting and Interpretation of Ion-Exchange Isotherms in Zeolite Systems. *Sep. Sci. Technol.* **16**, 173–183 (1981).

37. Townsend, R. P. Ion Exchange in Zeolites: Some Recent Developments in Theory and Practice. *Stud. Surf. Sci. Catal.* **28**, 273–282 (1986).

38. Barrer, R. M. & Klinowski, J. Ion-exchange selectivity and electrolyte concentration. *J. Chem. Soc. Faraday Trans. 1 Phys. Chem. Condens. Phases* **70**, 2080–2091 (1974).

39. Barrer, R. M., Klinowski, J. & Sherry, H. S. Zeolite exchangers. Thermodynamic treatment when not all ions are exchangeable. *J. Chem. Soc. Faraday Trans. 2 Mol. Chem. Phys.* **69**, 1669–1676 (1973).

40. Dyer, A., Hudson, M. J. & Williams, P. A. *Progress in Ion-exchange Advances and Applications*. (1997).

41. Franklin, K. R. & Townsend, R. P. Multicomponent ion exchange in zeolites. Part 1.—Equilibrium properties of the sodium/calcium/magnesium–zeolite A system. *J. Chem. Soc. Faraday Trans. 1 Phys. Chem. Condens. Phases* **81**, 1071–1086 (1985).

42. Franklin, K. R. & Townsend, R. P. Multicomponent ion exchange in zeolites. Part 4.—The exchange of magnesium ions in zeolites X and Y. *J. Chem. Soc. Faraday Trans. 1 Phys. Chem. Condens. Phases* **84**, 2755–2770 (1988).

43. Adams, C. J., Araya, A., Carr, S. W., Chapple, A. P., Franklin, K. R., Graham, P., Minihan, A. R., Osinga, T. J. & Stuart, J. A. Zeolite map: The new detergent zeolite. *Stud. Surf. Sci. Catal.* **105**, 1667–1674 (1997).

44. Hulanicki, A., Glab, S. & Ingman, F. Chemical sensors: definitions and classification. *Pure Appl. Chem.* **63**, 1247–1250 (1991).

45. Fine, G. F., Cavanagh, L. M., Afonja, A. & Binions, R. Metal Oxide Semi-Conductor Gas Sensors in Environmental Monitoring. *Sensors* **10**, 5469–5502 (2010).

46. Goldstein, M. Carbon Monoxide Poisoning. *J. Emerg. Nurs.* **34**, 538–542 (2008).

47. Struttmann, T., Scheerer, A., Scott Prince, T. & Goldstein, L. Unintentional Carbon Monoxide Poisoning From an Unlikely Source. *J. Am. Board Fam. Pract.* **11**, 481–484 (1998).

48. *Encyclopaedia of Spectroscopy and Spectrometry*. (eds. Lindon, J. C., Tranter, G. E. & Holmes, J. L.) vol. 2 (Academic Press, 1999).

49. Nandy, T., Coutu, R. A. & Ababei, C. Carbon monoxide sensing technologies for next-generation cyber-physical systems. *Sensors (Switzerland)* **18**, (2018).

50. Kosterev, A. A., Bakhirkin, Y. A. & Tittel, F. K. Ultrasensitive gas detection by quartz-enhanced photoacoustic spectroscopy in the fundamental molecular absorption bands region. *Appl. Phys. B Lasers Opt.* **80**, 133–138 (2005).

51. Li, L., Cao, F., Wang, Y., Cong, M., Li, L., An, Y., Song, Z., Guo, S., Liu, F. & Wang, L. Design and characteristics of quantum cascade laser-based CO detection system. *Sensors Actuators B Chem.* **142**, 33–38 (2009).

52. Wiegleb, G. & Heitbaum, J. Semiconductor gas sensor for detecting NO and CO traces in ambient air of road traffic. *Sensors Actuators B Chem.* **17**, 93–99 (1994).

53. *Carbon Monoxide Detector Market - Forecasts from 2021 to 2026*. (2021).

54. Wilson, M. S. & Gottesfeld, S. Thin-film catalyst layers for polymer electrolyte fuel cell electrodes. *J. Appl. Electrochem.* **22**, 1–7 (1992).

55. Guan, Y., Dai, M., Liu, T., Liu, Y., Liu, F., Liang, X., Suo, H., Sun, P. & Lu, G. Effect of the dispersants on the performance of fuel cell type CO sensor with Pt-C/Nafion electrodes. *Sensors Actuators, B Chem.* **230**, 61–69 (2016).

56. Anderson, G. & Hadden, D. *The Gas Monitoring Handbook*. (Avocet Press Inc., 1999).

57. Sahner, K., Hagen, G., Schönauer, D., Reiß, S. & Moos, R. Zeolites - Versatile materials for gas sensors. *Solid State Ionics* **179**, 2416–2423 (2008).

58. Simon, U., Flesch, U., Maunz, W., Müller, R. & Plog, C. The effect of NH3 on the ionic conductivity of dehydrated zeolites Na beta and H beta. *Microporous Mesoporous Mater.* **21**, 111–116 (1998).

59. Franke, M. E. & Simon. U. Characteristics of Proton Hopping in Zeolite H-ZSM5 - Franke - 2000 - physica status solidi (b) - Wiley Online Library. *Microporous Mesoporous Mater* **41**, 1 (2000).

60. *Proton conductors Solids, Membranes and Gels - Materials and Devices (Chemistry of solid state materials)*. (ed. Colomban, P.) (University Press, 1992).

61. Kelemen, G. & Schön, G. Ionic conductivity in dehydrated zeolites. *J. Mater. Sci.* **27**, 6036–6040 (1992).

62. Nakagawa, M., Okabayashi, T., Fujimoto, T., Utsunomiya, K., Yamamoto, I., Wada, T., Yamashita, Y. & Yamashita, N. A new method for recognizing organic vapor by spectroscopic image on cataluminescence-based gas sensor. *Sensors Actuators B Chem.* **51**, 159–162 (1998).

63. Yang, P., Lau, C., Liang, J.-Y., Lu, J.-Z. & Liu, X. Zeolite-based cataluminescence sensor for the selective detection of acetaldehyde. *Luminescence* **22**, 473–479 (2007).

64. Vilaseca, M., Coronas, J., Cirera, A., Cornet, A., Morante, J. R. & Santamaria, J. Gas detection with SnO2 sensors modified by zeolite films. *Sensors Actuators B Chem.* **124**, 99–110 (2007).

65. Sahner, K., Schönauer, D., Moos, R., Matam, M. & Post, M. L. Effect of electrodes and zeolite cover layer on hydrocarbon sensing with p-type perovskite SrTi0.8Fe0.2O3-δ thick and thin films. *J. Mater. Sci.* **41**, 5828–5835 (2006).

66. Hugon, O., Sauvan, M., Benech, P., Pijolat, C. & Lefebvre, F. Gas separation with a zeolite filter, application to the selectivity enhancement of chemical sensors. *Sensors Actuators B Chem.* **67**, 235–243 (2000).

67. Barsan, N. & Weimar, U. Conduction Model of Metal Oxide Gas Sensors. *J.*

Electroceramics 2001 **7**, 143–167 (2001).

68. Bard, A. J. & Faulkner, L. *Electrochemical Methods: Fundamentals and Applications*. (Wiley, 2000).

69. Cremer, M. Z. Über die Ursache der elektromotorischen Eigenschaften der Gewebe, zugleich ein Beitrag zur Lehre von den polyphasischen Elektrolytketten. *Biol.* **47**, 596 (1906).

70. Buhlmann, P. & Chen, L. D. Ion-Selective Electrodes With Ionophore-Doped Sensing. in *Supramolecular Chemistry: From Molecules to Nanomaterials* (eds. Gale, P. A. & Steed, J. W.) 2539–2579 (Wiley-VCH Verlag, 2012).

71. Moore, C. & Pressman, B. C. Mechanism of action of valinomycin on mitochondria. *Biochem. Biophys. Res. Commun.* **15**, 562–567 (1964).

72. Armstrong, R. D. & Horvai, G. Properties of PVC based membranes used in ion-selective electrodes. *Electrochim. Acta* **35**, 1–7 (1990).

73. Bakker, E., Buhlmann, P. & Pretsch, E. Carrier-Based Ion-Selective Electrodes and Bulk Optodes. 1. General Characteristics. *Chem. Rev.* **97**, 3083–3132 (1997).

74. Marshall, C. E. *The use of zeolitic membrane electrodes*. (1939).

75. Barrer, R. M. & James, S. D. Electrochemistry of crystal-polymer membranes. Part II. Membrane potentials. *J. Phys. Chem.* **64**, 421–427 (1960).

76. Wang, J. & Walcarius, A. Zeolite-modified carbon paste electrode for selective monitoring of dopamine. *J. Electroanal. Chem.* **407**, 183–187 (1996).

77. Johansson, G. & Risinger, L. A cesium-selective electrode prepared from a crystalline Synthetic zeolite of the mordenite type. *Anal. Chim. Acta* **119**, 25–32 (1980).

78. Demertzis, M. & Evmiridis, N. P. Potentials of Ion-exchanged Synthetic Zeolite-Polymer Membranes. *J. Chem. Soc., Faraday Trans. I* **82**, 3647–3655 (1986).

79. Evmiridis, N. P., Demertzis, M. A. & Vlessidis, A. G. Effect of treatment of synthetic zeolite-polymer membranes on their electrochemical-potential response characteristics. *Fresenius. J. Anal. Chem.* **340**, 145–152 (1991).

80. Matysik, S., Matysik, F. M., Mattusch, J. & Einicke, W. D. Application of Zeolite-Polydimethylsiloxane Electrodes to Potentiometric Studies of Cationic Species.

Electroanalysis **10**, 98–102 (1998).

81. Wang, J. & Walcarius, A. Zeolite containing oxidase-based carbon paste biosensors. *J. Electroanal. Chem.* **404**, 237–242 (1996).

82. Walcarius, A. Zeolite-modified paraffin-impregnated graphite electrode. *J. Solid State Electrochem.* **10**, 469–478 (2006).

83. Maximiano, E. M., de Lima, F., Cardoso, C. A. L. & Arruda, G. J. Modification of carbon paste electrodes with recrystallized zeolite for simultaneous quantification of thiram and carbendazim in food samples and an agricultural formulation. *Electrochim. Acta* **259**, 66–76 (2018).

84. Walcarius, A. Zeolite-modified electrodes in electroanalytical chemistry. *Anal. Chim. Acta* **384**, 1–16 (1999).

85. *Practical Guide to Chemometrics*. *Technometrics* (ed. Gemperline, P.) (Taylor & Francis Group, 2006). doi:10.2307/1269627.

86. Brereton, R. G. *Applied Chemometrics for Scientists*. (John Wiley & Sons, Ltd, 2007).

87. Stuart, B. H. *Infrared Spectroscopy: Fundamentals and Applications*. *Infrared Spectroscopy: Fundamentals and Applications* (2005). doi:10.1002/0470011149.

88. Skoog, D. A., West, D. M., Holler, J. & Crouch, S. R. *Fundamentals of Analytical chemistry, 9th ed*. (Brooks/Cole, 2013).

89. Housecroft, C. E. & Sharpe, A. G. *Inorganic Chemistry*. *Inorganic Chemistry* (2018).

90. Pavia, D. L., Lampman, G. M., Kriz, G. S. & Vyvyan, J. R. *Introduction to Spectroscopy*. (Cengage Learning, 2013).

91. *Applied Infrared Spectroscopy*. (ed. Kendall, D. N.) (Reinhold Publishing, 1966).

92. Seitz, J. & Tong, C. *Application Report LMP91051 NDIR CO2 Gas Detection System*. www.ti.com (2013).

93. Echlin, P. *Handbook of Sample Preparation for Scanning Electron Microscopy and X-Ray Microanalysis*. (Springer, 2009).

94. Leng, Y. *Materials Characterization Introduction to Microscopic and Spectroscopic Methods*. (Wiley-VCH Verlag, 2013).

95. *Scanning Transmission Electron Microscopy Of Nanomaterials Basics of Imaging and Analysis*. (ed. Tanaka, N.) (Intenational College Press, 2015).

96. Goldstein, J. I., Newbury, D. E., Michael, J. R., Ritchie, N. W. M., Scott, J. H. J. & Joy, D. C. *Microscopy and X-Ray Microanalysis*. (2018).

Chapter 2

Preparation and screening of Cu-modified zeolites utilised as potential environmental CO sensors

2.1 Introduction

Carbon monoxide is a product of incomplete combustion of organic materials, such as petrol, oil or gas. The concentrations are particularly high in industries, where fossil fuels are combusted for energy generation, and in cities with high levels of traffic. CO is a colourless and odourless gas, which is impossible for humans to detect. Also, it is the leading cause of poisoning in the United States and may account for more than 50% of fatal poisonings reported in many industrial countries.[1] CO binds irreversibly to the iron centre of haemoglobin, the oxygen transport molecule in blood, and in that way prevents oxygen transfer throughout the organism. The maximum time-weighted average exposure value ascribed by the United States National Institute of Occupational Safety and Health is 35 ppm over an 8 h period, while exposure to more than 800 ppm causes a headache and dizziness, and exposure to 12800 ppm results in death within 2-3 minutes.[2,3] Therefore, it is of crucial interest to monitor CO levels.

At the same time, carbon monoxide is a common probe molecule in FTIR characterisation of extraframework cations, metals and acid sites in zeolites.[4] It forms complexes with alkali, alkaline-earth, and transition metal cations at low temperatures (77 K).[5] In the interaction with alkaline and alkaline-earth cations, mainly weak σ-bonds or electrostatic interactions are formed between the C end of CO and the metal cation. No π-back donation can further stabilise the complex since no d electrons are present in the outer shell.[6] However, with transition metals both the cations themselves and the negative charge of the zeolite framework contribute to the stability of the formed complexes.[7] For the applicability of environmental CO sensors, stability of complexes at room temperature or higher is required. A good example of such a stable complex is Cu^+-CO. However, copper can commonly exist as Cu^0, Cu^+ or Cu^{2+}. Due to its electron configuration, CO is preferentially adsorbed on Cu^+ ions because both σ bond and π-back donation stabilize the carbonyl complex that is formed.[5,6,8] Only weak bonding is

observed between CO and Cu^{2+} ions, because the σ component is almost insignificant, and no π back-donation is present. Moreover, with Cu^0 atoms CO forms mainly a π-bond, and those complexes are relatively unstable and tend to dissociate below room temperature.[6] Therefore, this work aims to introduce copper(I) into the zeolites to obtain a functional environmental sensor at room temperature.

Apart from impregnation and ion exchange that are widely used, the introduction of gaseous CuCl as a Cu^+ source was reported previously.[9] However, that procedure requires a specialised setup, and high energy consumption, so it would not be viable for mass production of the potential sensor. Thus, the former two were chosen as copper insertion methods and $CuSO_4$, $Cu(NO_3)_2$ and $Cu(OAc)_2$ solutions as copper sources.

Even though the observed Cu^+-$(CO)_x$ species were well studied and characterised by FTIR, to the best of our knowledge, Cu-containing zeolite species have not been utilised as CO monitoring sensors. Therefore, the aim of this chapter is to demonstrate whether the Cu-modified zeolites can be utilised as potential room-temperature CO sensors.

Also, water coadsorption is a common interference to zeolite performance.[10] To overcome this challenge, hydrophobic zeolites can be utilised. Zeolite hydrophobicity can be achieved by decreasing the aluminium content. [11] However, purely siliceous zeolites (e.g. Silicalite 1) have almost no ion-exchange capacity that is required for the Cu^+ content in the sensor. Therefore, isomorphous substitution by other tetravalent cations (Sn, Ti, Zr, Ga) and fluoride-assisted synthesis provides an alternative approach.[12,13] A good example of such a zeolite is Sn-BEA, which is widely used as a selective biomass-conversion catalyst resistant to degradation by water.[14] Due to its catalytic importance, the synthetic procedures have been optimised to be reproducible in order to prepare crystalline, nearly defect-free zeolites. Hence, Sn-BEA was chosen as a hydrophobic sensor material because the fluoride assisted synthesis allows it to be

hydrophobic, while the Sn in the framework (Si/Sn=64) facilitates the ion-exchange and impregnation.

2.2 Experimental Section

2.2.1 Materials

Commercial zeolites NaX (Si/Al=1.2), ZSM-5 (Si/Al=40), NaY (Si/Al=2.5), MOR (Si/Al=10), FER (Si/Al=10), BEA-12 (Si/Al=12.5) and BEA-19 (Si/Al=19) (all from Zeolyst), copper sulphate pentahydrate ($CuSO_4 \cdot 5H_2O$), copper nitrate trihydrate ($Cu(NO_3)_2 \cdot 3H_2O$) and copper acetate monohydrate $Cu(CH_3COO)_2 \cdot H_2O$ (Acros), NH_4OH 35% water solution, fumed silica (SiO_2) (Sigma), tetraethylorthosilicate ($Si(OC_2H_5)_4$) tetraethylammonium hydroxide ($(C_2H_5)_4N(OH)$, 40%), tin (IV) chloride pentahydrate ($SnCl_4 \cdot 5H_2O$) hydrofluoric acid (HF, 48%) (Sigma Aldrich).

2.2.2 Sensor preparation

As illustrated in Figure 2.1, commercial zeolites were impregnated and ion-exchanged by stirring 3g of a specific zeolite in 60 mL of the 0.1 M $CuSO_4$, $Cu(NO_3)_2$ and $Cu(CH_3COO)_2$ solutions, respectively. For the impregnated samples, after the addition of a zeolite to the solution, the pH of the initial solution (from pH=3.5 for nitrate solution to pH= 4.5 for acetate solution) was adjusted to pH range 5-6 using 35% NH_4OH solution. pH adjustment was carried out to prevent the zeolite structure degradation in acidic media. The maximum possible amount of impregnated copper species on a zeolite was 2000 μmol/g.

The reaction mixture was stirred vigorously for 2 hours at 40°C. In the following step, both the impregnated and ion-exchanged samples were centrifuged for 10 minutes at 5000 rpm, then decanted and washed with 20 mL of distilled water and centrifuged again. The washing process was repeated twice. Samples were then dried at 50°C overnight.

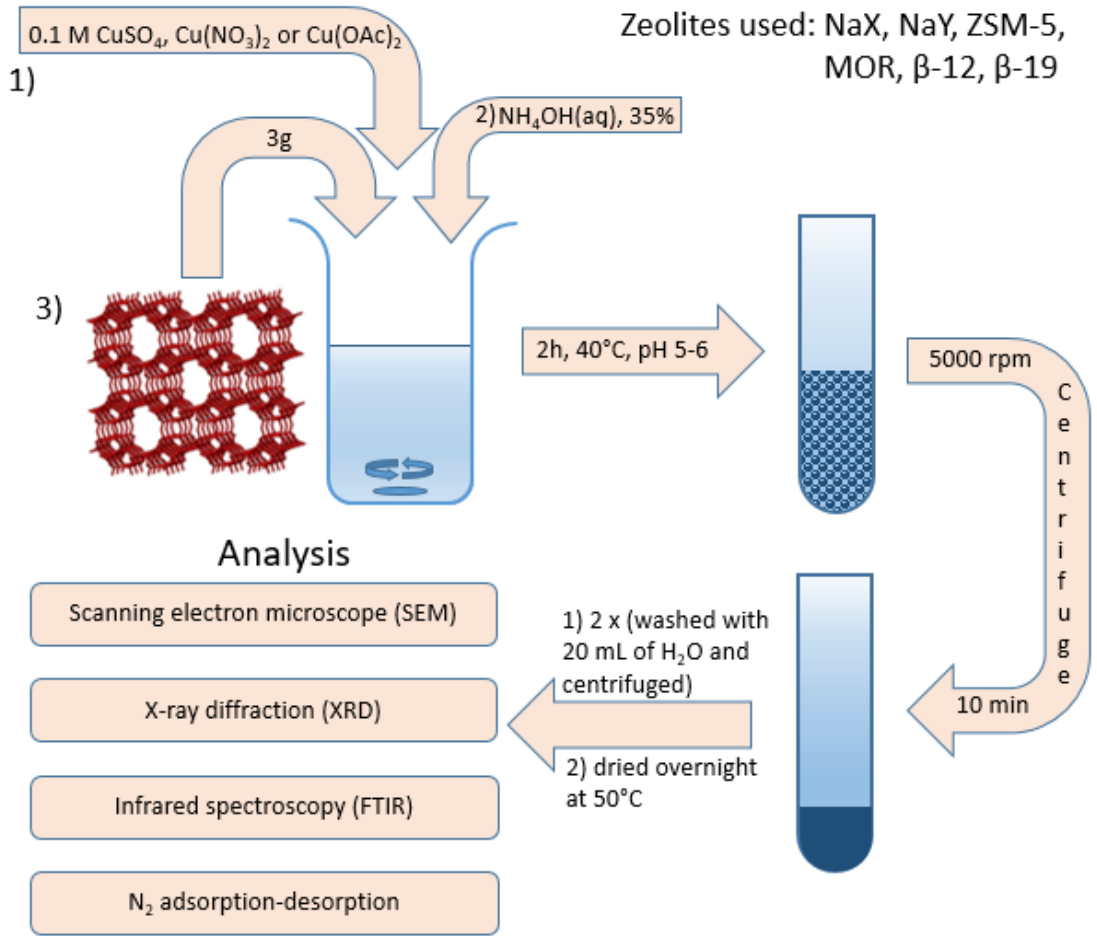

Figure 2.1. Cu-zeolite preparation scheme.

2.2.3 Zeolite synthesis

The hydrophobic Sn-BEA was prepared according to the procedure from ref[15]. Briefly, 5 g of commercial BEA-19 was dealuminated in 125 mL of concentrated nitric acid for 16h at 80 °C. Subsequently, the dealuminated sample was washed 6 times with 25mL of deionized water and dried overnight. Thus prepared material was used as a seed in further steps. The synthesis gel was prepared by mixing 6.98 g of tetraethylorthosilicate and 7.67 g of tetraethylammonium hydroxide. Subsequently, 0.12 g of tin (IV) chloride pentahydrate was dissolved in 0.6 mL of water and added dropwise to the gel. The Si/Sn molar ratio in the gel was 100. The gel was stirred for 12h in a closed container and then 3 days in an open container. After allowing the

excess water and ethanol to evaporate, 0.74 g of hydrofluoric acid was added to the gel. 0.085 g of seeds suspended in 0.58 g of water was added to a homogenized gel and mixed thoroughly. The mixture was then heated for 6 days at 140 °C in an autoclave. The products were then washed 5 times by 25 mL of water, followed by washing 5 times by 25 mL of acetone. Samples were dried overnight.

2.2.4 Preparation of sensors for in situ flow experiments

Sensors were made according to the previously described procedure[16]. Silicon wafers were cut to 10x10 mm squares and cleaned with ethanol and acetone. The as-prepared sample was dispersed in acetone (4 wt%), mixed with 3-propylcelulose as a surfactant and deposited in several layers as a thin film on silicon wafers (10x10 mm) by spin coating (Laurell spin coater, model WS-400B-6NPP-LITE). Prepared films were then calcined for 30 minutes at 450 °C (ramp rate 5 °C/min).

2.2.5 Sensor characterisation

Zeolite samples were characterised by scanning electron microscopy (SEM) (Hitachi TM 3000 with Bruker EDX (energy-dispersive X-ray analysis) analytical system at 500x magnification, 300s EDX exposition time), X-ray powder diffraction (XRD) (Bruker D8 Advance diffractometer, Cu Kα at 40 kV and 40 mA, 2θ=5−60°), in situ XRD experiments (Bruker D8 Advance, Cu Kα at 40 kV and 40 mA, 2θ=5−60°, ramp 1 °C/min to 450 °C, pattern collected at 200 °C), thermogravimetric analysis (TGA) (Rheometric Scientific STA 1500, 20-800 °C, 10°C/min, 40 mL/min N_2 flow) and Fourier transform infrared spectroscopy (FTIR) (Thermo iS10 spectrometer with a custom-made vacuum cell, 6000−1000 cm^{-1}, 64 scans, 4 cm^{-1} resolution, transmission mode).

Prior to collecting SEM micrographs and the EDX analysis, samples were pressed into pellets (13mm, 50-60 mg) by a hydraulic press, mounted on aluminium holders, fixed by carbon

cement and carbon-coated. Due to the limitations of the instrument, the used magnification was 500X, which provided an observation area of ~300x300 μm. The samples had to be carbon-coated, hence, carbon percentage was excluded from elemental analysis, which only affected the analysis of copper-acetate-treated samples. In addition, oxygen was omitted due to its constant ratio throughout the zeolite samples. Elements of interest were silicon, aluminium, and copper for all the samples and sulphur and nitrogen for sulphate- and nitrate-based samples, respectively.

Before FTIR analysis samples were also pressed into pellets (13 mm diameter, 10−15 mg), activated in a vacuum cell (Figure 2.2) by heating to 450 °C (ramp 1 °C/min), kept 5 h at 450 °C, then the sample was cooled to 30 °C in a vacuum, and its IR spectrum was collected. In a preliminary test 1 mbar of CO was introduced into the cell at 30 °C, the IR spectrum of the sample was collected in the CO atmosphere, the sample was evacuated for 10 minutes, and another spectrum was collected. In the titration experiment, ~1.2 μmol of CO was added to the cell before collecting each spectrum.

Figure 2.2. FTIR spectrometer and vacuum cell.

2.2.6 Operando gas detection

Experiments testing the sensor performance were conducted using a custom-made operando cell in a flow system, with argon as a carrier gas containing 100 ppm of water. Prior to the controlled adsorption of individual gas mixtures (20 to 5000 ppm of CO, CO_2, NO or NO_2 in Ar) the samples were activated in situ at 250 °C for 30 minutes (ramp rate 3 °C/min) and cooled down to the ambient temperature. The spectra were collected using a Thermo iS50 spectrometer, equipped with an MCT detector, using 64 scans at 4 cm^{-1} resolution in the 6000−1000 cm^{-1} spectral range. All presented sensor performance data are the difference spectra obtained by subtraction of the zeolite spectrum prior to the gas adsorption experiment from the spectrum of a sample at a specific concentration of the target gas. Since some water vapour was inherently present in the argon flow, gas-phase water correction was applied.

2.3 Results and discussion

To prepare the optimal zeolite-based CO sensor for environmental applications, a screening of a variety of commercially available zeolites was undertaken. Selected zeolites were chosen because of their wide range of Si/Al ratios (Si/Al=1-40), pore width (5.0-7.4 Å) and channel networks (1D-3D), and crystallite sizes (0.04-0.80 μm), Table 2.1.[17]

Table 2.1 Zeolite properties of the zeolites used in this chapter,
Si/Al values were determined by the manufacturers

	Si/Al	**Pore Size, Å**	**Largest Channel, MR**	**Channel Network**	**Crystallite Size, µm**	**Extraframework Cation**
MOR	10.0	6.7	12	1D	0.74	NH_4^+
BEA-12	12.5	6.8	12	3D	0.04	NH_4^+
BEA-19	19.0	6.8	12	3D	0.04	NH_4^+
ZSM-5	40.0	5.5	10	2D	0.52	NH_4^+
NaX	1.3	7.4	12	3D	0.78	Na^+
NaY	2.6	7.4	12	3D	0.78	Na^+
FER	10.0	5.0	10	2D	0.6	Na^+

2.3.1 SEM and EDX

In the beginning, both copper introduction methods were compared on a model system, using MOR and the solution of $Cu(NO_3)_2$. SEM-EDX was used to determine the chemical composition. The silicon to aluminium ratio was monitored to detect the possible structure degradation due to the dealumination of a zeolite in acidic media. The atomic percentages data for all the used samples are summarised in Table 2.2.

From Table 2.2 can be concluded that the copper loading for the MOR impregnated by $Cu(NO_3)_2$ was more than five times greater than the ion-exchanged one. Since the higher copper loading should lead to the higher total capacity of the sensor towards CO, impregnation was chosen as a method for screening the sensing performance of other zeolites. Additionally, the Si/Al ratio of the ion-exchanged sample increased, indicating the potential damage to zeolite frameworks during ion-exchange using nitrate solution (pH < 7).

Table 2.2. EDX characterisation data of Cu-impregnated samples (*ion-exchanged sample).

Zeolite	Si (at.%)	Al (at.%)	Cu (at.%)	Si/Al	Cu/Al
BEA-12 $CuSO_4$	78.8	6.3	11.6	12.5	1.8
BEA-12 $Cu(NO_3)_2$	63.7	5.2	13.5	12.2	2.6
BEA-12 $Cu(OAc)_2$	84.2	6.6	9.2	12.8	1.4
BEA-19 $CuSO_4$	80.1	4.2	12.5	19.0	3.0
BEA-19 $Cu(NO_3)_2$	80.0	4.5	15.5	17.9	3.5
BEA-19 $Cu(OAc)_2$	87.2	4.5	8.4	19.5	1.9
ZSM-5 $CuSO_4$	84.1	2.4	10.8	35.2	4.5
ZSM-5 $Cu(NO_3)_2$	68.5	2.0	13.4	33.7	6.6
ZSM-5 $Cu(OAc)_2$	87.1	2.4	10.5	36.1	4.4
MOR $CuSO_4$	76.6	8.2	12.6	9.3	1.5
MOR $Cu(NO_3)_2$	78.4	8.4	13.2	9.4	1.6
MOR $Cu(OAc)_2$	80.5	8.1	11.4	9.9	1.4
NaX $CuSO_4$	39.9	30.4	11.7	1.3	0.4
NaX $Cu(NO_3)_2$	42.1	31.6	11.0	1.3	0.4
NaX $Cu(OAc)_2$	44.9	31.7	8.6	1.4	0.3
NaY $CuSO_4$	54.5	20.3	12.6	2.7	0.6
NaY $Cu(NO_3)_2$	55.4	20.4	15.3	2.7	0.7
NaY $Cu(OAc)_2$	59.9	21.6	9.1	2.8	0.4
FER $CuSO_4$	81.3	8.4	8.2	9.7	1.0
FER $Cu(NO_3)_2$	74.3	7.4	11.4	10.1	1.5
FER $Cu(OAc)_2$	82.6	8.7	8.8	9.5	1.0
MOR $Cu(NO_3)_2$ *	89.4	8.3	2.3	10.7	0.3

It can be observed that the Si/Al ratios of the zeolites in Table 2.2 are close to the listed in the product specifications of parent zeolites, which is indicative of zeolite framework preservation during the impregnation process. Copper loadings showed a trend that samples from acetate solutions have the lowest value, increasing to sulphate and nitrate. Differences between the highest and the lowest value for each zeolite were in most cases ~3%, while in the case of BEA-19, the difference was the highest (~7%).

2.3.2 XRD

As mentioned above, impregnation methods were used to introduce copper to the zeolites since ion-exchanged zeolites had a significantly lower Cu-loading. In this work, the difference between the two mentioned copper introduction methods was in the pH of an exchange solution. When the pH depended only on the initial solution of the copper salt, the ion exchange occurred. In cases where the pH of a solution was adjusted, no ammonia complexes are detected, only the basic analogues of initial copper salts precipitated (Figure 2.3). For example, from $Cu(NO_3)_2$ solution, $Cu_2(NO_3)(OH)_3$ has precipitated, which is in nature present in two polymorphic forms as minerals gerhardtite (orthorhombic) and rouaite (monoclinic). In these reaction conditions, only the monoclinic form is noticed. The XRD patterns of precipitated salts were compared to the calculated patterns from the Inorganic Chemical Structural Database (ICSD) and International Centre for Diffraction Data (ICDD) databases (Figure 2.3a). From the $CuSO_4$ solution several basic salts could precipitate, but only $CuSO_4 \cdot 3Cu(OH)_2$, known as brochantite, was observed (Figure 2.3b). In the case of $Cu(OAc)_2$ solution $[Cu(OAc)_2]_2 \cdot Cu(OH)_2 \cdot 5H_2O$ precipitated, which is known as a blue-green colour pigment blue Verdigris (Figure 2.3c). The presence of the basic salts was detected by comparison of XRD patterns of parent and impregnated zeolites before high-temperature activation on the example of $Cu(NO_3)_2$ treated MOR (Figure 2.4).

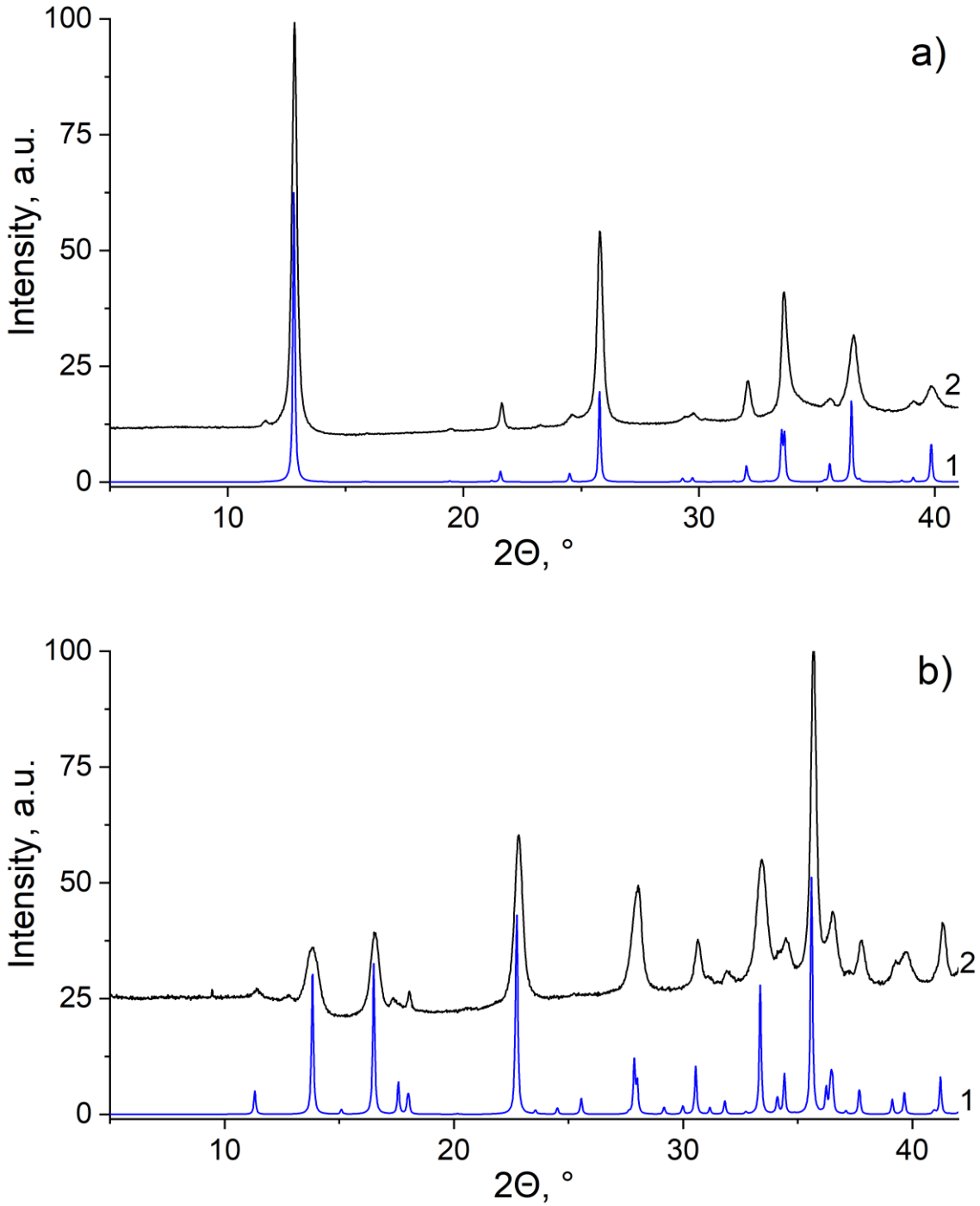
a)
Intensity, a.u.
100
75
50
25
0
10
20
30
40
2Θ, °
2
1
b)
Intensity, a.u.
100
75
50
25
0
10
20
30
40
2Θ, °
2
1

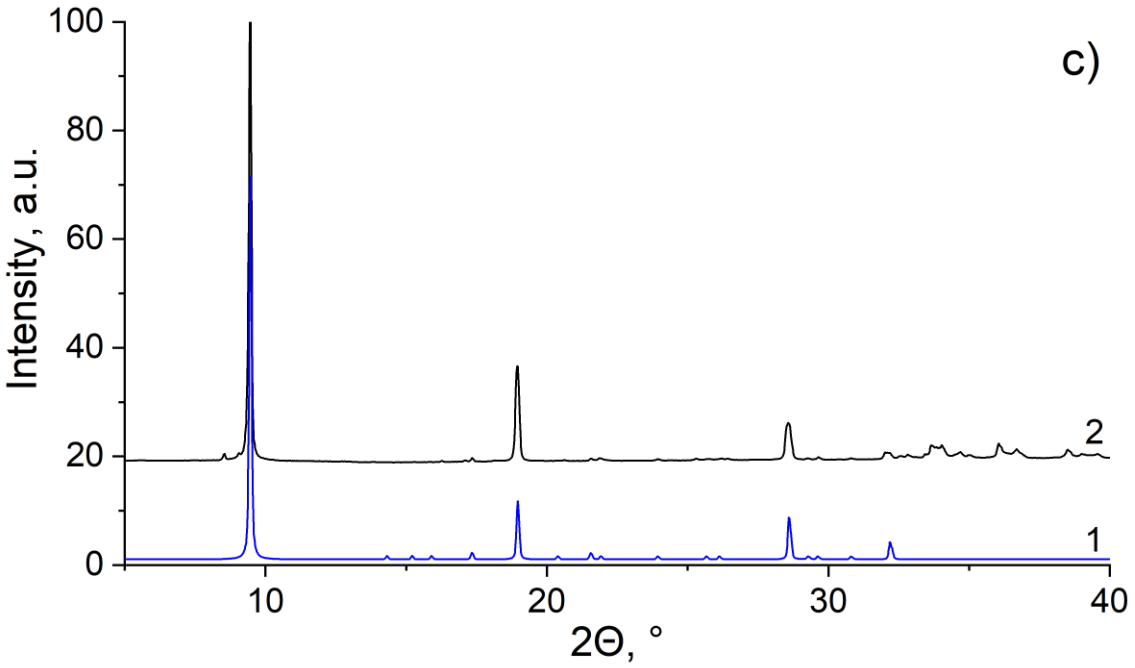

Figure 2.3. Calculated (1) and experimental (2) XRD patterns of $Cu_2(NO_3)(OH)_3$ (a), $CuSO_4 \cdot 3Cu(OH)_2$ (b) and $[Cu(OAc)_2]_2 \cdot Cu(OH)_2 \cdot 5H_2O$ (c); calculated patterns are simulated from the structures deposited in ICSD and ICDD.

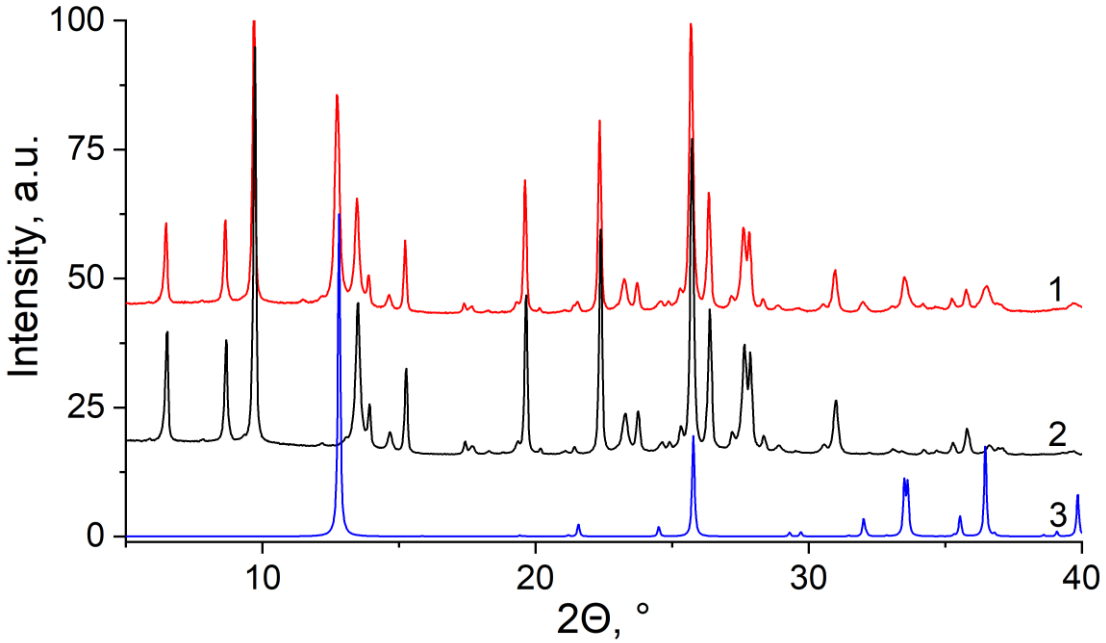

Figure 2.4. XRD patterns of Cu-MOR (1), MOR (2), and $Cu_2(NO_3)(OH)_3$ (3), patterns are offset for clarity.

In Figure 2.4, XRD patterns of MOR and Cu-MOR have been collected from experimental samples, while the XRD pattern of $Cu_2(NO_3)(OH)_3$ is calculated from the structure deposited in ICSD. In the Cu-MOR pattern, four additional peaks can be noticed (2Θ= 12.8°, 32.0°, 33.5°, 36.4°) that do not appear in the parent MOR pattern, but they correspond to the peaks from the calculated $Cu_2(NO_3)(OH)_3$ pattern. Therefore, it can be concluded that the new phase is present in the copper impregnated sample.

Prior to FTIR characterisation samples were pressed into pellets (S=1.22 cm^2, m=10−15 mg), and activated under vacuum at 450 °C for 5 hours to remove the adsorbed water and reduce from Cu^{2+} to Cu^+.[5,9,18] After the activation process, the pellets changed the colour from distinctive blue-green to black. This was an indication that the portion of Cu-complexes adsorbed on the zeolite surface, transformed into copper (II) oxide (Figure 2.5). This statement was confirmed by the in situ XRD experiment simulating the activation conditions. The vacuum conditions during the activation process were simulated by the flow of N_2 as an inert gas. Before the activation $Cu_2(NO_3)(OH)_3$ phase was present, whose peaks (2Θ= 12.8°, 32.0°, 33.5°, 36.4°) disappeared after the activation and new peaks (2Θ= 29.5°, 32.5°, 35.5°, 38.8°) appeared which correspond to copper (II) oxide, while no copper (I) oxide peaks were observed (Figure 2.6).

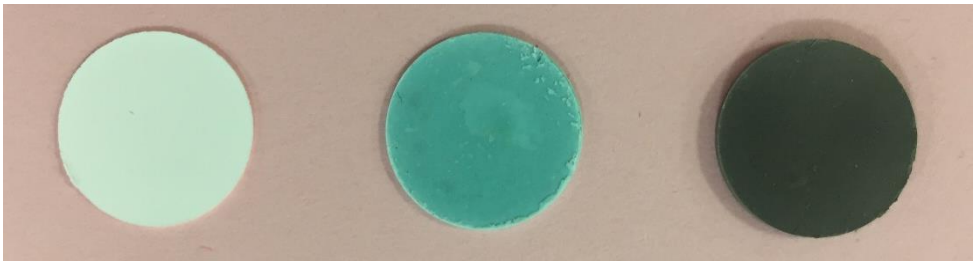

Figure 2.5. Zeolite samples pressed into pellets, parent zeolite MOR (left),
copper impregnated zeolite before activation (middle),
copper impregnated zeolite after activation (right).

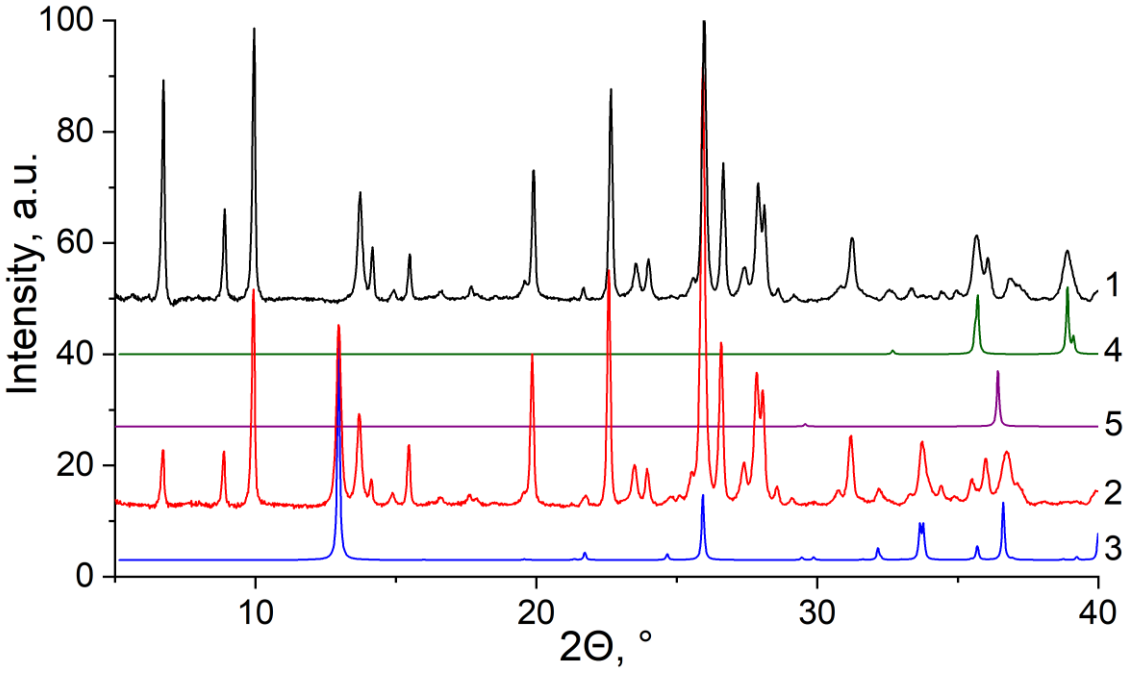

Figure 2.6. XRD patterns of MOR $Cu(NO_3)_2$ after activation (1), MOR $Cu(NO_3)_2$ before activation (2), the calculated pattern of $Cu_2(NO_3)(OH)_3$ (3), the calculated pattern of CuO (4), the calculated pattern of Cu_2O (5) patterns are offset and calculated patterns are scaled for clarity.

2.3.3 FTIR

During FTIR characterisation, the area of most interest has been 2000-2200 cm^{-1} where characteristic bands of Cu···CO complexes appear. Absorption peaks of gaseous CO are observed between 2171 and 2120 cm^{-1}, while the bands representing Cu^+-CO interaction within the zeolite framework are observed from 2150 to 2160 cm^{-1}. Apart from the main Cu^+-CO band, the Cu^+-$(CO)_2$ and Cu^+-$(CO)_3$ bands have been described. [5,6] During the CO adsorption-desorption measurements performed in this research, the most intense band has been detected at ~2155 cm^{-1}, which corresponds to the symmetric stretching vibration of the Cu^+-CO bond, while bands at ~2125 and 2177 cm^{-1} appeared as shoulders too. Those two bands can be assigned to Cu^+-$(CO)_2$ symmetric and antisymmetric stretching, respectively.[5,8]

Table 2.3. FTIR bands of CO adsorbed on Cu-impregnated zeolites,
*data collected during this work.

Zeolite	Cu^+-CO*, cm^{-1}	Cu^+-$(CO)_2$*, cm^{-1}	Cu^+-CO, cm^{-1}	Cu^+-$(CO)_2$, cm^{-1}
NaX	2153	2176, 2113	-	
NaY	2148	2157, 2108	2143[19]	2168, 2135[19]
MOR	2156	2178, 2108	2159[20]	2180, 2152[20]
FER	2177	2155, 2115	2157[21]	2178, 2142[21]
BEA-12	2154	2180, 2130	2157,[19] 2158[22]	2180, 2152[19] 2180, 2152[22]
BEA-19	2157	2179, 2132	-	
ZSM-5	2156	2176, 2133	2158, [19] 2157 [23]	2178, 2150[19] 2178, 2151[23]

Since Cu^{2+} and Cu^0 interactions with CO are too weak to be detectable at room temperature, all the observed IR bands can be assigned to Cu^+-CO. Zeolites are a crucial component of a Cu^+-based sensor since basic copper salts impregnated on non-zeolitic systems such as silica have shown no response towards CO at room temperature (Figure 2.7). Zeolite structure favours the existence of single Cu^+ cations by having dispersed cationic sites and smaller cages that would further stabilise the isolated Cu^+ cations.[5] Also, the presence of Bronsted acid sites within the framework can contribute to the controlled reduction of Cu^{2+} to Cu^+, rather than the complete reduction to elementary copper.

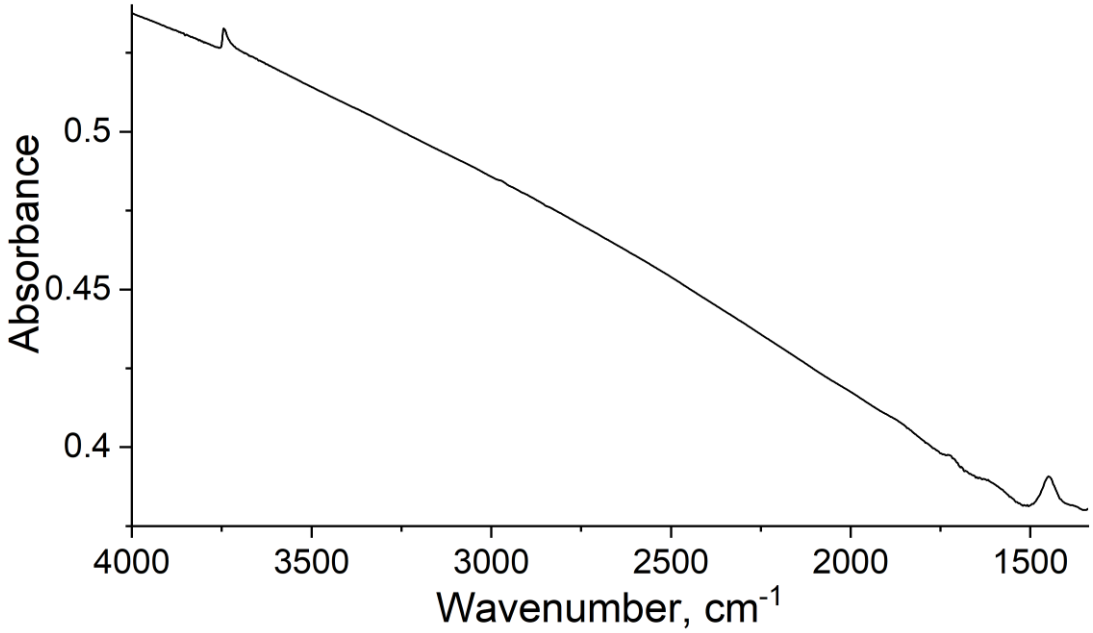

Figure 2.7. FTIR spectrum of CO adsorbed on $Cu(NO_3)_2$-impregnated fumed silica.

The reduction of Cu^{2+} to Cu^{+} has been observed only within the zeolite channels. Using MOR treated by $Cu(NO_3)_2$ solution as an example, both the ion-exchanged and impregnated samples have similar peak shapes and positions, but the total peak area is more than three times higher for the impregnated sample (Figure 2.8). This ratio is smaller than the copper loading ratio determined by EDX, which can be explained by the distribution of Cu within the zeolites, which is not completely dispersed as isolated Cu^{+} ions, rather than a mixture with Cu^{0} and Cu^{2+},[8] indeed, bulk CuO has been observed XRD patterns (Figures 2.5 and 2.6).

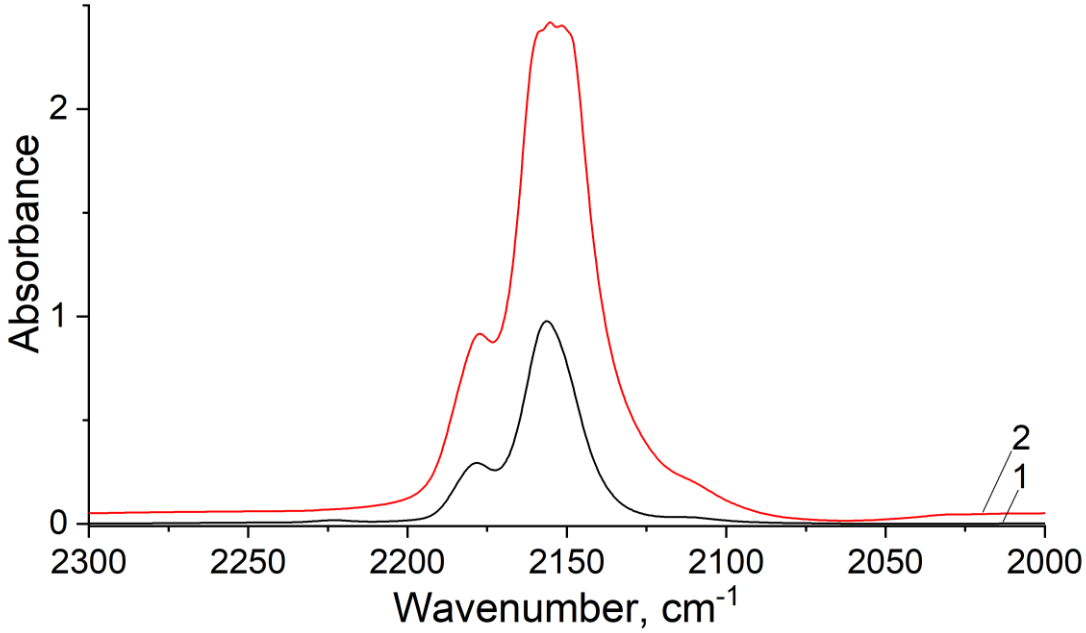

Figure 2.8. Difference FTIR spectra of CO adsorbed on MOR ion-exchanged (one) and impregnated (two) by $Cu(NO_3)_2$ solution.

Dependence on the copper source is demonstrated in the example of BEA-12, where different copper sources have minor variations in peak shape and position (Figure 2.9).

The theoretical calculations have shown that the Cu^+-CO interaction depends not only on the position of copper ions but on the surrounding framework as well.[7] FTIR spectra collected in this work are in agreement with these findings and indicate that the positions and relative intensities of the peaks vary for different zeolite frameworks (Figure 2.10).

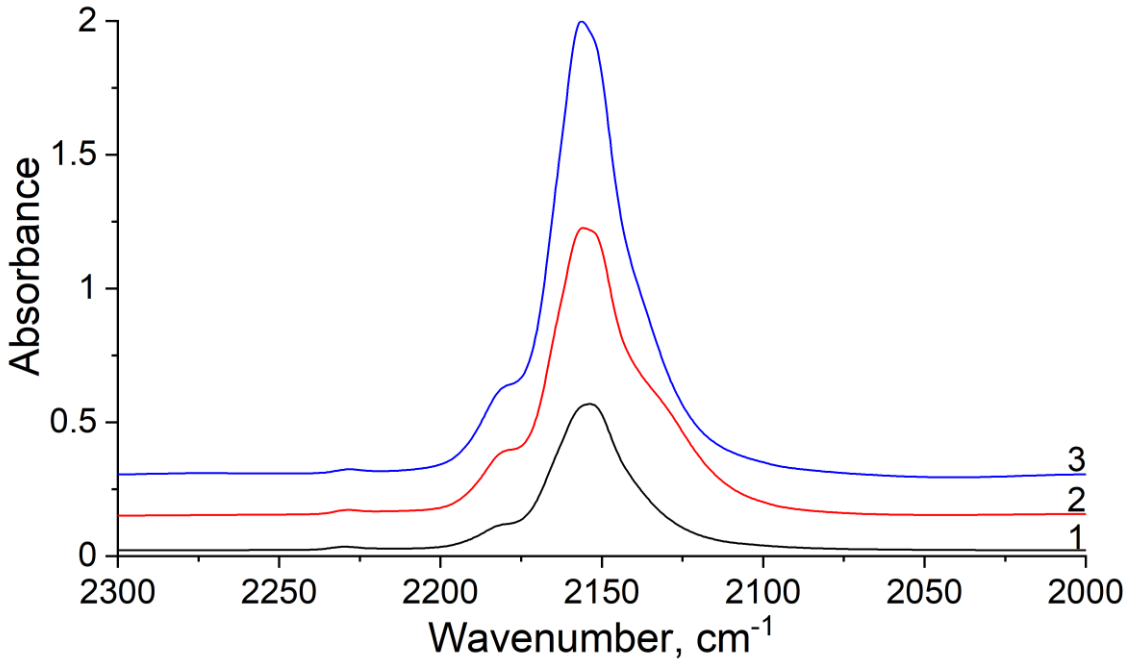

Figure 2.9. Difference FTIR spectra of CO adsorbed on BEA-12 impregnated with $CuSO_4$ (1), $Cu(NO_3)_2$ (2), $Cu(OAc)_2$ (3), spectra are offset for clarity.

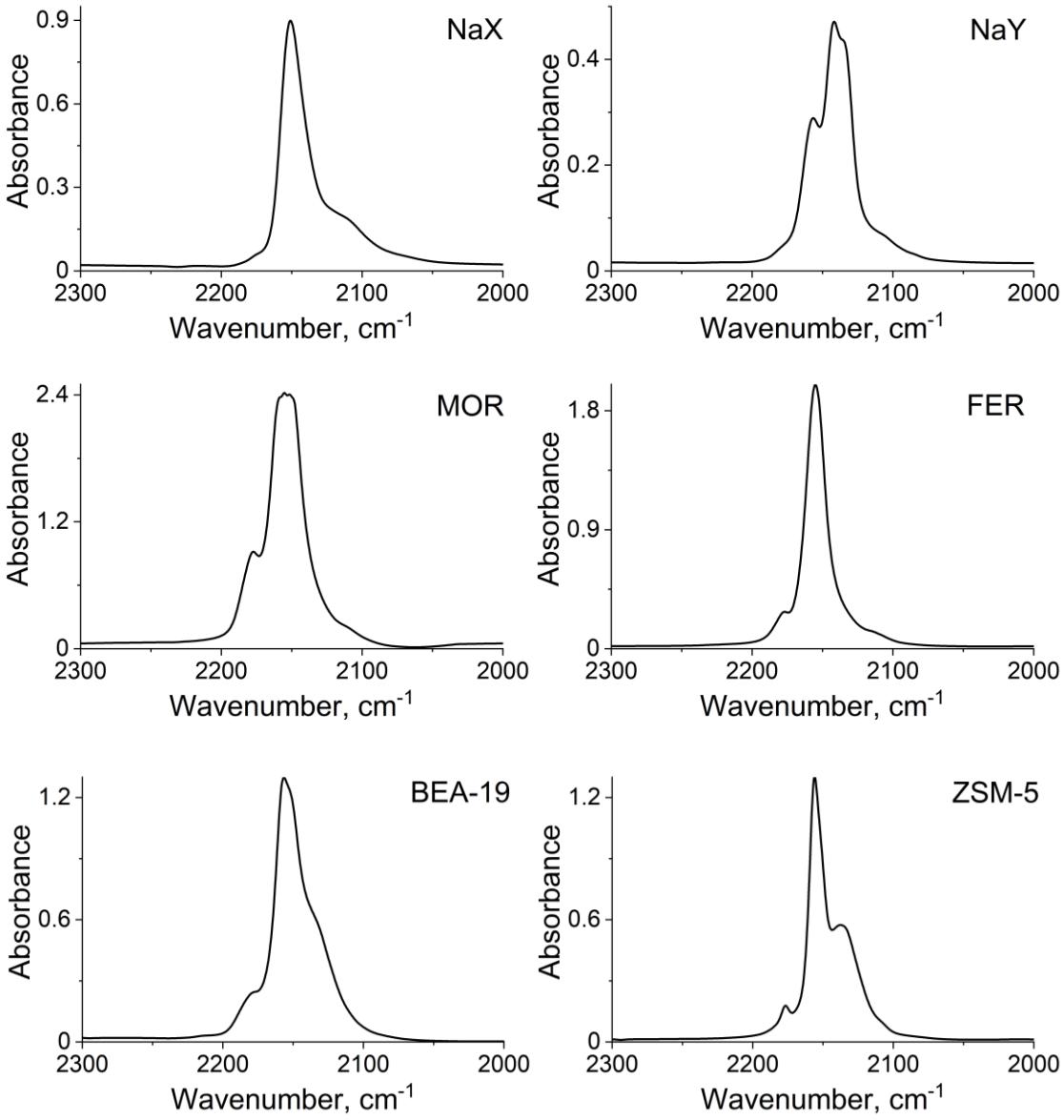

Figure 2.10. Difference FTIR spectra of CO adsorbed on $Cu(NO_3)_2$ impregnated zeolites.

From the measured peak area, the total amount of adsorbed CO can be calculated by the Beer-Lambert law (equation 1).[24]

$$n(CO) = \frac{A(peak) \cdot S(sample)}{\varepsilon(peak) \cdot m(sample)}$$

where (ε) is the molar extinction coefficient acquired from the literature.[6] A is for the peak area [cm^{-1}], S is the sample surface pressed into a disk [cm^2], ε is a symbol for molar extinction coefficient of a Cu-CO^+ interaction [cm μmol^{-1} g^{-1}], m is mass of a sample [g] and n is the

amount of CO [μmol]. Data for all the used zeolites are summarised in Table 2.4. Even though the observed peaks are a combination of bands representing symmetric stretching of Cu^{+}-CO and symmetric and asymmetric stretching of Cu^{+}-$(CO)_2$, the total area of the peaks is assumed as the 1:1 complex since only the molar extinction coefficient of the Cu^{+}-CO band has been published.[6] Also, bearing in mind the most likely sensor design which will utilise non-dispersive infrared (NDIR) technology, where the spectral resolution is significantly lower, this approximation seems satisfactory. Since there has been an excess of CO in the system, then the calculated amount of CO equals the amount of Cu^{+} in the sample (Table 2.4). Not all copper in the samples is Cu^{+}, due to autoreduction and disproportionation during which Cu^{2+} and Cu^{0} are formed.[8] From the total amount of copper in the sample, a portion is utilised for the detection and sensing of CO. This leads to a goal for future research, which is to optimize the percentage of copper (I) either by controlled reduction during activation or by impregnation using different copper sources.

Table 2.4. CO adsorption-desorption FTIR data, scaled to 10 mg, ε = 13.5 cm μmol^{-1},[6] *ion-exchanged sample, #determined by FTIR, †determined by EDX, **n(CO) ≈ n(Cu^+).

Zeolite	Area CO	μmol CO/g of zeolite #	μmol Cu/g of zeolite, total †	Cu^+/Cu**
BEA-12 $CuSO_4$	25.4	164	1545	0.1
BEA-12 $Cu(NO_3)_2$	25.9	370	1279	0.3
BEA-12 $Cu(OAc)_2$	51.6	495	1192	0.4
BEA-19 $CuSO_4$	27.9	181	1190	0.2
BEA-19 $Cu(NO_3)_2$	25.4	417	1126	0.4
BEA-19 $Cu(OAc)_2$	65.3	628	735	0.9
ZSM-5 $CuSO_4$	27.8	102	1498	0.1
ZSM-5 $Cu(NO_3)_2$	26.8	307	1315	0.2
ZSM-5 $Cu(OAc)_2$	56.7	292	797	0.4
MOR $CuSO_4$	76.9	672	1227	0.5
MOR $Cu(NO_3)_2$	114.4	801	1101	0.7
MOR $Cu(OAc)_2$	62.0	549	899	0.6
NaX $CuSO_4$	19.7	148	1173	0.1
NaX $Cu(NO_3)_2$	25.4	236	1096	0.2
NaX $Cu(OAc)_2$	26.8	432	858	0.5
NaY $CuSO_4$	7.2	52	1228	0.0
NaY $Cu(NO_3)_2$	16.3	144	1432	0.1
NaY $Cu(OAc)_2$	10.4	121	829	0.1
FER $CuSO_4$	29.3	265	820	0.3
FER $Cu(NO_3)_2$	46.7	422	1135	0.4
FER $Cu(OAc)_2$	44.5	402	877	0.5
MOR $Cu(NO_3)_2$ *	26.2	237	229	1.0

It can be concluded from the table that the highest Cu^+/Cu ratio is in the ion-exchanged sample. However, in terms of the total amount of Cu^+ sites, impregnated counterpart has more than three times as much Cu^+ that could interact with CO. From the maximum possible amount of 2000 μmol of copper per gram of a zeolite, impregnated samples contained between 735 - 1545 μmol of Cu. Considering the data presented in Table 2.4, a trend of the greatest Cu^+/Cu ratios

of copper in acetate samples can be seen. In general, copper nitrate impregnated samples showed the greatest values in the total amount of Cu in the sample. Copper acetate impregnated sample ($Cu(NO_3)_2$ BEA-19, Table 2.4) demonstrated the highest percentage of copper (I) and the sample with the highest value of the total copper present in the sample were MOR impregnated by $Cu(NO_3)_2$. In general, faujasite samples showed the lowest values in both categories, while on the other hand, MOR and BEA samples showed the highest values. Several factors could contribute to these results, e.g. Si/Al ratio, channel network and pore size. In the zeolites such as NaX and NaY, with Si/Al ratio is close to 1.3 - 2.6, it is more favourable to exchange them with double charged cations since the aluminium sites and thus the negative charges are positioned in greater proximity compared to the zeolites with high Si/Al ratio. Additionally, the proximity of two copper cations within the framework gives them a higher probability of disproportionation and autoreduction. For the zeolites with lower Si/Al ratios, the probability for single charged points to be located further away from each other is higher, so it should be more favourable for Cu^+ species to exist. However, the higher the Si/Al ratio, the lower the number of possible exchange sites for Cu^+ cations. The sensitivity of ZSM-5 zeolite (Si/Al=40) was among the lowest, most likely due to the lower total amount of possible Cu^+ sites. It could be concluded that the optimal values are from Si/Al=10-20 since MOR and BEA-19 showed the best Cu^+/Cu ratios among the impregnated samples. Also, it has been found that most of the Cu^+ species in MOR are located in the side pockets of the main channel and therefore less likely to undergo disproportionation or autoreduction.[5] Compared to the FER that has the same Si/Al ratio, but a different type of framework, it could be concluded that the presence of side pockets in the MOR framework does help in the stabilisation of Cu^+ cations. Moreover, higher Cu^+/Cu ratios were observed in MOR, BEA and ZSM-5 zeolites as compared to NaX, NaY. This could be explained by the fact that the larger pore size (e.g. faujasite-type zeolites) facilitates the formation of copper nanoparticles within the zeolite,

where it is easier for copper to be disproportionated and autoreduced.[8] Therefore, MOR and BEA-19 were chosen for further research.

2.3.4 CO titration and stepwise desorption at different temperatures $Cu(NO_3)_2$- impregnated MOR

MOR $Cu(NO_3)_2$ sample was first submitted to a titration experiment at room temperature (Figures 2.11 and 2.12) to determine if it was possible to discriminate different concentrations of CO.

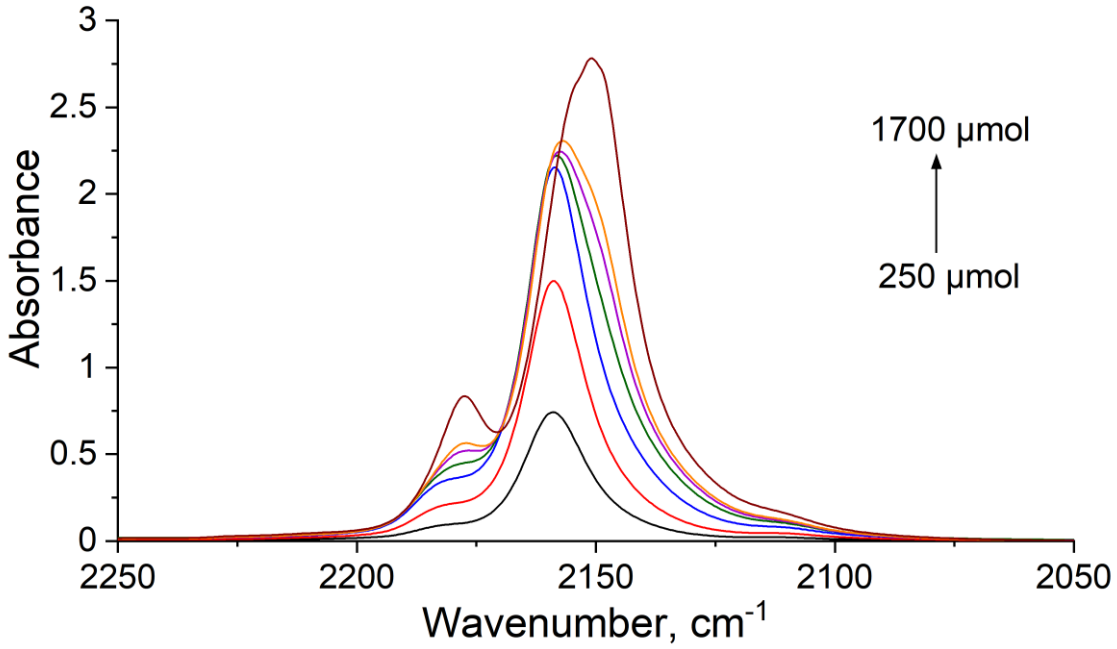

Figure 2.11. CO titration experiment, Difference FTIR spectra of CO adsorbed on $Cu(NO_3)_2$ impregnated MOR.

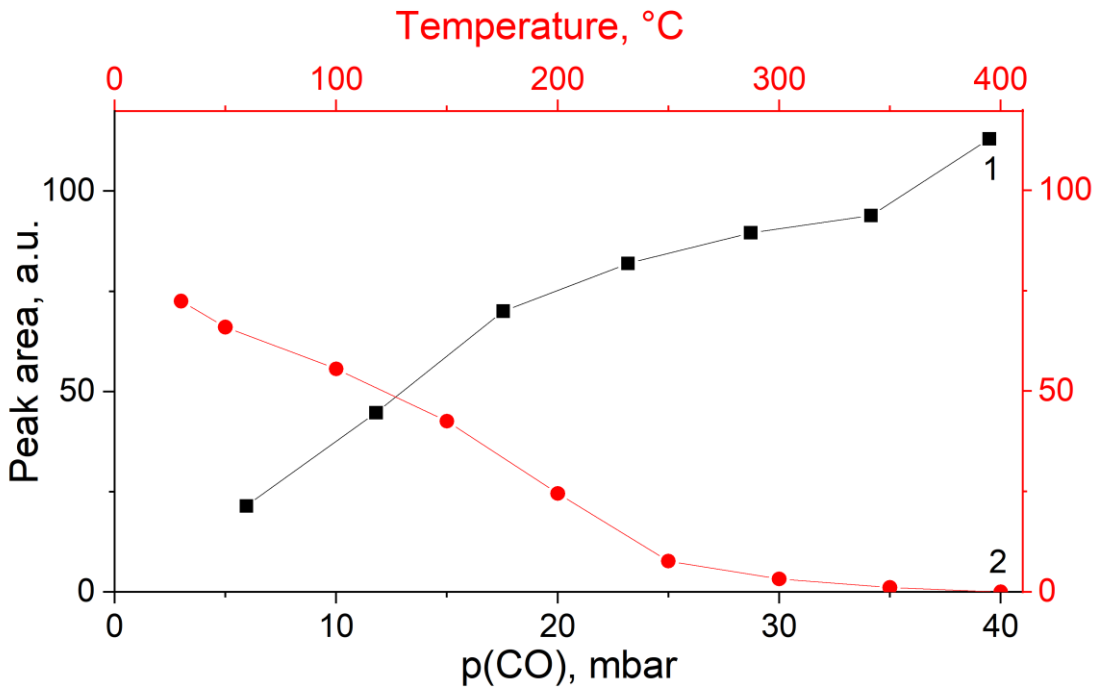

Figure 2.12 Evolution of the IR peak area following CO adsorption on $Cu(NO_3)_2$ impregnated MOR (1) and evolution of IR peak area during stepwise desorption at different temperatures of CO on $Cu(NO_3)_2$ impregnated MOR (2).

In the presented experiment, the pelletized sample was titrated with doses of 5 torr (250 μmol) of CO at room temperature. From the collected FTIR spectra, it has been possible to distinguish different concentrations of CO in the controlled atmosphere. Initially, only the 2159 cm^{-1} peak was present, but at higher concentrations, shoulders at 2177 and 2150 cm^{-1} appeared too. Those bands could be ascribed to Cu^{+}-$(CO)_2$ stretching. Eventually, at the highest CO partial pressure, the shoulder at 2150 cm^{-1} became the most intense. In addition, stepwise desorption at different temperatures was conducted (Figure 2.13) to determine the regeneration temperature of a sensor. The sample was initially left at room temperature to determine the rate of desorption at room temperature. During the first 30 min, a drop of 36 % in peak area could be noticed, but the peak intensity remained stable for another 30 minutes. The peak corresponding to Cu^{+}-CO interactions remained stable, while the bands ascribed to $Cu^{+}(CO)_2$ species decrease in

intensity. The data demonstrated that the Cu^{+}-CO interactions are strong. Hence, the sample must be regenerated at a minimum of 400 °C to desorb all the CO from the sample (Figure 2.13). This feature also indicates that the sensor could be utilised up to 400 °C, but with the intensity calibration at each specific temperature.

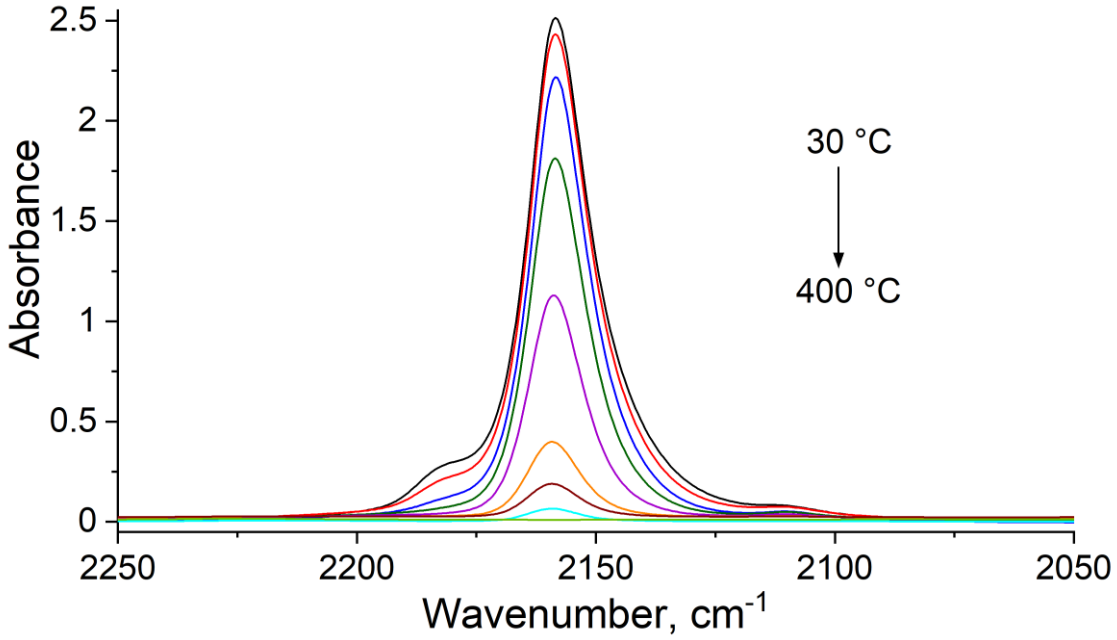

Figure 2.13. Stepwise desorption at different temperatures, Difference FTIR spectra of CO adsorbed on $Cu(NO_3)_2$ impregnated MOR.

All the former experiments were conducted in a controlled atmosphere in a vacuum system but to simulate the working conditions of a sensor, an atmospheric test was undertaken (Figure 2.14). In this experiment, the activation procedure was the same as for all the previous samples and then the sensor was exposed to the atmospheric conditions for 5 minutes. After the spectrum of the blank sample had been collected, the sample was exposed for 2 minutes to ~100 ppm of CO in air.

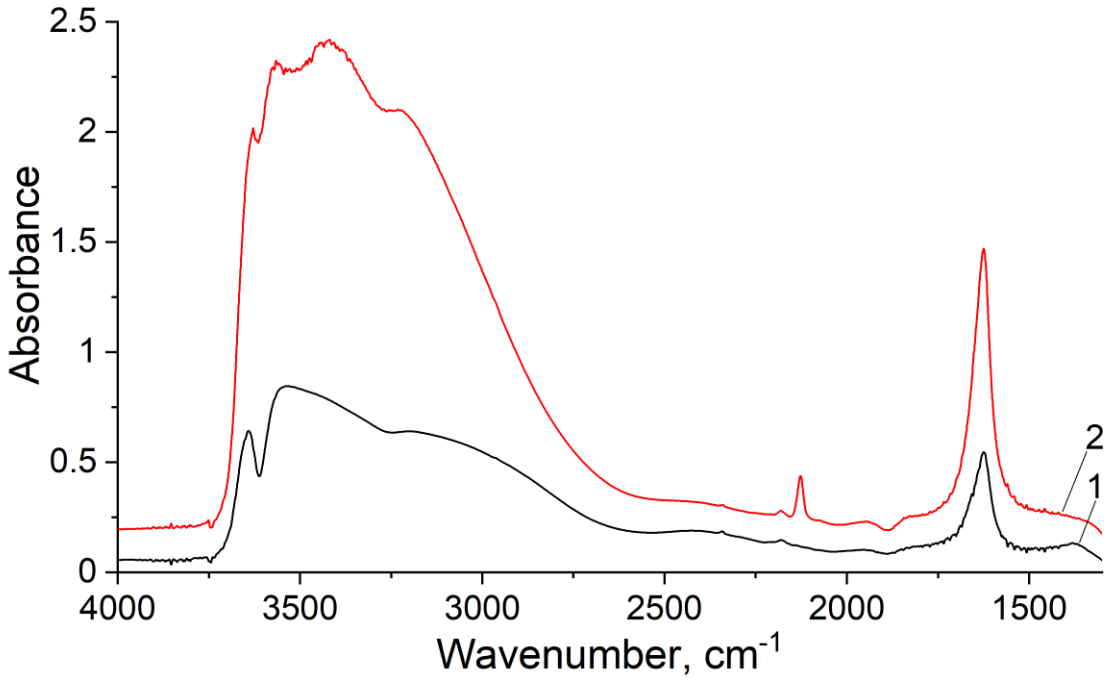

Figure 2.14. Difference FTIR spectra of $Cu(NO_3)_2$-impregnated MOR:
exposed to air for 5 minutes (1),
exposed to CO in the air for 2 minutes (2).

Even though the bands at 1640 cm^{-1} and from 2500-3700 cm^{-1}, that can be ascribed to water adsorbed on a zeolite, are the most significant, the peak corresponding to the Cu^{+}-CO (2159 cm^{-1}) interaction could still be observed (Figure 2.14). However, this means that the atmospheric water would significantly disturb the operational performance of a sensor.

2.3.5 In situ CO adsorption on $Cu(NO_3)_2$ - impregnated MOR

In the next experiment, $Cu(NO_3)_2$- impregnated MOR sample was deposited on a Si wafer and tested using in situ flow system (15-900 ppm of CO in Ar atmosphere, 100 ppm H_2O), Figure 2.15. Unlike the experiments performed in vacuum, a transition from 2157 cm^{-1} to 2135 cm^{-1} occurs at higher CO concentrations, Figure 2.15. The transition can be ascribed to the presence of water vapour in the test gases. It has been reported previously that the peaks corresponding to CO adsorbed on zeolites reversibly shift to lower wavenumbers in presence of water.[6] Even

though the shift is present, it does not affect the total area of both peaks, Figure 2.16. It can be observed that the total peak area increases with increasing CO concentration.

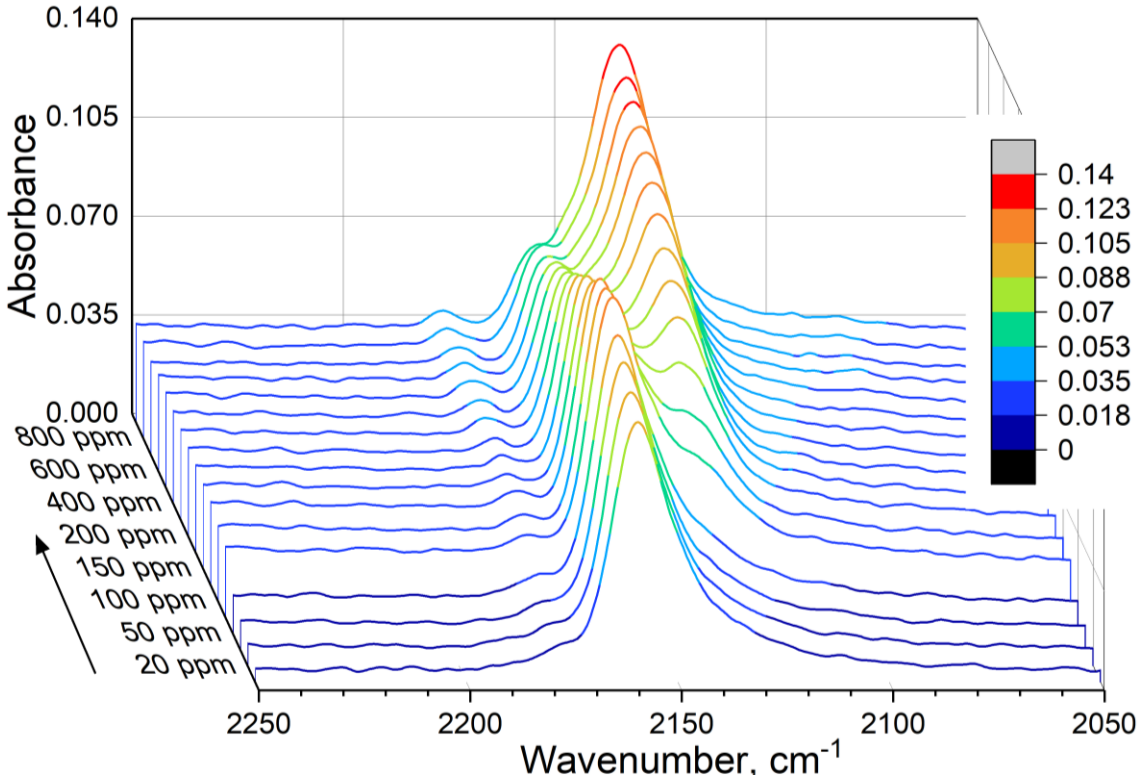

Figure 2.15. Waterfall graph of difference FTIR spectra of CO Adsorbed on CuMOR in Ar flow, spectra are offset for clarity.

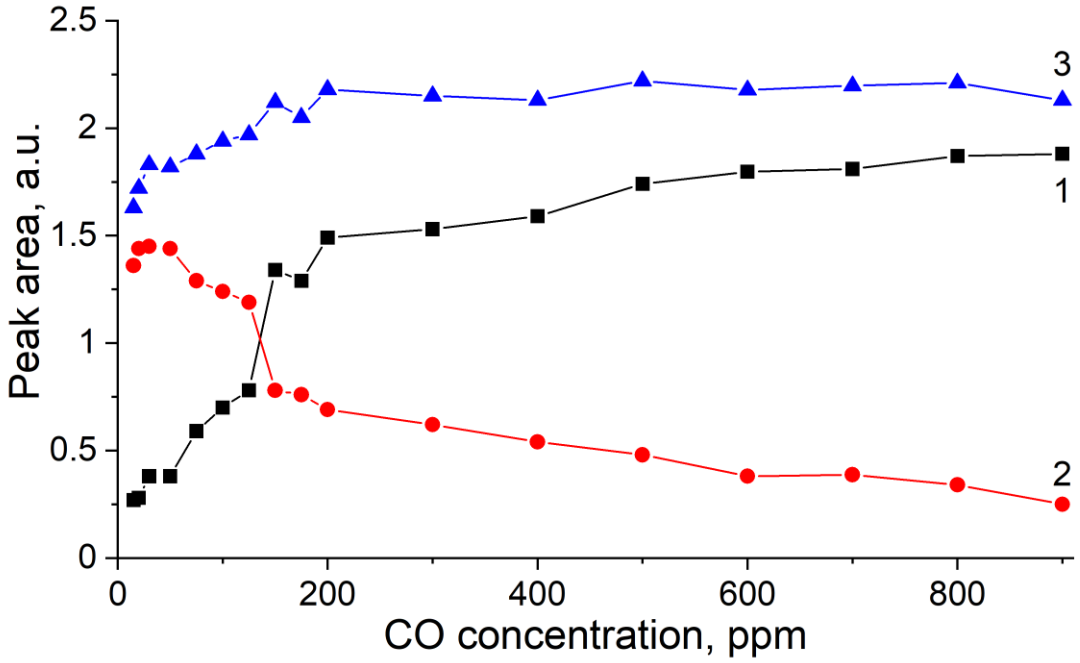

Figure 2.16. Evolution of peak area of 2135 cm^{-1} peak (1), 2157 cm^{-1} peak (2) and the total peak area (3) of CO adsorbed on $Cu(NO_3)_2$- impregnated MOR.

2.3.6 In vacuo CO – H_2O coadsorption on $Cu(NO_3)_2$ - impregnated MOR

The effect of water vapour on CO adsorption was further studied using the vacuum cell setup. The concentration of CO was recalculated based on CO potential pressure to allow comparison between the two sets of experiments. 0.05 mbar of CO that would correspond to 50 ppm in the flow system, was introduced to the vacuum cell, Figure 2.17, step (A). Subsequently, water was added in 0.1 µL steps (5.55 µmol, ~150 ppm) to monitor the transition from the peak at 2157 cm^{-1} to 2135 cm^{-1}, step (B). The complete transition was observed after the addition of 0.6 µL of H_2O. To confirm that the shift is reversible, the sample was evacuated for 30 minutes (step C) and another 0.6 µL of H_2O was stepwise added to the vacuum cell (step D) and the peak intensities, shapes and positions were reproducible, Figures 2.17 and 2.18 . This leads to

a conclusion that in the potential real-life exposure of the sensor, where changes in humidity are frequent, the sensor should keep its functionality.

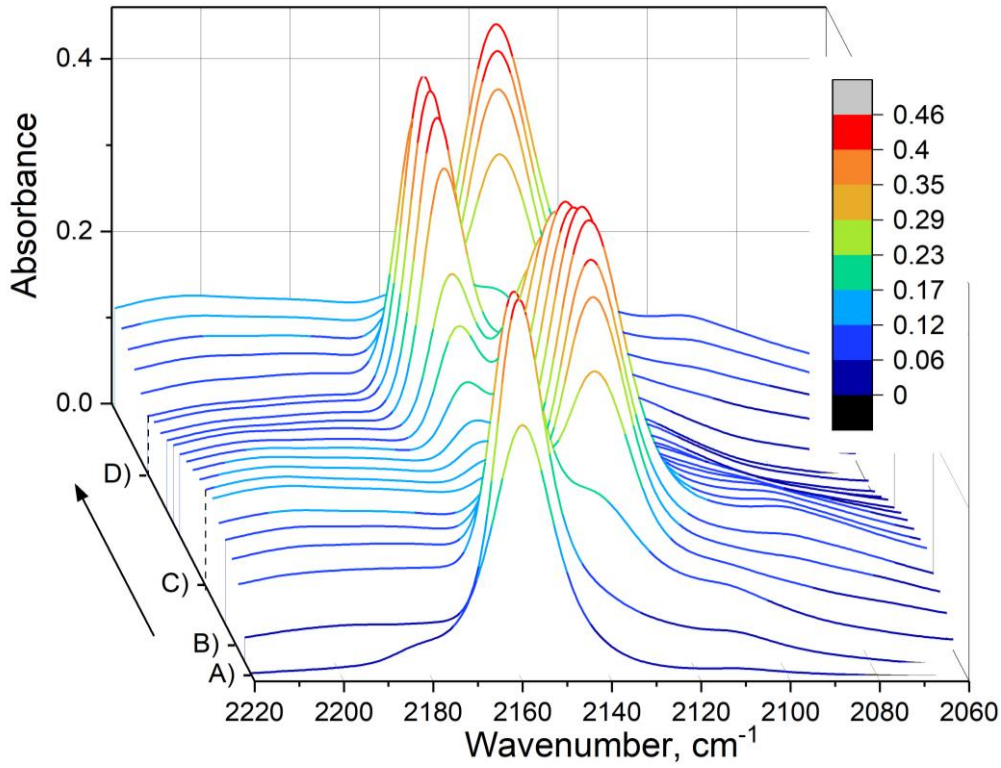

Figure 2.17. Waterfall graph of difference FTIR spectra of CO Adsorbed on $Cu(NO_3)_2$-impregnated MOR, 50 ppm of CO adsorbed (step A) followed by stepwise H_2O adsorption (step B), evacuation (step C) and H_2O readsorption (step D), spectra are offset for clarity, colour legend represents the intensity scale.

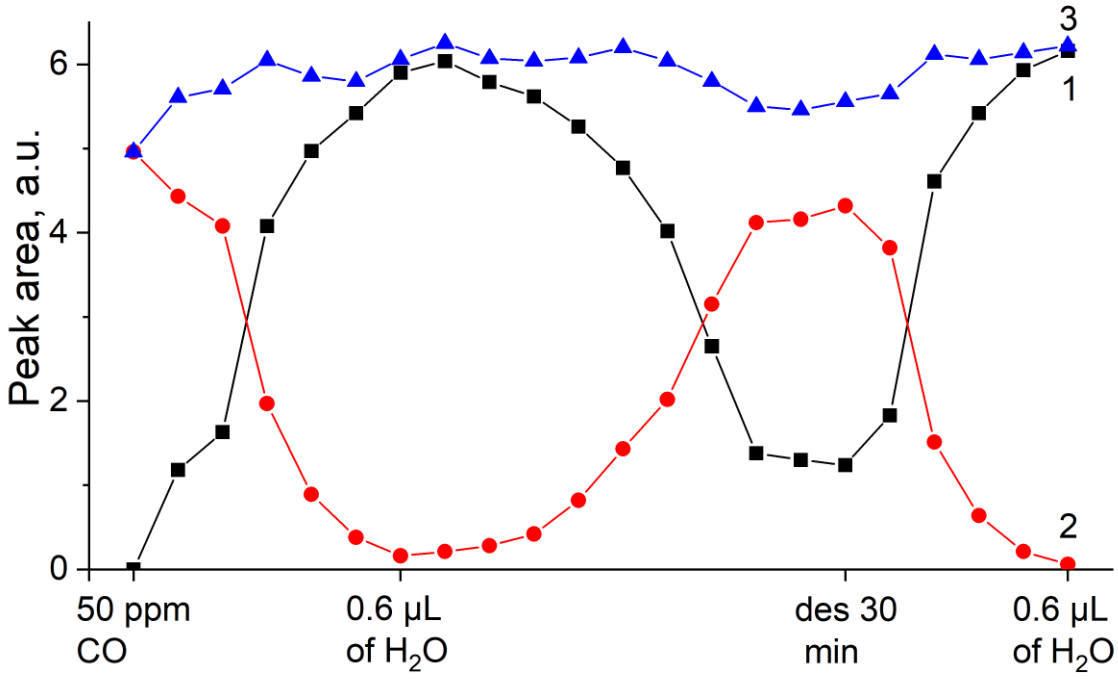

Figure 2.18. Peak evolution of CO adsorbed on $Cu(NO_3)_2$ - impregnated MOR during water adsorption-desorption experiment;
2135 cm^{-1} peak (1), 2157 cm^{-1} peak (2) and the total peak area (3).

Additionally, the sensor was first exposed to 1 µL of water (55.5 µmol, ~1500 ppm), Figure 2.19 – step A, followed by a CO adsorption (50 to 1000 ppm), step B. It can be observed that at the lower concentrations the peak intensity is significantly lower than on a dry sample (Figure 2.19). However, after the sample was exposed to CO concentrations that were comparable to the initial water concentration, the peak shapes and intensities were regained. The evacuation experiment demonstrated that the water adsorption was reversible, Figure 2.19-step C. At the same time, the high-temperature activation before CO detection was necessary.

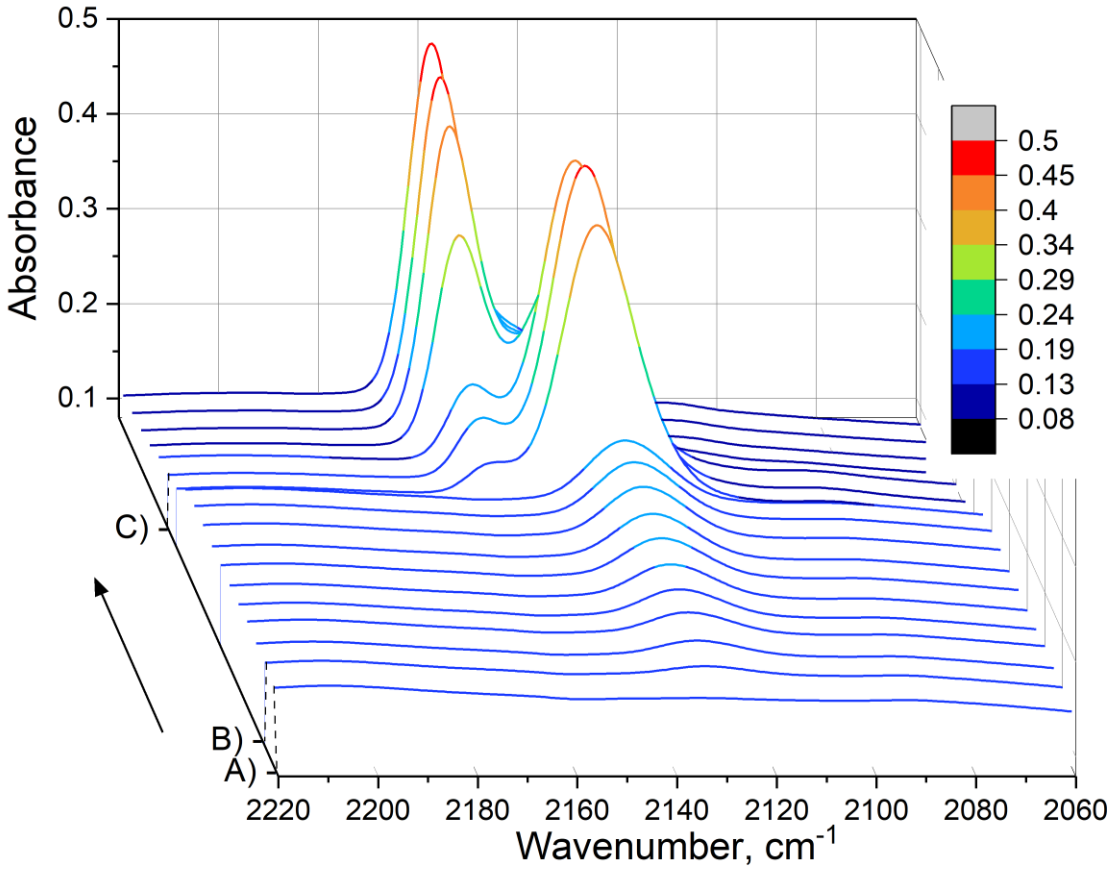

Figure 2.19. Waterfall graph of difference FTIR spectra of CO Adsorbed on $Cu(NO_3)_2$-impregnated MOR after 1µL H_2O adsorption (step A), followed by CO introduction at different partial pressures (50-1000 ppm) (step B) and evacuation (step C), spectra are offset for clarity, colour legend represents the intensity scale.

Even though that the total area of the peaks, which would be detected by NDIR-type sensor, was not affected both during in situ and vacuum experiments, the CO detection sensor is significantly more sensitive in the absence of water. Therefore, a more suitable sensor material should be found. It was decided to utilise the sensor based on zeolite BEA-19, which is less hydrophilic and showed promising results during the initial screening, also (Table 2.4).

2.3.7 Cu-impregnated Sn-BEA

BEA-19 was used as a starting material for the preparation of hydrophobic Sn-BEA zeolite. The goal was to prepare hydrophobic material that would still possess a considerable ion-exchange capacity. This was accomplished by the fluoride-assisted synthesis, where the silanols that are initially present on the zeolite surface were replaced by fluoride groups.[15,25]. $Cu(NO_3)_2$- impregnated Sn-BEA was characterised by XRD to confirm that the prepared material has the BEA framework and the basic copper salt (Figure 2.20). A more detailed characterisation of hydrophobic Sn-BEA and application as selective NO_2 sensor is presented in chapter 3.

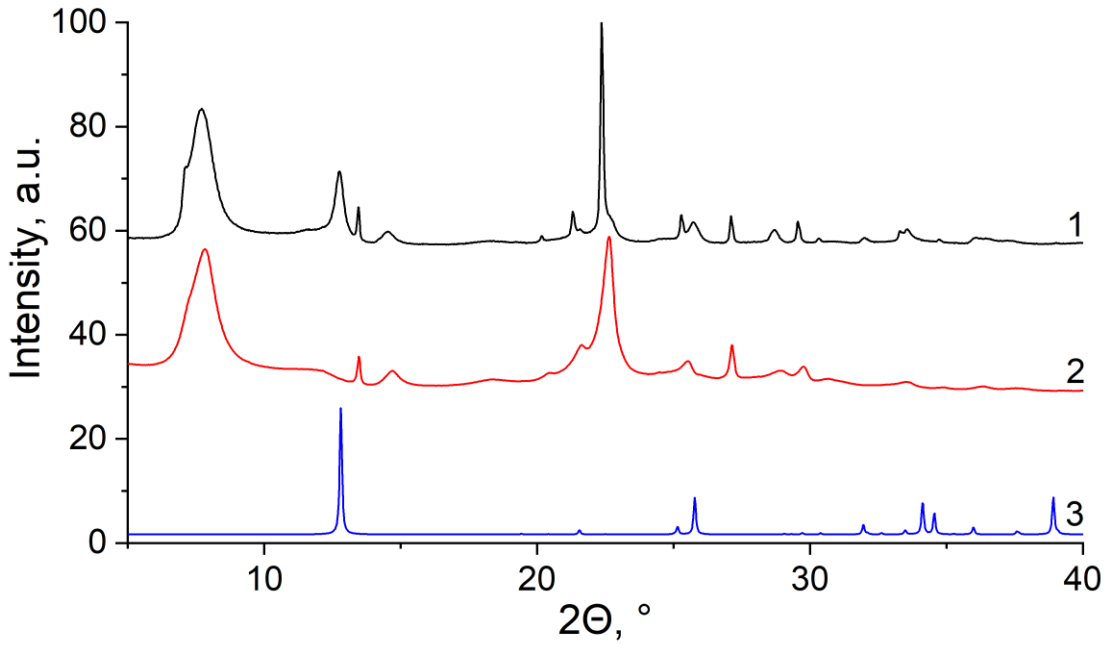

Figure 2.20. XRD patterns of CuSn-BEA (1), BEA-19 (2), calculated basic copper nitrate (3), patterns are offset for clarity.

From the TGA curves shown in Figure 2.21, it can be noticed that MOR contains almost 10 wt.% of water that could block the microporous channels and prevent or interfere with the CO adsorption on copper sites. On the other hand, the weight loss due to water in Sn-BEA is only

1 wt.%. Therefore, it is expected that such a hydrophobic sample should perform better under environmental conditions, where high humidity levels are relatively high.

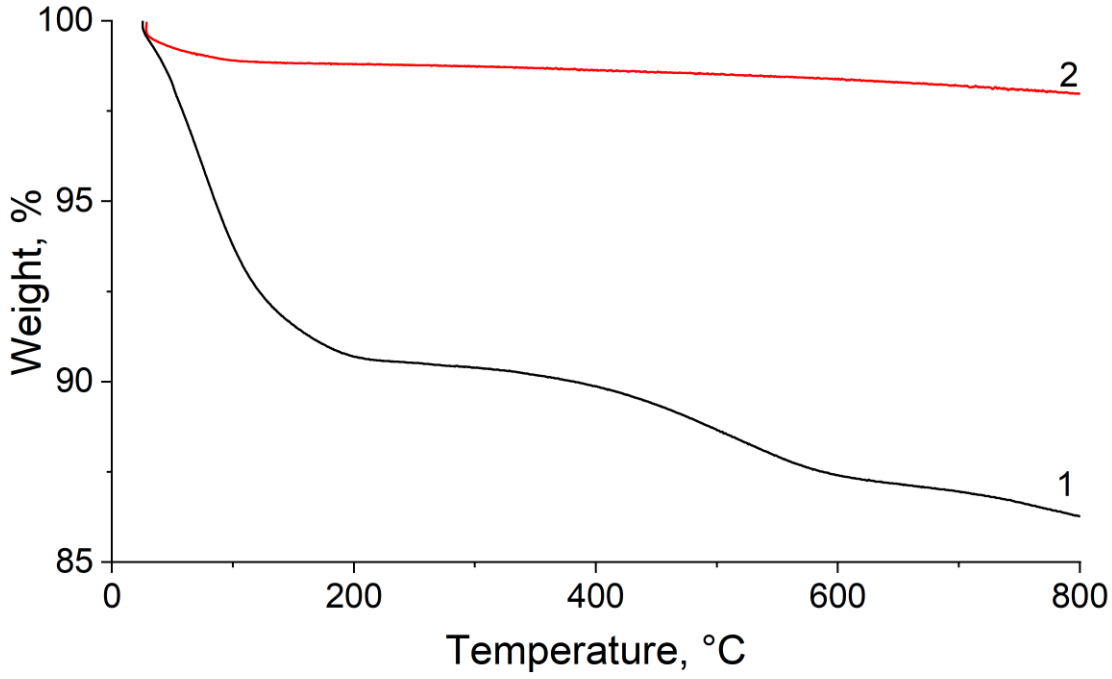

Figure 2.21. TGA curves of $Cu(NO_3)_2$ impregnated MOR (1) and Sn-BEA (2).

$Cu(NO_3)_2$- impregnated Sn-BEA (CuSn-BEA) was also subjected to an in situ CO adsorption experiment in Ar flow (Figure 2.22). The two main bands were observed, sharp at 2149 cm^{-1} and a broad one centred at 2132 cm^{-1}. At concentrations greater than 600 ppm of CO in the flow, the 2149 cm^{-1} peak remains at a stable value, indicating the saturation of Cu^{+}-CO species. However, the sensor is still able to discriminate the higher CO concentrations due to the increase in the 2132 cm^{-1} band, which should correspond to stretching vibrations of Cu^{+}-$(CO)_2$ species.

The 100 ppm of water vapour present in the test gases did not affect the peak positions in the CuSn-BEA, therefore this sensor appears to be a more promising material for the proposed sensor because no water interference effects could be noticed. Also, the total peak areas followed a similar trend to Cu-MOR (Figure 2.23).

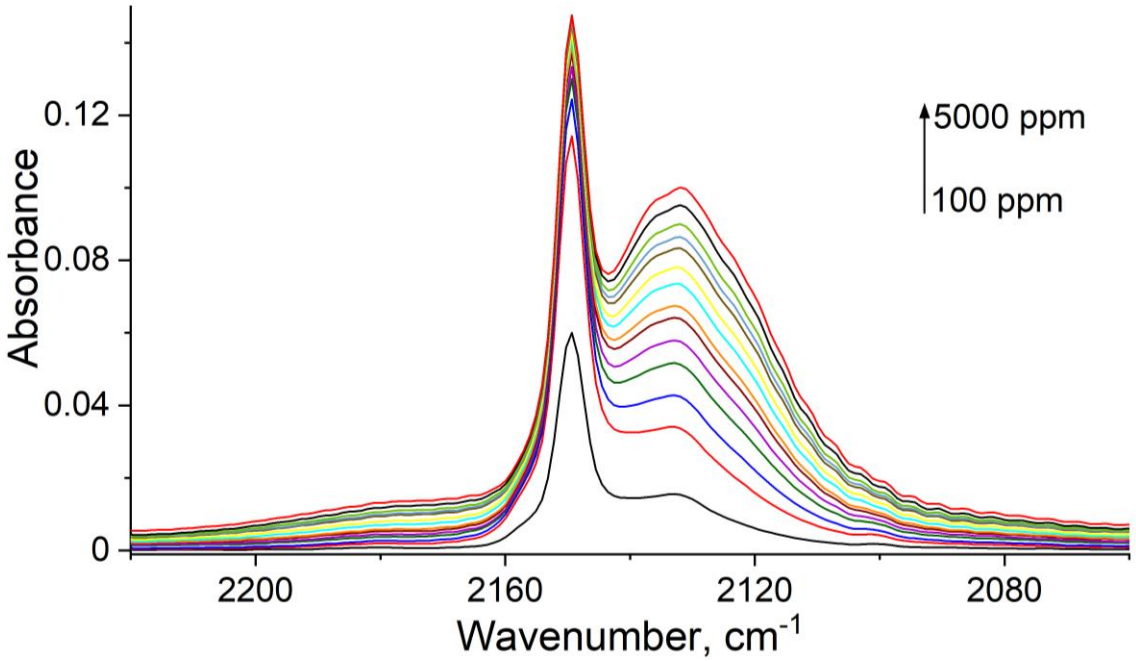

Figure 2.22. Difference FTIR spectra of CO adsorbed on CuSn-BEA, 100-5000 ppm.

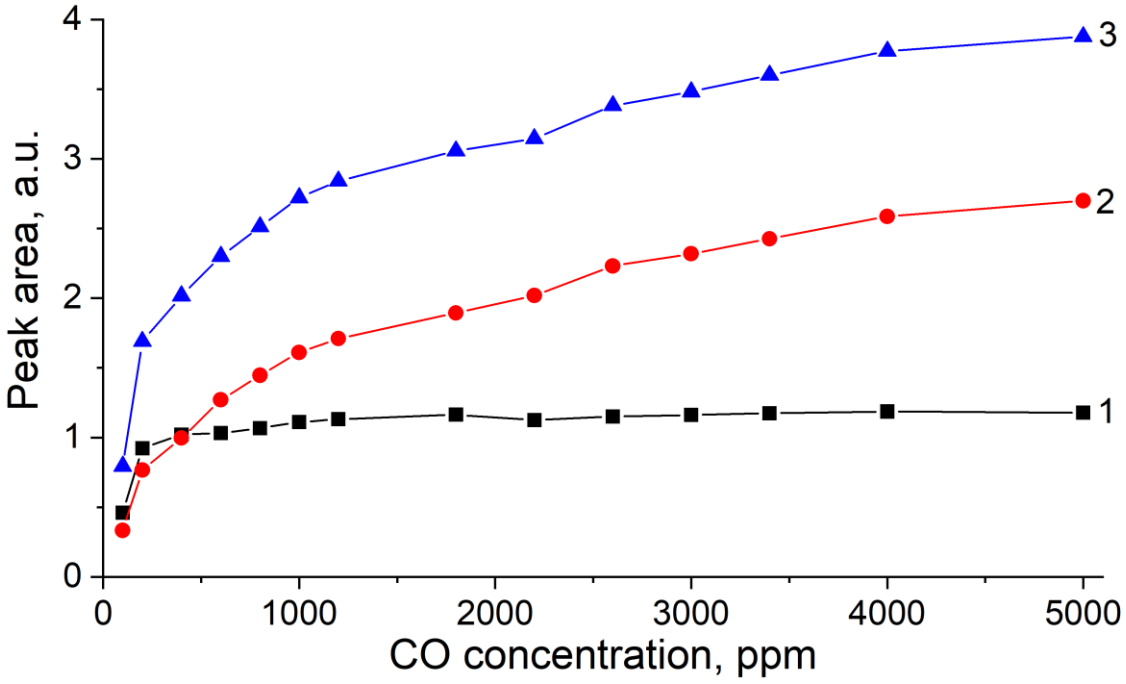

Figure 2.23. Evolution of the total peak area of CO adsorbed on CuSn-BEA, 100-5000 ppm. 2149 cm^{-1} peak (1), 2132 cm^{-1} peak (2) and the total peak area (3).

2.3.8 In vacuo CO – H_2O coadsorption on CuSn-BEA

To determine the amount of water required to interfere with the CO adsorption, CuSn-BEA was also subjected to water interference experiments in the vacuum system. An equivalent of 50 ppm of CO was introduced to the cell (Figure 2.24, step A), following the stepwise addition of 0.1 µL H_2O, to the total of 0.5 µL, step B. Please note, due to the difficulty of the presentation of the data because of peak overlapping, in Figure 2.24 the spectra are aligned from back to front, as opposed to all other waterfall-type figures in this chapter. A part of the 2149 cm^{-1} peak was shifted to lower wavenumbers, in contrast to $Cu(NO_3)_2$-impregnated MOR sample, this amount of water was insufficient to shift the peak completely (Figure 2.24, step C).

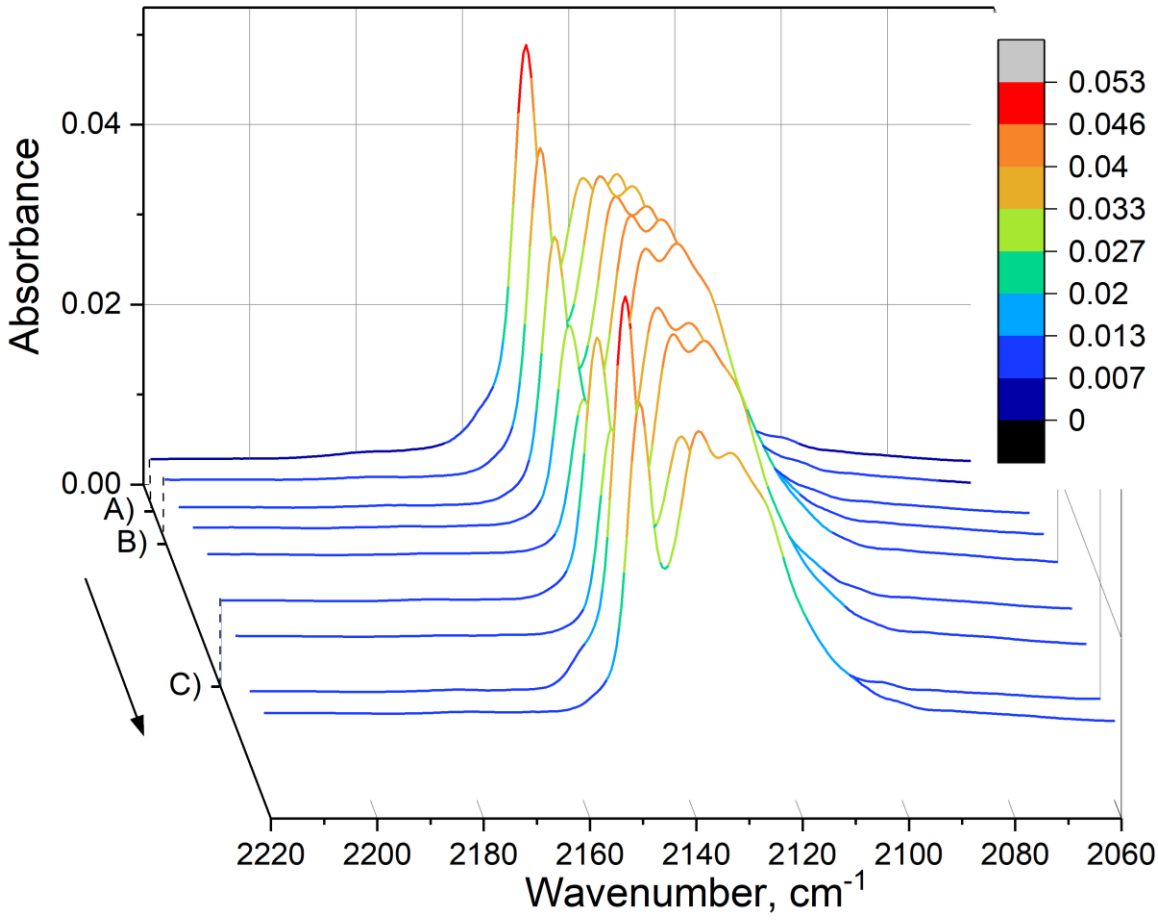

Figure 2.24. Waterfall graph of difference FTIR spectra of CO adsorbed on CuSn-BEA (step A), water interference experiment (step B) and desorption experiment (step C), spectra are aligned from back to front and offset for clarity, colour legend represents the intensity scale.

The reversibility of water adsorption was tested by stepwise desorption (step C) and the readsorption part of the experiment. Due to difficulty in overlapping the resulting spectra in Figure 2.24, the part of the experiment with full evacuation (step D) and water readsorption (step E) is presented in Figure 2.25. Upon 45 minutes of evacuation, the intensity of the 2149 cm^{-1} peak was completely recovered. Subsequently, during the water readsorption phase, a total of 1.6 µL of H_2O (88.8 µmol, ~2400 ppm), was required to fully red-shift the 2149 cm^{-1} band to 2132 cm^{-1}, Figure 2.25 -step E. Figures 2.24 and 2.25 demonstrate that the total peak area (2170-2110 cm^{-1}) remains largely unchanged. Although, there is a reversible intensity redistribution upon adsorption-desorption of water.

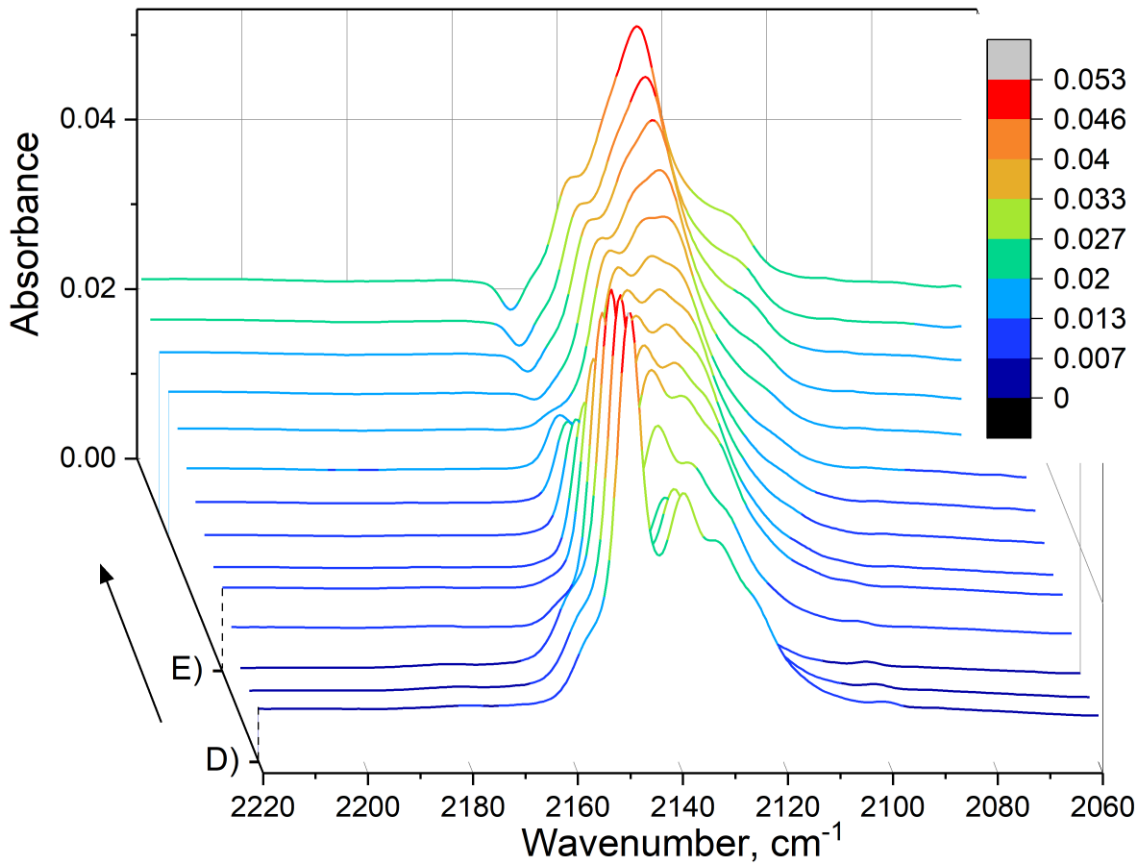

Figure 2.25. Waterfall graph of difference FTIR spectra of CO adsorbed on CuSn-BEA in vacuo, evacuation (step D) and water readsorption (step E), spectra are offset for clarity, colour legend represents the intensity scale.

Finally, the CuSn-BEA sensor was exposed to 1 µL of H_2O (Figure 2.26 -step A) prior to CO titration to 1000 ppm, step B. It can be observed that the IR peaks at lower concentrations of CO are redshifted, but the water interference is less prominent than in the MOR sample. This is in agreement with the previous experiment (Figure 2.25). Additionally, the peak area was redistributed upon water desorption (Figure 2.26 -step C). These data demonstrate that CuSn-BEA could be the optimum material from the studied zeolite samples for the intended environmental CO sensor.

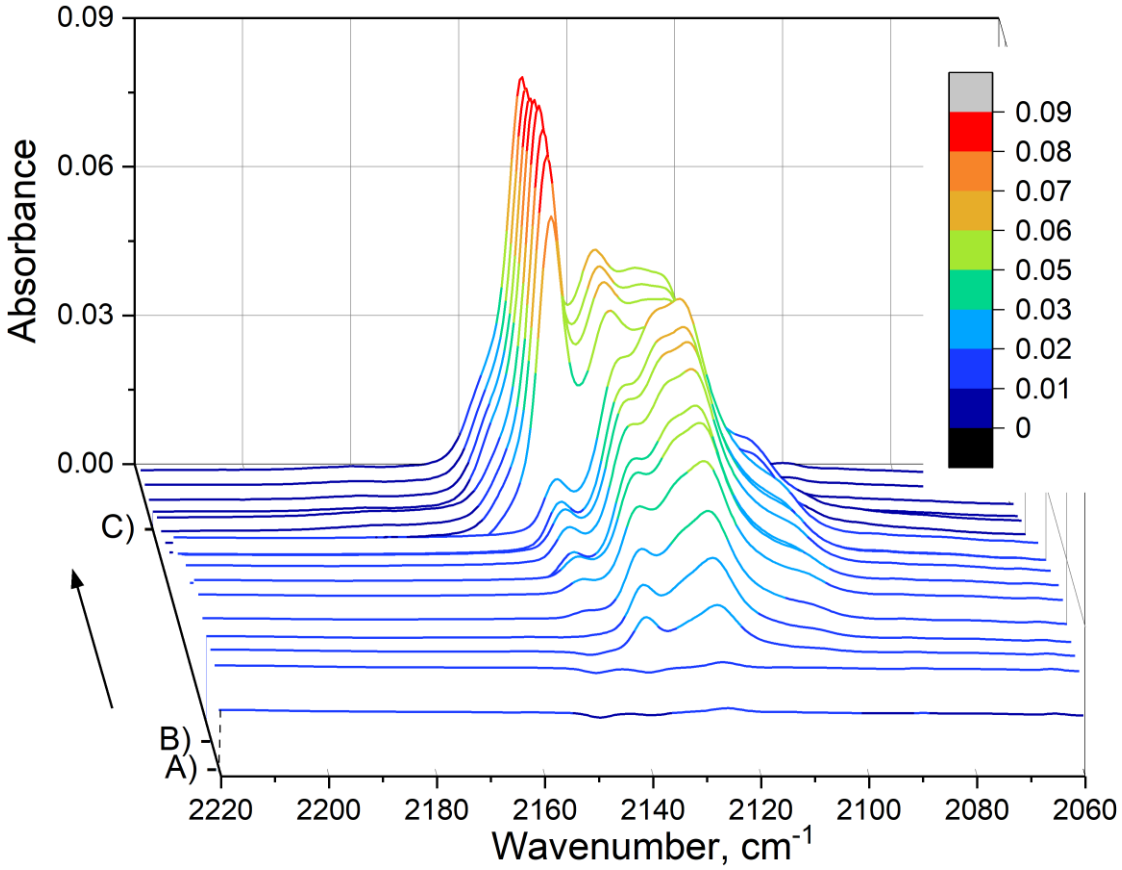

Figure 2.26. Waterfall graph of difference FTIR spectra of CuSn-BEA in vacuo after saturation with 1 µL of H_2O (step A), followed by CO adsorption (step B) and evacuation (step C), spectra are offset for clarity, colour legend represents the intensity scale.

2.4 Conclusions and further research

The aim of this chapter was to prepare Cu^{+}-containing zeolites and test them as potential room-temperature IR-based CO sensors. The commercial samples (NaX, NaY, MOR, FER, BEA-12, BEA-19, ZSM-5) and Sn-BEA were ion-exchanged and impregnated using $CuSO_4$, $Cu(NO_3)_2$ and $Cu(OAc)_2$ as copper sources. The highest Cu^{+} content was detected in $Cu(NO_3)_2$-impregnated MOR, which was further tested in environmental conditions. To counter significant water interference, $Cu(NO_3)_2$-impregnated hydrophobic Sn-BEA was established as the optimal sensor material.

To the best of our knowledge, this is the first report on Cu-modified zeolites utilised as CO sensors. The Cu^{+}-containing zeolites successfully demonstrated the ability to discriminate CO concentrations from 10 to 5000 ppm at room temperature. Also, the sensors have shown to be operational at environmental levels of humidity. This provides an opportunity to test zeolites modified by other transition metals for gas sensing performance. However, further optimisation is required to be competitive against the sensors currently available on the market. The response selectivity, reproducibility and repeatability have to be evaluated and the water interference effects calibrated. Considering that the expected operational time of competing sensors is 5-10 years, the lifespan and regeneration system of the proposed sensor must be determined.

2.5 References

1. Cobb, N. & Etzel, R. A. Unintentional Carbon Monoxide—Related Deaths in the United States, 1979 Through 1988. *JAMA* **266**, 659–663 (1991).

2. Goldstein, M. Carbon Monoxide Poisoning. *J. Emerg. Nurs.* **34**, 538–542 (2008).

3. Struttmann, T., Scheerer, A., Scott Prince, T. & Goldstein, L. Unintentional Carbon Monoxide Poisoning From an Unlikely Source. *J. Am. Board Fam. Pract.* **11**, 481–484 (1998).

4. *Introduction to Zeolite Science and Practice*. (eds. Cejka, J., van Bekkum, H., Corma, A. & Schuth, F.) (Elsevier Science, 2007).

5. Bordiga, S., Lamberti, C., Bonino, F., Travert, A. & Thibault-Starzyk, F. *Probing zeolites by vibrational spectroscopies Chemical Society Reviews Probing zeolites by vibrational spectroscopies*. (2015).

6. Hadjiivanov, K. I. & Vayssilov, G. N. Characterization of oxide surfaces and zeolites by carbon monoxide as an IR probe molecule. *Adv. Catal.* **47**, 307–511 (2002).

7. Nachtigallová, D., Bludský, O., Otero Aerán, C., Bulánek, R. & Nachtigall, P. The vibrational dynamics of carbon monoxide in a confined space-CO in zeolites. *Phys. Chem. Chem. Phys* **8**, 4849–4852 (2006).

8. Kharchenko, A., Zholobenko, V., Vicente, A., Fernandez, C., Vezin, H., De Waele, V. & Mintova, S. Formation of copper nanoparticles in LTL nanosized zeolite: Spectroscopic characterization. *Phys. Chem. Chem. Phys.* **20**, 2880–2889 (2018).

9. Spoto, G., Zecchma, A., Bordiga, S., Ricchiardi, G., Martra, G., Leofanti, G. & Petrini, G. Cu (I)-ZSM-5 zeolites prepared by reaction of H-ZSM-5 with gaseous CuCl:

Spectroscopic characterization and reactivity towards carbon monoxide and nitric oxide*. *Appl. Catal. B Environ.* **3**, 151–172 (1994).

10. Bekkum, H., Flaningen & Jacobs. *Introduction to zeolite science and practice*. vol. 3 (1385).

11. Flanigen, E. M., Bennett, J. M., Grose, R. W., Cohen, J. P., Patton, R. L., Kirchner, R. M. & Smith, J. V. Silicalite, a new hydrophobic crystalline silica molecular sieve. *Nature* **271**, 512–516 (1978).

12. Luo, H. Y., Consoli, D. F., Gunther, W. R. & Román-Leshkov, Y. Investigation of the reaction kinetics of isolated Lewis acid sites in Beta zeolites for the Meerwein-Ponndorf-Verley reduction of methyl levulinate to γ-valerolactone. *J. Catal.* **320**, 198–207 (2014).

13. Bui, L., Luo, H., Gunther, W. R. & Román-Leshkov, Y. Domino reaction catalyzed by zeolites with Brønsted and Lewis acid sites for the production of γ-valerolactone from furfural. *Angew. Chemie - Int. Ed.* **52**, 8022–8025 (2013).

14. Corma, A., Nemeth, L. T., Renz, M. & Valencia, S. Sn-zeolite beta as a heterogeneous chemoselective catalyst for Baeyer–Villiger oxidations. *Nature* **412**, 423–425 (2001).

15. Harris, J. W., Cordon, M. J., Di Iorio, J. R., Vega-Vila, J. C., Ribeiro, F. H. & Gounder, R. Titration and quantification of open and closed Lewis acid sites in Sn-Beta zeolites that catalyze glucose isomerization. *J. Catal.* **335**, 141–154 (2016).

16. Kobler, J., Abrevaya, H., Mintova, S. & Bein, T. High-Silica Zeolite-: From Stable Colloidal Suspensions to Thin Films. *J. Phys. Chem. C* **112**, 14274–14280 (2008).

17. Baerlocher, C., Mccusker, L. B. & Olson, D. H. *Atlas of Zeolite Framework types*. (Elsevier, 2007).

18. Bordiga, S., Lamberti, C., Geobaldo, F., Zecchina, A., Palomino, G. T. & Areán, C. O.

Fourier-Transform Infrared Study of CO Adsorbed at 77 K on H-Mordenite and Alkali-Metal-Exchanged Mordenites. *Langmuir* **11**, 527–533 (1995).

19. Palomino, G. T., Zecchina, A., Giamello, E., Fisicaro, P., Berlier, G., Lamberti, C. & Bordiga, S. Polycarbonylic and polynitrosylic species in Cu I-exchanged ZSM-5, β, Mordenite and Y zeolites: Comparison with homogeneous complexes. *Stud. Surf. Sci. Catal.* **130 C**, 2915–2920 (2000).

20. Lamberti, C., Bordiga, S., Zecchina, A., Salvalaggio, M., Geobaldoc, F. & Otero, C. XANES, EXAFS and FTIR characterization of copper-exchanged mordenite. *J. Chem. Soc., Faraday T rans* **94**, (1998).

21. Turnes Palomino, G., S. Bordiga, Lamberti, C., Zecchina, A. & Otero Areán, C. Vibrational and optical spectroscopic studies on copper-exchanged ferrierite. *Stud. Surf. Sci. Catal.* **1142**, 199–206 (2002).

22. Giordanino, F., Vennestrøm, P. N. R., Lundegaard, L. F., Stappen, F. N., Mossin, S., Beato, P., Bordiga, S. & Lamberti, C. Characterization of Cu-exchanged SSZ-13: a comparative FTIR, UV-Vis, and EPR study with Cu-ZSM-5 and Cu-β with similar Si/Al and Cu/Al ratios. *Dalt. Trans* **42**, 12741 (2013).

23. Lamberti, C., Bordiga, S., Salvalaggio, M., Spoto, G., Zecchina, A., Geobaldo, F., Vlaic, G. & Bellatreccia, M. XAFS, IR, and UV−Vis Study of the CuI Environment in CuI-ZSM-5. *J. Phys. Chem. B* **101**, 344–360 (1997).

24. Zholobenko, V., Freitas, C., Jendrlin, M., Bazin, P., Travert, A. & Thibault-Starzyk, F. Probing the acid sites of zeolites with pyridine: Quantitative AGIR measurements of the molar absorption coefficients. *J. Catal.* **385**, 52–60 (2020).

25. Corma, A., Nemeth, Laszlo, T., Renz, M. & Valencia, S. Sn-zeolite beta as a

heterogeneous chemoselective catalyst for Baeyer-Villiger oxidations. *Nature* **412**, 423–425 (2001).

Chapter 3

Hydrophobic Sn-BEA as a selective gas sensor for exhaust fumes

3.1 Introduction

In the contemporary world, air pollution is a growing problem that presents a significant threat to human health. Combustion engines and the gas exhaust fumes they produce are stated as key sources of pollutants. [1,2] Exhaust fumes consist mostly of harmless O_2, N_2 and water vapour (up to 80%), but CO_2, CO, NO_x and SO_x are produced in quantities sufficient to cause negative environmental and health effects.[3] Reports from major environmental governing bodies mainly focus on the control of NO_x, SO_x, O_3 and CO in addition to the fine particulate matter.[2,4] Therefore, effective monitoring of these gases is required employing a range of gas sensors.

Gas sensors utilise a variety of physical and chemical phenomena to detect species of interest. Over 50% of the market share is represented by electrochemical, semiconductor and infrared-based gas sensors.[5] Electrochemical sensors utilise solid electrolytes, such as yttria stabilised zirconia, as the main active components in a galvanic cell.[6,7] The response of the cell is related to the concentration of the specified gas via the Nernst equation. This type of sensors has found the most important application as the oxygen sensor in gas exhaust systems. However, electrochemical sensors for most gas analyses lack long-term stability and selectivity if oxygen is present as the main interfering gas.[6,7] Semiconductor sensors utilise the conductometric response of a variety of metallic oxides (TiO_2, WO_3, ZrO_2, SnO_2)[8–10] with SnO_2 being the most common as it is responsive towards CO, NO_2 and NH_3.[8–10] However, these sensors require high operating temperatures (>150 °C) and the presence of oxygen, they also often lack selectivity.[8–10] These characteristics could be optimised either by the incorporation of noble metals or by mixing several types of oxides, however, such modifications lead to a rise in manufacturing costs. Most of the widely available infrared sensors are based on non-dispersive

infrared technology.[11] These sensors are characterised by low power consumption, however, the poor detection limits and water interference present a major problem.[11]

Materials that could enhance the selectivity of gas sensors are zeolites. Zeolites are highly-ordered crystalline microporous aluminosilicates. They are also widely used as molecular sieves, industrial catalysts and in water treatment,[12] their porosity and high adsorption capacity make them viable materials for gas sensor applications.[13–16] Zeolites have been utilised both as the active sensing components and as auxiliary phases (e.g. filter or sieving layer, or an immobilisation template).[14,15] As active sensing components, zeolites have been mostly used in gas sensors that are based on ion conductivity, potentiometry and cataluminescence.[14,15] Sensing properties of zeolite are dependent on the metal ions present in the zeolite pores. An alternative way of zeolite modification is by isomorphous substitution, that is by incorporating other metals (Ti, Ga, Zr, Sn)[17–22] into the structure instead of aluminium. These metal-containing zeolites are extensively used in heterogeneous catalysis, including some of the commercially exploited framework types such as BEA, MFI, CHA and FAU [22–31]. For instance, Sn-containing BEA zeolites are highly selective catalysts in biomass conversion: enhanced activity and product selectivity were reported in Meerwin-Pondorf-Verlein reduction,[20] Baeyer-Villiger oxidation,[22] sugar isomerisation [23–28] and epimerisation.[23,32] Optimised synthetic procedures resulted in the preparation of highly crystalline, nearly defect-free Sn-BEA materials.[22,33–35] Their superior catalytic activity is attributed to Lewis acid sites associated with the Sn atoms incorporated in the zeolite framework. Unlike in SnO_2, where Sn is octahedrally coordinated, in zeolites, Sn is tetrahedrally coordinated.[22,36–39] The tetrahedrally coordinated Sn atoms are observed in two main forms that are referred to as open and closed sites. Open sites correspond to $Sn(OSi)_4$ and closed sites to $Sn(OSi)_3(OH)$ species.[35,38] In addition, a 3-dimensional network of channels with 12-membered ring apertures offers good accessibility to a variety of species. This

combination of highly effective active sites and microporous properties of Sn-BEA makes it a promising material for a number of potential applications.

Although Sn-BEA zeolites have been widely utilised in catalysis and pure SnO_2 gas sensors are well-known, to the best of our knowledge no application of Sn-BEA based gas sensors has been reported. In this work, we explore the potential of combining the sensing properties of Sn-based compounds with the zeolite pore confinement effects aiming to produce a new type of selective gas sensors. A hydrophobic Sn-BEA zeolite has been synthesised and characterised using a range of physicochemical techniques. A prototype Sn-BEA based sensor has been prepared and tested under realistic operating conditions. The research presented in this chapter demonstrates the potential of this material as a NO_2-selective gas sensor for the analysis of exhaust fumes in the presence of CO, CO_2, O_2 and H_2O.

3.2 Experimental Section

3.2.1 Zeolite synthesis

Zeolite preparations followed the procedure from Ref[35]. In a typical experiment, 5 g of commercial BEA-19 (Zeolyst, Si/Al= 19.0) was dealuminated in 125 mL of concentrated nitric acid (HNO_3, 68%, Fisher Scientific) for 16h at 80 °C. Subsequently, the dealuminated BEA (deAl-BEA) sample was washed 6 times with 25mL of deionized water (Elga Purewater system, <0.067 μS/cm) and dried overnight. As-prepared deAl-BEA was used as a seed material in further steps. The synthesis gel was prepared by mixing 6.98 g of tetraethylorthosilicate ($Si(OC_2H_5)_4$, Sigma Aldrich) and 7.67 g of tetraethylammonium hydroxide ($(C_2H_5)_4N(OH)$, 40%, Sigma Aldrich). Subsequently, 0.12 g of tin (IV) chloride pentahydrate ($SnCl_4 \cdot 5H_2O$, Sigma Aldrich) was dissolved in 0.6 mL of water and added dropwise to the gel. The Si/Sn molar ratio in the gel was 100. The gel was stirred for 12h in a closed container and then 3 days in an open container. After allowing the excess water and ethanol to evaporate, 0.74 g of hydrofluoric acid (HF, 48%, Aldrich) was added to the gel. The gel was homogenised and 0.085 g of deAl-BEA seeds in 0.58 g of water was added and mixed thoroughly. The prepared gel was heated in an autoclave for 6 days at 140 °C. The products were then removed from the autoclave, washed 5 times with 25 mL of water, followed by washing 5 times with 25 mL of acetone (VWR Chemicals). Samples were dried overnight and a part of the sample was calcined in a muffle furnace for 1h at 400 °C in a nitrogen flow, followed by calcination for 5h at 550 °C in an oxygen flow, Figure 3.1.

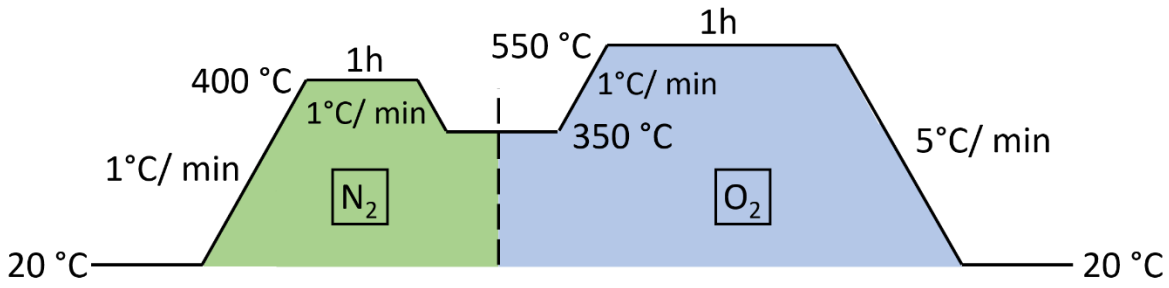

Figure 3.1. Sn-BEA calcination scheme.

3.2.2 Zeolite characterization

Zeolite samples were characterised by X-ray powder diffraction (Bruker D8 Advance diffractometer, Cu Kα at 40 kV and 40 mA, 2θ=5−60°), scanning electron microscopy (Hitachi TM 3000 with Bruker EDX system at 500x magnification, 300 s EDX data collection time), N_2 adsorption-desorption (Micrometrics Model ASAP2020), solid-state MAS NMR (Bruker Avance III-HD 500, 11.7 T, operating at 99.3 MHz, using a zirconia rotor of 4 mm outer diameter spun at 12 kHz), thermogravimetric analysis (Rheometric Scientific STA 1500, 20-800 °C, 10°C/min, 40 mL/min N_2 flow), and FTIR (Thermo iS10 spectrometer with a custom-made cell, 6000−1000 cm^{-1}, 64 scans, 4 cm^{-1} resolution, transmission mode).

Prior to FTIR characterisation, zeolite samples were pressed into self-supported pellets (13 mm diameter, 10-15 mg). Activation was carried out in a vacuum system at 450 °C (ramp rate 1 °C/min, $<10^{-5}$ Torr) for 450°C, then the sample was cooled to ambient temperature under vacuum, and its IR spectrum was collected. Pyridine characterisation was conducted according to ref [40,41]. Following the activation procedure, the sample was kept at 150 °C and small portions of pyridine (C_5H_5N, Arcos Organics, 99.5%, dried over 3A molecular sieve) were introduced into the cell until the saturation of the acid sites. Physisorbed pyridine was removed by evacuation at 150 °C. Omnic software (Thermo) was used to analyse the obtained spectra.

The molar absorption coefficients were ε(Py-B)=1.26 cm/μmol and ε(Py-L)=1.79 cm/μmol, according to ref. [41]

For ^{29}Si MAS NMR, a single pulse excitation (30° flip angle) was used with a recycle delay of 30 s. For {^{1}H}^{29}Si CP-MAS NMR, a contact time of 5 ms and a recycle delay of 2 s were used, respectively. Chemical shifts were referenced to tetramethylsilane (TMS). All MAS NMR spectra were recorded using a 4mm MAS probe-head at a spinning rate of 12 kHz. Adsorption of trimethylphosphine oxide (TMPO, $(CH_3)_3PO$, Aldrich) as a probe-molecule was followed by ^{31}P NMR under ^{1}H decoupling. Samples were dehydrated at 400 °C under vacuum (~4×10^{-5} Torr) while a solution of TMPO in dichloromethane was prepared. TMPO solution was added to the dehydrated zeolite sample under an argon atmosphere in a glovebox, and the resulting suspension was treated in an ultrasonic bath for 15 min. The suspension was dried by evaporating the solvent under a vacuum for 2 h. The TMPO loaded zeolites were then packed in zirconium rotors for the NMR characterisation. ^{31}P π/2 and π-pulses lengths were 7 and 14 μs respectively for all measurements.

3.2.3 Sensor preparation

Sensors were made according to the procedure described in ref[42]. Silicon wafers were cut to 10x10 mm squares and cleaned with ethanol (95%, VWR chemicals) and acetone. The as-prepared sample was dispersed in acetone (4 wt%), mixed with 3-propylcelulose as a surfactant and deposited in several layers as a thin film on silicon wafers (10x10 mm) by spin coating (Laurell spin coater, model WS-400B-6NPP-LITE). Prepared films were then calcined for 30 minutes at 450 °C (ramp rate 5 °C/min).

3.2.4 Operando gas detection

Experiments testing the sensor performance were conducted using a custom-made operando cell in a flow system, with argon as a carrier gas containing 100 ppm of water. Prior to the

controlled adsorption of individual gas mixtures (20 to 5000 ppm of CO, CO_2, NO or NO_2 in Ar) the samples were activated in situ at 250 °C for 30 minutes (ramp rate 3 °C/min) and cooled down to the ambient temperature. The spectra were collected using a Thermo iS50 spectrometer, equipped with an MCT detector, using 64 scans at 4 cm^{-1} resolution in the 6000−1000 cm^{-1} spectral range. All presented sensor performance data are the difference spectra obtained by subtraction of the zeolite spectrum prior to the gas adsorption experiment from the spectrum of a sample at a specific concentration of the target gas. Since some water vapour was inherently present in the argon flow, gas-phase water correction was applied.

3.3 Results and Discussion

3.3.1 SEM and the ICP elemental analysis

A summary of the elemental analysis data and textural properties of the parent BEA-19, dealuminated BEA-19 (DeAl-BEA) and Sn-BEA samples is presented in Table 3.1 and their SEM micrographs are presented in Figures 3.2 -3.4. The observed particle size is in the range 0.5-2 μm, which is considerably smaller than those reported in the literature (5-20 μm) [20–27,32,35–37,43–49] Particles in the sub-micron range are necessary for the preparation of viable films for gas sensors. The obtained values agree with those reported in the literature[35], e.g. the attained Si/Sn ratio of 64 corresponds to 1.3% (calculated as Si/(Si+Sn)x100%), which is marginally higher than the reported values of 0.25-1 % reported for similar procedures[20–27,32,35–37,43–49].

Table 3.1. Summary of BEA-19, DeAl-BEA and Sn-BEA characterisation data.

	BEA-19	**DeAl-BEA**	**Sn-BEA**
Si/Al ratio	19.2	497	1541
Si/Sn ratio	-	-	64
w (H_2O) (%)	16	14	1
Crystallite size (XRD) (μm)	0.3	0.3	0.6
Particle size (SEM) (μm)	0.5-2	0.5-2	0.5-2
BET area (m^2/g)	640	572	504
BAS (μmol/g)	395	16	3
LAS (μmol/g)	106	6	20

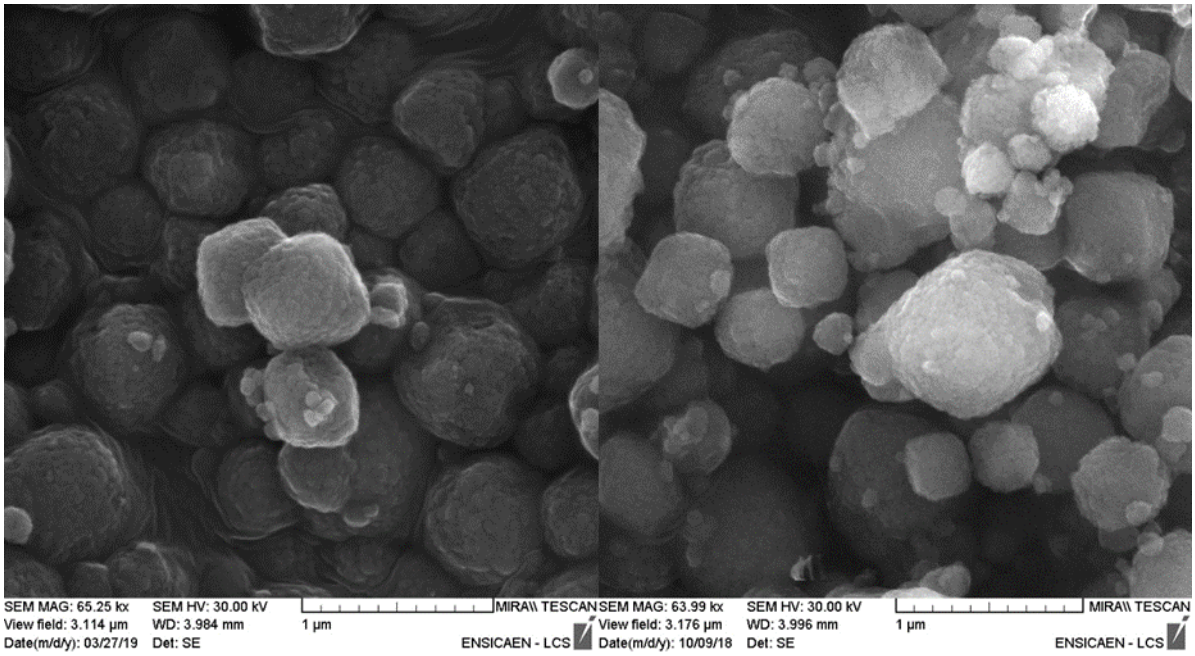

Figure 3.2. SEM micrographs of BEA-19 (left), DeAl-BEA (right).

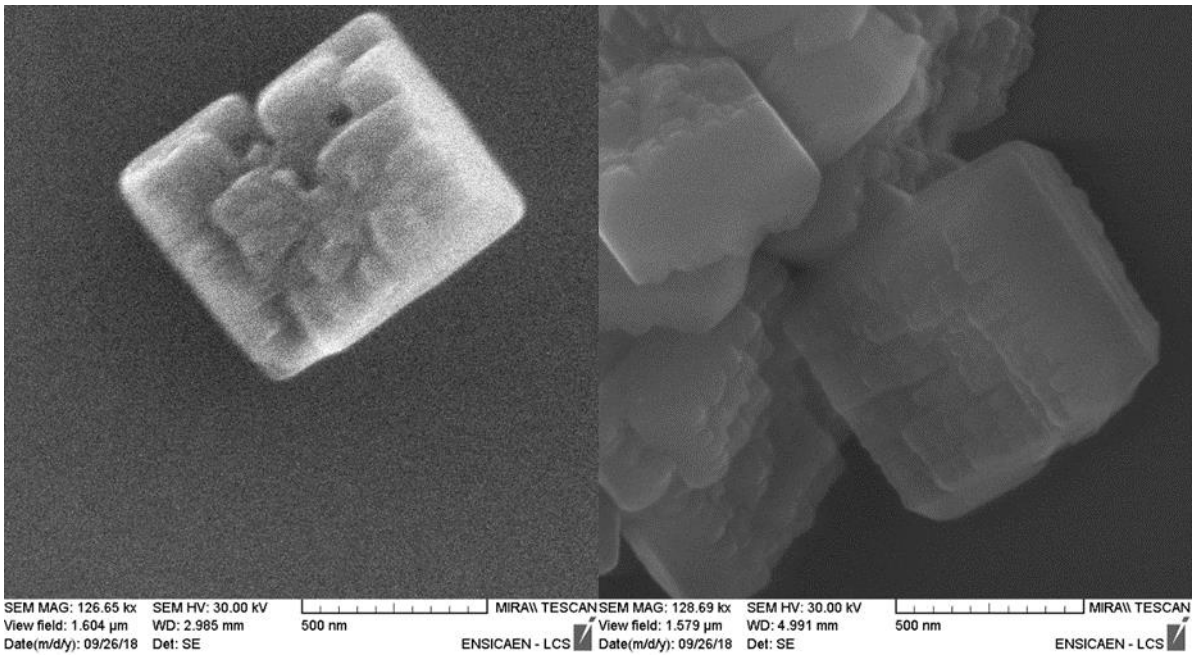

Figure 3.3. SEM micrographs of Sn-BEA.

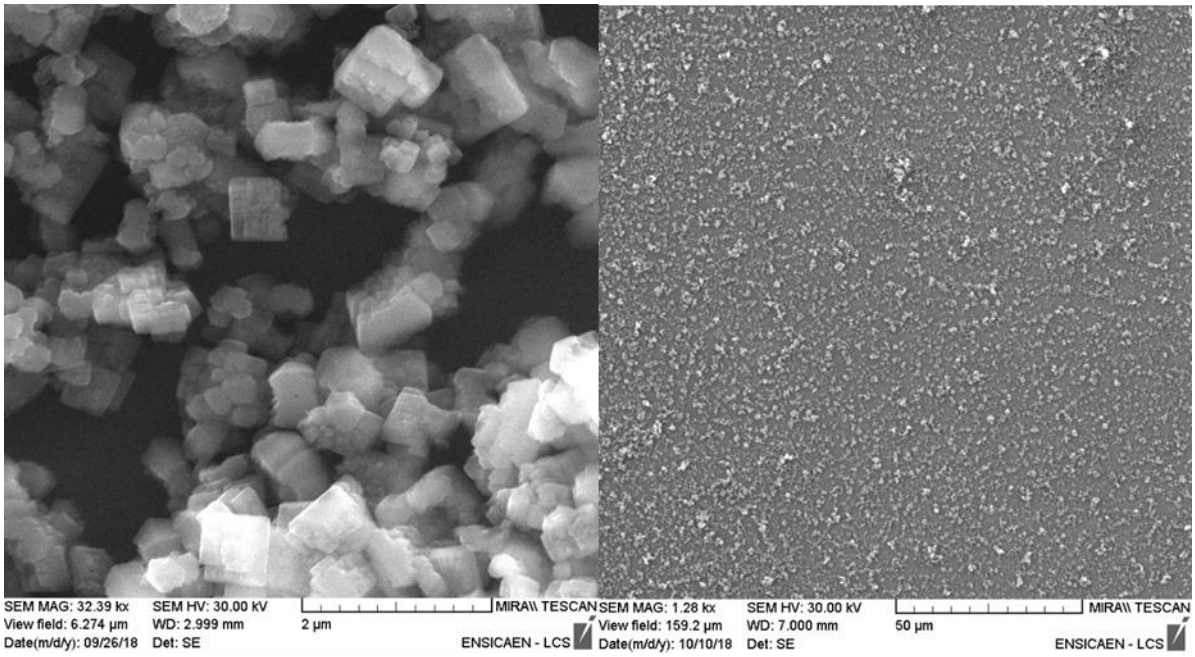

Figure 3.4. SEM micrographs of Sn-BEA powder (left), Sn-BEA (right).

3.3.2 XRD

XRD patterns of the parent BEA-19, dealuminated BEA-19 (DeAl-BEA) and Sn-BEA are presented in Figure 3.5. The collected patterns correspond to those previously reported in the literature.[34,35,44] Both DeAl-BEA and Sn-BEA maintain all the peaks characteristic of the BEA framework and no other zeolite phases have been detected.[50] Based on the peak intensities at 5-9, 13-15 and 17-19° 2Θ, the ratio polymorph A : polymorph B is 0.6 : 0.4 [50]. The peaks in the Sn-BEA pattern are well-defined as compared to those for BEA-19 and DeAl-BEA, indicating a larger size of the crystalline domains and fewer defects. They are also shifted to lower 2θ values relative to the parent zeolites, reflecting an increase in the lattice parameters because of Sn insertion into the framework. Peaks corresponding to the bulk SnO_2 phase (19.1, 26.5, 33.8, 37.6 and 51.5° 2Θ) have not been observed in the pattern of freshly prepared Sn-BEA. However, low-intensity peaks (19.1 and 26.5° 2Θ) have been detected 9 months after the sample preparation (Figure 3.6), which is probably due to the partial degradation of the Sn-

containing framework via hydrolysis of Si-O-Sn bonds and eventual formation of SnO_2 clusters and Si-OH groups.[43]

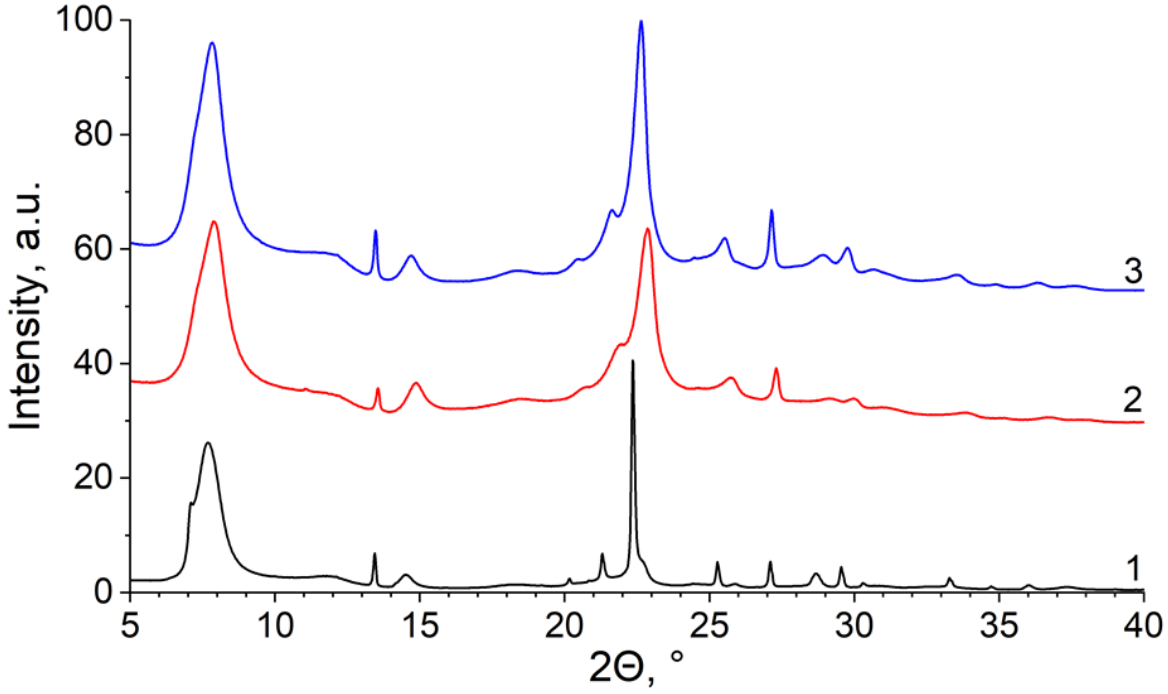

Figure 3.5. XRD patterns of Sn-BEA (1), DeAl-BEA-19 (2) and BEA-19 (3); patterns are offset for clarity.

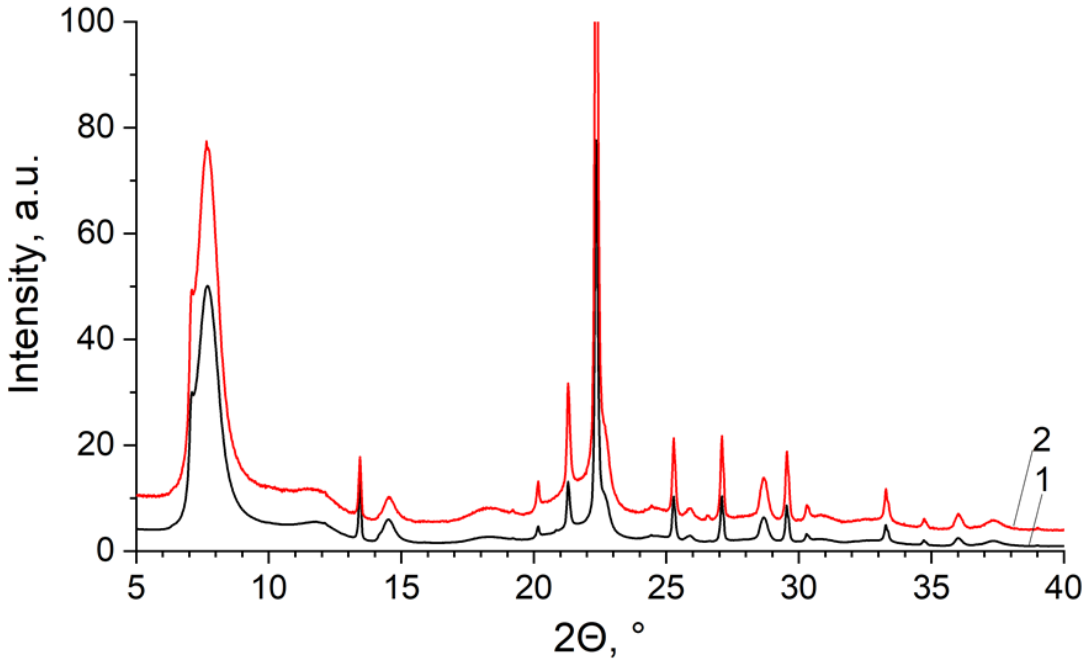

Figure 3.6. XRD patterns of Sn-BEA new (1), Sn-BEA after 9 months (2).

3.3.3 UV-VIS

The DR-UV spectrum of Sn-BEA (Figure 3.7) shows an intense peak at 222 nm, which is characteristic of the tetrahedral Sn atoms in the zeolite framework interacting with water molecules. A low-intensity peak around 290 nm indicates a minor contribution of SnO_2 in the sample.[35,49] These data further support a high level of Sn atoms substitution in the BEA structure, rather than the presence of a mixture of SnO_2 and a siliceous zeolite.

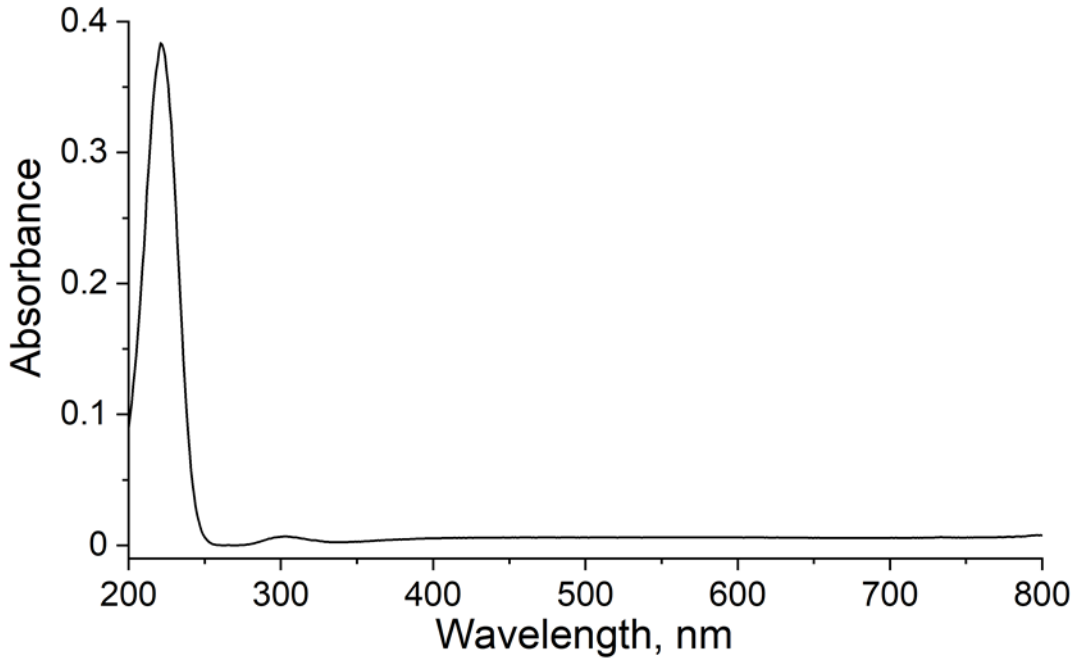

Figure 3.7. DRUV-VIS spectrum of Sn-BEA.

3.3.4 TGA

The results of the thermogravimetric analysis are presented in Figure 3.8. Calcined Sn-BEA shows a negligible water loss (1%) compared to parent BEA-19 (16%) and DeAl-BEA (14%) upon heating to 200 °C. The water loss for both BEA-19 and DeAl-BEA is similar because of the presence of bridging OH-groups in the former and silanol nests in the latter, both of which increase the degree of hydrophilicity. Importantly, this characterisation technique indicated the

high level of hydrophobicity of the Sn-BEA sample, which would be a beneficial feature for a sensor operating in humid environments.

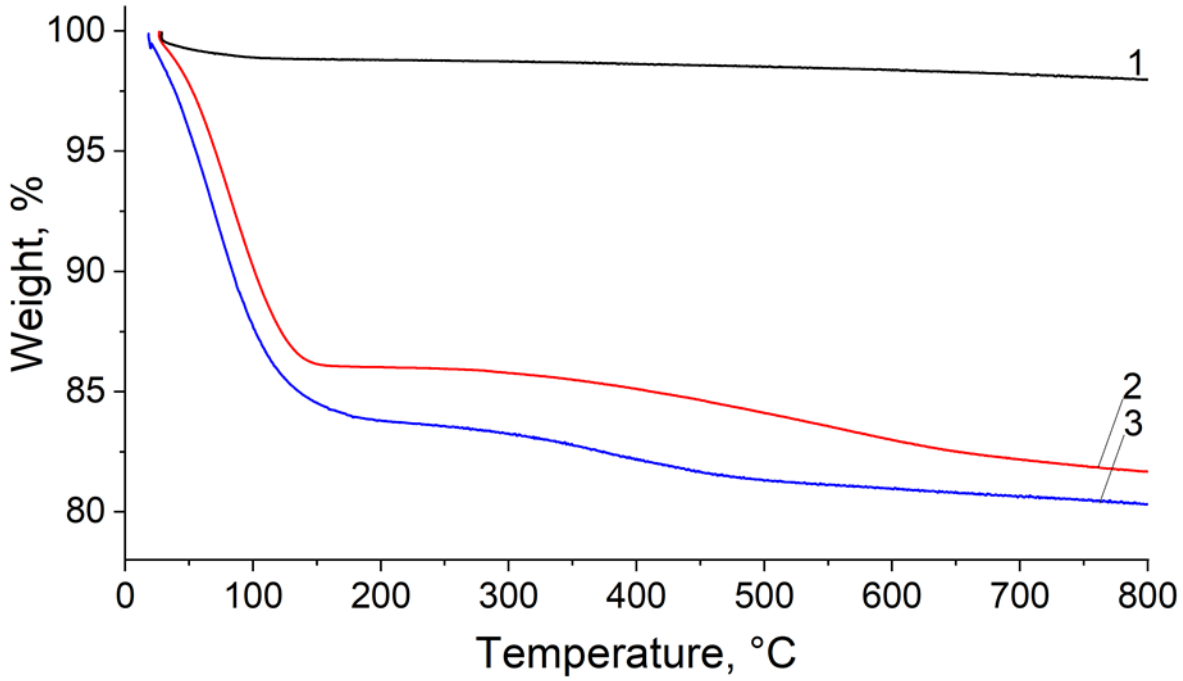

Figure 3.8. TGA curve of Sn-BEA (1), DeAl-BEA (2) and BEA-19 (3).

3.3.5 NMR

^{29}Si MAS NMR spectra Sn-BEA demonstrate that all the peaks (-111.6, -112.2, -113.1, -115.7 ppm) are in the Q^4 region for the BEA framework (Figure 3.9). The well-defined narrow peaks in this region are indicative of a highly siliceous zeolite with very few structural defects in the framework.[51] In contrast, the spectrum of parent BEA-19 shows relatively broad overlapping peaks in the regions corresponding to Q^3 and Q^4 species, such as $Si(OAl)_x(OSi)_{4-x}$ or $Si(OH)_x(OSi)_{4-x}$, where x is 0 or 1.[28,37] These samples have been further characterised using ^{29}Si-^{1}H cross-polarization (Figure 3.10**)**. In the ^{29}Si-^{1}H CP MAS NMR spectrum of Sn-BEA, three ill-defined peaks (-104, -114 and -118 ppm) have been detected. These peaks correspond

to the Q^3 and Q^4 regions of the spectrum.[52] However, the signal intensity is very low, which further confirms that there are almost no silanol groups present in the Sn-BEA sample.

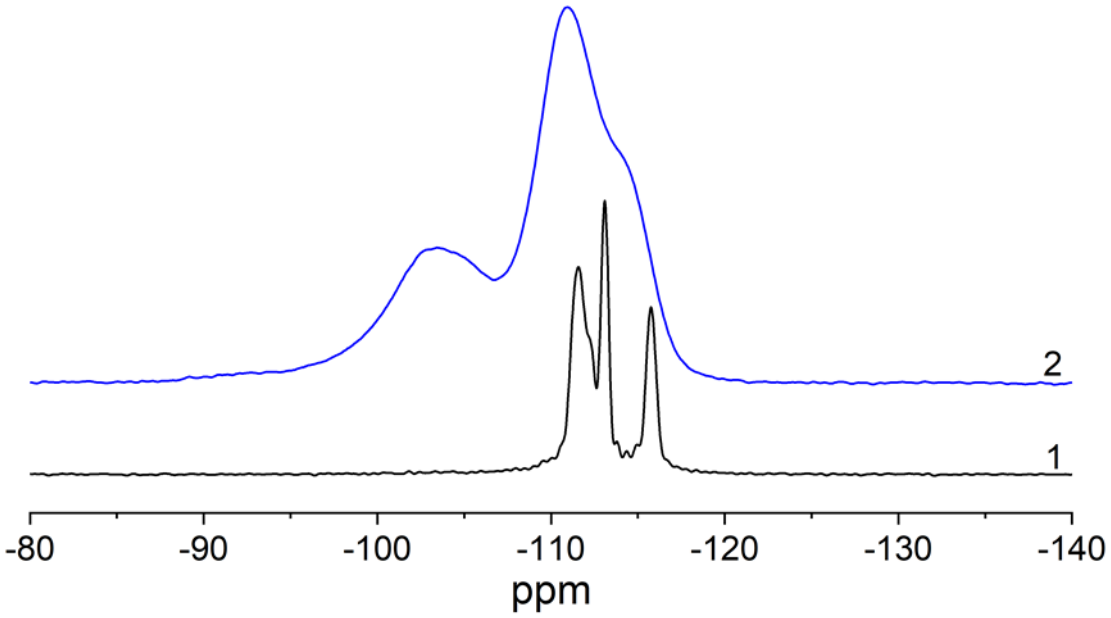

Figure 3.9. ^{29}Si MAS NMR spectra of Sn-BEA (1) and BEA-19 (2).

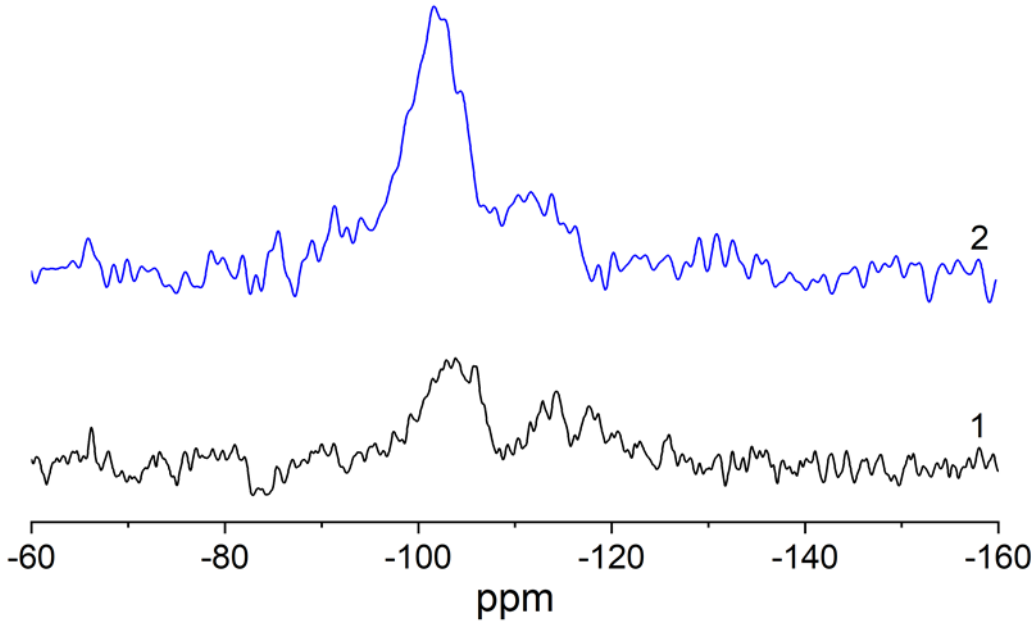

Figure 3.10. ^{29}Si-^{1}H CP MAS NMR spectra of Sn-BEA (1), BEA-19 (2).

In the ^{31}P NMR spectrum of TMPO adsorbed on DeAl-BEA, only one peak around 50 ppm is observed (Figure 3.11), which can be assigned to TMPO interacting with weak BAS, i.e. silanol groups.[38,53,54] No peak at this position is found for the Sn-BEA sample, further indicating that there are very few defects in the structure. The spectrum of TMPO adsorbed on Sn-BEA contains two distinctive peaks, a low-intensity sharp one at 43.2 ppm and an intense broad peak at 35.9 ppm. There is some discussion in the literature regarding the interpretation of the ^{31}P NMR spectra of TMPO adsorbed on zeolites. Indeed, according to [38,54] the peak around 43 ppm should be attributed to physisorbed TMPO. Lewis et al.,[38] who first reported characterisation of Sn-containing zeolites, stated that the physisorbed TMPO is represented by wide peaks (fwhm>9 ppm) and the bound TMPO has narrow peaks (fwhm <1.5 ppm). On the other hand, Dubray et al.[53] reported a different interpretation of adsorbed TMPO on Mo-containing MFI zeolites, describing the narrow peaks as physisorbed TMPO and the broad peaks as the molybdenum bound TMPO. Overall, the interpretation of TMPO spectra is not unambiguous. Therefore, the narrow peak observed in this work at 43.2 ppm is tentatively ascribed to physisorbed TMPO. The more intense broad peak at 35.9 ppm (fwhm> 9 ppm) is not symmetrical. This results from an overlap of two peaks at 35.9 ppm and 40.8 ppm with an intensity ratio of approximately 3:1, as shown by the spectral deconvolution presented in Figure 3.12. This ratio is similar to that reported by Lewis et al.[38] for peaks 58.6 ppm and 54.9 ppm, which were attributed to penta-coordinated Sn-sites. As the downfield shift in the TMPO spectra is generally related to the TMPO adsorbed on stronger LAS or BAS, the peaks at 35.9 ppm and 40.8 ppm found in this work could be assigned to TMPO interacting with weak LAS associated with Sn atoms in the zeolite framework. Their upfield shift could be also explained by the presence of residual F^- ions in the BEA structure. [23,38]

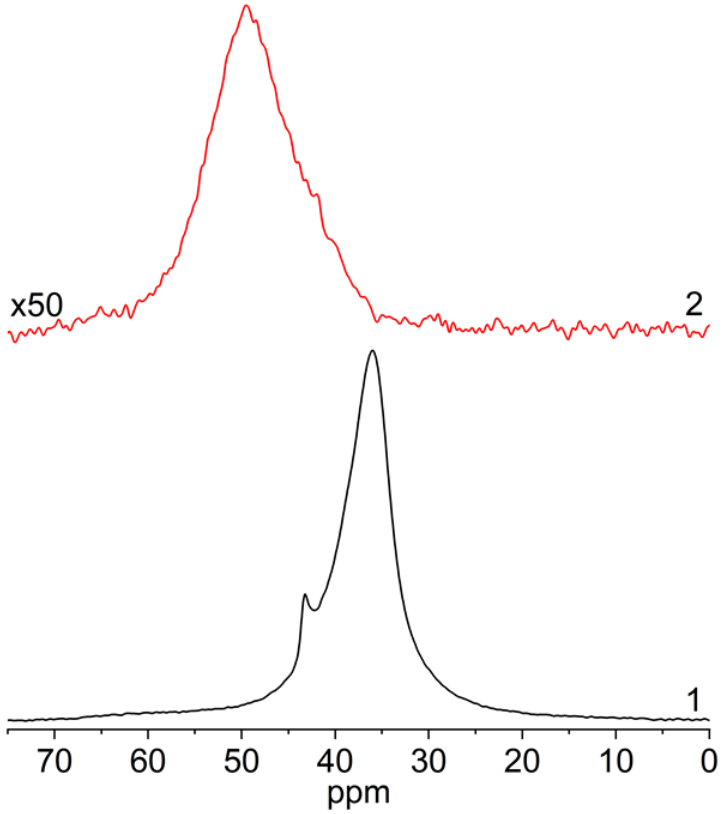

Figure 3.11. ^{31}P MAS NMR spectra of TMPO adsorbed on Sn-BEA (1) and DeAl-BEA (2, intensity is multiplied by a factor of 50).

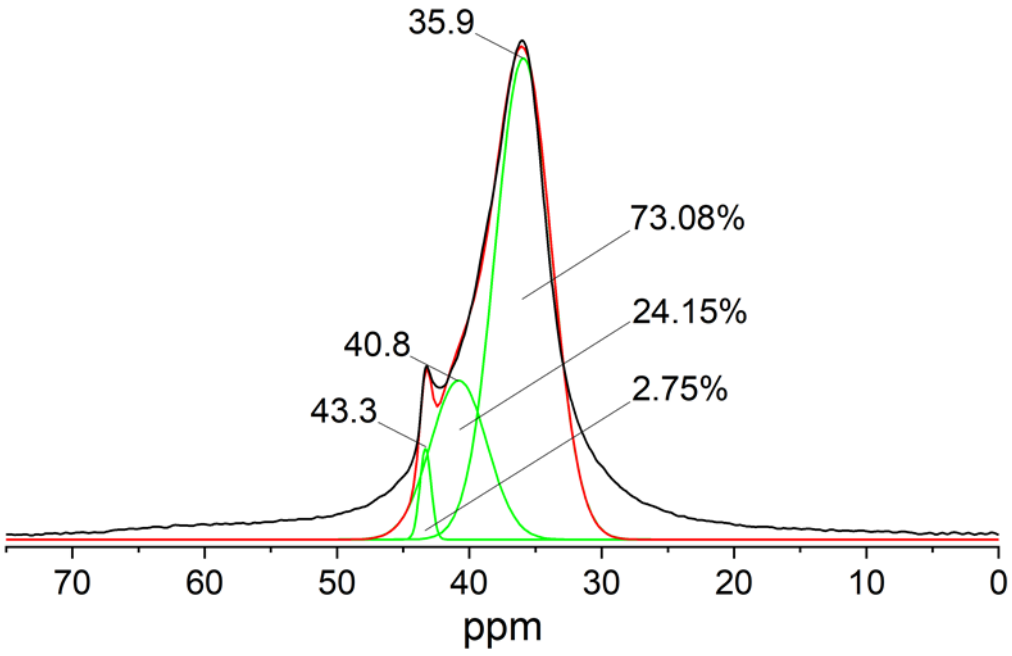

Figure 3.12. Deconvoluted ^{31}P MAS NMR spectrum of TMPO adsorbed on Sn-BEA (black), fitted cumulative peak (red), single fitted peaks (green).

3.3.6 FTIR

FTIR spectra of the studied zeolites before and after adsorption of Py are presented in Figures 3.13 and 3.14, and the number of BAS and LAS is summarised in Table 3.1. Most of the aluminium from the initial BEA-19 sample was removed during the dealumination process, which has been confirmed by the elemental analysis (Table 3.1). Following this procedure, "silanol nests" are generated in the parts of the structure where aluminium is removed, which can be observed in the 3800-3500 cm^{-1} region, as the peak corresponding to Si-OH groups (~3740 cm^{-1} for BEA-19 and ~3727 cm^{-1} for DeAl-BEA) broadens and increases in intensity as compared to the parent sample due to hydrogen bonding within the newly formed silanol nests (Figure 3.13).

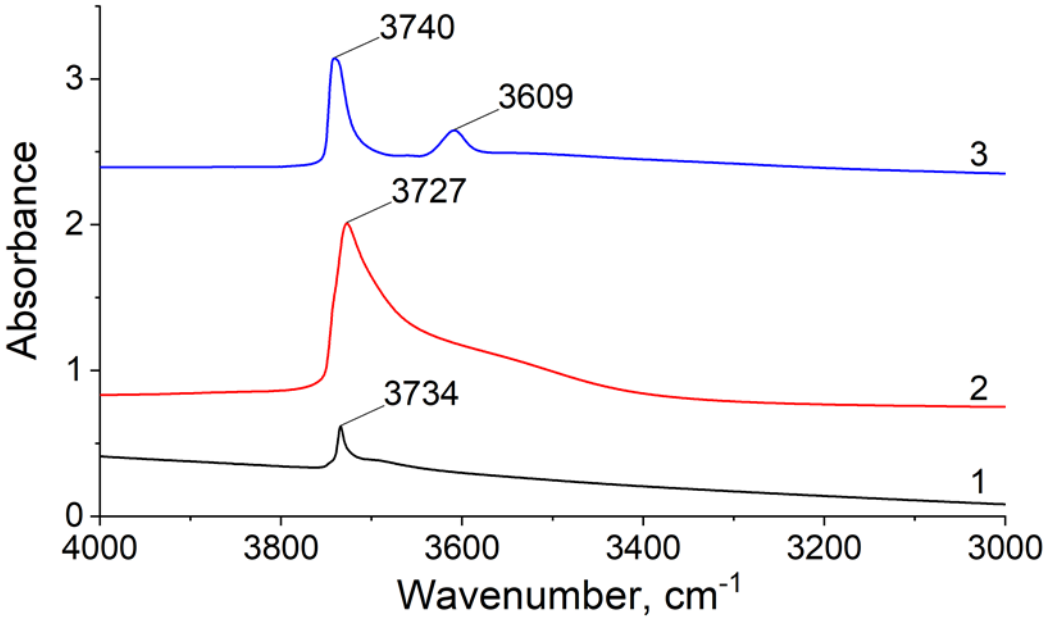

Figure **3.13**. Difference FTIR spectra of Sn-BEA (1), DeAl-BEA (2), BEA-19 (3); spectra are offset for clarity.

The number of B-Py (~1545 cm^{-1}) and L-Py (~1455 cm^{-1}) complexes detected via Py adsorption on the parent BEA-19 is 395 and 106 μmol/g, but only 16 and 6 μmol/g on the

DeAl-BEA, confirming successful dealumination of the original zeolite. For Sn-BEA, the number of detected BAS is less than 3 μmol/g, indicating almost a complete loss of OH-groups in the structure during the fluoride mediated synthesis, whereas the number of LAS has increased to 20 μmol/g in comparison with the DeAl-BEA sample. Note that the number of Sn atoms introduced into Sn-BEA is 1.5% of T atoms. Importantly, the peak position of the Py-L complexes has shifted from 1455 cm^{-1} for BEA-19 to 1450 cm^{-1} for Sn-BEA (Figure 3.14), which corresponds to Py interacting with weak LAS.[41] All these data are indicative of tin incorporation into the BEA framework.[37]

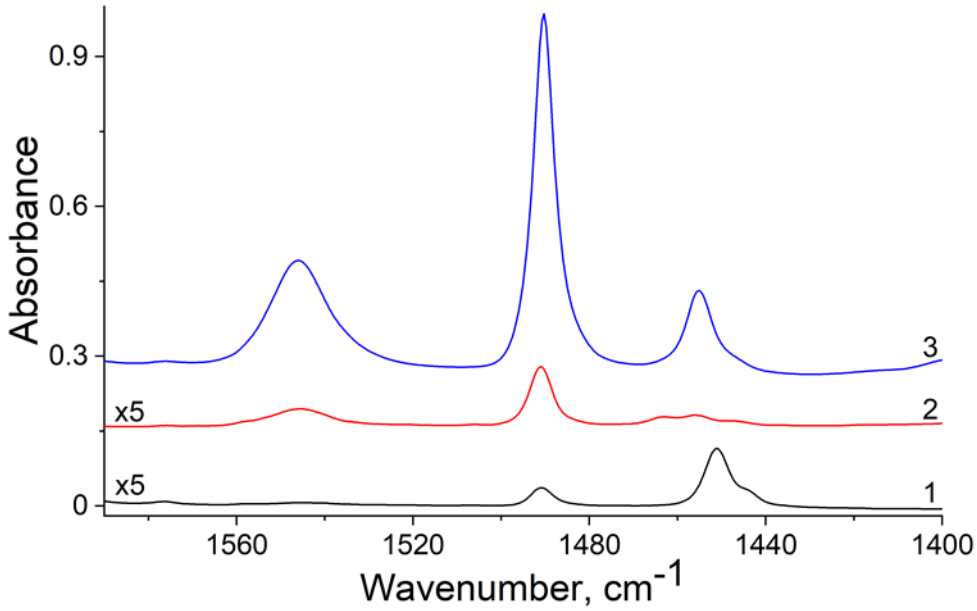

Figure **3.14**. Difference FTIR spectra of Sn-BEA (1), DeAl-BEA (2) and BEA-19 (3); spectra are offset for clarity.

The difference FTIR spectra (Figure 3.15) show negative peaks in the 3600-3800 cm^{-1} region. The negative peak of low intensity at ~3741 cm^{-1} for Sn-BEA results from Py interaction with a small number of external silanols. For DeAl-BEA, the negative peak at 3728 cm^{-1} (with a shoulder at ~3741 cm^{-1}) is due to Py interacting mostly with internal and with some external silanol groups. This could be explained by the insertion of Sn atoms in the "silanol nests" in

the framework of DeAl-BEA, used as the seed material, which is in accord with the collected TGA and NMR data, hence confirming that the Sn-BEA sample is largely silanol-free and thus hydrophobic.

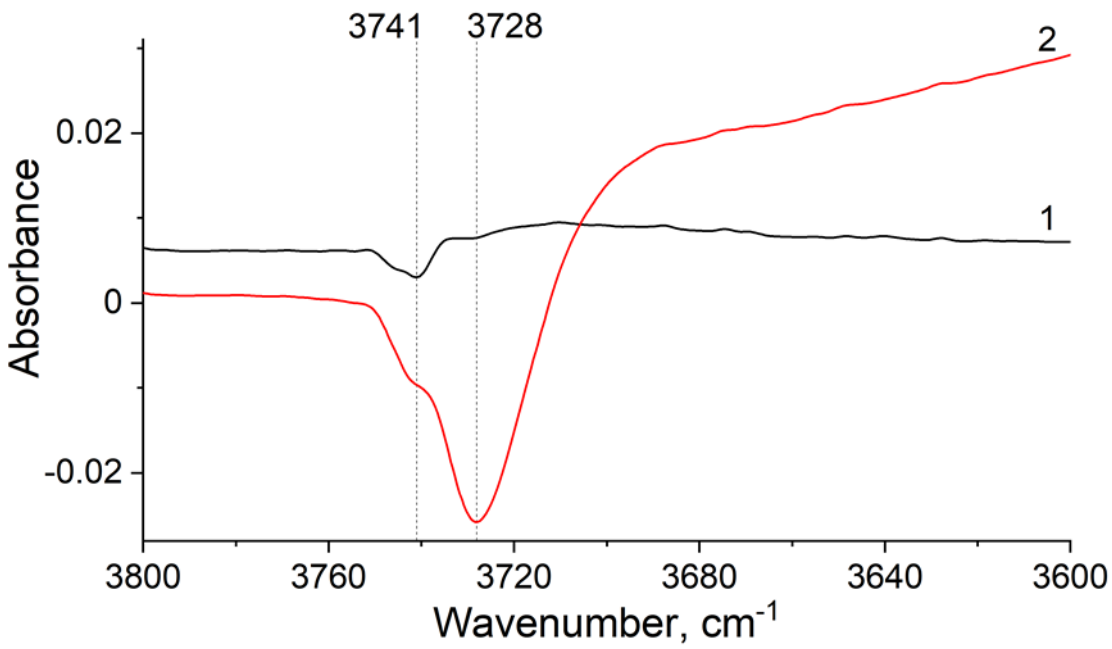

Figure 3.15. Difference FTIR spectra of Sn-BEA (1) and DeAl-BEA (2) in the OH region following pyridine adsorption.

3.3.7 CO, CO_2, NO, NO_2 adsorption on Sn-BEA and DeAl-BEA

The response of the prototype sensors based on Sn-BEA and the parent DeAl-BEA zeolites towards adsorption of specific gases and water vapour has been monitored by operando FTIR and the data are presented in Figures 3.16-3.20 and 7.64 -7.72. Both Sn-BEA and DeAl-BEA have shown selective response towards NO_2, (Figures 3.16, 3.17, 7.67 and 7.72), while the DeAl-BEA has also been responsive to CO_2 (Figures 7.69 and 7.70). When no significant gas adsorption is observed, e.g. for CO and NO, mostly the peaks corresponding to the gas phase of the used target gas and water vapour have been observed, along with the peaks in the 1620-1640 cm^{-1} region assigned to the bending vibration mode of water adsorbed on the zeolite

surface.[55] As mentioned previously, the adsorbed water stems from the water vapour introduced into the carrier gas to provide a more realistic model of the tested gas flows. For the adsorption of CO_2 on DeAl-BEA (Figures 7.69 and 7.70), the peak observed at 2344 cm^{-1} is ascribed to physisorbed CO_2, probably on the surface OH-groups.[55] Since this peak is overlaying with the gas phase peaks of CO_2, the gas phase correction was applied to quantify the data (Figure 7.70).

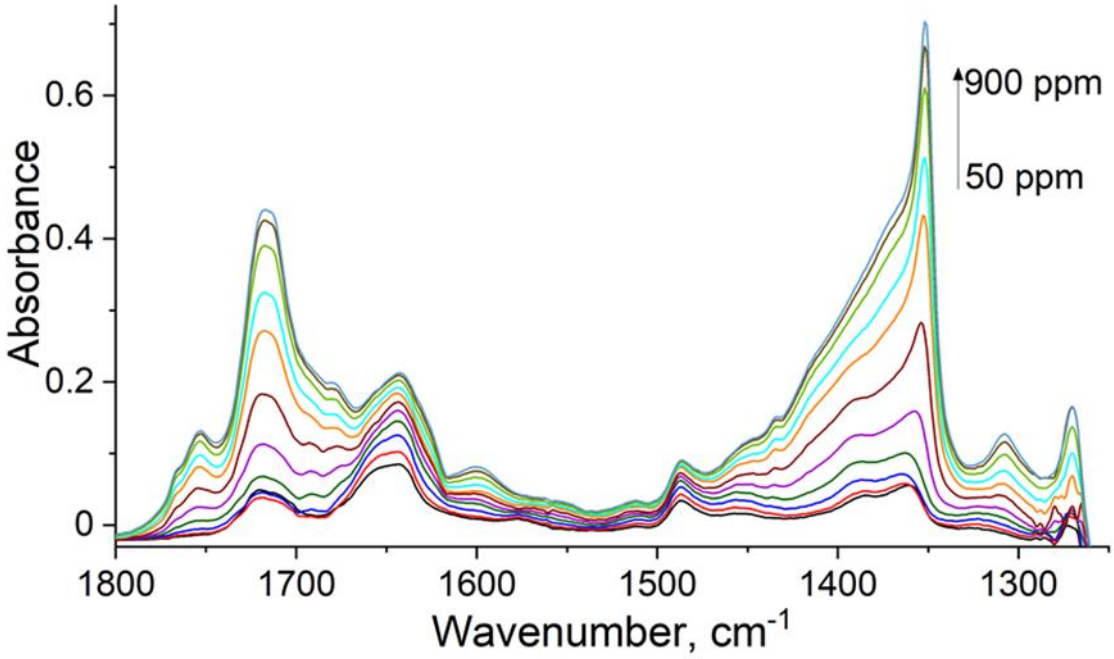

Figure 3.16. Difference FTIR spectra of NO_2 adsorbed on Sn-BEA, 50 ppm (black); 50-100 ppm in 25 ppm increments; 100-900 ppm in 100 ppm increments.

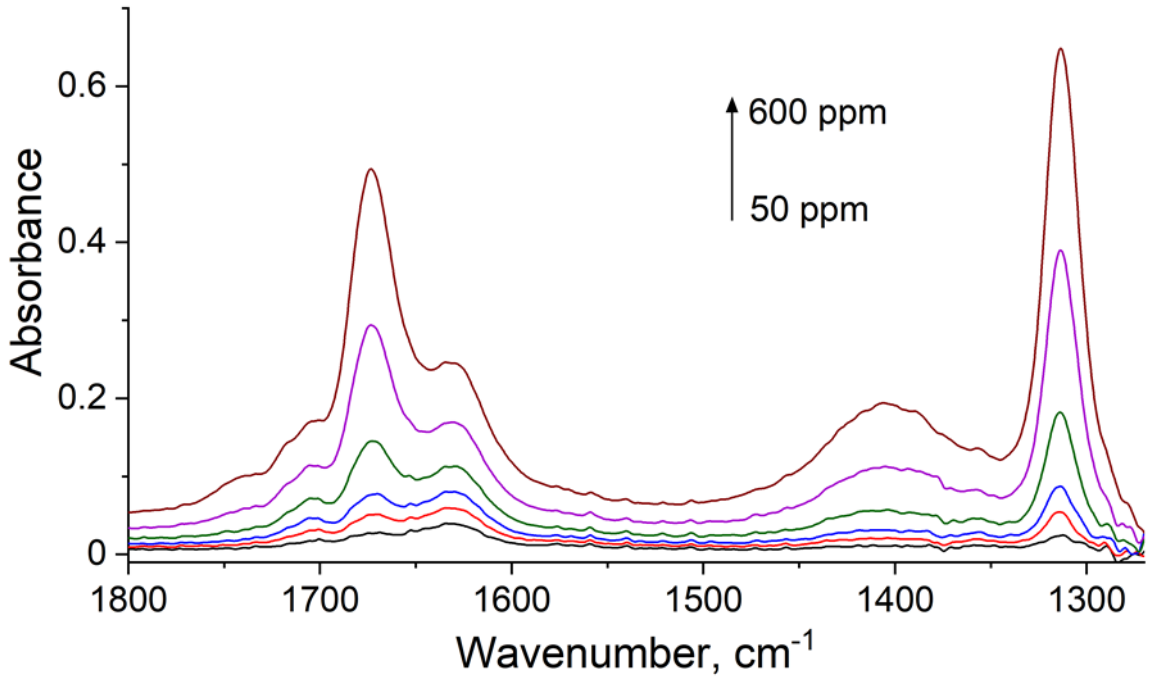

Figure 3.17. Difference FTIR spectra of NO_2 adsorbed on DeAl-BEA, 50 ppm (black), 75 ppm (red), 100 ppm (blue), 200 ppm (green), 400 ppm (purple), 600 ppm (dark red).

Probably, the most interesting result of these tests is the observed selective response of both Sn-BEA and DeAl-BEA towards the adsorption of NO_2. Two main regions of the spectrum containing distinctive peaks indicative of the interaction of the sensors with NO_2 are 1800-1600 cm^{-1} (region A) and 1500-1300 cm^{-1} (region B). In region A for Sn-BEA, only two peaks at 1645 and 1720 cm^{-1} can be detected at lower concentrations (50-400 ppm). At 50 ppm of NO_2, the peak ratio is approximately 2:1, with the ratio decreasing as the concentration increases to 400 ppm (Figure 3.16). At higher concentrations (>500 ppm), the peak at 1720 cm^{-1} becomes the most intense. Further peaks appear at 1600 and 1755 cm^{-1}, and a shoulder at 1685 cm^{-1}. For DeAl-BEA, only a band at 1630 cm^{-1} is found initially. As more NO_2 is introduced, additional peaks develop at 1670 and 1700 cm^{-1} (Figure 3.17). The peak at ~1670 cm^{-1} is increasing in intensity with a peak at 1700 cm^{-1} merging as a shoulder to the central peak as the concentration of NO_2 increases. In region B for Sn-BEA, the main peaks are

observed at ~1310, 1360 (most intense with a broad shoulder) and 1485 cm^{-1} (Figure 3.16). For the DeAl-BEA sample, the major peaks are found at 1315 and 1405 cm^{-1} (Figure 3.17).

In agreement with the literature, the peaks appearing upon NO_2 adsorption can be attributed to the disproportionation of NO_2 on contact with solid catalysts, resulting in the formation of a range of monodentate, bidentate or bridging NO^+, NO_2^- and NO_3^- species as well as more complex structures resulting from their transformations.[56–58] Since the Sn-loading of Sn-BEA is relatively low, the formation of bridging species could be excluded. Furthermore, as no peaks have been detected in the 2200-2000 cm^{-1} region of the spectrum, the presence of -NO^+ and -$NO^+(NO_2)$ species on the samples prepared in this work should probably be ruled out.[56,57] Based on the NO_2 adsorption data for Sn-MFI and Fe-exchanged MFI and BEA zeolites, peaks in the 1800-1600 cm^{-1} region can be assigned to nitro- species bound to either Al or Sn. The peaks at ~1760-1710 cm^{-1} are commonly attributed to N_2O_4 dimers.[13,56–61] This is in accord with their occurrence at higher concentrations of NO_2. The peaks at ~1645 cm^{-1} for Sn-BEA and 1630 cm^{-1} for DeAl-BEA could be interpreted as coordinated nitro-species, however, they can also originate from potentially overlapping peaks of adsorbed water, found in experiments with all the gases containing 100 ppm of water in the Ar flow (Figures 7.73 and 7.74). The peak positions in region A for Sn-BEA are blue-shifted as compared to those for DeAl-BEA, Si- and Sn-MFI. The peaks in region B can be attributed to nitrate or nitrite species.[56–61] This interpretation is further confirmed by the room-temperature desorption experiments (Figures 3.20 and 7.75). Most peaks in region A are partially removed, which is characteristic of relatively weakly bound species, such as NO_2 or N_2O_4. Indeed, the 1601 cm^{-1} peak disappeared instantly after stopping the NO_2 flow, while the intensity of other peaks, e.g. at 1645 cm^{-1}, decreases gradually. This could indicate that the latter peak results from a superposition of nitro-species and adsorbed water. The IR peaks in region B demonstrate only very minor changes throughout the desorption period, which can be attributed to subtle transformations of

NO_3^- and NO_2^-, while the total peak area in the B region is virtually unchanged (Figure 3.20), as would be expected for the nitrate and nitrite species.[58]

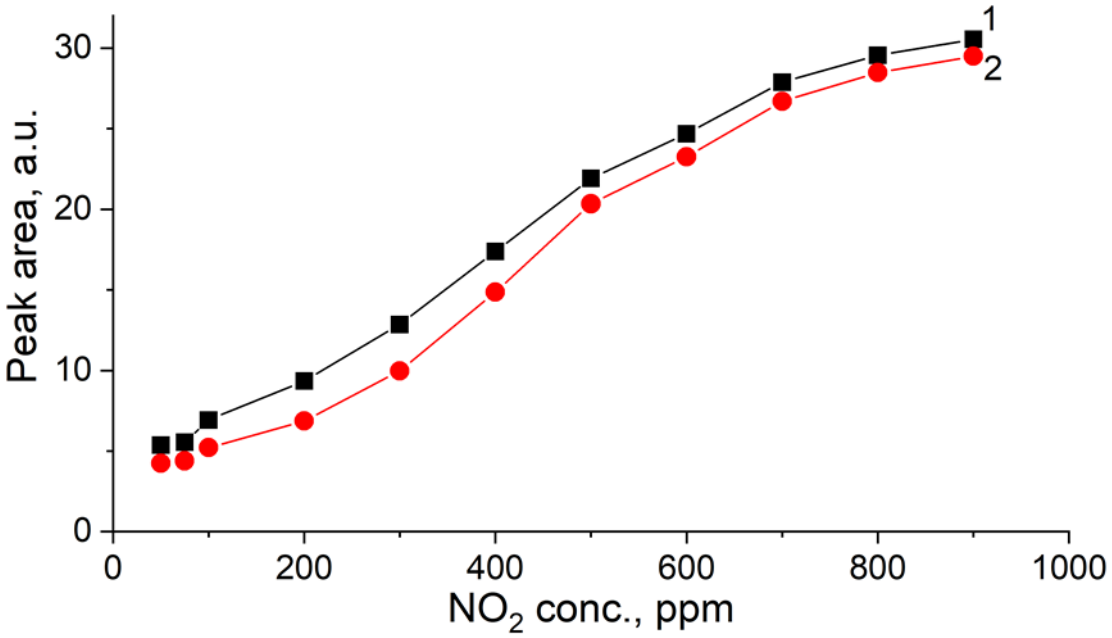

Figure **3.18**. Evolution of the IR peak areas following NO_2 adsorption on Sn-BEA: 1800-1600 cm^{-1} (1), 1500-1300 cm^{-1} (2).

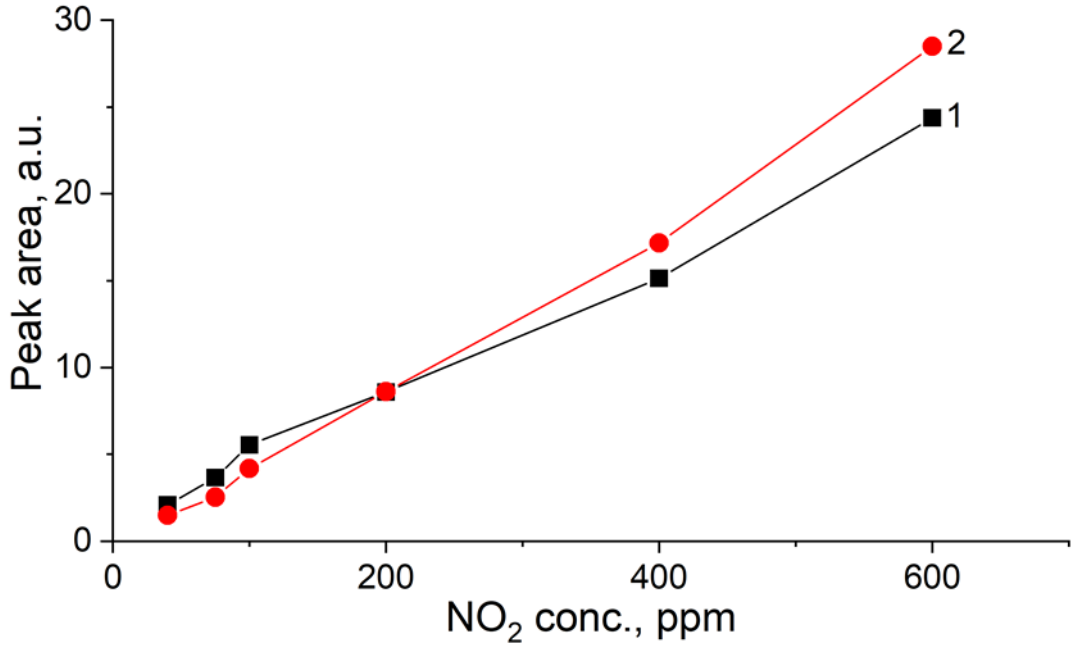

Figure **3.19**. Evolution of the IR peak areas following NO_2 adsorption on DeAl-BEA: 1800-1600 cm^{-1} (1), 1500-1300 cm^{-1} (2).

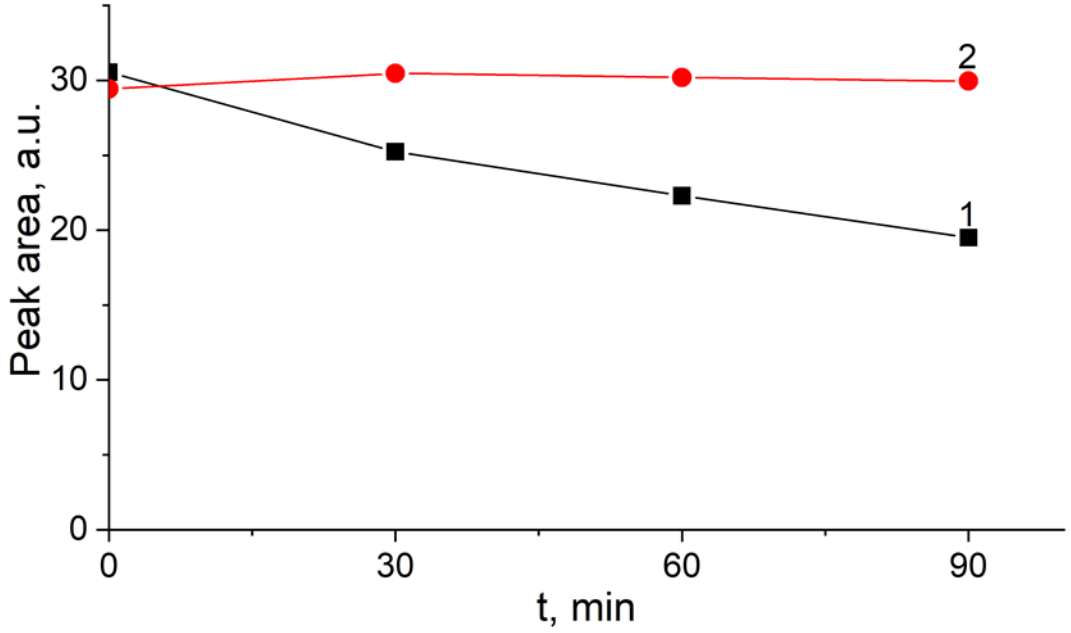

Figure 3.20. Evolution of the IR peak areas of NO_2 adsorbed on Sn-BEA upon desorption in Ar flow at room temperature: 1800-1600 cm^{-1} (1) and 1500-1300 cm^{-1} (2).

For the actual sensor performance, the areas of all peaks in a specific part of the spectrum, e.g. regions A and B, are more important since the portable IR sensors do not possess spectral resolution comparable to research-grade laboratory instruments.[11] Therefore, for the performance of a sensor, it is more useful to quantify the peak area of the "target" regions that corresponds to a specific concentration value. For Sn-BEA and DeAl-BEA, the absorption peaks of various NxOy species in both regions (1800-1600 and 1500-1300 cm^{-1}) are evolving in a similar fashion (Figures 3.18 and 3.19). The growth is not quite linear, and it is comparable to the Sn-MFI system.[13] As mentioned above, the peaks in the 1800-1600 cm^{-1} region can be partially removed upon desorption of NO_2 from Sn-BEA at room temperature, while the peaks from 1500 to 1300 cm^{-1} cannot. Therefore, in the 1800-1600 cm^{-1} region the sensor could be used to determine dynamic changes in the current concentration, while the 1500-1300 cm^{-1} region would allow detecting the maximum concentration of NO_2 in the monitored system during a certain period.

3.4 Conclusions

Exhaust fumes gas sensors containing Sn-BEA and dealuminated BEA zeolites have been prepared and extensively characterised. The prepared Sn-BEA sample has a nearly defect-free structure, high hydrophobicity and a sub-micron particle size. Sn-BEA has been utilised as an IR-based gas sensor at room temperature and its performance has been compared to that of DeAl-BEA. Both sensors have been evaluated for their response to CO, CO_2, NO and NO_2 in the presence of water.

Prepared materials were successfully applied as gas sensors. Sn-BEA displayed a selective response to NO_2, while DeAl-BEA responded to CO_2 and NO_2. Also, the Sn-BEA demonstrated the potential to determine both the current concentration of the analyte gas and the peak concentration during a certain period. This presents a valuable starting point for evaluation of sensor performance for zeolite catalysts with other isomorphously incorporated metals (e.g. Ti, Zr, Mo). The future work on Sn-BEA should focus on the optimisation of synthesis and composition of hydrophobic zeolite-based sensors. Also, the sensor performance under realistic conditions, including elevated temperatures and humidity levels needs to be evaluated and the studied operational concentration range should be expanded.

3.5 Acknowledgments

The work presented in this chapter was conducted in collaboration with prof. Svetlana Mintova's group (J. Grand, L. Lakiss, F. Dubray, P. Bazin, J. El Fallah) from Normandie Univ, ENSICAEN, CNRS, Laboratoire Catalyse et Spectrochimie, France.

3.6 References

1. WHO-OEHT. *WHO Air quality guidelines for particulate matter, ozone, nitrogen dioxide and sulfur dioxide*. (2006).

2. European Environment Agency (EEA). *Air quality in Europe - 2020 report*. *EEA Report* (2020).

3. Sassykova, L. R., Aubakirov, Y. A., Sendilvelan, S., Tashmukhambetova, Z. K., Faizullaeva, M. F., Bhaskar, K., Batyrbayeva, A. A., Ryskaliyeva, R. G., Tyussyupova, B. B., Zhakupova, A. A. & Sarybayev, M. A. The Main Components of Vehicle Exhaust Gases and Their Effective Catalytic Neutralization. *Orient. J. Chem.* **35**, 110–127 (2019).

4. Department for Environment Food and Rural Affairs. *What are the causes of air Pollution Pollutant Description and main UK sources Potential effects on health/environment Particulate*. (2011).

5. Wadhwani, P. & Yadav, S. Gas Sensors Market Size & Share - Global Forecasts 2026. *GMI Pulse* (2020).

6. Fergus, J. W. Materials for high temperature electrochemical NOx gas sensors. *Sensors Actuators, B Chem.* **121**, 652–663 (2007).

7. Park, C. O., Fergus, J. W., Miura, N., Park, J. & Choi, A. Solid-state electrochemical gas sensors. *Ionics (Kiel).* **15**, 261–284 (2009).

8. Gardon, M. & Guilemany, J. M. A review on fabrication, sensing mechanisms and performance of metal oxide gas sensors. *J. Mater. Sci. Mater. Electron.* **24**, 1410–1421 (2013).

9. Wang, C., Yin, L., Zhang, L., Xiang, D. & Gao, R. Metal oxide gas sensors: Sensitivity and influencing factors. *Sensors* **10**, 2088–2106 (2010).

10. Dey, A. Semiconductor metal oxide gas sensors: A review. *Mater. Sci. Eng. B Solid-State Mater. Adv. Technol.* **229**, 206–217 (2018).

11. Dinh, T.-V., Choi, I.-Y., Son, Y.-S. & Kim, J.-C. A review on non-dispersive infrared gas sensors: Improvement of sensor detection limit and interference correction. *Sensors*

Actuators B **231**, 529–538 (2016).

12. *Introduction to Zeolite Science and Practice*. (eds. Cejka, J., van Bekkum, H., Corma, A. & Schuth, F.) (Elsevier Science, 2007).

13. Talapaneni, S. N., Grand, J., Thomas, S., Ahmad, H. A. & Mintova, S. Nanosized Sn-MFI zeolite for selective detection of exhaust gases. *Mater. Des.* **99**, 574–580 (2016).

14. Xu, X., Wang, J. & Long, Y. Zeolite-based materials for gas sensors. *Sensors* **6**, 1751–1764 (2006).

15. Sahner, K., Hagen, G., Schönauer, D., Reiß, S. & Moos, R. Zeolites - Versatile materials for gas sensors. *Solid State Ionics* **179**, 2416–2423 (2008).

16. Yang, P., Ye, X., Lau, C., Li, Z., Liu, X. & Lu, J. Design of Efficient Zeolite Sensor Materials for n-Hexane. *Anal. Chem.* **79**, 1425–1432 (2007).

17. Corma, A., Camblor, M. A., Esteve, P., Martínez, A. & Pérez-Pariente, J. Activity of Ti-Beta Catalyst for the Selective Oxidation of Alkenes and Alkanes. *Journal of Catalysis* vol. 145 151–158 (1994).

18. Zhou, W., Sun, P., Navrotsky, A., Kim, S. H. & Hong, S. B. Formation and dehydration enthalpies of gallosilicate materials with different framework topologies and Ga contents. *Microporous Mesoporous Mater.* **121**, 200–207 (2009).

19. Bui, L., Luo, H., Gunther, W. R. & Román-Leshkov, Y. Domino reaction catalyzed by zeolites with Brønsted and Lewis acid sites for the production of γ-valerolactone from furfural. *Angew. Chemie - Int. Ed.* **52**, 8022–8025 (2013).

20. Luo, H. Y., Consoli, D. F., Gunther, W. R. & Román-Leshkov, Y. Investigation of the reaction kinetics of isolated Lewis acid sites in Beta zeolites for the Meerwein-Ponndorf-Verley reduction of methyl levulinate to γ-valerolactone. *J. Catal.* **320**, 198–207 (2014).

21. Lewis, J. D., Van De Vyver, S. & Román-Leshkov, Y. Acid-Base Pairs in Lewis Acidic Zeolites Promote Direct Aldol Reactions by Soft Enolization. *Angew. Chemie - Int. Ed.* **54**, 9835–9838 (2015).

22. Corma, A., Nemeth, Laszlo, T., Renz, M. & Valencia, S. Sn-zeolite beta as a heterogeneous chemoselective catalyst for Baeyer-Villiger oxidations. *Nature* **412**, 423–425 (2001).

23. Hwang, S. J., Gounder, R., Bhawe, Y., Orazov, M., Bermejo-Deval, R. & Davis, M. E. Solid State NMR Characterization of Sn-Beta Zeolites that Catalyze Glucose Isomerization and Epimerization. *Top. Catal.* **58**, 435–440 (2015).

24. Bermejo-Deval, R., Assary, R. S., Nikolla, E., Moliner, M., Román-Leshkov, Y., Hwang, S.-J., Palsdottir, A., Silverman, D., Lobo, R. F., Curtiss, L. A. & Davis, M. E. Metalloenzyme-like catalyzed isomerizations of sugars by Lewis acid zeolites. *PNAS* **109**, 9727–9732 (2012).

25. Moliner, M., Román-Leshkov, Y. & Davis, M. E. Tin-containing zeolites are highly active catalysts for the isomerization of glucose in water. *Proc. Natl. Acad. Sci. U. S. A.* **107**, 6164–6168 (2010).

26. Román-Leshkov, Y., Moliner, M., Labinger, J. A. & Davis, M. E. Mechanism of glucose isomerization using a solid lewis acid catalyst in water. *Angew. Chemie - Int. Ed.* **49**, 8954–8957 (2010).

27. Taarning, E., Saravanamurugan, S., Holm, M. S., Xiong, J., West, R. M. & Christensen, C. H. Zeolite-catalyzed isomerization of triose sugars. *ChemSusChem* **2**, 625–627 (2009).

28. Dijkmans, J., Gabriëls, D., Dusselier, M., De Clippel, F., Vanelderen, P., Houthoofd, K., Malfliet, A., Pontikes, Y. & Sels, B. F. Productive sugar isomerization with highly active Sn in dealuminated β zeolites. *Green Chem.* **15**, 2777–2785 (2013).

29. Zhu, Z., Xu, H., Jiang, J., Liu, X., Ding, J. & Wu, P. Postsynthesis of FAU-type stannosilicate as efficient heterogeneous catalyst for Baeyer-Villiger oxidation. *Appl. Catal. A Gen.* **519**, 155–164 (2016).

30. Harris, J. W., Liao, W.-C., Di Iorio, J. R., Henry, A. M., Ong, T.-C., Comas-Vives, A., Copéret, C. C., Gounder, R. & Davidson, C. D. Molecular Structure and Confining Environment of Sn Sites in Single-Site Chabazite Zeolites. *Chem. Mater.* **29**, 8824–8837 (2017).

31. Skeels, G. W. & Flanigen, E. M. Zeolite Chemistry VII-Framework Substitution for Aluminum in Zeolites VIA Secondary Synthesis Treatment. *Stud. Surf. Sci. Catal.* **49**, 331–344 (1989).

32. Gunther, W. R., Wang, Y., Ji, Y., Michaelis, V. K., Hunt, S. T., Griffin, R. G. & Román-

Leshkov, Y. Sn-Beta zeolites with borate salts catalyse the epimerization of carbohydrates via an intramolecular carbon shift. *Nat. Commun.* **3**, 1–8 (2012).

33. Yakimov, A. V, Kolyagin, Y. G., Tolborg, S. & Vennestrøm, P. N. R. Accelerated synthesis of Sn-BEA in fluoride media: effect of H_2O content in the gel †. *New J. Chem* **40**, 4367 (2016).

34. Chang, C. C., Wang, Z., Dornath, P., Je Cho, H. & Fan, W. Rapid synthesis of Sn-Beta for the isomerization of cellulosic sugars. *RSC Adv.* **2**, 10475–10477 (2012).

35. Harris, J. W., Cordon, M. J., Di Iorio, J. R., Vega-Vila, J. C., Ribeiro, F. H. & Gounder, R. Titration and quantification of open and closed Lewis acid sites in Sn-Beta zeolites that catalyze glucose isomerization. *J. Catal.* **335**, 141–154 (2016).

36. Boronat, M., Concepción, P., Corma, A., Renz, M. & Valencia, S. Determination of the catalytically active oxidation Lewis acid sites in Sn-beta zeolites, and their optimisation by the combination of theoretical and experimental studies. *J. Catal.* **234**, 111–118 (2005).

37. Sushkevich, V. L., Ivanova, I. I. & Yakimov, A. V. Revisiting Acidity of SnBEA Catalysts by Combined Application of FTIR Spectroscopy of Different Probe Molecules. *J. Phys. Chem. C* **121**, 11437–11447 (2017).

38. Lewis, J. D., Ha, M., Luo, H., Faucher, A., Michaelis, V. K., Román-Leshkov, Y. & Románroman-Leshkov, Y. Distinguishing Active Site Identity in Sn-Beta Zeolites Using ^{31}P MAS NMR of Adsorbed Trimethylphosphine Oxide. *ACS Catal.* **8**, 3076–3086 (2018).

39. Josephson, T. R., Jenness, G. R., Vlachos, D. G. & Caratzoulas, S. Distribution of open sites in Sn-Beta zeolite. *Microporous Mesoporous Mater.* **245**, 45–50 (2017).

40. Freitas, C., Barrow, N. S. & Zholobenko, V. Accessibility and Location of Acid Sites in Zeolites as Probed by Fourier Transform Infrared Spectroscopy and Magic Angle Spinning Nuclear Magnetic Resonance. *Johnson Matthey Technol. Rev.* **62**, 279–290 (2018).

41. Zholobenko, V., Freitas, C., Jendrlin, M., Bazin, P., Travert, A. & Thibault-Starzyk, F. Probing the acid sites of zeolites with pyridine: Quantitative AGIR measurements of the molar absorption coefficients. *J. Catal.* **385**, 52–60 (2020).

42. Kobler, J., Abrevaya, H., Mintova, S. & Bein, T. High-Silica Zeolite-: From Stable Colloidal Suspensions to Thin Films. *J. Phys. Chem. C* **112**, 14274–14280 (2008).

43. Sushkevich, V. L., Kots, P. A., Kolyagin, Y. G., Yakimov, A. V, Marikutsa, A. V, Ivanova, I. I. & Topchiev, A. V. Origin of Water-Induced Brønsted Acid Sites in Sn-BEA Zeolites. *J. Phys. Chem. C* **123**, 5540–5548 (2019).

44. Corma, A., Nemeth, L. T., Renz, M. & Valencia, S. Sn-zeolite beta as a heterogeneous chemoselective catalyst for Baeyer-Villiger oxidations. *Nature* **412**, 423–425 (2001).

45. Van De Vyver, S., Odermatt, C., Romero, K., Prasomsri, T. & Román-Leshkov, Y. Solid Lewis acids catalyze the carbon-carbon coupling between carbohydrates and formaldehyde. *ACS Catal.* **5**, 972–977 (2015).

46. Pacheco, J. J. & Davis, M. E. Synthesis of terephthalic acid via Diels-Alder reactions with ethylene and oxidized variants of 5-hydroxymethylfurfural. *Proc. Natl. Acad. Sci. U. S. A.* **111**, 8363–8367 (2014).

47. Holm, M. S., Pagán-Torres, Y. J., Saravanamurugan, S., Riisager, A., Dumesic, J. A. & Taarning, E. Sn-Beta catalysed conversion of hemicellulosic sugars. *Green Chem.* **14**, 702–706 (2012).

48. Bermejo-Deval, R., Gounder, R. & Davis, M. E. Framework and extraframework tin sites in zeolite beta react glucose differently. *ACS Catal.* **2**, 2705–2713 (2012).

49. Hammond, C., Conrad, S. & Hermans, I. Simple and scalable preparation of highly active lewis acidic Sn-β. *Angew. Chemie - Int. Ed.* **51**, 11736–11739 (2012).

50. *Collection of Simulated XRD Powder Patterns for Zeolites*. (eds. Treacy, M. M. J. & Higgins, J. B.) (Elsevier, 2001).

51. Al-Ani, A., Haslam, J. J. C., Mordvinova, N. E., Lebedev, O. I., Vicente, A., Fernandez, C. & Zholobenko, V. Synthesis of nanostructured catalysts by surfactantlating of large-pore zeolites. *Nanoscale Adv.* **1**, 2029–2039 (2019).

52. Protsak, I. S., Morozov, Y. M., Dong, W., Le, Z., Zhang, D. & Henderson, I. M. A 29 Si, 1 H, and 13 C Solid-State NMR Study on the Surface Species of Various Depolymerized Organosiloxanes at Silica Surface. *Nanoscale Res. Lett.* **14**, 160 (2019).

53. Dubray, F., Moldovan, S., Kouvatas, C., Grand, J., Aquino, C., Barrier, N., Gilson, J.-

P., Nesterenko, N., Minoux, D. & Mintova, S. Direct Evidence for Single Molybdenum Atoms Incorporated in the Framework of MFI Zeolite Nanocrystals. *J. Am. Chem. Soc.* **141**, 8689–8693 (2019).

54. Zheng, A., Liu, S.-B. & Deng, F. 31P NMR Chemical Shifts of Phosphorus Probes as Reliable and Practical Acidity Scales for Solid and Liquid Catalysts. *Chem. Rev.* **117**, 12475–12531 (2017).

55. Ohlin, L., Bazin, P., Frédé, F., Thibault-Starzyk, F., Hedlund, J. & Grahn, M. Adsorption of CO^2, CH^4, and H^2O in Zeolite ZSM-5 Studied Using In Situ ATR-FTIR Spectroscopy. *J. Phys. Chem. C* **117**, 16972–16982 (2013).

56. Szanyi, J., Kwak, J. H., Moline, R. A. & Peden, C. H. F. The adsorption of NO_2 and the $NO+O_2$ reaction on Na-Y,FAU: an in situ FTIR investigation. *Phys. Chem. Chem. Phys* **5**, 4045–4051 (2003).

57. Szanyi, J., Kwak, J. H. & Peden, C. H. F. The Effect of Water on the Adsorption of No2 in Na- and Ba-Y, FAU Zeolites: A combined FTIR and TPD Investigation. *J. Phys. Chem. B* **108**, 3746–3753 (2004).

58. Hadjiivanov, K. I. Identification of neutral and charged NxOy surface species by IR spectroscopy. *Catal. Rev. - Sci. Eng.* **42**, 71–144 (2000).

59. Kumar, M. S., Schwidder, M., Grünert, W., Bentrup, U. & Brückner, A. Selective reduction of NO with Fe-ZSM-5 catalysts of low Fe content: Part II. Assessing the function of different Fe sites by spectroscopic in situ studies. *J. Catal.* **239**, 173–186 (2006).

60. Brosius, R., Bazin, P., Thibault-Starzyk, F. & Martens, J. A. Operando FTIR study of reaction pathways of selective catalytic reduction of NO_x with decane in the presence of water on iron-exchanged MFI-type zeolite. *J. Catal.* **234**, 191–198 (2005).

61. Ahrens, M., Marie, O., Bazin, P. & Daturi, M. Fe-H-BEA and Fe-H-ZSM-5 for NO_2 removal from ambient air – A detailed in situ and operando FTIR study revealing an unexpected positive water effect. *J. Catal.* **271**, 1–11 (2010).

Chapter 4

Ion sensing pencil: Draw your own sensor

4.1 Introduction

The development of information technology facilitated the remote monitoring and control of physical devices and everyday objects over the internet. The Internet of Things (IoT), as this concept is named, has penetrated many aspects of life. Among many other applications, specialized IoT devices can monitor the health and general wellbeing of citizens,[1–3] provide data to optimize food production,[4] control air and water quality,[5] and increase the quality of the services offered to the citizens, while reducing the operational costs of the public administrations,[6] etc. Such systems utilise a range of sensors for monitoring relevant key parameters. However, IoT systems utilise very few truly chemical sensors.

Chemical information (if relevant) is typically inferred from a range of physical sensors (position, vibration, temperature, humidity)[4,7] or image analysis. Despite significant recent advances,[8–10] chemical sensors still require relatively complex handling protocols (storage, calibration, cleaning), which drives their price beyond the possibility to be routinely used in IoT. Interestingly, the same disadvantages limit penetration of chemical sensors in Citizen Science (CS) as a field that some view as the next frontier in the expansion of research.[11,12] Involving citizens in large scientific projects opens up exciting opportunities in many application fields.[13] Unfortunately, chemical sensors are not yet at the stage of development that would allow routine operations by non-specialists and integration into large, autonomous sensor networks which are seen as essential for applications in CS and IoT. If chemical sensors are to be applied for the acquisition of large arrays of chemically relevant information, they have to be readily available, extremely simple to use and versatile (able to obtain a variety of relevant chemical information). Ideally, their price would be affordable, and they could be plugged into a simple, readily available, non-specialized read-out system.

Arguably, a pencil is one of the simplest, ubiquitous, and versatile (in terms of colour range) tools. Thus, pencil-like chemical sensors would have a great opportunity for penetration into fields where their applications are currently severely limited. A pencil-type sensor concept has very recently been investigated by utilising carbon nanotubes (CNTs) or metal-organic frameworks (MOFs).[14–17] However, these approaches rely on long and laborious modifications of experimental protocols and substantial chemical changes to the bulk or surface of materials to achieve the required selectivity for specific ions or gasses. Therefore, a suitable solution for this complex challenge lays in exploiting relevant advantages of existing very low-cost materials.

Graphite is interesting as it has a long history of use in analytics,[18–20] while its price is >1000 times lower than simplest, non-modified commercially available CNTs. Zeolites attracted our attention due to their selective ion exchange properties exploited effectively in areas such as petroleum industry, catalysis, water purification,[21] as well as elements in electrochemical sensors.[22–24] Zeolites are microporous aluminosilicate materials that can accommodate a variety of cations e.g. Na^+, K^+, Ca^{2+}, Mg^{2+}, etc). The functionality of zeolites is based on the selective exchange of these ions influenced by the topology, pore size, and Si:Al ratio within the zeolite framework.[22,23,25] Thus, the selectivity of a zeolite framework for a target ion offers an opportunity for utilisation in chemical sensing in analogy to ion-selective electrodes (ISEs), while zeolite's solid structure allows mechanical compression into stable pencil lead-like shapes.

In this chapter is suggested that compression of a simple solid mixture of graphite and a zeolite enables the preparation of chemical sensors that look and can be operated as a pencil but offer analytical characteristics analogous to ISEs. A total of 14 zeolites were used to prepare 14 ISPs and their responses to 9 cations were recorded. The choice of zeolites and ions was guided by

the expectations of selectivity to a specific ion in environmental samples as a function of zeolite's affinity to that ion.[24–26]

4.2 Experimental

4.2.1 Materials

Graphite powder (<20 μm, synthetic), sodium chloride (NaCl), potassium chloride (KCl), ammonium chloride (NH_4Cl), calcium chloride ($CaCl_2$), magnesium chloride ($MgCl_2$), zinc chloride ($ZnCl_2$)), 2-nitrophenyl-octyl-ether (>99.0 %), tetra-n-butylammonium tetrafluoroborate (TBA-TBB) tris(hydroxymethyl)aminomethane hydrochloride (Tris-HCl) were purchased from Sigma-Aldrich, UK. Hydrochloric acid (HCl), manganese chloride ($MnCl_2$) and iron (III) chloride ($FeCl_3$) were obtained from Fisher while nickel chloride ($NiCl_2$) and copper (II) chloride ($CuCl_2$) from Harris reagents. All the chemicals were used without further purification. All the standard aqueous solutions were prepared with ultrapure water obtained from Pico Pure 3 water system. OHP universal film removable top stripe 100 (clear 4243, 100 μm) from Q-connect was used as a substrate. Zeolites NaX, KX, NaY, KY were obtained from Riogen, USA. Zeolites NaA and KA were from Crosfield, UK. Zeolites NH_4-MOR, NH_4-FER, NH_4-BEA-12, NH_4-BEA-19, and NH_4-ZSM-5, were from Zeolyst, Netherlands, Zeolite K-LTL was from Tosoh, Japan. Natural zeolite HEU-A (USA) and natural zeolite HEU-B (Bulgaria) were from Zeodex, UK and natural zeolite HEU-C was generously provided by Prof A. Walcarius (Universite de Lorraine, France).

4.2.2 Ion-sensitive pencil preparation

A zeolite of choice and graphite powder were thoroughly mixed using a ball mill. The solid mixture was transferred into a pellet die and compressed in a hydraulic bench press by applying the necessary pressure to obtain a mechanically robust pellet (a.k.a ISP lead). It was inserted

into a pencil clutch prepared using a 3D printer (PLA filament, Wanhao Duplicator 4S). Obtained ISP was used to draw a line onto a hydrophobic surface to obtain an electrode as illustrated in Figure 4.1.

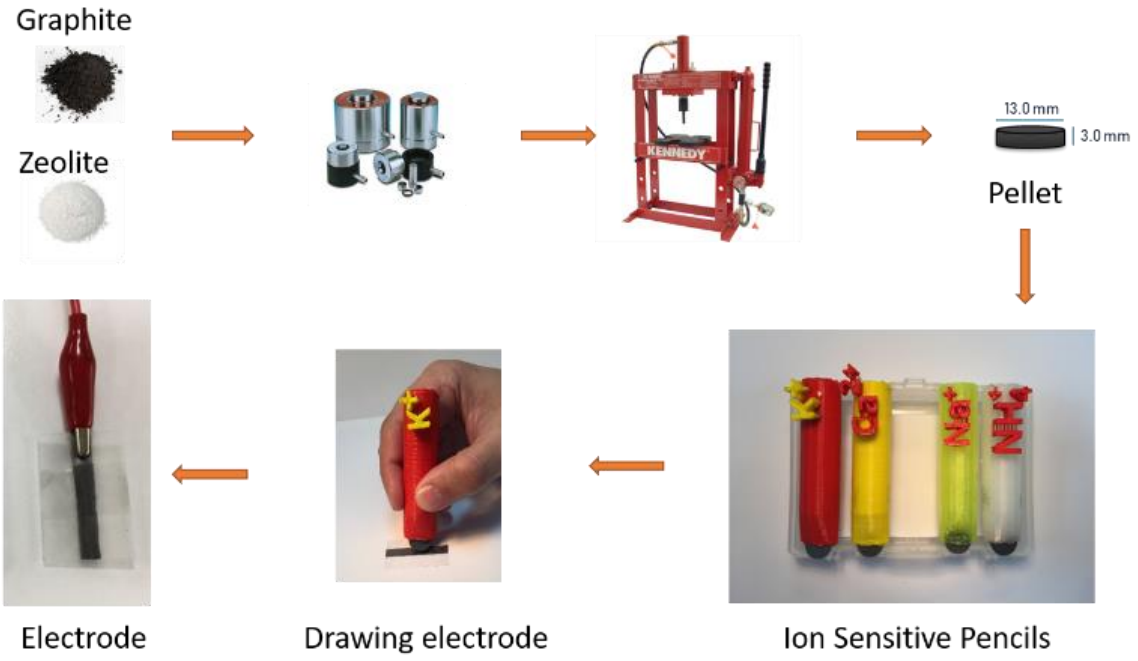

Figure 4.1 Process of preparation of Ion Selective Pencil and electrodes.

4.2.3 Electrode substrate preparation and characterisation

The hydrophobic electrode substrates were prepared by cutting a PET sheet (2.0 3.0 cm) as a single electrode from a parent PET sheet, which was then etched with the aluminium oxide (grit 240) for 30 s to provide the rough surface with enhanced porosity and improved adhesion of ISP lead onto the surface of the PET. The zeolite-graphite line was subsequently drawn onto the PET sheet by abrasion until the resistance of the drawn line was lower than 3.0 kΩ as suggested previously.[27] The midsection of the line is insulated using a simple sticky tape Fabrication of electrode substrate is illustrated in Figure 4.2.

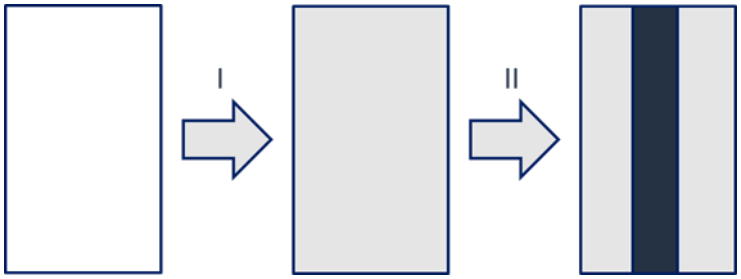

Figure 4.2 Schematic representation of the proposed PET sheet-based electrode fabrication via mechanical abrasion. Step I: PET sheet slightly roughened by sandpaper. Step II: line applied by hand.

4.2.4 Polymer membrane-based reference electrode

Polymer-membrane reference electrode was prepared according to the previously reported procedure.[28] Briefly, a 10.0 x 3.0 cm strip was cut from the parent PET sheet and prepared as explained above. A line was subsequently drawn by pencil (Staedtler, HB). Each reference electrode was partially overlaid with a mask of sticky tape. A hole of 0.3 cm in diameter was punched on one top end of the sticky tape. An aliquot (~20 µL) containing 12.5 wt.% tetrabutylammonium tetrabutylborate (TBA-TBB), PVC (29.2 wt.%) and o-NPOE (58.3 wt.%) in 1.5 mL THF was drop cast onto the top of the electrode, and further left at room temperature to dry overnight. The following day, reference electrodes were conditioned in 0.01 M KCl solution for 18 h prior to the potentiometric experiments.

4.2.5 Potentiometry

Responses of all electrodes were recorded using the Lawson Labs Inc. 16-channel EMF-16 interface (3217 Phoenixville Pike Malvern, PA 19355, USA) in the stirred solution against a double-junction Ag/AgCl reference electrode with a 1.0 M of LiOAc bridge electrolyte (Fluka). For the measurement of analytes, all ISPs were immersed into 200.0 mL of ultra-pure water in a beaker followed by stepwise addition of known concentration of the standard. Electrodes were rinsed with ultra-pure water and dried before immersing into the next sample to avoid

carryover. Potential responses (EMF) were then measured, and activities were calculated from the calibration curve using the Nikolsky-Eisenman equation. Activity coefficients (log a) were calculated according to the Debye-Hückel approach. At least three electrodes of the same type were used. Selectivity coefficients were determined using separate solutions method utilising dry ISPs. Signal was obtained by exposure to calibration solutions of no longer than 5 min for each calibration point and no longer than 30 min overall. Following the recording of the response to a specific ion, ISPs were thoroughly dried using absorbing paper and the protocol was repeated for the next ion.

4.2.6 Instrumental characterization

Electrodes and the precursor materials were characterised by X-ray powder diffraction (XRD), Scanning electron microscopy (SEM), thermogravimetric analysis (TGA), attenuated total reflectance Fourier-transform infrared spectroscopy (ATR-FTIR), and contact angle measurements. XRD patterns were collected using a Bruker D8 Advance diffractometer with a Cu anode at 40 kV and 40 mA, the 2θ range was set from 5 to 60°. SEM micrographs were obtained using the Hitachi TM 3000 at 600x magnification. Prior to collecting SEM micrographs samples were mounted on aluminium holders, fixed by carbon cement, and carbon-coated. TGA analyses were carried out utilising a Rheometric Scientific STA 1500, from 20 to 800 °C, at a heating rate of 10 °C/min with the 40 mL/min airflow). ATR-FTIR spectra were acquired using a Thermo iS10 spectrometer equipped with a DTGS detector and an ATR attachment with a diamond crystal. The spectral range was 4000- 600 cm^{-1}, 64 scans, 4 cm^{-1} resolution. The contact angle was measured on a custom setup using a camera with an attached magnification lens (Carl Zeiss, Jena; GF-P 10x) and analysed using ImageJ software with the “Contact angle” plugin.

4.2.7 Multisensor array data processing

In the case of analysis of model mixtures containing four different inorganic cations, the set of zeolite-based sensors was considered as a sensor array. To relate the response of the sensors in the mixtures with the content of metal ions, partial least squares (PLS) regression was employed.[29] The derived models were validated using segmented cross-validation with a random split of samples leaving three samples out of calibration at each of the six-folds. Root mean square error of cross-validation (RMSECV) was used to evaluate models' performance. All calculations were performed in collaboration with prof. Dmitry Kirsanov from St. Petersburg State University using The Unscrambler 9.7 software package (CAMO, Oslo, Norway).

4.2.8 Analysis of bottled water and instant soup samples

Three bottled drinking water and an instant-tomato soup were purchased from a local shop. Firstly, the calibration curve was obtained by using two-point calibration at 5.0×10^{-5} and 5.0×10^{-3} M of Na^+ concentrations. Signal was obtained using a digital multimeter (WhiteGold WG 023 digital multimeter) and a polymer-based solid-contact reference electrode (TBA-TBB). Three bottled drinking water samples were directly analysed without any sample preparation and tomato soup was diluted 1000-fold using 10 μM Tris-HCl buffer solution (pH 7.50).

To test the concept of ISP, a range of zeolite types was used, including Faujasite (FAU), Linde Type A (LTA), Mordenite (MOR), Ferrierite (FER), Beta type (BEA), MFI for Mobil five (also known as ZSM-5 for zeolite Socony Mobil-five after the company that invented it), Linde Type L (LTL), and naturally occurring zeolites of Heulandite type (HEU) of USA, Bulgarian, and Romanian origin. The rationale for using such a wide variety of zeolite types was to scan zeolites for various factors affecting their selectivity (e.g. pore size, topology, and Si:Al ratio)

for the potential to be utilised in ISPs. A more detailed study of the impact of these factors on ISP's functionality will be discussed in Chapter 5.

4.3 Results and discussion

4.3.1 ISP composition optimisation

ISPs were prepared using 0, 1, 10, 20, 40, and 60 wt.% of zeolite in graphite and compressions of 2, 4, and 6 tonnes. ISPs prepared with 40 wt.% of zeolite compressed with 4 tonnes of pressure exhibited near-Nernstian slopes and these conditions were adopted as optimal (Table 4.1). The ISP composition optimisation was done using NaX as a zeolite, but the conclusions were applied to all the other ISPs.

Table 4.1. Conditions for preparation of ISP pellet used to produce electrodes and their electrochemical response to Na^+ cations (in mV/decade).

Composition	**Compression load**		
(wt.% of NaX zeolite)	**2 tonnes/slopes**	**4 tonnes/slopes**	**6 tonnes/slopes**
0%	1.9	2.8	2.5
1%	10.0	11.9	9.94
10%	30.63	30.32	30.58
20%	40.5	46.10	42.86
40%	35.2	55.1	51.19
60%	N/A*	N/A*	N/A*

*The resistance of the ISP pellets with 60%:40% zeolite: graphite ratio was ~5-10 kΩ higher than the rest of electrodes, pellets were very brittle, and the drawing was very difficult so they were not used at all.

The calibration plot of ISP prepared by compressing 40 wt.% of NaX zeolite using 4 tonnes of pressure is presented in Figure 4.3. It is noteworthy that ISPs with no zeolite (0 wt.%) showed

slopes of >3 mV/decade thus indicating that the potentiometric response indeed originates from a zeolite.

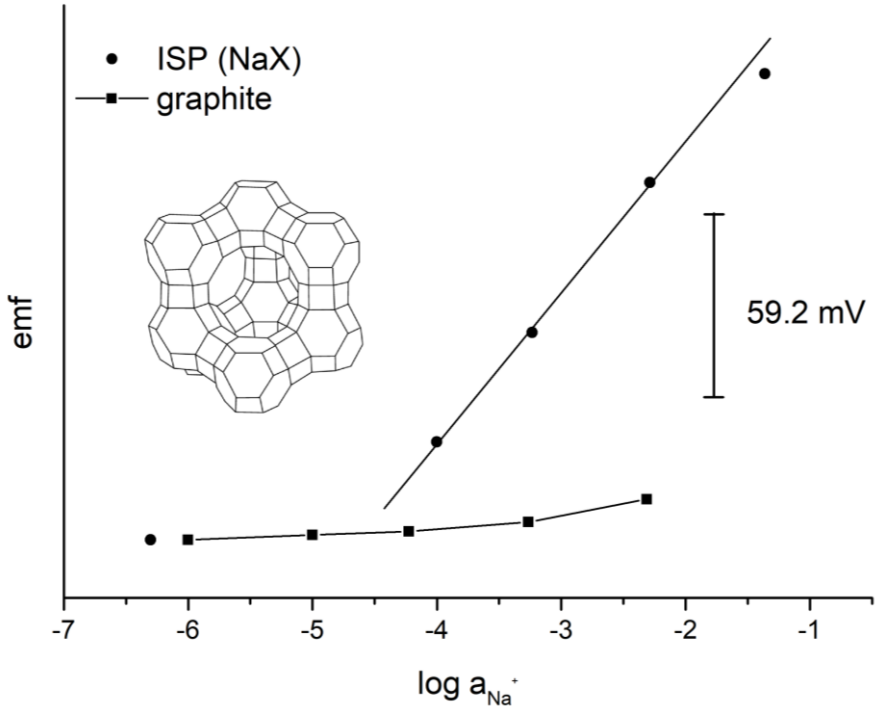

Figure 4.3. The potentiometric response of NaX-based ISP (circles) and pure graphite (squares) to Na^+. Slope of NaX-based ISP =55.1 mV/decade, limit of detection (LOD) = 2×10^{-5}M. An inset provides the structure of faujasite (FAU).

4.3.2 Electrode components characterisation

4.3.2.1 Graphite

The disadvantage of using graphite as the electrode matrix is its well-known sensitivity to pH. Indeed, Figure 4.4 illustrates the response of a blank electrode made by drawing a line onto the electrode substrate using a typical 3B pencil (Staedtler). This implies the need to either buffer a sample solution or determine its pH in parallel to analyte measurements.

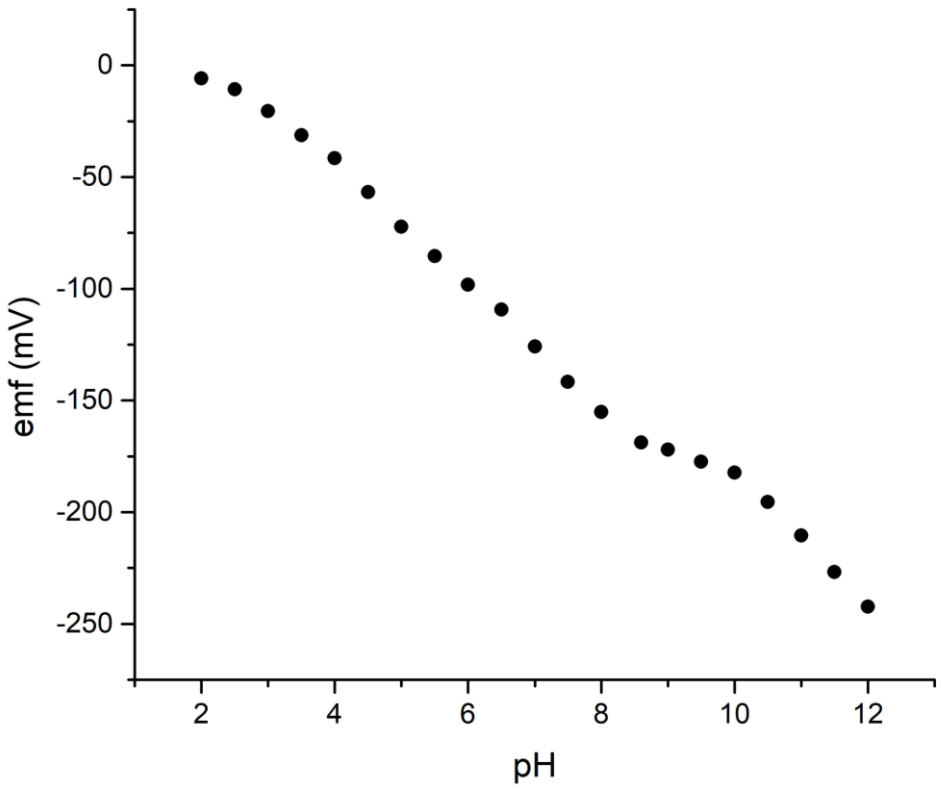

Figure 4.4.The response of an electrode prepared by drawing a line on the sensor substrate using a 3B pencil.

A typical polymer membrane-based ISE requires a readout device with high input impedance to avoid polarization of the sensor. Note that electrode polarization has been utilized in so-called pulstrodes.[30] The resistance of typical PVC-based ISE is in order of MΩ[31] thus requiring readout systems with input impedance in GΩ range. The resistance of membranes based on popular acrylate-based polymers can be even higher. The inclusion of lipophilic salts into the membrane was used as a strategy to reduce membrane resistance.[32] Previous characterization of graphite as an intermediate layer for ISEs using electrochemical impedance spectroscopy[27] revealed two important benefits of graphite:

1) Both the phase transfer of ions through the solution/matrix interface and transduction from ionic into an electronic signal at the matrix/solid contact interface are fast.

Similar behaviour is observed with traditional ion-selective membranes prepared with conductive polymer as an intermediate layer.[33]

2) The overall resistance of ISP is in the order of kΩ, thus requiring less sophisticated readout systems.

This was an encouragement to utilize a simple multimeter as a readout device. Since its input impedance is about 1000 times higher than the resistance of ISP it is reasonable to expect that it should be sufficient to suppress sensor polarization. In summary, zeolites offer suitable chemical functionality and preparation of ISP that can be used immediately off the shelf, while graphite as a matrix offers ion-to-electron conductivity and sufficiently low resistance so that less sophisticated readout instrumentation can be used than required by its counterpart polymer membrane-based ISE.

4.3.2.2 Substrate

An electrode substrate was characterised by the ATR-FTIR spectroscopy and SEM. Using FTIR spectroscopy, it was determined that the substrate sheet consists of two phases, polyethylene terephthalate (PET) and poly(ethylene vinyl alcohol) (PEVA). Spectra of both phases were collected (Figures 4.5, 4.6) and compared with the database entries.[34]

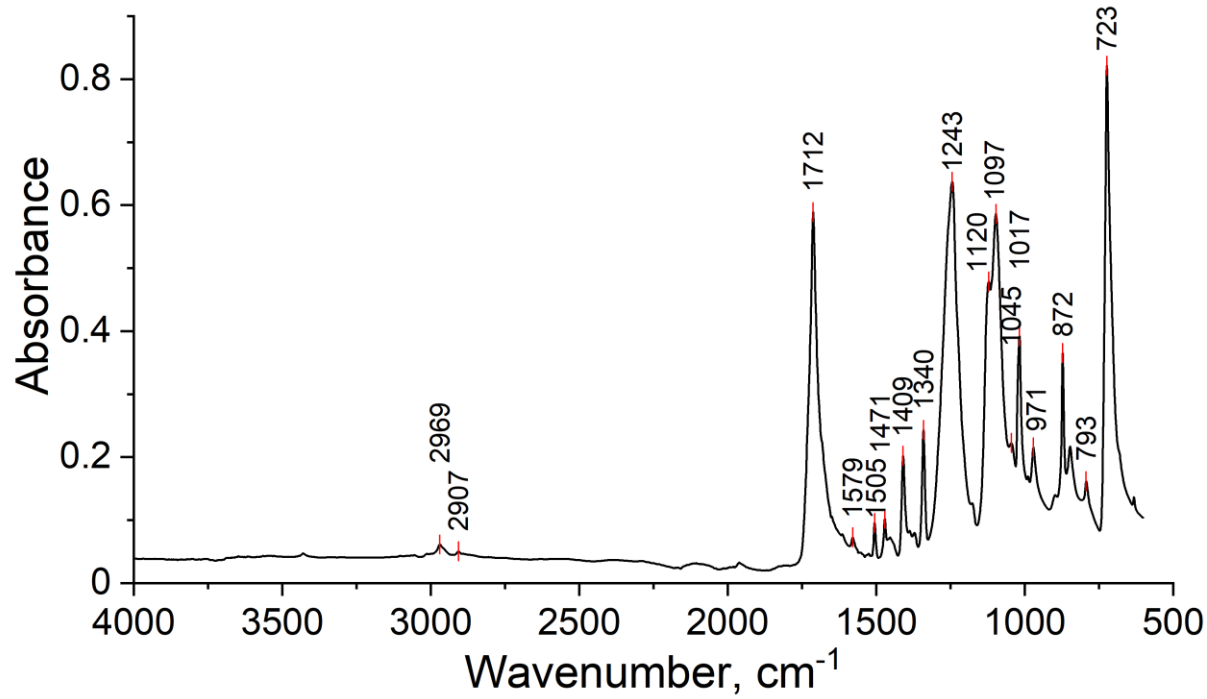

Figure 4.5. ATR-FTIR spectrum of PET.

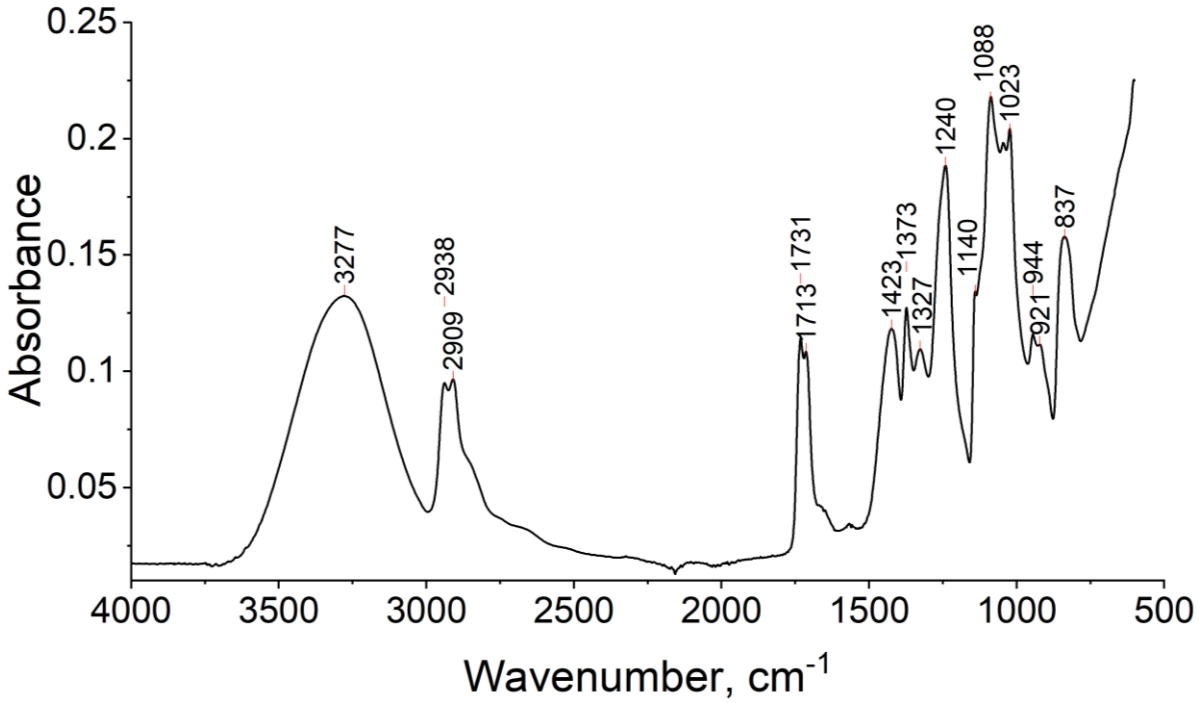

Figure 4.6. ATR-FTIR spectrum of PEVA.

SEM micrographs show that the thickness of the PET sheet is 100 ± 3 µm (Figure 4.7), which is in agreement with the technical specifications of the PET sheet,[35] while the thickness of the etched PET sheet is 90-95 µm (Figure 4.7). SEM micrographs confirmed that the substrate sheet consists of two phases, 95 µm and 5 µm thick, respectively. In comparison with the ATR-FTIR results, it was determined that the 95 µm thick layer is PET and the 5 µm layer is PEVA (Figure 4.7).

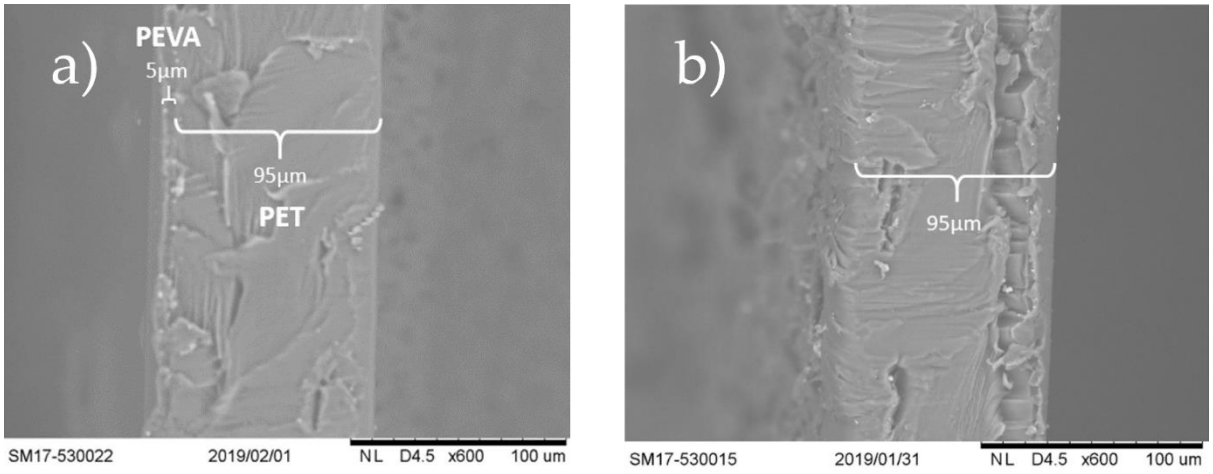

Figure 4.7. SEM micrographs of (a) unetched PET sheet, (b) etched PET sheet.

4.3.3 SEM

Electrodes were observed using SEM providing a top-view and a side-view. The top view of the etched substrate is shown in Figure 4.8(a), while in the top view of the ISP-drawn electrode (Figure 4.8 (b)) darker shade of graphite and lighter zeolite particles can be observed. Collected images from both the top- and side-view confirmed that the electrode material is deposited on the PET sheet, but from the side view of the substrate and the ISP-drawn electrode (Figure 4.8(c) and (d)), it was not possible to determine the thickness of the applied layer.

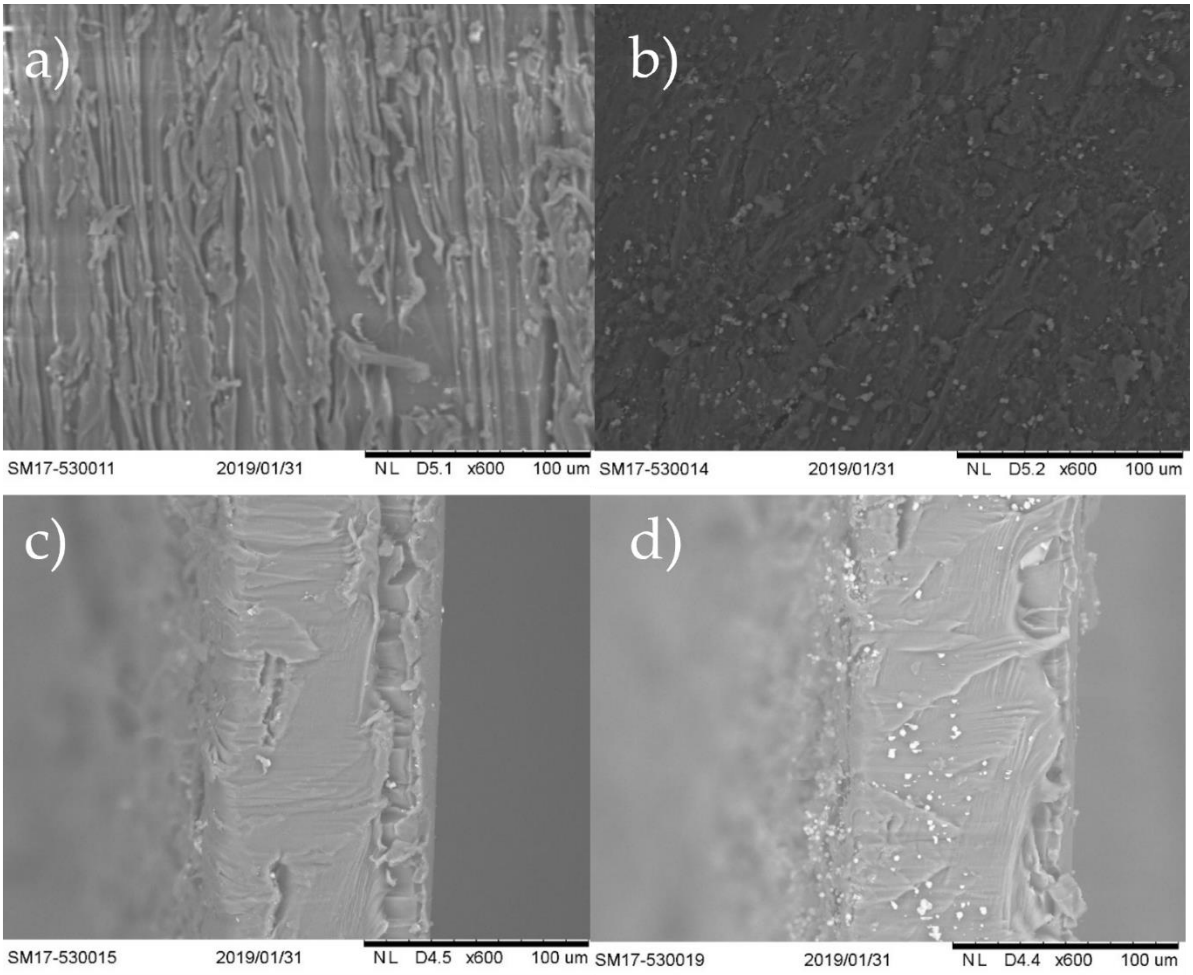

Figure 4.8. SEM micrographs of (a) etched surface of the PET sheet, (b) ISP-drawn electrode, (c) side-view of the etched PET sheet, (d) side-view of the ISP-drawn electrode.

Electrodes are hand-drawn, so the difference in the thickness of the applied layer is inevitable, but as an estimate, the thickness was determined using the equation below,

$$l = \frac{V}{A} = \frac{m}{\rho A}$$

where l [μm] is the thickness of the ISP applied layer, V [cm^3] is the volume and A [cm^2] is the surface of the layer, m [g] and ρ [g cm^{-3}] are the mass and the density of the applied layer, respectively, Table 4.2. Density was calculated from the mass and the volume of the pressed pellet.

Table 4.2. Electrode material layer thickness calculation data.

Pellet density (*ρ*)	**PET sheet area (*A*)**	**Layer mass (*m*)**	**Layer thickness (*l*)**
1.57 gcm^{-3}	6.95 cm^2	12.4 mg	11.3 μm

4.3.4 XRD

XRD pattern of the electrode containing NaX zeolite as a model zeolite was compared with the patterns of the precursor materials (Figures 4.9-4.11). The full list of the peaks is listed in Table 4.3.

Table 4.3. List of XRD pattern peaks of the NaX-containing ISP-drawn electrode.

2θ peak position, °	**Precursor**	**2θ peak position, °**	**Precursor**
6.157	NaX	30.379	NaX
10.139	NaX	31.036	NaX
11.812	NaX	32.078	NaX
15.475	NaX	33.680	NaX
18.502	NaX	34.305	NaX
20.095	NaX	37.526	NaX
23.105	NaX	40.874	NaX
23.386	NaX	41.335	NaX
26.029	PET sheet	53.801	PET sheet
26.567	Graphite	54.629	Graphite

PET sheet peak (2Θ= 26.029°) is predominant in the pattern since the thickness of a sheet is 90-95 μm, and the drawn layer of the electrode is approximately 10 ± 3 μm. The second most

intense peak stems from the graphite phase. The position of that peak (2Θ =26.567°), from which the d-spacing is calculated using the Braggs' law (d= 3.35Å) corresponds to the d_{002} plane spacing between graphite layers.[36] Figure 4.11 indicates that the positions of the NaX peaks correspond to the peaks from the ISP pattern, but the intensities are low in comparison with the graphite and PET ones, therefore the peaks in the 2Θ range 22-30° are masked by PET and graphite peaks. Since no additional peaks are appearing in the pattern, it could be concluded that no other crystalline phases are present in the electrode.

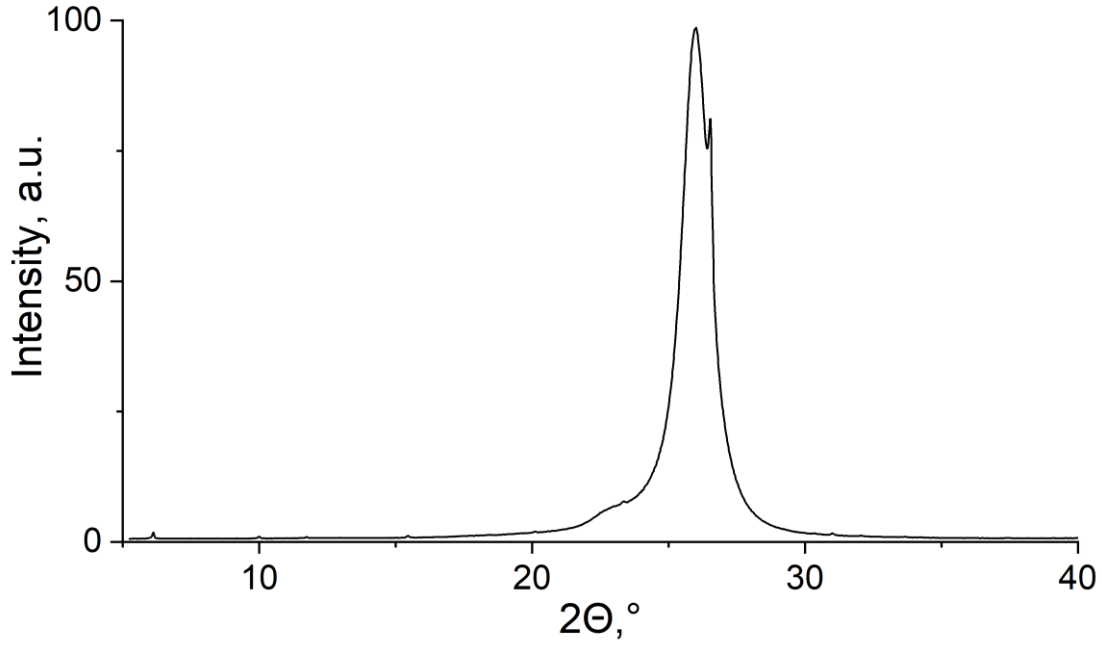

Figure 4.9. XRD pattern of the ISP-drawn electrode.

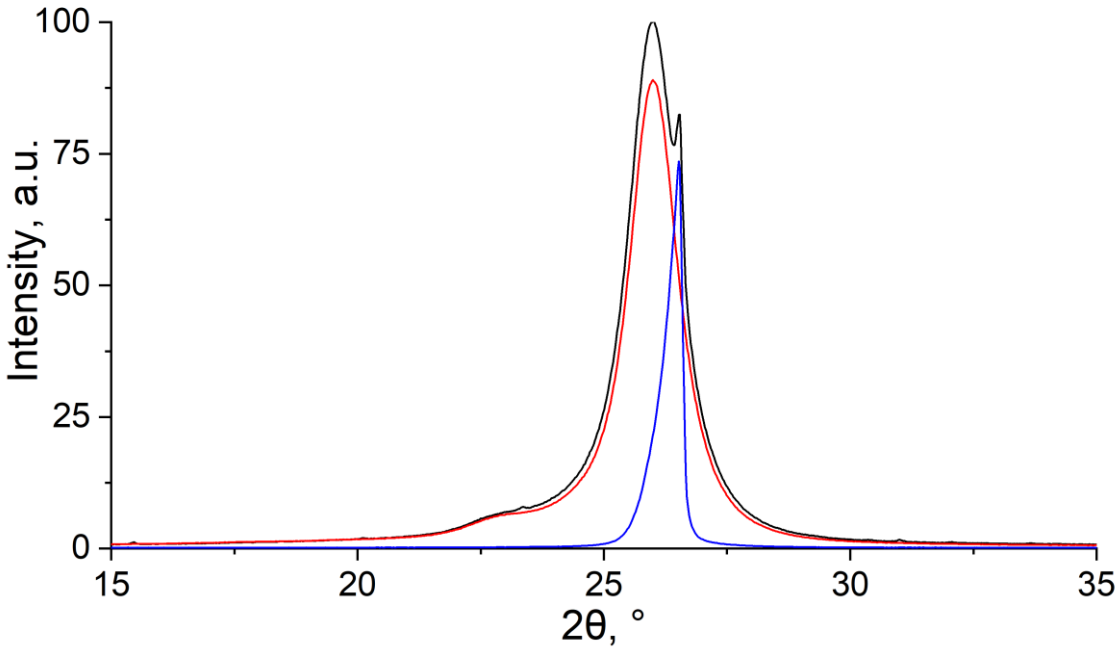

Figure 4.10. XRD patterns of the NaX-containing ISP-drawn electrode (black), PET sheet (red) and graphite (blue).

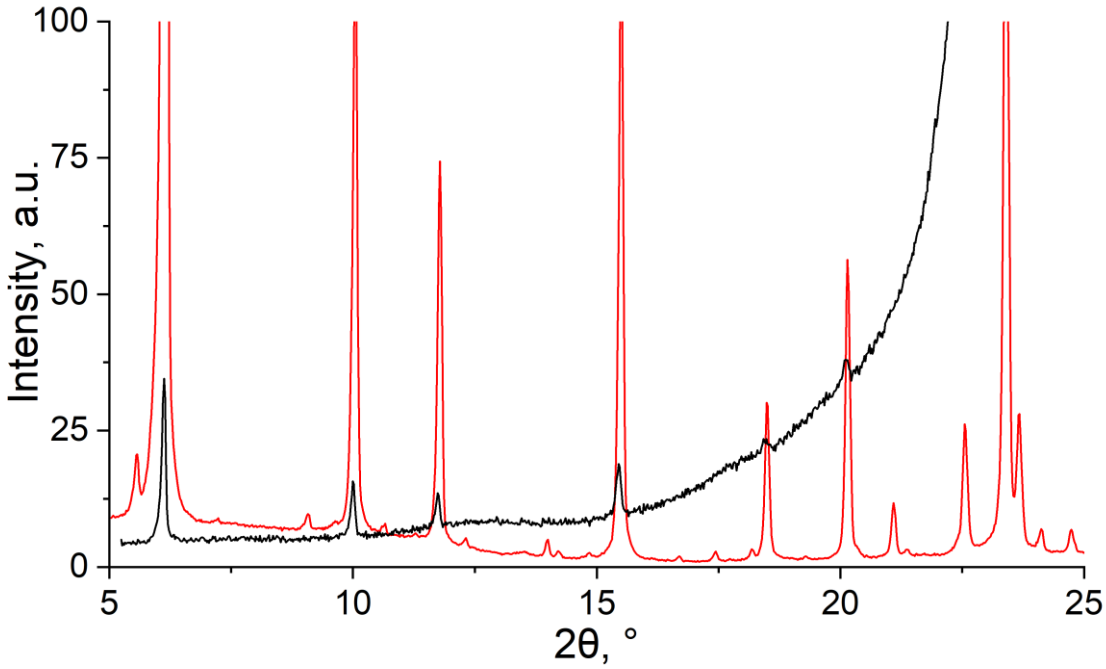

Figure 4.11. XRD patterns of the NaX-containing ISP-drawn electrode (black) and NaX zeolite (red).

4.3.5 ATR FTIR

ATR-FTIR spectra of the ISP-drawn electrode, NaX zeolite and graphite samples have also been collected (Figure 4.12). It can be observed that the ISP-drawn electrode spectrum has contributions from both graphite and NaX, just as in the XRD patterns.[37] In the ATR-FTIR spectra of the NaX zeolite intense peak from 800-1200 cm^{-1} corresponds to symmetrical and asymmetrical O-T-O stretching (T= Si, Al) bonds, while the peaks from 600-750 cm^{-1} correspond to O-T-O bending vibrations in the zeolite structure.[25] Based on XRD patterns and ATR-FTIR spectra it can be concluded that both graphite and NaX zeolite are present in the ISP-drawn electrode.

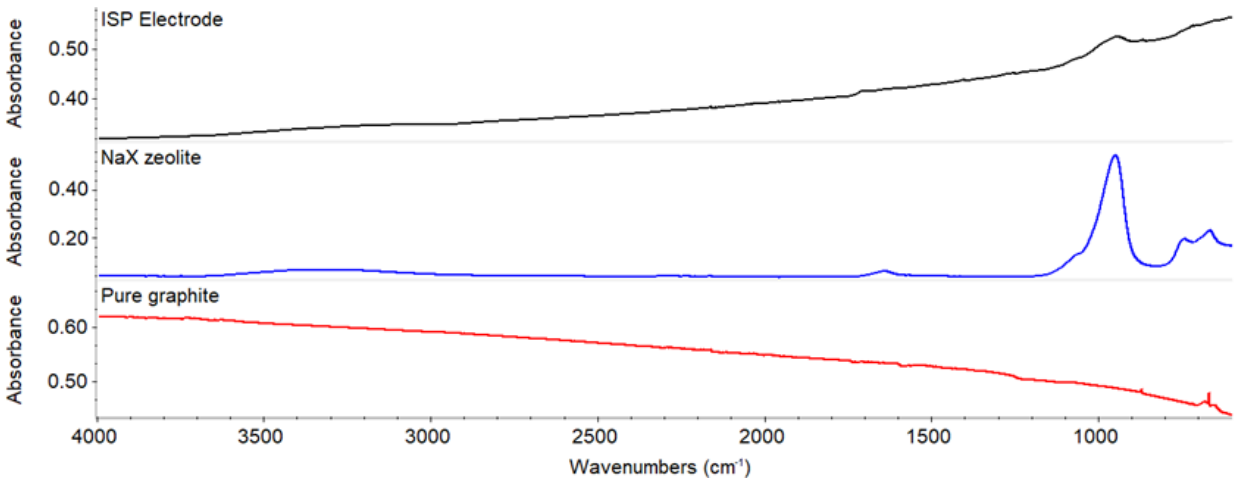

Figure 4.12. ATR-FTIR spectra of NaX-containing ISP-drawn electrode (black), graphite (red) and NaX zeolite (blue).

Before moving to demonstrate the application potential of ISP, it is important to point out an issue observed with more hydrophilic zeolites (types X, Y). Namely, attempts to apply conditioning protocol traditional for ISEs (~12 h of continuous exposure of the sensor to an aqueous solution of target ion) resulted in a slow and steady signal drift ending in the almost complete loss of response (Figure 4.13) most likely originating from adsorption of water within

the zeolite.[25] The return of the near-Nernstian response after drying overnight confirms this hypothesis.

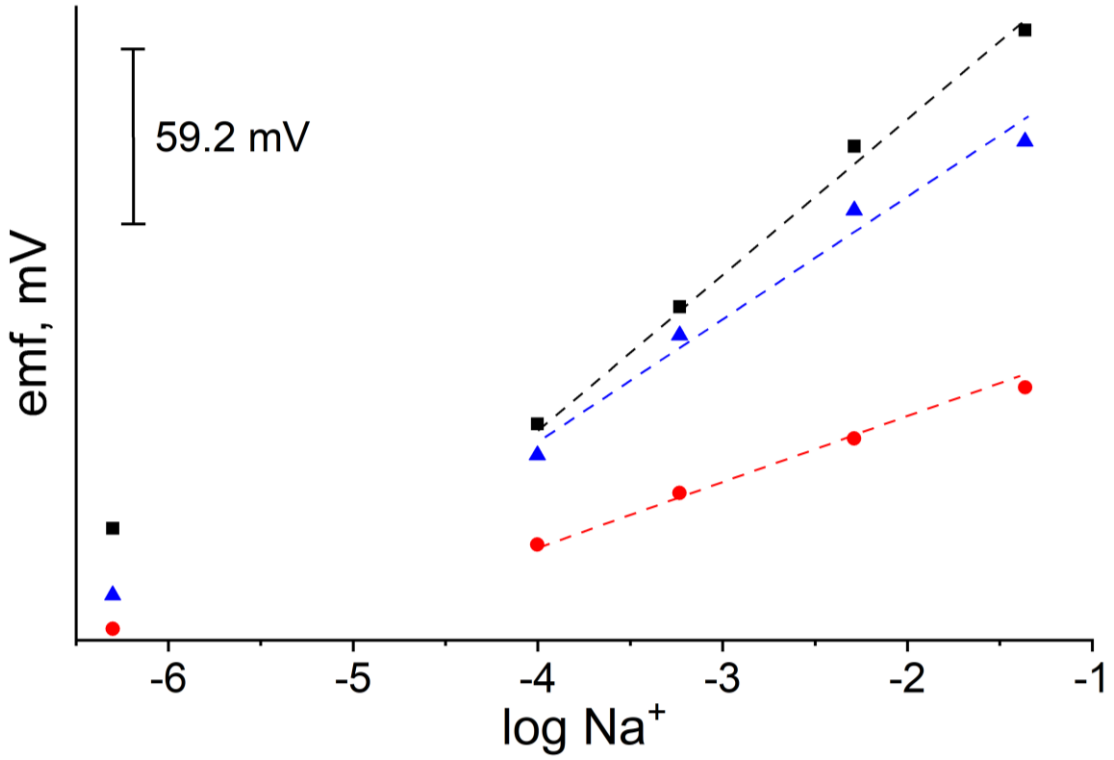

Figure 4.13. The potentiometric response to Na^+ using a fresh electrode (black), an electrode after overnight exposure to the target ion solution (red), and after drying the electrode overnight (blue).

Figure 4.14 presents the potentiometric response of the proposed ISP-drawn electrode. Electrodes were first calibrated immediately after preparation as explained above. Electrodes were then left in the 10^{-3} M solution followed by a new calibration. Response slopes decreased from the original 48.8 mV/decade to 25.7 mV/decade after 12 hours of exposure to water. However, the response slope recovered to 42.7 mV/decade after drying overnight at room temperature, Figure 4.13.

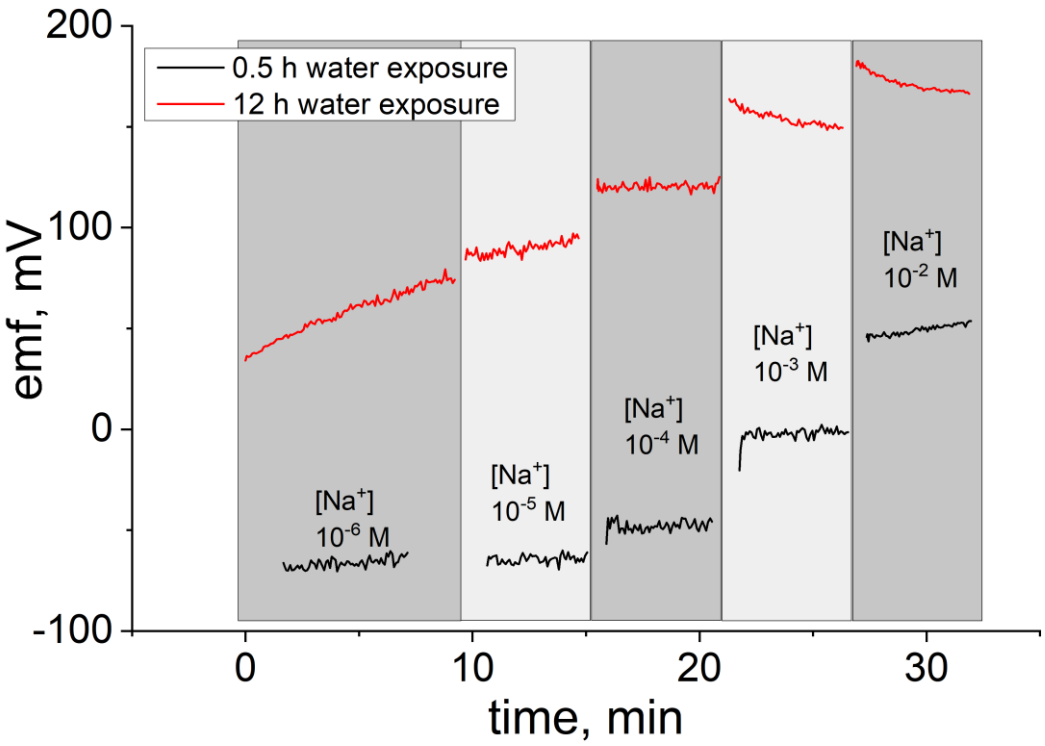

Figure 4.14. Time traces of the potentiometric response of NaX-containing ISP-drawn electrodes to Na^+ from 10^{-6} to 10^{-2} M after water exposure of 0.5 h (black) and 12 h (red).

The signal drifts were significantly smaller or non-existent in other, more hydrophobic zeolites. However, in the spirit of critical analysis, the results for NaX are shown as the example of a zeolite demonstrating the strongest drift. While the water uptake may present as an issue for long-term use of ISP-drawn electrodes, it should be kept in mind that ISPs are conceived as sensors that are inexpensive and extremely simple to use. Thus, ISP-drawn electrodes can be treated as disposable. ISPs can be used to simply draw additional sets of electrodes.

4.3.6 Water uptake characterisation

In order to clarify the loss of the response after the electrode has been submerged in water for 12 hours, the water uptake and contact angles were measured. Graphite, zeolite and electrode pellets were weighed before and after submerging in water. The data are presented in Table 4.4. It is demonstrated that both graphite and NaX zeolite uptake a substantial amount of water.

Due to interaction with water, the availability of active sites in the zeolite structure would be reduced. Moreover, the contact angle of the same pellets was measured (Table 4.4, Figure 4.15). Zeolite pellet absorbed water instantly, so it was not possible to measure the contact angle. The dry graphite pellet measured angle was in accordance with the one reported recently.[38] The contact angle of the samples after 12h exposition to water increased, which also confirmed that the surface was more hydrophilic.

Table 4.4. Water uptake and contact angle data.

Pellet composition	**Water uptake**	**Dry sample contact angle**	**Wet sample contact angle**
Graphite	26%	63.1°	30.9°
Zeolite NaX	41%	-	-
Electrode 40:60	32%	65.2°	50.2°

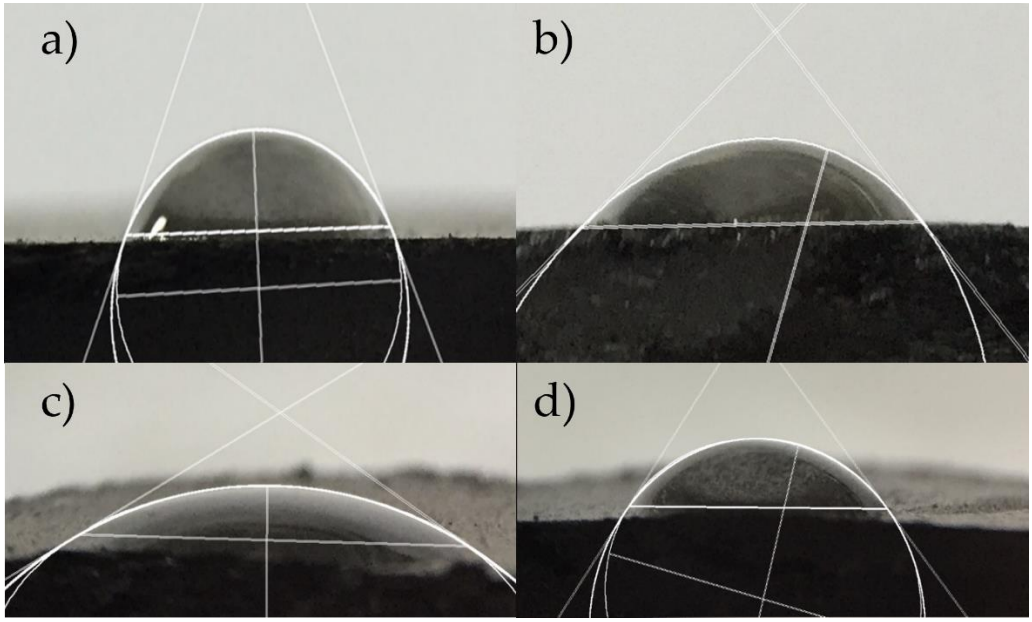

Figure 4.15. Contact angle measurement data. (a) dry graphite pellet, (b) dry ISP 60:40 electrode pellet, (c) wet graphite pellet, (d) wet ISP 60:40 electrode pellet.

The graphite-zeolite pellet used to draw electrodes has been subjected to TGA to determine its composition since the graphite autoignition temperature was known from the literature.[39] From the TGA curve (Figure 4.16) it can be observed that the residual mass after heating the pellet to 900 °C is 31.2% of the initial mass, which indicates that only the zeolite is left in the crucible. The recorded result is smaller than 40% that is declared in the initial ratio due to the water loss from the zeolite structure, which, in the case of NaX, is almost 28% of the zeolite mass (Figure 4.17).

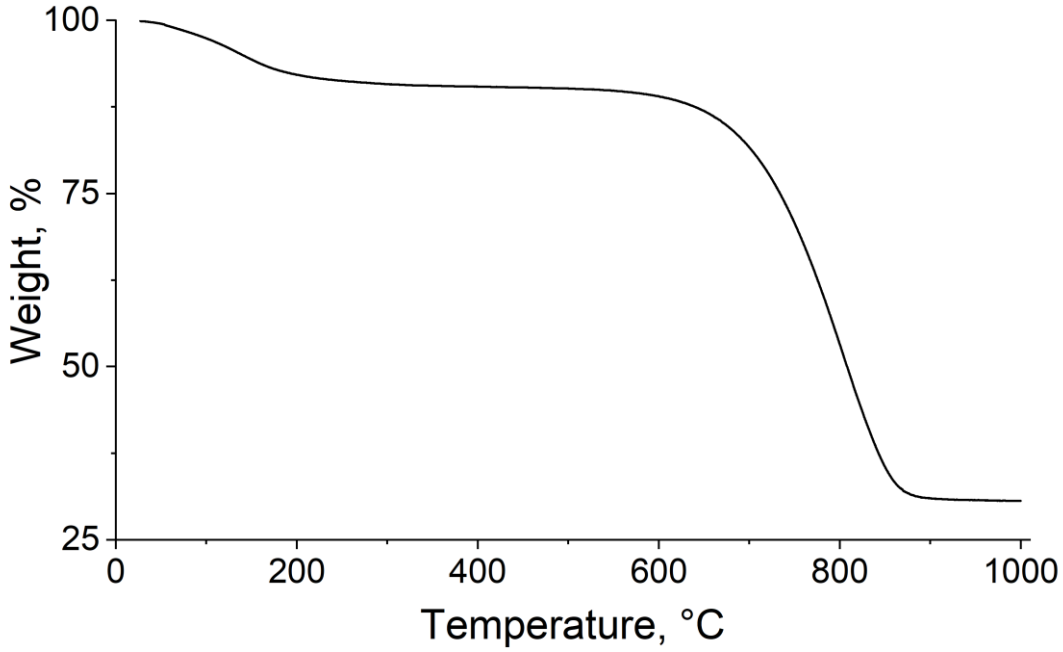

Figure 4.16 TGA curve of NaX-containing ISP

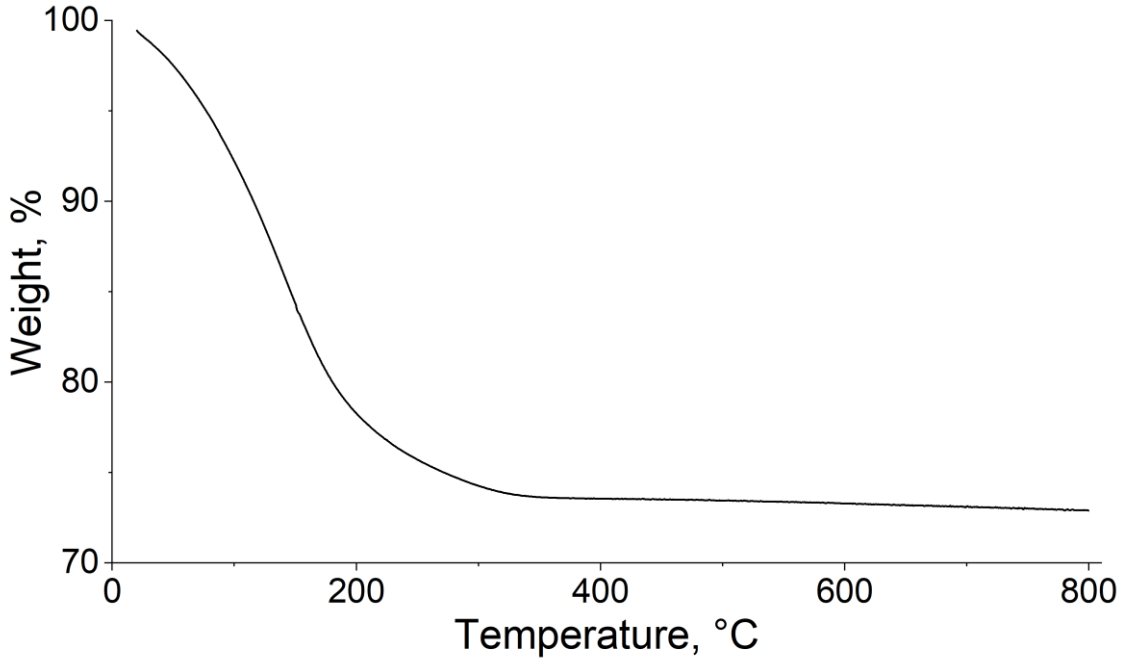

Figure 4.17. TGA curve of the NaX zeolite.

4.3.7 Analytical characterization and application of ISPs

The sensing functionality of ISP-drawn electrodes was characterized using potentiometry analogous to ISEs. The response of electrodes prepared using 14 different ISPs was determined against a double-junction Ag/AgCl reference electrode. Electrodes were immersed into a beaker filled with a known volume of ultra-pure water followed by stepwise addition of known concentration of the standard solution of the measured ion. Figure 4.18 demonstrates the heat map of potentiometric sensitivities with the bar illustrating obtained slopes. It is important to note that responses were obtained from the freshly prepared, dry ISP-based electrodes without any pre-treatment. This was quite exciting as it offered desired functionality; sensors can be easily stored at home without the need for any special handling prior to the measurement while demonstrating sensitivity expressed as near-Nernstian response slopes. Response slopes of 59.2 mV/dec and 29.6 mV/dec are considered theoretical (Nernstian) for single- and double-charged ions respectively.

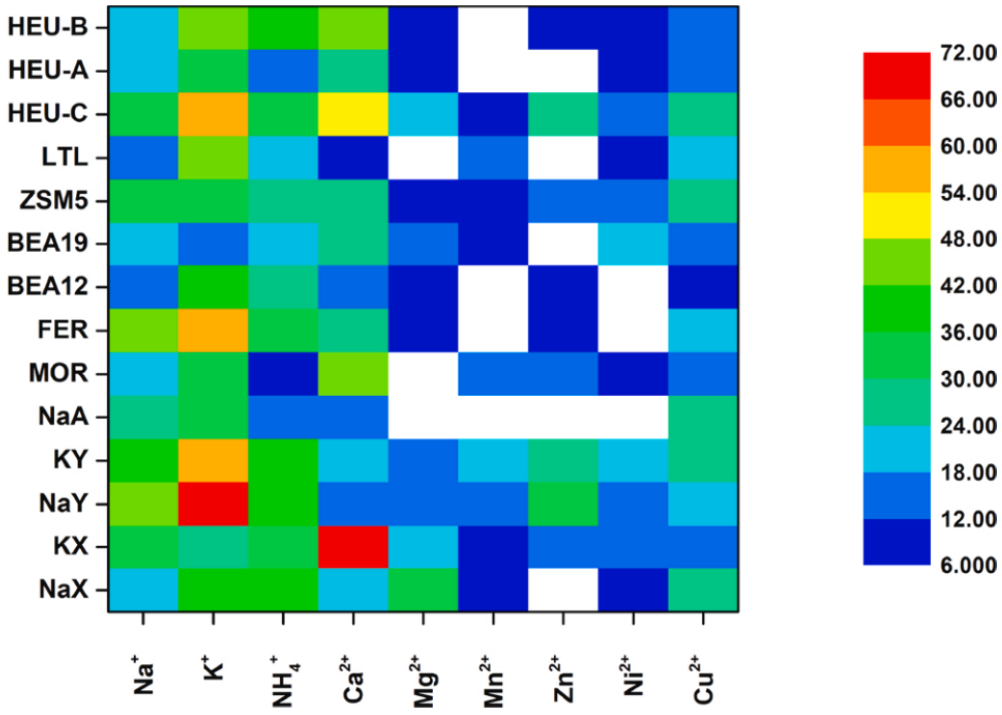

Figure 4.18. ISP sensitivity heatmap illustrating response slope in mV/dec (bar on the right). ISPs are based on the given zeolite (vertical axis) and response slopes are obtained for each of the analysed ions (horizontal axis). Slopes of <6 mV/dec are not shown (white).

4.3.8 Multi-sensing system in complex mixtures

Critical analysis of responses reveals that ISP-drawn electrodes exhibit responses and selectivities that are inferior to classical ionophore-based ISEs.

Table 4.5 Selectivity coefficients obtained using ISP and a classical Na^+-selective ionophore.

	NaX zeolite containing ISP-drawn electrode (this work)	**Na^+-selective ISEs based on Na *X* ionophore** [40]
Ion	$logK_{I,J}^{pot}$	$logK_{I,J}^{pot}$
Na^+	0	0
K^+	-0.09±0.1	-1.9
NH_4^+	-0.09±0.1	-
Ca^{2+}	-1.75±0.5	-2.5
Mg^{2+}	-4.25±1.5	>-6
H^+	+1.3±0.9	-

To avoid confusion due to naming conventions, in Table 4.5 'X' in the zeolite (NaX) signifies zeolite type (FAU), while '*X*' in the ionophore name is a Roman numeral signifying Na ionophore 'ten' as per Sigma's naming convention for ionophores.

This result was expected given that the selectivity of zeolite-containing electrodes is known to be inferior to ionophores.[22,41] However, this is a compromise that should be made to demonstrate sensors that can be easily prepared and handled. Since arrays of nonspecific, low selectivity sensors exhibiting cross-sensitivity to different species in the solution are well-established analytical tools,[42] it seems that the combination of easy preparation with relatively low selectivity dictated that ISP-drawn electrodes could be best utilised as a multi-sensor system in the analysis of complex mixtures, for instance in the evaluation of water quality. To the best of our knowledge, this is the first reported case of using zeolite-based electrodes in multi-sensing array systems. Having in mind the potential application of the multi-sensing array system in environmental analysis, a model solution that contained some of the major plant nutrients (K^+, NH_4^+, Ca^{2+}, and Mg^{2+}) was prepared. In this mixture, it was attempted to quantify Mg^{2+} ion in such a mixture using an array of all 14 ISP-drawn electrodes. Concentrations of all ions in this mixture varied from 10^{-4} to 10^{-2} mol dm^{-3}. A total of 20 different mixtures were prepared. The concentration of each ion in the mixture was determined according to the uniform experimental design for multivariate calibration.[29] The composition of the mixtures is given in Table 4.6. The relationship of the response of the array of 14 ISPs in these complex mixtures to the [Mg^{2+}] was determined using partial least squares (PLS) regression.[43] Root mean square error of cross-validation (RMSECV) was used to evaluate the model's performance. At the first step PLS model was cross-validated using the procedure described in the Experimental section 'Multisensor Array data processing'. The optimal number of latent variables in the model was found to be five. Fig. 4 shows the resulted "added vs found" plot. The R^2 coefficient in cross-validation was 0.83 and RMSECV was 0.34

log[Mg^{2+}]. These values indicate the applicability of the ISP array for quantitative analysis of complex multi-component solutions. At the next step, six randomly chosen samples were set aside and the PLS model was constructed with the rest of the samples. This model was then applied for predicting [Mg^{2+}] in the test set.

Table 4.6. Composition of multicomponent solutions, mol/L. All components were added as nitrate salts.

#	[Ca^{2+}]	[Mg^{2+}]	[K^{+}]	[NH_4^{+}]
1	1.93E-03	7.30E-03	1.92E-03	1.00E-02
2	1.05E-04	1.31E-03	7.07E-03	4.31E-03
3	3.42E-04	5.50E-04	1.00E-02	1.03E-04
4	8.95E-04	2.17E-04	2.38E-04	1.88E-03
5	4.99E-03	1.02E-04	3.77E-04	6.41E-03
6	4.06E-04	2.94E-04	5.07E-04	1.42E-04
7	1.27E-03	9.84E-03	9.57E-04	3.32E-04
8	1.93E-03	6.01E-04	2.29E-03	1.32E-04
9	1.03E-03	1.01E-04	2.39E-03	4.79E-04
10	7.25E-04	9.58E-03	1.39E-04	1.11E-04
11	1.01E-04	7.40E-03	1.39E-03	4.07E-03
12	2.50E-04	8.69E-03	6.30E-03	7.81E-04
13	2.09E-04	2.58E-03	7.59E-04	1.10E-04
14	1.05E-04	1.25E-04	2.25E-04	3.37E-03
15	4.41E-03	1.41E-04	4.77E-04	1.24E-04
16	1.18E-04	1.18E-04	1.71E-03	9.61E-03
17	9.97E-03	1.99E-03	1.77E-03	3.66E-04
18	2.64E-03	7.46E-03	3.45E-04	2.28E-03
19	1.85E-04	2.13E-04	6.07E-03	1.22E-03
20	5.39E-04	1.61E-03	6.27E-04	2.16E-03

An excellent correlation between predicted and real [Mg^{2+}] was obtained (Pearson's r = 0.944) as shown in Table 4.7 and Figures 4.19 and 4.20. The value of the mean relative error for six

studied samples is 8.4 %. Considering the extreme simplicity of the proposed sensor architecture and ultimately inexpensive and widely available production materials, it could be concluded that these results provide a proof of concept for ISP-drawn arrays.

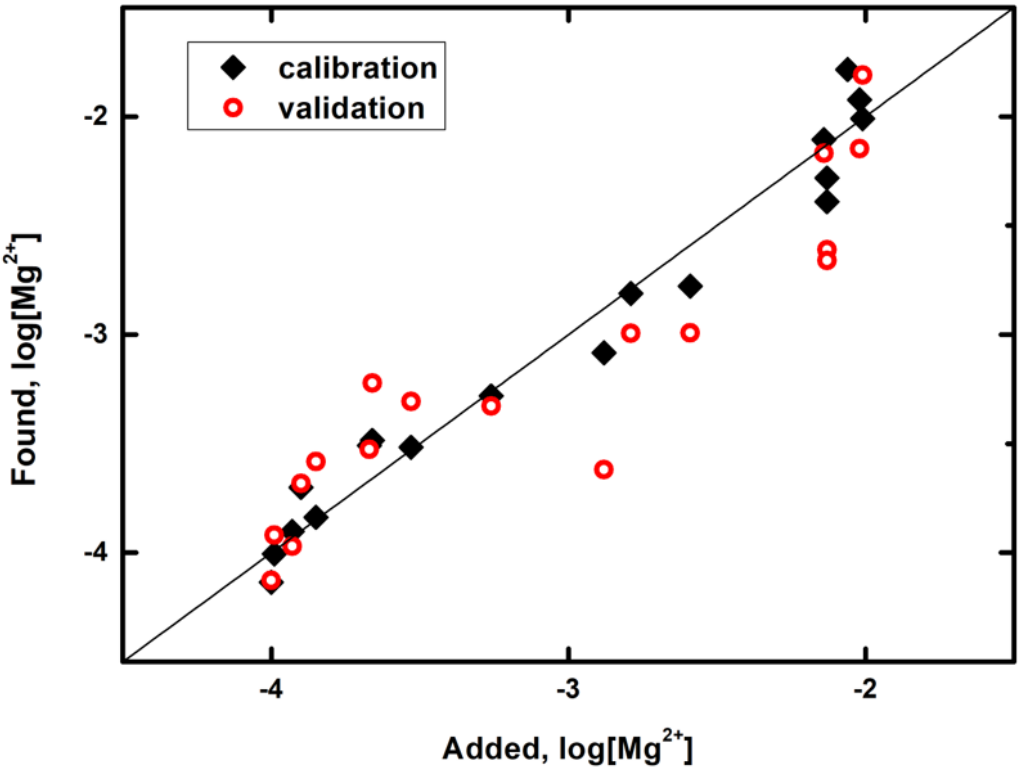

Figure 4.19. Found vs added plot for cross-validated PLS model predicting Mg^{2+} content in the mixtures of four salts.

Table 4.7. Prediction of magnesium concentration in test set samples.

#	log [Mg^{2+}], added	log [Mg^{2+}], predicted by PLS model	Relative error, %
1	-3.260	-3.298	1.2
2	-3.990	-.3764	5.7
3	-2.590	-3.099	19.7
4	-3.900	-3.692	5.3
5	-3.850	-3.468	9.9
6	-2.130	-2.311	8.5

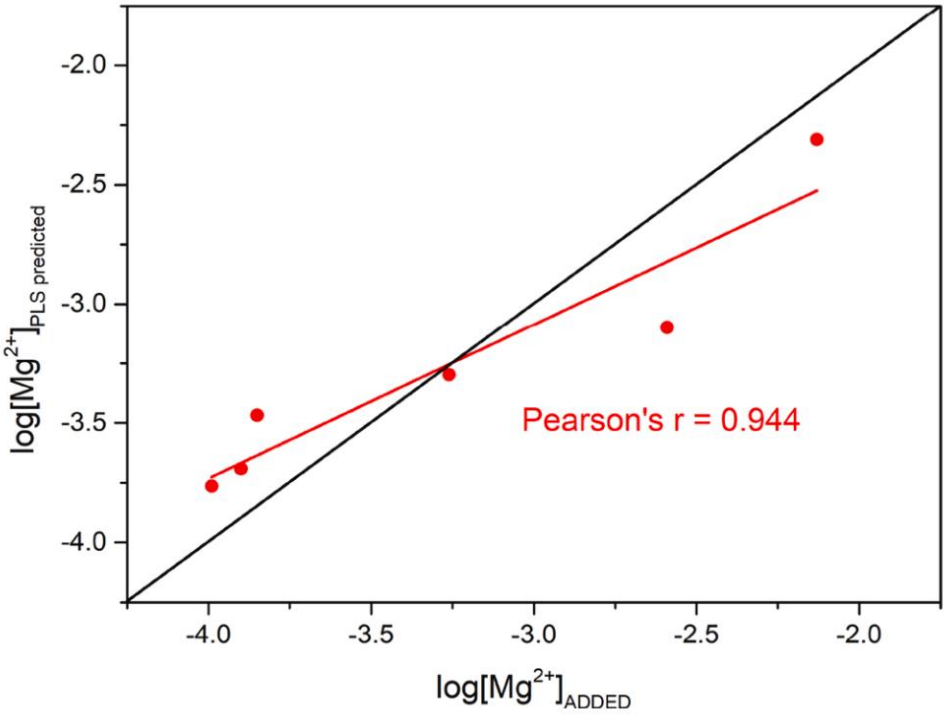

Figure 4.20. Correlation of [Mg^{2+}] obtained as PLS predicted vs added, with Pearson's r = 0.944.

4.3.9 ISPs as a tool for use by non-trained personnel

In the introduction part of this chapter, it was argued that the penetration of chemical sensors in fields such as IoT and CS depends on the simplicity of preparation and handling of chemical sensors. So far, it was demonstrated that handling of ISPs and operation protocols for ISP-

drawn electrodes have the required level of simplicity for such applications while their real power lays in multi-sensing systems combined with a chemometric approach. Owing to the simplicity of handling and the level of data processing automation using chemometrics, it is reasonable to believe that the ISPs could be used even by non-trained personnel. It has also been argued that data collected using readout devices that are present in many homes, can open very interesting applications. At present, we are not aware of devices suitable for use with multi-sensor systems. However, using a non-optimal, single-electrode setup is indeed possible. To showcase the simplicity and the potential for ISP-based electrodes to be used by non-trained personnel, it was decided to demonstrate its use in the determination of total salt content in bottled water and store-bought soup. Firstly, a simple experimental protocol for calibration and measurement was developed, analogous to the protocol for using pH electrodes (two-point calibration followed by the determination of signal using direct potentiometry). The analysis is completed in <10 min (up to ~3 min per measurement for the total of three measurements including calibration). In the protocol digital multimeter served as a readout device, NaX-based ISP-drawn electrode, and polymer membrane-based reference electrode. The setup was evaluated using a classical data logger (EMF 16), and glass reference electrode (Figure 4.21).

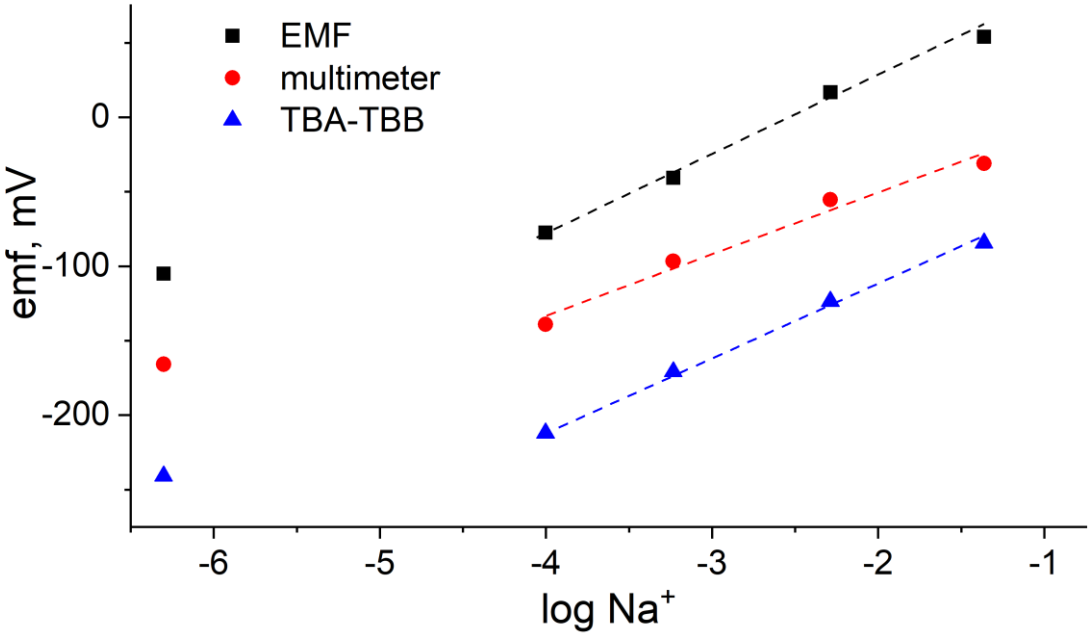

Figure 4.21. Evaluation of the protocol setup used for the determination of the salt content in bottled water and soup samples. The response of NaX-based electrode against Ag/AgCl glass reference electrode recorded using EMF 16 data logger (squares) the response of NaX-based electrode against Ag/AgCl glass reference electrode recorded using a digital multimeter (circles), the response of NaX-based electrode against polymer (TBA-TBB) membrane-based reference electrode recorded using a digital multimeter (triangles), the responses are offset for clarity.

Table 4.8. Concentrations of Na^+ in three bottled drinking water (sample 1-3) and instant soup samples (sample 4) obtained using ISP and from the corresponding package label.

	ISP (mmol L^{-1})	**Bottle label (only Na^+) (mmol L^{-1})**	**Bottle label (all cations) (mmol L^{-1})**
Water sample 1	1.8 ± 0.6	0.36	2.40[a]
Water sample 2	1.2 ± 0.5	0.50	1.28[a]
Water sample 3	1.3 ± 0.3	0.34	1.28[a]
Instant soup	260 ± 50[b]	-	120[c]

[a] Total salt concentration including Na^+, K^+, Ca^{2+}, Mg^{2+}.
[b] After 10-fold dilution.
[c] Labelled as 'salt'.

This protocol enabled even the use of NaX-based electrodes despite it exhibiting the strongest signal drift as discussed earlier. In other words, relatively short measurement time provided the use of NaX-based ISP-drawn electrode effectively Also, a digital multimeter was used as an example of a readout device present in many homes with the caveat that it allows only a single electrode setup. Finally, a hand-made reference electrode was prepared to showcase the simplicity of the experimental setup. The possibility to develop a reference electrode pencil (REP) was envisioned. which will, in an ideal case scenario, present as the optimal example of the utilisation of drawn electrodes. While the work on the development of REP is in progress, a reference electrode for this set of experiments was prepared by the deposition of a polymer-based membrane utilising a lipophilic salt as first reported by Mattinen onto the hand-drawn,[28] PET-based substrate as suggested previously.[44] Such a setup seems like a suitable transition from classical ISE:glass electrode to fully pencil-drawn system. The suitability of ISP:polymer membrane-based reference electrode setup was confirmed through an initial characterization against a glass reference electrode and using a classical high input impedance data logger.

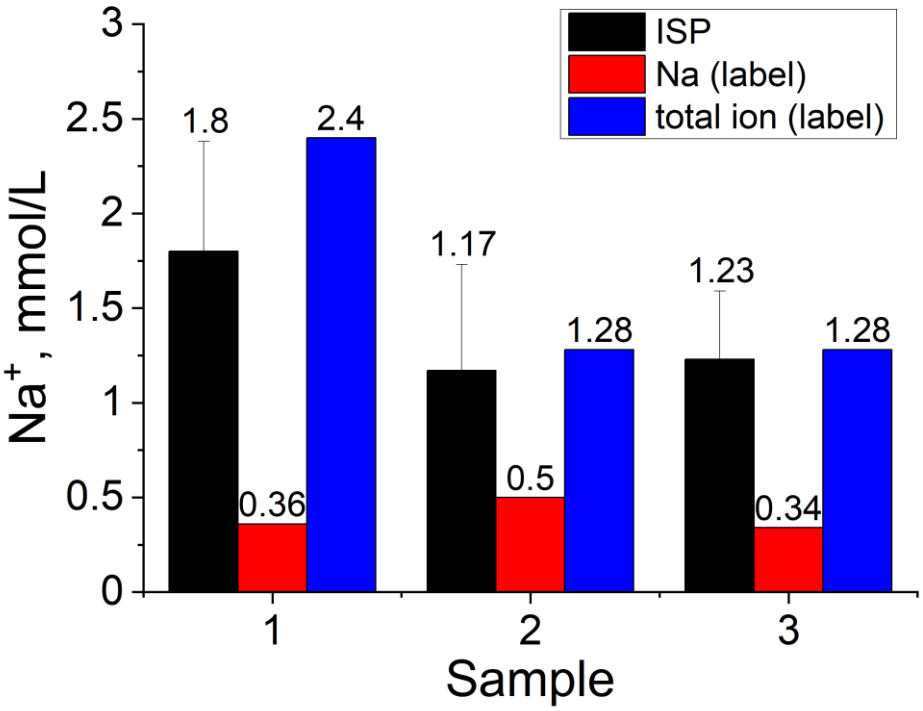

Figure 4.22. The concentration of Na^+ in 3 different bottled water samples obtained by ISP (black) with associated error bars and compared against the labelled concentration of Na^+ (red) and the total ion concentration from the label (blue).

An MS Excel sheet has also been developed for calculations of unknown concentration and its associated standard deviation according to protocols suggested by Wiora and Wiora.[45] This offered simplicity and automation of data processing thus further contributing to the notion of the suitability of the use of ISPs by non-trained personnel. Figure 4.23 illustrates the use of a digital multimeter as a readout device for determining salt content in bottled drinking water and instant soup purchased from a local shop. Obtained data are presented in

Table 4.8, where it is shown that the overall salt content was determined in both samples with a good degree of agreement with the data presented on the labels. Simplifications of the electrode preparation, handling, measuring protocols, and calculations allowed to recruit persons with basic training in chemistry (1st-year chemistry students) to perform sample

analysis with very limited instructions. This opens unprecedented opportunities for the generation of chemical information by non-trained personnel (i.e. general public).

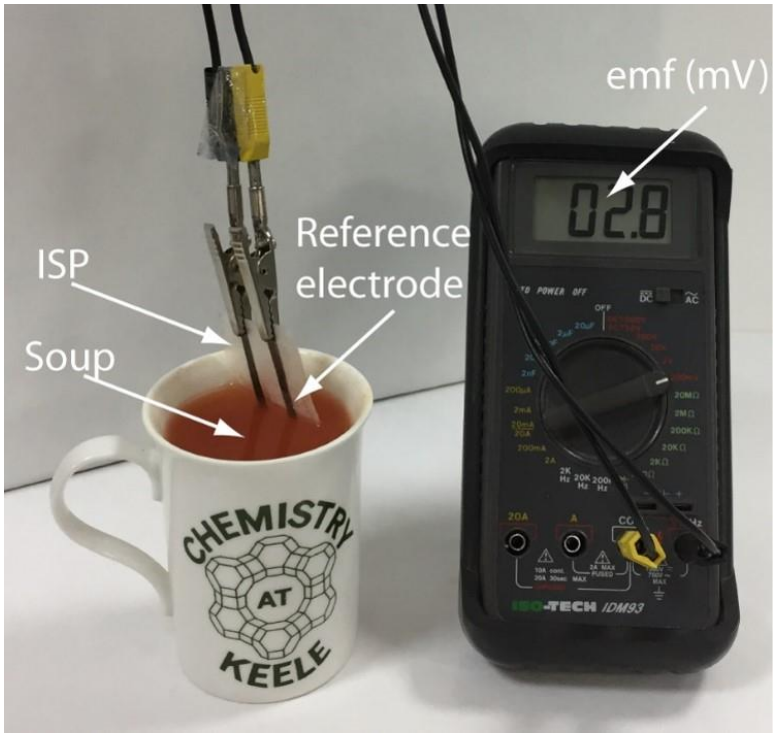

Figure 4.23. Illustration of experimental setup using digital multimeter and ISP in conjunction with simplified reference electrode to determine salt content in store-bought soup.

4.4 Conclusions

In this chapter, the concept of an ion-sensitive pencil was demonstrated. The ISP is prepared by mixing graphite and a zeolite in 60:40 wt.%, and compression of the uniform mixture using a hydraulic press. An array of 14 ISP-drawn electrodes was tested against 9 different cations relevant for environmental water quality measurements. To improve discrimination power, the array was utilised as a multi-sensor system enhanced by the partial least square statistical model as exemplified by the analysis of magnesium ion concentration in a complex mixture containing 3 strongly interfering ions (ammonium, potassium, and calcium).

The new design of zeolite-modified electrodes can simply be “hand-drawn”, does not need any conditioning prior to application and uses a very simple readout device that can be found in an average household. Most sensors exhibited near-Nernstian responses to alkali and alkaline earth cations, where the zeolite functionality as ion-exchangers was employed. Compared to classical organic ionophores, the observed responses and selectivities were lower. However, the sensor preparation, handling, and measuring protocols are so simple that persons with basic training in chemistry were able to use ISP with minimal instructions and determine salt content in store-bought water and soup albeit in a non-optimal, single electrode setup. At the moment, the sensor performance is still inferior to ion-selective electrodes, but coupling the simplicity of operation and extremely low cost of ISPs offer an unprecedented opportunity for the application of chemical sensors in areas that require a large number of sensors and inclusion of the general public such as IoTs and CS. The key limitations of ISP open further opportunities for chemists, for example, to develop zeolites and ISPs with better selectivity while unlocking the potential for collaboration with IT engineering and science communication experts in projects that were previously considered impossible.

4.5 Acknowledgments

The work presented in this chapter was conducted in collaboration with prof. Proespichaya Kanatharana’s group (S. Khumngern, A. Numnuam, P. Thavarungkul) from Prince of Songkla University, Thailand, prof. Dmitry Kirsanov from St. Petersburg State University, Russia and Dr Lukasz Mendecki.

4.6 References

1. Suri, J. T., Cordes, D. B., Cappuccio, F. E., Wessling, R. A. & Singaram, B. Continuous Glucose Sensing with a Fluorescent Thin-Film Hydrogel. *Angew. Chemie Int. Ed.* **42**, 5857–5859 (2003).

2. Zhao, J., Lin, Y., Wu, J., Nyein, H. Y. Y., Bariya, M., Tai, L.-C., Chao, M., Ji, W., Zhang, G., Fan, Z. & Javey, A. A Fully Integrated and Self-Powered Smartwatch for Continuous Sweat Glucose Monitoring. *ACS Sensors* **4**, 1925–1933 (2019).

3. Chung, A. E., Jensen, R. E. & Basch, E. M. Leveraging Emerging Technologies and the "Internet of Things" to Improve the Quality of Cancer Care. *J. Oncol. Pract.* **12**, 863–866 (2016).

4. Bouzembrak, Y., Klüche, M., Gavai, A. & Marvin, H. J. P. Internet of Things in food safety: Literature review and a bibliometric analysis. *Trends Food Sci. Technol.* **94**, 54–64 (2019).

5. Zin, M. C., Lenin, G., Chong, L. H. & Prassana, M. Real-time water quality system in internet of things. *IOP Conf. Ser. Mater. Sci. Eng.* **495**, 012021 (2019).

6. Zanella, A., Bui, N., Castellani, A., Vangelista, L. & Zorzi, M. Internet of things for smart cities. *IEEE Internet Things J.* **1**, 22–32 (2014).

7. Güder, F., Ainla, A., Redston, J., Mosadegh, B., Glavan, A., Martin, T. J. & Whitesides, G. M. Paper-Based Electrical Respiration Sensor. *Angew. Chemie Int. Ed.* **55**, 5727–5732 (2016).

8. Cammann, K., Lemke, U., Rohen, A., Sander, J., Wilken, H. & Winter, B. Chemical Sensors and Biosensors—Principles and Applications. *Angew. Chemie Int. Ed. English* **30**, 516–539 (1991).

9. Swager, T. M. Sensor Technologies Empowered by Materials and Molecular Innovations. *Angew. Chemie Int. Ed.* **57**, 4248–4257 (2018).

10. Wang, X., Sun, M., Ferguson, S. A., Hoff, J. D., Qin, Y., Bailey, R. C. & Meyerhoff, M. E. Ionophore-Based Biphasic Chemical Sensing in Droplet Microfluidics. *Angew. Chemie Int. Ed.* **58**, 8092–8096 (2019).

11. Bonney, R., Shirk, J. L., Phillips, T. B., Wiggins, A., Ballard, H. L., Miller-Rushing, A. J. & Parrish, J. K. Next steps for citizen science. *Science (80-.).* **343**, 1436–1437 (2014).

12. Newman, G., Wiggins, A., Crall, A., Graham, E., Newman, S. & Crowston, K. The future of citizen science: emerging technologies and shifting paradigms. *Front. Ecol. Environ.* **10**, 298–304 (2012).

13. Jollymore, A., Haines, M. J., Satterfield, T. & Johnson, M. S. Citizen science for water quality monitoring: Data implications of citizen perspectives. *J. Environ. Manage.* **200**, 456–467 (2017).

14. Ko, M., Aykanat, A., Smith, M. K. & Mirica, K. A. Drawing Sensors with Ball-Milled Blends of Metal-Organic Frameworks and Graphite. *Sensors 2017, Vol. 17, Page 2192* **17**, 2192 (2017).

15. Liu, Y.-Q., Zhang, Y.-L., Jiao, Z.-Z., Han, D.-D. & Sun, H.-B. Directly drawing high-performance capacitive sensors on copying tissues. *Nanoscale* **10**, 17002–17006 (2018).

16. Mirica, K. A., Azzarelli, J. M., Weis, J. G., Schnorr, J. M. & Swager, T. M. Rapid prototyping of carbon-based chemiresistive gas sensors on paper. *Proc. Natl. Acad. Sci.* **110**, 3265–3270 (2013).

17. Mirica, K. A., Weis, J. G., Schnorr, J. M., Esser, B. & Swager, T. M. Mechanical Drawing of Gas Sensors on Paper. *Angew. Chemie Int. Ed.* **51**, 10740–10745 (2012).

18. Unwin, P. R., Güell, A. G. & Zhang, G. Nanoscale Electrochemistry of sp^2 Carbon Materials: From Graphite and Graphene to Carbon Nanotubes. *Acc. Chem. Res.* **49**, 2041–2048 (2016).

19. Foster, C. W., Brownson, D. A. C., Souza, A. P. R. de, Bernalte, E., Iniesta, J., Bertotti, M. & Banks, C. E. Pencil it in: pencil drawn electrochemical sensing platforms. *Analyst* **141**, 4055–4064 (2016).

20. Kawahara, R., Sahatiya, P., Badhulika, S. & Uno, S. Paper-based potentiometric pH sensor using carbon electrode drawn by pencil. *Jpn. J. Appl. Phys.* **57**, 04FM08 (2018).

21. Jansen, J. C., Stocker, M., Karge, H. G. & Weitkamp, J. *Advanced zeolite science and applications*. (eds. Jansen, J. C., Stocker, M., Karge, H. G. & Weitkamp, J.) (Elsevier, 1994).

22. Walcarius, A. Zeolite-modified electrodes in electroanalytical chemistry. *Anal. Chim. Acta* **384**, 1–16 (1999).

23. Walcarius, A., Rozanska, S., Bessière, J. & Wang, J. Screen-printed zeolite-modified carbon electrodes. *Analyst* **124**, 1185–1190 (1999).

24. Hamlaoui, M. L., Kherrat, R., Marrakchi, M., Jaffrezic-Renault, N. & Walcarius, A. Development of an ammonium ISFET sensor with a polymeric membrane including zeolite. *Mater. Sci. Eng. C* **21**, 25–28 (2002).

25. *Introduction to Zeolite Science and Practice*. (eds. Cejka, J., van Bekkum, H., Corma, A. & Schuth, F.) (Elsevier Science, 2007).

26. Haralambous, A., Maliou, E. & Malamis, M. The Use of Zeolite for Ammonium Uptake. *Water Sci. Technol.* **25**, 139–145 (1992).

27. Fayose, T., Mendecki, L., Ullah, S. & Radu, A. Single strip solid contact ion selective electrodes on a pencil-drawn electrode substrate. *Anal. Methods* **9**, 1213–1220 (2017).

28. Mattinen, U., Bobacka, J. & Lewenstam, A. Solid-Contact Reference Electrodes Based on Lipophilic Salts. *Electroanalysis* **21**, 1955–1960 (2009).

29. Kirsanov, D., Panchuk, V., Agafonova-Moroz, M., Khaydukova, M., Lumpov, A., Semenov, V. & Legin, A. A sample-effective calibration design for multiple components. *Analyst* **139**, 4303–4309 (2014).

30. Makarychev-Mikhailov, S., Shvarev, A. & Bakker, E. Pulstrodes: Triple Pulse Control of Potentiometric Sensors. *J. Am. Chem. Soc.* **126**, 10548–10549 (2004).

31. Radu, A., Anastasova-Ivanova, S., Paczosa-Bator, B., Danielewski, M., Bobacka, J., Lewenstam, A. & Diamond, D. Diagnostic of functionality of polymer membrane – based ion selective electrodes by impedance spectroscopy. *Anal. Methods* **2**, 1490–1498 (2010).

32. Chumbimuni-Torres, K. Y., Rubinova, N., Radu, A., Kubota, L. T. & Bakker, E. Solid Contact Potentiometric Sensors for Trace Level Measurements. *Anal. Chem.* **78**, 1318–1322 (2006).

33. Bobacka, J. Conducting Polymer-Based Solid-State Ion-Selective Electrodes. *Electroanalysis* **18**, 7–18 (2006).

34. ThermoFisher-Scientific. Omnic. (2016).

35. Qonnect. PET Technical specifications. https://www.qonnect.com/sites/default/files/downloads/technical_data_sheets/KF26074 - Datasheet.pdf.

36. Pierson, H. O. Handbook of carbon, graphite, diamond, and fullerenes : properties, processing, and applications. 399 (1993).

37. Kartick, B., Srivastava, S. K. & Srivastava, I. Green synthesis of graphene. *J. Nanosci. Nanotechnol.* **13**, 4320–4324 (2013).

38. Kozbial, A., Zhou, F., Li, Z., Liu, H. & Li, L. Are Graphitic Surfaces Hydrophobic? *Acc. Chem. Res.* **49**, 2765–2773 (2016).

39. Moormann, R. Phenomenology of graphite burning in air ingress accidents of HTRs. *Sci. Technol. Nucl. Install.* **2011**, (2011).

40. Cadogan, A. M., Diamond, D., Smyth, M. R., Deasy, M., McKervey, M. A. & Harris, S. J. Sodium-selective polymeric membrane electrodes based on calix[4]arene ionophores. *Analyst* **114**, 1551–1554 (1989).

41. Marshall, C. E. *The use of zeolitic membrane electrodes*. (1939).

42. *Multisensor Systems for Chemical Analysis*. (eds. Lvova, L., Kirsanov, D., Di Natale, C. & Legin, A.) (Pan Stanford Publishing, 2014). doi:10.1201/b15491.

43. Wold, S., Sjöström, M. & Eriksson, L. PLS-regression: A basic tool of chemometrics. in *Chemometrics and Intelligent Laboratory Systems* vol. 58 109–130 (Elsevier, 2001).

44. Choosang, J., Numnuam, A., Thavarungkul, P., Kanatharana, P., Radu, T., Ullah, S. & Radu, A. Simultaneous Detection of Ammonium and Nitrate in Environmental Samples Using on Ion-Selective Electrode and Comparison with Portable Colorimetric Assays. *Sensors 2018, Vol. 18, Page 3555* **18**, 3555 (2018).

45. Wiora, J. & Wiora, A. Measurement Uncertainty Calculations for pH Value Obtained by an Ion-Selective Electrode. *Sensors 2018, Vol. 18, Page 1915* **18**, 1915 (2018).

Chapter 5

Zeolite-modified electrochemical sensors: performance modelling

5.1 Introduction

Zeolites are crystalline microporous aluminosilicates. Their uniform porosity, thermal stability, non-swelling in water, ion-exchange capacity and structural diversity make them suitable for a wide range of commercial applications. They are established as core materials in industrial catalysis and water treatment facilities, but zeolites can also be utilised as sensor components, serving either as matrices for other active constituents or as functional sensing elements that are of considerable interest in zeolite science.[1] As sensing components, zeolites could be applied for the detection of gaseous substances [2–6] or as electrochemical sensors of dissolved species.[7–10] In the latter group, which is a subgroup of chemically modified electrodes, zeolites are utilised in zeolite-modified electrodes (ZME).[11] Since zeolites are electrical insulators, they have to be in contact with a conductive matrix in order to be used as sensing electrode components. Among the reported zeolite-containing electrodes, two main groups can be distinguished: zeolite-conductive polymer membranes [12–16] and zeolite-graphite matrices, among which the zeolite-modified carbon paste electrodes [17–19] are the most common.

In the electrochemical characterisation of various species, voltammetric, amperometric, conductometric and potentiometric techniques have been used.[7–10] Among these techniques, potentiometry, although a very simple method, is rather infrequently used for the detection of cationic species. Interestingly, the first reports on zeolites utilised as electrode components [16,20] were potentiometry-based.

According to the literature data,[7–10] zeolites can, to a certain degree, selectively detect a variety of species: cationic dyes,[21] detergents,[15] pesticides and fungicides,[22] neurotransmitters and vitamins,[12,23] amino acids [24,25] and inorganic cations [26–28] (see Table 5.1). The potentiometric selectivity values presented in Table 5.1 were either calculated by separate solution method or, if not explicitly stated, they were determined from the reported

responses of electrodes to specific species. However, the selectivity of zeolite is relatively poor compared to classical ionophore-based electrodes. This fact has probably discouraged a wider use of ZMEs, therefore a reduced amount of research has been conducted on elucidating the detection mechanisms and the parameters affecting the potentiometric response of ZME. Zeolites with adsorbed cationic exchangers [29,30] should be mentioned as a separate category since these components are not confined only within the zeolites, but rather are deposited on the external surface of the zeolites. Therefore, zeolites serve only as immobilisation matrices rather than as electroactive components. The observed selectivity in this group of sensors has been mainly following the Hoffmeister series of anions.

Most of the reported work is confined to the use of zeolites with the faujasite (FAU) framework, such as NaX and NaY,[15,31,32] with several other framework types described less frequently. Additionally, reports are also focused on the detection performance rather than on elucidating the detection mechanism and the structure-function relationship. An attempt to relate the electrochemical responses to the chemical and physical parameters of the analytes and zeolites have been reported for cyclic voltammetry [26,33] and indirect amperometry techniques,[34] only. The steric factors (cation diameter, zeolite pore size) and charge separation have been stated as the limiting factors of the ZME performance. Even though some interesting insight has been provided, only a limited number of zeolites frameworks has been used, thus not covering a wider range of zeolite features available.[26,33,34] Moreover, the studied parameters have been targeted more on the optimisation of the specific electrochemical technique, so the conclusions provided may not be applied completely to potentiometric applications.

In this study, the observed electrochemical responses of zeolite-containing electrodes to mono- and divalent cations are determined by potentiometric studies and systematically analysed using chemometric techniques. Such an approach is essential for the rational design of ZME, particularly in the case of multi-sensor arrays. Indeed, such systems with varying

response patterns can significantly improve the selectivity of the zeolite-based sensors.[35] However, to the best of our knowledge, this is the first comprehensive investigation relating zeolite properties (Si/Al ratio, pore size, etc) to their performance as the materials for potentiometric sensing. The work discussed in this chapter demonstrates that the performance of zeolite-containing electrodes can be rationalised based on the system parameters and that predictive models can be developed using statistical approaches.

Table 5.1. A summary of the literature data on ZME potentiometric studies.

Species of interest	Observed selectivity	LOD (M)	Linear range (M)	Zeolite used	Preparation method	Ref.
Na^+	Na^+>> TEA^+ (a)		0.7−2	NaA	Epoxy resin membrane	[16]
K^+	Cs^+> Rb^+> K^+> Na^+> Li^+	$1x10^{-5}$ $2x10^{-5}$ $2.5x10^{-5}$ $4x10^{-5}$	10^{-4} – 0.1	CaA	Low−viscosity epoxy resin membrane	[13]
Cs^+	Cs^+> Ag^+, K^+> Na^+> Li^+ Cs^+>> Ba^{2+}> Ca^{2+}> Cu^{2+}	$2x10^{-5}$	$3x10^{-5}$ – 0.1	MOR	Epoxy resin membrane	[14]
Cd^{2+}	Cd^{2+}> Al^{2+}	–	$1x10^{-5}$ – $1x10^{-2}$	NaA	Polysulfone coated zeolite on glassy carbon	[36]
Cs^+	Cs^+> K^+> Na^+> Li^+	$3x10^{-5}$	$5x10^{-4}$ – 0.1	NaX	Polydimethoxysilane membrane on Ir disks	[15]
HDPCL	HDPCL> DTACL(b)	–	–	NaA	Polydimethoxysilane membrane on Ir disks	[15]
K^+	K^+> Ca^{2+}> Ba^{2+}>Li^+	–	–	CHA	Neat-pressed zeolite disk	[20]
H^+	H^+>> Li^+> Na^+> NH_4^+> K^+> Fe^{2+}> Ca^{2+}	$1x10^{-12}$	$1x10^{-12}$ – 0.1	“Natural zeolite” (Si/Al= 5.5)	Screen−printed sol−gel graphite mix	[37]

Species of interest	Observed selectivity	LOD (M)	Linear range (M)	Zeolite used	Preparation method	Ref.
Cd^{2+}	Pb^{2+}> Cd^{2+}	–	$1x10^{-6}$ – $1.5x10^{-2}$	NaY	TEOS "healed" zeolite membrane [c]	[38]
NH_4^+	NH_4^+>> K^+, Na^+, H^+	$1x10^{-8}$	$1x10^{-7}$ – $1x10^{-4}$	Clinoptilolite	Siloprene– zeolite membrane (ISFET) [d]	[39]
Urea	NH_4^+>> K^+, Na^+, H^+ Urea> Hg^{2+}, Cu^{2+}, Ag^+	$3x10^{-5}$	$3×10^{-5}$ – $5×10^{-3}$	Clinoptilolite	Siloprene–zeolite–urease membrane (ISFET, ENFET) [e]	[40]
Cs^+, Na^+	Na^+> Cs^+	–	–	NaY, NaA, MOR	Neat-pressed zeolite disks	[41]
Cs^+	Cs^+> K^+> NH_4^+> Na^+> Ca^{2+}> Cd^{2+}> Pb^{2+}> Mg^{2+}> Cu^{2+}> Li^+> Ni^{2+}	$4x10^{-5}$	$1x10^{-4}$ – 0.1	KY	PTEV [f] (benzyl acetate), silicone oil	[42]
Thionine	Thionine> RB6G> RB^+> Na^+> NH_4^+> MB^+ [g]>> Sr^{2+}>> Ca^{2+}> Zn^{2+}> Ni^{2+}> Co^{2+}> Al^{2+}> Mn^{2+}> Fe^{2+}	$8x10^{-7}$	$1x10^{-6}$ – $1x10^{-2}$	MOR (ion-exchanged by thionine)	PVC (DBP) [h] membrane	[21]

Species of interest	Observed selectivity	LOD (M)	Linear range (M)	Zeolite used	Preparation method	Ref.
Cs^+	$Cs^+ > Tl^+ > Cr^{2+} > NH_4^+, Na^+ > Cu^{2+}, Li^+, Al^{2+} > Mg^{2+} > Bi^{2+} > Ca^{2+} > Ba^{2+}, Mn^{2+}, Cd^{2+} > Zn^{2+}, Co^{2+} > Ni^{2+}$	7.3×10^{-6}	$1 \times 10^{-5} – 0.1$	KY	Sol−gel matrix	[43]
Cs^+	$Cs^+ > NH_4^+ > Pb^{2+} > Zn^{2+} > Cd^{2+} > Ca^{2+} > Ni^{2+} > Hg^{2+} > Mg^{2+}$	5.2×10^{-5}	$1.0 \times 10^{-4} – 0.1$	KY	PVC (DBP)	[44]

Table 5.1 notes:

[a] TEA^+- tetraethylammonium cation

[b] HDPCL- hexadecylpyridinium chloride, DTACL- Dodecyltrimethylammonium chloride (cationic detergents)

[c] TEOS- tetraethylorthosilicate

[d] ISFET- ion-selective field-effect transistor

[e] ENFET- enzyme-linked field-effect transistor

[f] PTEV- poly(tetrafluoroethylene-co-ethylene-co-vinyl acetate)

[g] RB6G- rhodamine B6G, RB- rhodamine B, MB- methylene blue (all mentioned compounds including thionine are cationic dyes)

[h] DBP-dibutyl phtalate

5.2 Experimental Section

Graphite powder (particle size <20μm, synthetic), sodium chloride (NaCl), potassium chloride (KCl), ammonium chloride (NH_4Cl), calcium chloride ($CaCl_2$), magnesium chloride ($MgCl_2$) and zinc chloride ($ZnCl_2$) were purchased from Sigma-Aldrich. Zeolites NaX (Si/Al=1.3), KX (Si/Al=1.3), NaY (Si/Al=2.6) and KY (Si/Al=2.6) were purchased from Riogen, USA. Zeolites MAP (Si/Al=1.0), NaA (Si/Al=1.0) and KA (Si/Al=1.0) were provided by Crosfield, zeolites MOR (Si/Al=10.0), FER (Si/Al=10.0), BEA-12 (Si/Al=12.5), BEA-19 (Si/Al=19.0) and ZSM-5 (Si/Al=40.0) were obtained from Zeolyst, and zeolite LTL (Si/Al=3.1) was supplied by Tosoh, Japan. Zeolites HEU-A and HEU-B were from Zeodex, UK, HEU-C was provided by Prof A. Walcarius (Université de Lorraine, France). OHP universal film (clear 4243-100μm) from Q-connect was used as a substrate. All the standard aqueous solutions were prepared with ultrapure water obtained using a Pico Pure 3 system.

5.2.1 Zeolite characterisation

Zeolites were characterised by powder X-ray diffraction (using a Bruker D8 Advance diffractometer Cu Kα at 40 kV and 40 mA, 2θ=5−60°), scanning electron microscopy (Hitachi TM 3000 with Bruker EDX system at 500x magnification, 300 s EDX data collection time) and FTIR spectroscopy (using Thermo iS10 spectrometer with a custom-made cell, 6000−1000 cm^{-1}, 64 scans, 4 cm^{-1} resolution, transmission mode) Further details are provided in Ref [45,46] and in Supplementary Information.

5.2.2 Ion-sensitive pencil (ISP) preparation

The detailed process of the ISP electrode preparation has been described in chapter 4.[47] Briefly, a zeolite and graphite powder were mixed in a 40:60 mass ratio using a ball-mill until a uniform mixture is obtained. Subsequently, the mixture was placed in a 13mm KBr pellet die

(Specac) and pressed by the hydraulic bench press applying 4 tonnes load to obtain a pellet (ISP). The electrode substrate was prepared by cutting a strip of a PET sheet (2.0x3.0 cm), which was then etched (aluminium oxide, grit 240). ISP was used to draw a line onto the PET sheet until the measured resistance of the electrode was less than 3 kΩ.

5.2.3 Potentiometric measurements

Responses of all freshly prepared, non-conditioned electrodes were recorded using the Lawson Labs Inc. 16-channel EMF-16 interface (3217 Phoenixville Pike Malvern, PA 19355, USA) in the stirred solution against a double-junction Ag/AgCl reference electrode with a 1.0 M of LiOAc bridge electrolyte (Fluka). For the measurement of the potentiometric responses, all the electrodes were immersed into 200 mL of ultra-pure water followed by stepwise addition of the standards of known concentration, which were prepared using 0.1 M stock solutions of various salts (Table 5.2**)**. Potentiometric responses were recorded after each addition. The electrodes were rinsed with ultra-pure water and dried before immersing into the next sample to prevent carryovers. Activities were calculated from the calibration curve using the Nikolsky-Eisenman equation, while the activity coefficients (log a) were calculated according to the Debye-Hückel approach. Six electrodes of the same kind were used, but for clarity reasons, the averaged responses and the standard deviations have been presented.

Table 5.2. Solution concentrations after each addition step, the initial sample volume was 200.00 mL, the stock solution concentration was 0.1 M.

The volume of stock solution added, µL	**Concentration, mol L^{-1}**	**Log c**
20	$1.0x10^{-5}$	-5.00
100	$6.0x10^{-5}$	-4.22
1000	$5.6x10^{-4}$	-3.25
10000	$5.3x10^{-3}$	-2.28

5.2.4 Data processing

All the calculations were performed using the Unscrambler 9.7 (CAMO, Norway) software. To study the influence of the zeolite type on the electrochemical response characteristics of the corresponding sensors we applied two different chemometric approaches. The first was based on principal component analysis (PCA). PCA is a common tool for exploratory data analysis that allows convenient visualization of the initial multivariate dataset in the form of 2D plots yielding valuable information on the similarity and dissimilarity of the studied samples (in our case sensors). A detailed description of PCA methodology can be found elsewhere.[48] In the case of PCA, the analysed data matrix was comprised of the zeolite properties data set obtained for all the studied materials.

The second approach was based on partial least squares regression (PLS). To relate the values of the sensor responses towards different ions with the physical and chemical properties of the utilised zeolites, the following multivariate regression model was built:

$$\boldsymbol{Sensitivity = b_0 + b_1 \times Property_1 + b2 \times Property_2 + \ldots + b_i \times Property_i.}$$

The values of $\boldsymbol{b_i}$ coefficients were calculated according to the PLS algorithm.[49] The zeolite properties are listed in Table 5.3. The matrix of properties was mean-centred and normalized column-wise with standard deviation values for each property prior to the calculations. The obtained values of regression coefficients $\boldsymbol{b_i}$ were used to judge the effect of different properties on the sensitivity values.

Table 5.3. Zeolite properties used as parameters in chemometric calculations, samples marked with (*) are of natural origin, Si/Al values were determined by the manufacturers.

	Si/Al	(Al/(Si+Al)	Pore size, Å	Largest channel, MR	Channel network	Extraframework ion	Crystallite size, µm	SEM-TEM, µm	Silanol intensity
NaX	1.3	0.435	7.4	12	3D	Na^+	0.78	2	0.050
KX	1.3	0.435	7.4	12	3D	0.4 Na^+, 0.6 K^+	0.78	2	0.055
NaY	2.6	0.278	7.4	12	3D	Na^+	0.8	2	0.207
KY	2.6	0.278	7.4	12	3D	0.2 Na^+, 0.8 K^+	0.8	2	0.040
NaA	1.0	0.500	4.2	8	3D	Na^+	0.9	3	0.001
KA	1.0	0.500	4.2	8	3D	0.6 Na^+, 0.4 K^+	0.9	3	0.001
MOR	10.0	0.091	6.7	12	1D	NH_4^+	0.74	0.3	0.669
FER	10.0	0.091	5.0	10	2D	Na^+	0.6	1	0.569
BEA 12	12.5	0.074	6.8	12	3D	NH_4^+	0.04	0.05	2.944
BEA 19	19.0	0.050	6.8	12	3D	NH_4^+	0.04	0.05	1.264
ZSM-5	40.0	0.024	5.5	10	2D	NH_4^+	0.52	0.2	1.500
LTL	3.1	0.244	7.1	12	1D	K^+	0.73	0.5	0.832
MAP	1.0	0.500	3.3	8	3D	Na^+	0.02	0.02	0.076
HEU-A*	4.5	0.182	5.0	10	2D	0.2 K^+, 0.5 Na^+, 0.1 Mg^{2+}, 0.2 Ca^{2+}	0.7	5	0.927
HEU-B*	5.5	0.154	5.0	10	2D	0.4 Na^+, 0.2 Mg^{2+}, 0.2 Ca^{2+}, 0.1 Fe^{3+}	0.6	5	3.063
HEU-C*	5.2	0.161	5.0	10	2D	0.3 K^+, 0.1 Na^+, 0.2 Ca^{2+}, 0.1 Fe^{3+}	0.4	0.4	0.85

5.3 Results and discussion

5.3.1 Zeolite characterisation

The range of zeolites utilised in this work includes sixteen materials, most of which are commercially available, with a significant variation of compositions and structural properties. This is important for the fabrication of inexpensive sensors as well as for generating a better prediction model for the selection of zeolites with superior performance for sensor applications.

Figure 5.1 presents a typical example of characterisation data for the NaY zeolite. The XRD pattern is indicative of a highly crystalline material with the FAU structure type and the size of crystalline domain of 0.8 μm, which is in accord with the electron microscopy data. This is also confirmed by the nitrogen adsorption results: NaY possesses a 3D channel network with the pore size of just over 7Å. The low intensity of the SiOH peak in the FTIR spectra is characteristic of a zeolite with a relatively large particle size and very few structural defects.

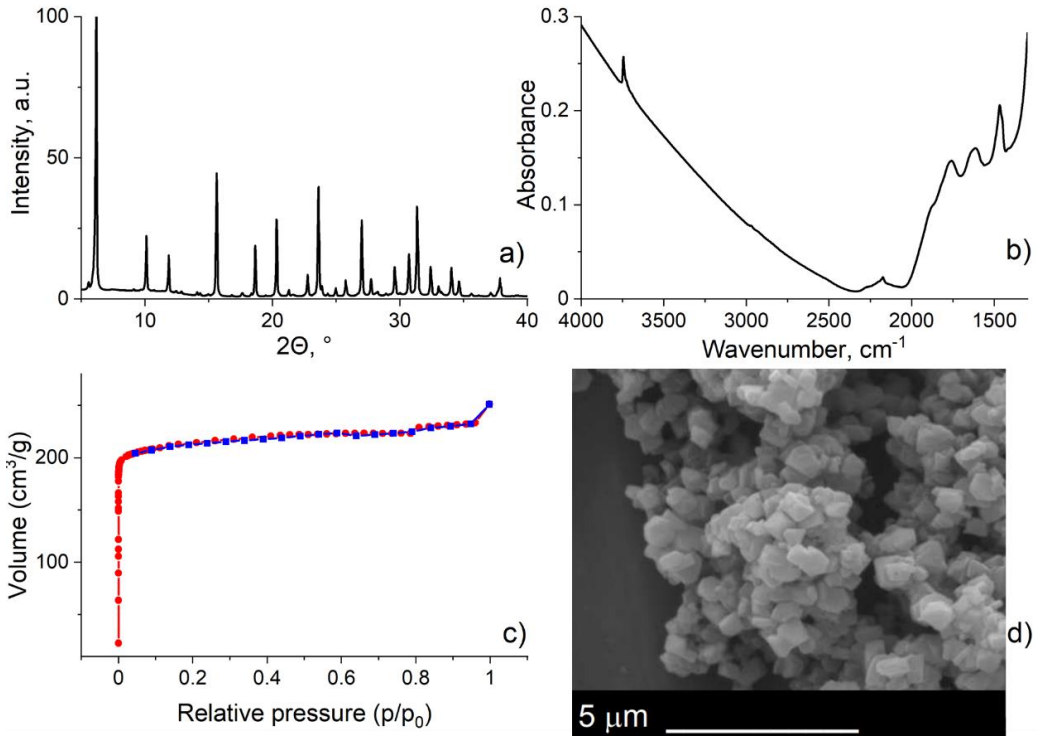

Figure 5.1. Characterisation data obtained for NaY zeolite: (a) XRD pattern, (b) FTIR spectrum., (c) nitrogen adsorption-desorption isotherm, and (d) SEM micrograph.

A complete set of characterisation results for all 16 zeolites utilised in this study is presented in the Supplementary Information section. The XRD patterns of the studied zeolites (Figures 7.10 -7.16) correspond to those available in the literature [50], with all materials demonstrating a high degree of crystallinity. The XRD data have been also used to determine the size of the crystalline domain (Table 5.3) which varied from 0.9 to 0.02 μm. The chemical composition data (SEM-EDX) show a wide range of Si/Al ratios (1-40) and the content of extraframework cations. Synthetic materials contain varying concentrations of NH_4^+, Na^+ and K^+ ions, while in the natural zeolites Ca^{2+}, Mg^{2+} and Fe^{3+} are present as well (Table 5.3).

Large-, medium- and small-pore zeolites have been utilised with the pore sizes from 3.3 to 7.5 Å. These materials possess 1D, 2D or 3D networks of channels and cages.[51] In addition, the studied zeolites demonstrate a diverse range of particle sizes (SEM or TEM measurements) and concentration of the terminal silanol groups (Si-OH) (Figures 7.17 -7.32). The latter is

expected to increase with decreasing crystal size (Table 5.3). All these properties can influence the interactions between the zeolite and cations in solution, leading to different selectivity and sensitivity of various zeolite-modified sensors.

In chapter 4,[47] as a proof of concept, the response of NaX-containing ISP-drawn electrodes to a number of cations was demonstrated (Figure 5.2). The obtained response for Na^+ was 55.1 mV/decade, which is close to a Nernstian response of 59.2 mV/decade. Examples of the sensor data obtained for five cations using ISP-drawn electrodes based on the slopes of calibration curves in the concentration range from 10^{-4} to 10^{-2} M are presented in Table 5.4. Most zeolites followed the Hoffmeister series of cations (e.g. $NH_4^+ > Cs^+ > Rb^+ > K^+ > Na^+ > Li^+ > Mg^{2+} > Ca^{2+}$), which has also been observed as a general trend for the literature values (Table 5.1 and references therein). In contrast, the sensitivity towards K^+ is higher than that for NH_4^+; also, K-containing zeolites have shown a high response to Ca^{2+} ions. Although many reports [13–15,42–44] have shown that the highest responses are observed for Cs^+, this cation has not been included in this study since the target application of our work is monitoring plant nutrients. The results presented demonstrate that the potentiometrically determined sensitivities deviate from the ideal Nernstian response, at the same time providing variability that can be related to the physical and chemical properties of the studied zeolites. PLS modelling has been used to relate these properties to potentiometric responses of the ISP-drawn electrodes, while PCA models have been employed to evaluate the zeolite properties data set.

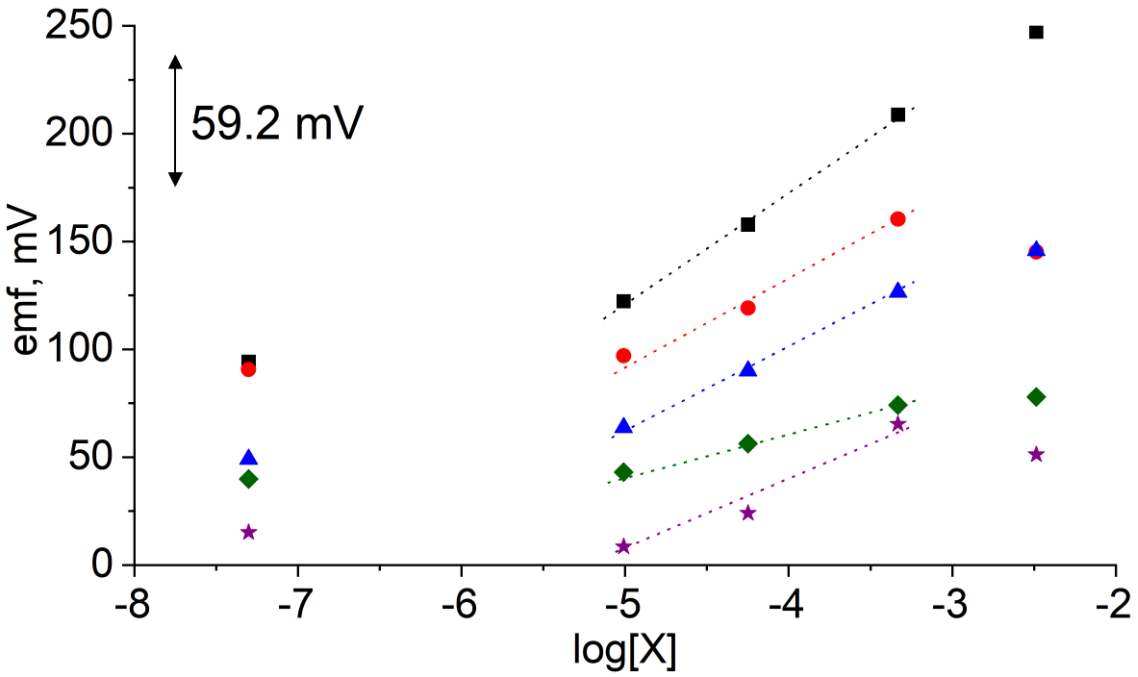

Figure 5.2. Sensitivity data obtained with NaX-containing ISP-drawn electrodes for Na^+ cations (black), K^+ (red), NH_4^+ (blue), Ca^{2+} (green), Mg^{2+} (purple), potentiometric responses were offset for clarity.

Table 5.4. Slopes of potentiometric responses of ISP-drawn electrodes (the slopes are measured in mV/dec, in the range of log[c] from -5 to -3.25 using chlorides of mono- and divalent cations and are presented as a mean of 6 measurements ± the standard deviation).

Zeolite	**Na^+**	**K^+**	**NH_4^+**	**Ca^{2+}**	**Mg^{2+}**
NaX	55 ± 4	37 ± 5	37 ± 4	19 ± 10	35 ± 7
KX	31 ± 5	30 ± 4	34 ± 8	72 ± 5	22 ± 6
NaY	42 ± 5	70 ± 3	39 ± 3	13 ± 3	17 ± 3
KY	28 ± 3	48 ± 3	42 ± 7	53 ± 7	18 ± 2
NaA	29 ± 2	34 ± 3	14 ± 2	15 ± 2	5 ± 3
KA	23 ± 5	31 ± 2	6 ± 1	45 ± 8	-6 ± 3
MOR	47 ± 4	57 ± 5	34 ± 4	28 ± 5	12 ± 5
FER	17 ± 5	41± 12	27 ± 6	14 ± 2	10 ± 2
BEA 12	21 ± 5	12 ± 5	23 ± 4	30 ± 10	15 ± 8
BEA 19	30 ± 4	35 ± 3	27 ± 4	29 ± 6	8 ± 3
ZSM-5	18 ± 3	42 ± 4	20 ± 5	11 ± 3	6 ± 5
LTL	33 ± 3	58 ± 7	35 ± 3	53 ± 10	20 ± 9
MAP	14 ± 5	28 ± 5	28 ± 3	35 ± 3	15 ± 3
HEU-A	19 ± 2	46 ± 6	40 ± 2	43 ± 2	11 ± 2
HEU-B	15 ± 4	8 ± 8	12 ± 2	8 ± 6	10 ± 2
HEU-C	22 ± 3	34 ± 13	15 ± 7	25 ± 7	12 ± 2

5.3.2 PCA modelling

PCA modelling has been performed to visualize the variability of zeolite properties (Figure 5.3). The following parameters have been used for the studied zeolites: Si/Al; Al/(Si+Al); Pore Size (Å); Largest Channel, MR; Channel Network; Extraframework Cations (Na^+, K^+, NH_4^+, Ca^{2+}, Mg^{2+} or Fe^{3+}); Crystallite Size (XRD); Particle Size (SEM-TEM); SiOH Intensity (Table 5.3). PCA score plots are the so-called maps of samples, where each point represents one zeolite. The location of the points in the PC space indicates their similarity or dissimilarity in terms of the variables employed for the calculation of PCs (here, these are the characteristics of zeolites). The points located close to each other are similar, and vice versa. A PCA loadings plot is a "map of variables". It shows the importance of a particular variable for the direction of PC. Each point represents one zeolite parameter. If the variables are close to each other in the loadings plot, they are positively correlated. If they are located opposite to each other relative to the graph origin, they are negatively correlated. The percentage variance is the amount of variability in the data taken into account by each PC. Thus, for PC1-PC2 space, where the explained variance is 56%, the Pore Size and Largest Channel variables are positively correlated, whereas the presence of Na^+ and NH_4^+ as extraframework cations are negatively correlated. It can also be observed that zeolites with the lower Al content (MOR, BEA-12, BEA-19, ZSM-5) are grouped opposite to zeolites with the higher Al content, such as NaX, NaY, NaA, KX, KY, KA. For example, it can be deduced from the PC1-PC2 plot that NaA is different from ZSM-5 largely due to the Pore Size, Al/(Si+Al), Na^+, NH_4^+ and Si/Al parameters (this conclusion is made considering both scores and loadings together), which agrees with their structural characterisation data, catalytic performance and spectroscopic analyses.

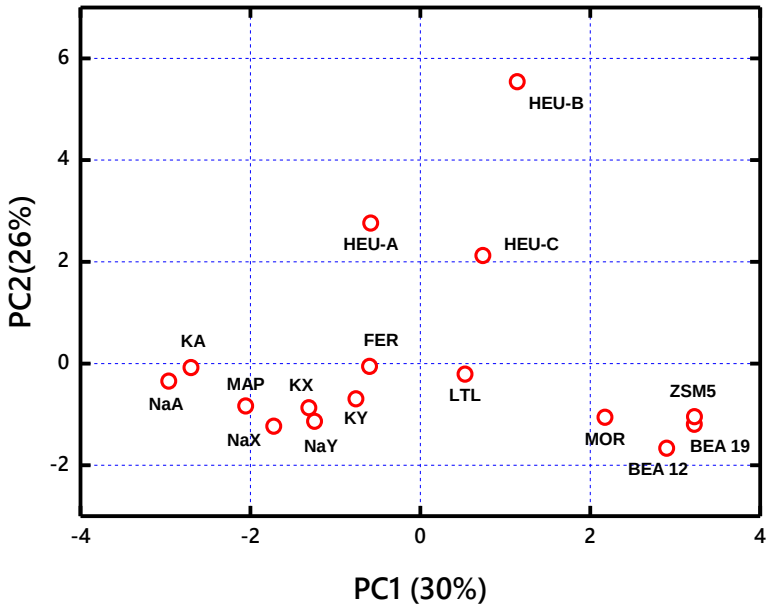
HEU-B
HEU-A
HEU-C
KA
FER
NaA
MAP
KX
KY
LTL
ZSM5
NaX
NaY
MOR
BEA 19
BEA 12
PC2(26%)
PC1 (30%)
6
4
2
0
-2
-4
-2
0
2
4

(a)

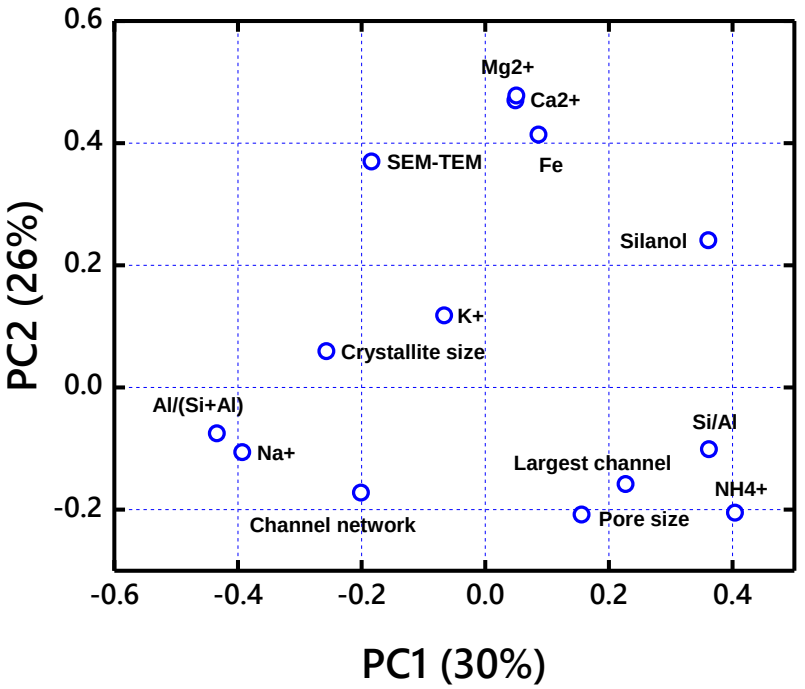
Mg2+
Ca2+
Fe
SEM-TEM
Silanol
K+
Crystallite size
Al/(Si+Al)
Na+
Si/Al
Largest channel
NH4+
Channel network
Pore size
PC2 (26%)
PC1 (30%)
0.6
0.4
0.2
0.0
-0.2
-0.6
-0.4
-0.2
0.0
0.2
0.4

(b)

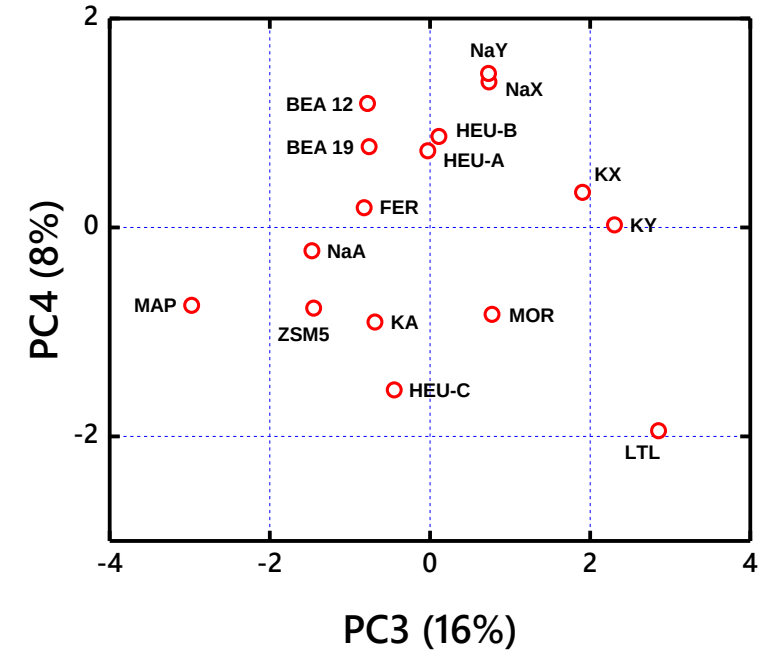

(c)

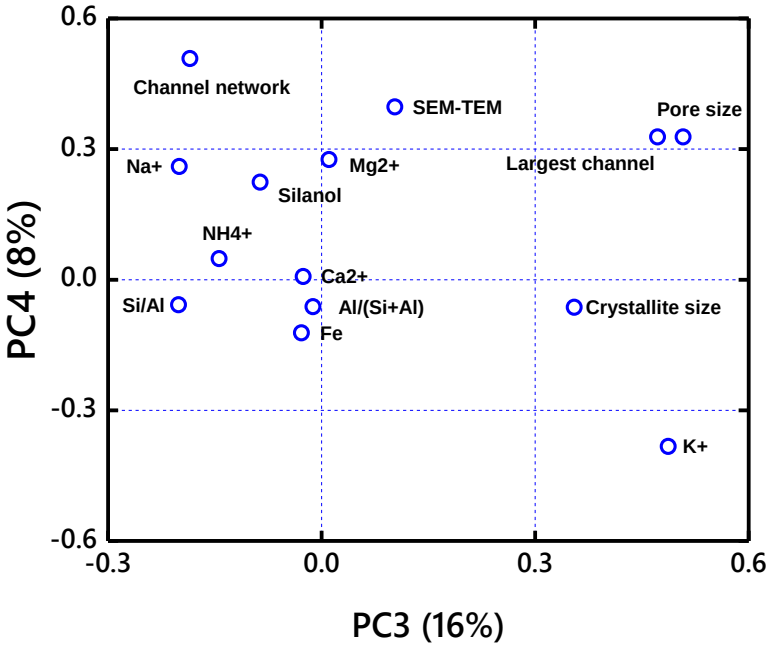

(d)

Figure 5.3. PCA score plot based on the properties of the zeolites PC1-PC2 (a), PCA loadings plot for PC1-PC2 (b), PCA score plot based on the properties of the zeolites PC3-PC4 (c), and PCA loadings plot for PC3-PC4 (d).

For the PC3-PC4 space, the explained variance is 24%, the parameters Pore Size and Largest Channel variables are positively correlated, similar to the PC1-PC2 plot. On the other hand, Crystallite Size and Silanol Intensity are negatively correlated, as are the presence of Na^+ and K^+ extraframework cations. It can also be observed that zeolites with larger pore size, i.e. NaX, NaY, KX, KY, are grouped opposite of zeolites with a smaller pore size such as NaA, KA or MAP. For example, it can be concluded from the PC3-PC4 plot that zeolite MAP is different from LTL mainly due to the Channel Network, Silanol Intensity, SEM-TEM, Na^+, K^+ and Si/Al parameters (this conclusion is made considering both scores and loadings together). Once again, this is in accordance with the characterisation data available for these materials.

Overall, these data confirm that the zeolites utilised in this work for the fabrication of ISPs demonstrate a significant variation of compositions and structural properties, which is important for a more reliable PLS modelling.

5.3.3 PLS modelling

Multivariate regression models were constructed to identify the most important properties of zeolites that impact the sensitivity of the potentiometric sensors. The set of parameters for all zeolites was related to the potentiometric sensitivity towards a particular ion. Since all parameters are in different units, their values have been autoscaled prior to modelling. The figures below are presented as "measured vs predicted" plots indicating real sensitivity values towards an ion (in mV/dec) and those predicted by the PLS model during calibration and cross-validation. The absolute values of the regression coefficients in the corresponding charts indicate the importance of particular zeolite parameters in the development of sensor response.

Figure 5.4a presents a PLS model predicting the sensor sensitivity towards NH_4^+ based on a number of zeolite characteristics. The model demonstrates that all the natural zeolites (HEU-A, HEU-B, HEU-C) and zeolite MAP are outliers. This can be explained by the less uniform

structure and composition of natural zeolites as compared to the synthetic counterparts, which could cause the potentiometric responses to vary from the rest of the zeolites. On the other hand, zeolite MAP is known for its flexible structure, indeed, the unit cell volume can change by up to 30% upon hydration-dehydration,[52] which may have an impact on the ability of ions to be exchanged into the zeolite channels. For zeolites as electroactive components to have an electrochemical response, a prerequisite requirement is that a cation can enter the zeolite channel network. If the zeolite pores are too small for solvated cations to enter, no or almost no electrochemical response is observed.[16,33,34] Therefore, HEU-A, HEU-B, HEU-C and MAP have been excluded from the initial model, leading to a significantly better regression model (Figure 5.4b, Table 5.5). This limits the predictions to the commercially available samples only, which is associated with their better defined characteristics. We believe that the exclusion of HEU and MAP zeolites should not hinder the applicability of the proposed model.

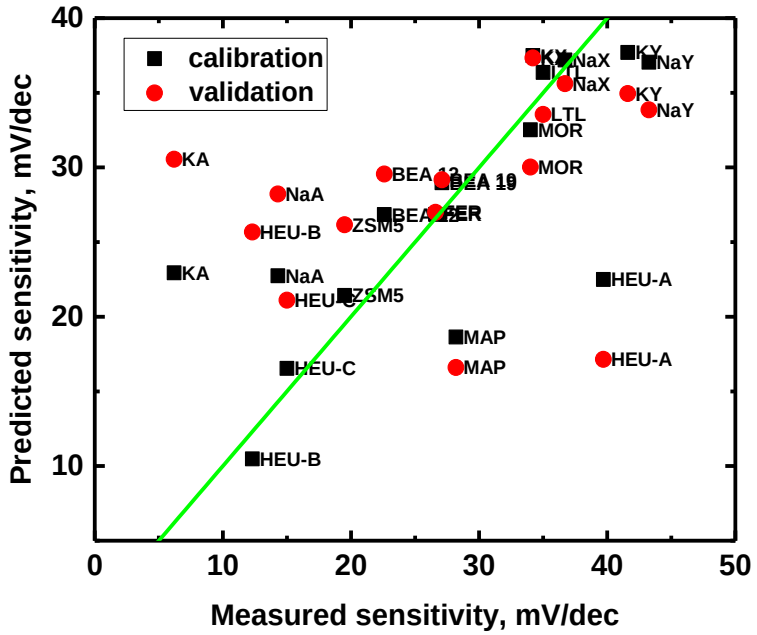

(a)

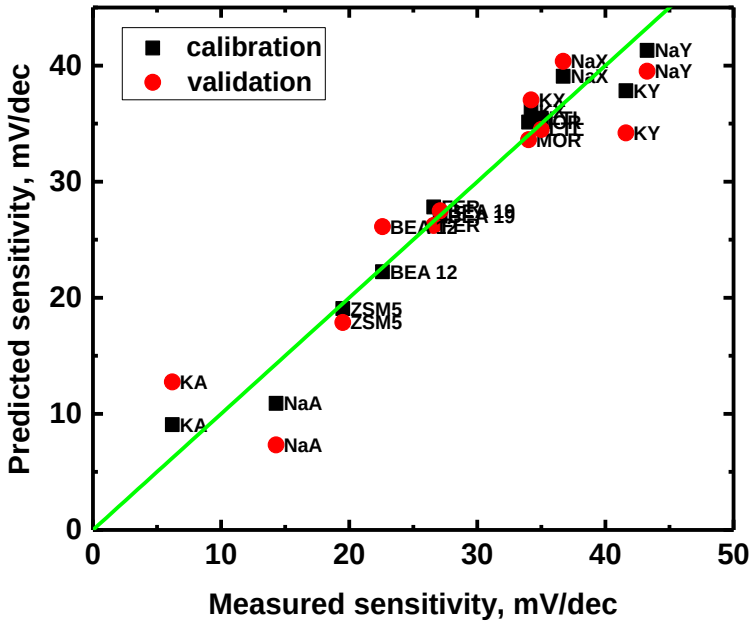

(b)

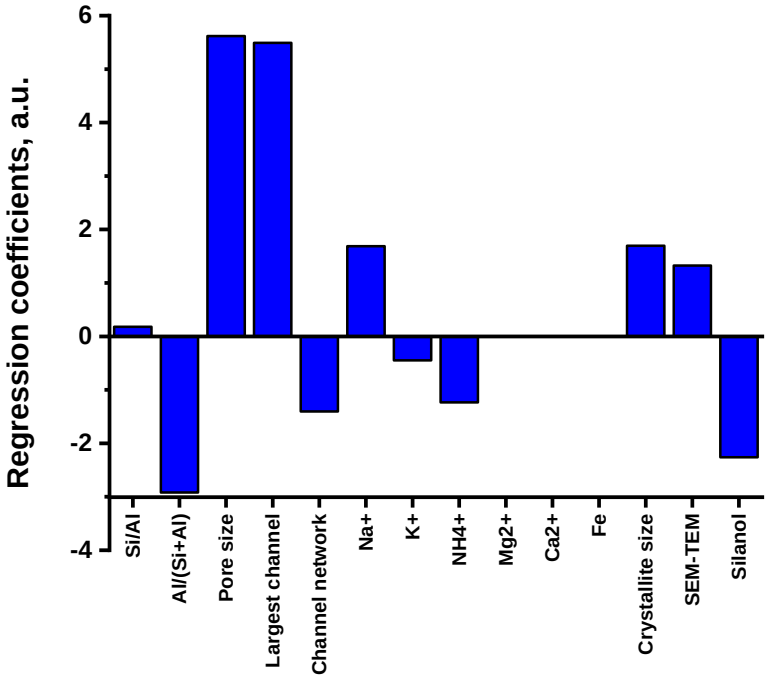

(c)

Figure 5.4 PLS regression model for the potentiometric sensitivity towards NH_4^+, (a) including all zeolites, (b) without MAP and HEU zeolites (RMSEC 2.1 mV/dec, RMSECV 4.1 mV/dec, R^2cal 0.96, R^2val 0.88), and (c) regression coefficients for the PLS regression model with 4 LVs for the potentiometric sensitivity towards NH_4^+, which excludes HEU and MAP zeolites.

The regression coefficients of this model (Figure 5.4c) indicate that in addition to Pore Size and Largest Channel, previously recognized as important parameters,[26,33,34] relevant parameters contributing to this model are Al/(Si+Al) and Silanol Intensity. The former is linked to the Si/Al ratio but is a better measure of the Al concentration, which affects the total ion-exchange capacity of a zeolite, while the latter is related to the particle size as smaller particles have a higher external surface area covered by silanols. These results may be linked to a better dispersion of the smaller zeolite particles in the graphite matrix. In addition, as the ion-exchange process is also limited by the diffusion of cations into zeolite channels, the potentiometric calibration experiments may not be carried out under equilibrium conditions. Therefore, cation diffusion in small and large zeolite crystals may have a significant effect on the sensitivity of ISP-drawn electrodes towards species of interest.

A PLS regression model "measured vs predicted" for the potentiometric sensitivity for Ca^{2+} is shown in Figure 5.5a alongside the bar chart with the regression coefficients presented in Figure 5.5b (with three natural zeolites and zeolite MAP excluded from the model).

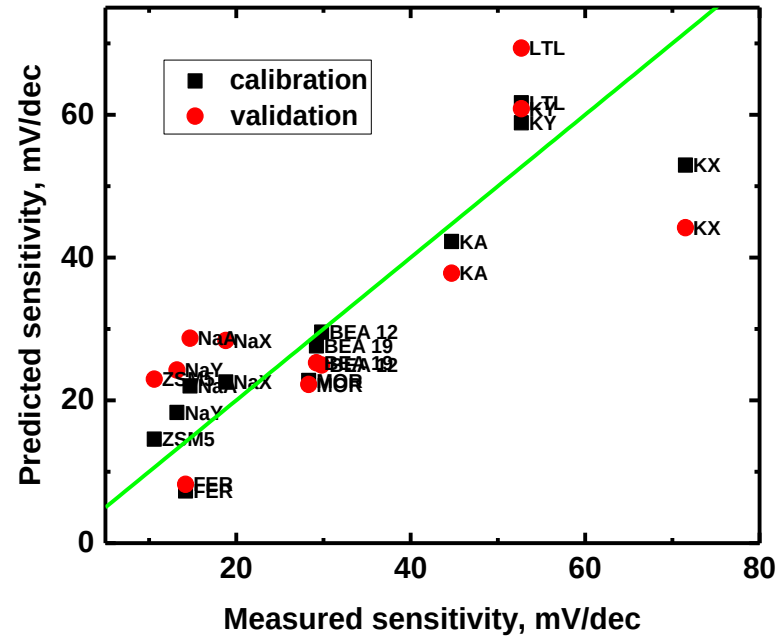

(a)

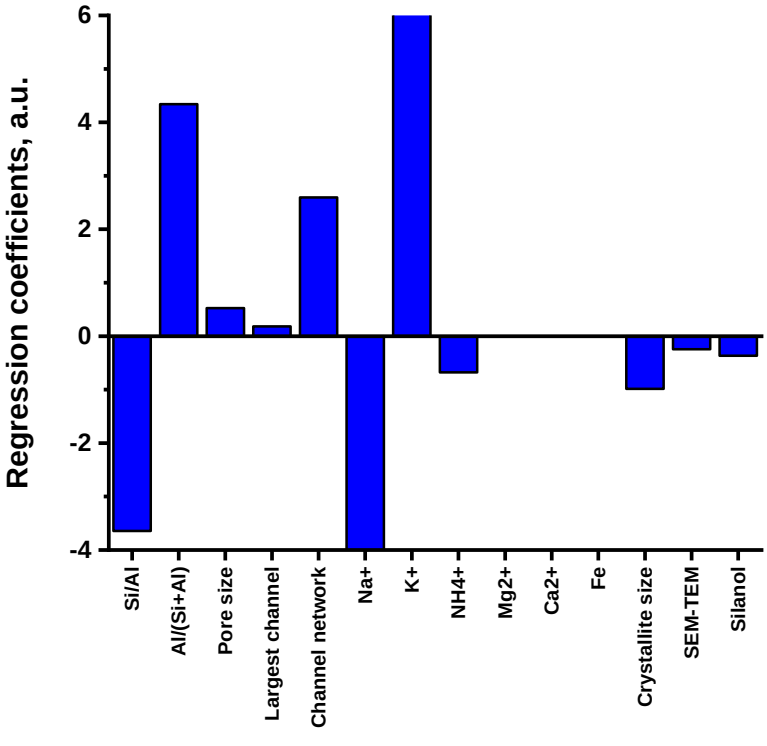

(b)

Figure 5.5. PLS regression model for the potentiometric sensitivity towards Ca^{2+} without MAP and HEU zeolites, (RMSEC 7.4 mV/dec, RMSECV 12.3 mV/dec, R^2cal 0.84, R^2val 0.64), b) PLS regression coefficients for the model with 3 LVs (b).

Parameters affecting the Ca^{2+} regression plot (Figure 5.5b) the most are the presence of sodium and potassium as extraframework cations and the aluminium content in zeolites, which is described by the Si/Al ratio and the Al fraction. In contrast to the NH_4^+ sensitivity model, the presence of K^+ and Na^+ are the most significant contributors. This feature has not been observed previously for other electrochemical techniques (cyclic voltammetry and indirect amperometry) as a relevant parameter. Indirectly, the potentiometric sensitivity can be enhanced by preconcentration of solutions containing the same kind of cations,[42–44] but the effect of extraframework cations present in a zeolite on the PLS regression model for the potentiometric response has not been reported. Si/Al ratio has been recognized as an important parameter in agreement with the general ion-exchange observations that the zeolites with a higher Al content have a greater affinity to multivalent cations, while the more siliceous zeolites have a greater affinity towards monovalent cations.[1]

The PLS regression model parameters for the rest of the studied cations are compiled in Table 5.5. In general, these data (in particular, RMSECV values, which are given in mV/dec) imply that semi-quantitative models for the prediction of zeolite sensor sensitivity can be constructed using PLS regression. The parameters of the models assume that the best correlation is observed for ammonium and calcium.

Table 5.5. PLS regression data for all the calculated systems.

Model cation	**RMSEC**	**RMSECV**	**R^2-cal**	**R^2-val**
$NH_4^{+\,(*)}$	2.1	4.1	0.96	0.88
$Ca^{2+\,(*)}$	7.41	12.3	0.84	0.64
$Mg^{2+\,(*)}$	4.2	7.8	0.81	0.46
K^+	4.2	9.0	0.90	0.59
$Na^{+\,(d)}$	2.1	6.0	0.94	0.52

(*) without HEUs and MAP
(d) without ZSM-5

During the initial characterisation of the ISP-drawn electrodes, the sensitivities towards several transition metal cations have been recorded.[47] However, the responses towards these cations have been very low and inconsistent, and therefore no viable models have been established. These findings can be linked to the complex nature of the ion-exchange processes involving transition metal ions, which are frequently accompanied by the precipitation on the external surface of zeolites.[1]

Using the data obtained so far, good quality models for the commercially available synthetic zeolites have been generated. However, they can be further improved by including a greater number of samples used for calibration. To have clearer trends, a certain property (Si/Al ratio, Extraframework cation, Particle size) should be compared with more than two zeolites. For example, using a number of zeolites with the same framework type (e.g. BEA) but different Si/Al ratios (e.g. 5, 12, 19, 150, …). Also, the effect of the particle size, which is believed to have a significant impact on cation diffusivity, needs to be further studied with a series of laboratory-synthesised zeolites because the used commercial samples have a standardised particle size.

Since the observed variance in PCA for PC1-PC2 space is 56% and for PC3-PC4 space is 24%, additional parameters should be considered to further explain the sample response. For example, channel shape (e.g. straight in ZSM-11; sinusoidal and straight in ZSM-5) and conduction activation energies should affect the cation diffusivity and therefore the sensor performance.[53,54] Additionally, potentiometric responses for a variety of natural zeolites are required, either to enhance the performance of the existing models containing both synthetic and natural zeolites or to establish a new model specifically for natural zeolites.

5.4 Conclusions

The potentiometric response of ISP-drawn zeolite-modified electrodes, prepared using thirteen synthetic and three natural zeolites, to Na^+, K^+, NH_4^+, Ca^{2+} and Mg^{2+} in aqueous solutions is related to a range of zeolite characteristics using PCA and PLS modelling. In addition to the previously stated steric factors, such as pore size, the important features, which by and large determine the sensor performance, are the Si/Al ratio and the presence of specific extraframework cations.

For the first time, the structure-performance relationship was established for zeolite-modified electrodes in a potentiometric setup. It was concluded that physical and chemical properties impact the zeolite-modified potentiometric sensor performance. Chemometrical techniques enabled us to elucidate that K^+ and Na^+ affect the potentiometric sensitivity towards Ca^{2+}, which has not been reported so far. The level of precision attained by the models implies that semi-quantitative predictions are possible. To improve the computational models further, a larger dataset with a wider range of zeolite-modified sensors is needed. The constituent materials of such sensors should have a set of well-defined properties, which can be designed and tuned for a particular application. It can be expected that synthetic rather than natural zeolites would satisfy such requirements. Indeed, although the latter are less expensive and are available in large quantities, it is challenging to control their properties. It should be noted that the selectivities of single zeolite-modified potentiometric sensors are limited, especially as compared to the traditional ion-selective electrodes. Therefore, incorporating them into multi-sensor arrays is required to optimise the operation of such sensors. This should ultimately lead to the improvement of multi-sensor array performance, both in terms of sensitivity and selectivity, in a range of analytical applications, including among many others agriculture, environmental monitoring and food science.

5.5 References

1. *Introduction to Zeolite Science and Practice*. (eds. Cejka, J., van Bekkum, H., Corma, A. & Schuth, F.) (Elsevier Science, 2007).

2. Xu, X., Wang, J. & Long, Y. Zeolite-based materials for gas sensors. *Sensors* **6**, 1751–1764 (2006).

3. Zheng, Y., Li, X. & Dutta, P. K. Exploitation of unique properties of zeolites in the development of gas sensors. *Sensors* **12**, 5170–5194 (2012).

4. Sahner, K., Hagen, G., Schönauer, D., Reiß, S. & Moos, R. Zeolites - Versatile materials for gas sensors. *Solid State Ionics* **179**, 2416–2423 (2008).

5. Talapaneni, S. N., Grand, J., Thomas, S., Ahmad, H. A. & Mintova, S. Nanosized Sn-MFI zeolite for selective detection of exhaust gases. *Mater. Des.* **99**, 574–580 (2016).

6. Yang, P., Ye, X., Lau, C., Li, Z., Liu, X. & Lu, J. Design of Efficient Zeolite Sensor Materials for n-Hexane. *Anal. Chem.* **79**, 1425–1432 (2007).

7. Walcarius, A. Zeolite-modified electrodes in electroanalytical chemistry. *Anal. Chim. Acta* **384**, 1–16 (1999).

8. Walcarius, A. Electroanalytical applications of microporous zeolites and mesoporous (organo)silicas: Recent trends. *Electroanalysis* **20**, 711–738 (2008).

9. Rolison, D. R. Zeolite-Modified Electrodes and Electrode-Modified Zeolites. *Chem. Rev.* **90**, 867–878 (1990).

10. Jansen, J. C., Stocker, M., Karge, H. G. & Weitkamp, J. *Advanced zeolite science and applications*. (eds. Jansen, J. C., Stocker, M., Karge, H. G. & Weitkamp, J.) (Elsevier, 1994).

11. Durst, R. A., Bäumner, A. J., Murray, R. W., Buck, R. P. & Andrieux, C. P. Chemically modified electrodes: Recommended terminology and definitions. *Pure Appl. Chem.* **69**, 1317–1323 (1997).

12. Walcarius, A., Ganesan, V., Larlus, O. & Valtchev, V. Low temperature synthesis of zeolite films on glassy carbon: Towards designing molecularly selective electrochemical devices. *Electroanalysis* **16**, 1550–1554 (2004).

13. Evmiridis, N. P., Demertzis, M. A. & Vlessidis, A. G. Effect of treatment of synthetic zeolite-polymer membranes on their electrochemical-potential response characteristics. *Fresenius. J. Anal. Chem.* **340**, 145–152 (1991).

14. Johansson, G. & Risinger, L. A cesium-selective electrode prepared from a crystalline Synthetic zeolite of the mordenite type. *Anal. Chim. Acta* **119**, 25–32 (1980).

15. Matysik, S., Matysik, F. M., Mattusch, J. & Einicke, W. D. Application of Zeolite-Polydimethylsiloxane Electrodes to Potentiometric Studies of Cationic Species. *Electroanalysis* **10**, 98–102 (1998).

16. Barrer, R. M. & James, S. D. Electrochemistry of crystal-polymer membranes. Part II. Membrane potentials. *J. Phys. Chem.* **64**, 421–427 (1960).

17. Walcarius, A. Zeolite-modified paraffin-impregnated graphite electrode. *J. Solid State Electrochem.* **10**, 469–478 (2006).

18. Walcarius, A., Vromman, V. & Bessiere, J. Flow injection indirect amperometric detection of ammonium ions using a clinoptilolite-modified electrode. *Sensors Actuators, B Chem.* **56**, 136–143 (1999).

19. Wang, J. & Walcarius, A. Zeolite-modified carbon paste electrode for selective monitoring of dopamine. *J. Electroanal. Chem.* **407**, 183–187 (1996).

20. Marshall, C. E. *The use of zeolitic membrane electrodes*. (1939).

21. Sohrabnejad, S., Zanjanchi, M. A., Arvand, M. & Mousavi, M. F. Evaluation of a PVC-based thionine-zeolite and zeolite free membranes as sensing elements in ion selective electrode. *Electroanalysis* **16**, 1033–1037 (2004).

22. Maximiano, E. M., de Lima, F., Cardoso, C. A. L. & Arruda, G. J. Modification of carbon paste electrodes with recrystallized zeolite for simultaneous quantification of thiram and carbendazim in food samples and an agricultural formulation. *Electrochim. Acta* **259**, 66–76 (2018).

23. Azizi, S. N., Ghasemi, S. & Amiripour, F. Nickel/P nanozeolite modified electrode: A new sensor for the detection of formaldehyde. *Sensors Actuators, B Chem.* **227**, 1–10 (2016).

24. Hashemi, H. S., Nezamzadeh-Ejhieh, A. & Karimi-Shamsabadi, M. A novel cysteine

sensor based on modification of carbon paste electrode by Fe(II)-exchanged zeolite X nanoparticles. *Mater. Sci. Eng. C* **58**, 286–293 (2016).

25. Nezamzadeh-Ejhieh, A. & Hashemi, H. S. Voltammetric determination of cysteine using carbon paste electrode modified with Co(II)-Y zeolite. *Talanta* **88**, 201–208 (2012).

26. Baker, M. D., Senaratne, C. & Zhang, J. Effects of Supporting Electrolyte and Zeolite Co-cations on the Electrochemical Response of Zeolite-modified Electrodes. *J. Chem. Soc., Faraday Trans* **88**, 3187–3192 (1992).

27. Walcarius, A., Lumberts, L. & Derouane, E. G. Cation determination in aqueous solution using the methyl viologen-doped zeolite-modified carbon paste electrode. *Electroanalysis* **7**, 120–128 (1995).

28. Kilinc Alpat, S., Yuksel, U. & Akcay, H. Development of a novel carbon paste electrode containing a natural zeolite for the voltammetric determination of copper. *Electrochem. commun.* **7**, 130–134 (2005).

29. Nezamzadeh-Ejhieh, A. & Badri, A. Surfactant modified ZSM-5 zeolite as an active component of membrane electrode towards thiocyanate. *Desalination* **281**, 248–256 (2011).

30. Hasheminejad, M. & Nezamzadeh-Ejhieh, A. A novel citrate selective electrode based on surfactant modified nano-clinoptilolite. *Food Chem.* **172**, 794–801 (2015).

31. Siara, L. R., De Lima, F., Cardoso, C. A. L. & Arruda, G. J. Electrochemically pretreated zeolite-modified carbon-paste electrodes for determination of linuron in an agricultural formulation and water. *Electrochim. Acta* **151**, 609–618 (2015).

32. Dong, J., Zhou, X., Zhao, H., Xu, J. & Sun, Y. Reagentless amperometric glucose biosensor based on the immobilization of glucose oxidase on a ferrocene@NaY zeolite composite. *Microchim. Acta* **174**, 281–288 (2011).

33. Walcarius, A., Barbaise, T. & Bessiere, J. Factors affecting the analytical applications of zeolite-modified electrodes preconcentration of electroactive species. *Anal. Chim. Acta* **340**, 61–76 (1997).

34. Walcarius, A. Factors affecting the analytical applications of zeolite modified electrodes: Indirect detection of nonelectroactive cations. *Anal. Chim. Acta* **388**, 79–91

(1999).

35. Kirsanov, D., Mukherjee, S., Pal, S., Ghosh, K., Bhattacharyya, N., Bandyopadhyay, R., Jendrlin, M., Radu, A., Zholobenko, V., Dehabadi, M. & Legin, A. A Pencil-Drawn Electronic Tongue for Environmental Applications. *Sensors 2021, Vol. 21, Page 4471* **21**, 4471 (2021).

36. Rolison, D. R., Nowak, R. J., Welsh, T. A. & Murray, C. G. Analytical implications of zeolites in overlayers at electrodes. *Talanta* **38**, 27–35 (1991).

37. Li, J. P., Peng, T. Z. & Fang, C. Screen-printable sol-gel ceramic carbon composite pH sensor with a receptor zeolite. *Anal. Chim. Acta* **455**, 53–60 (2002).

38. Senthilkumar, S., King, A. J., Holmes, S. M., Dryfe, R. A. W. & Saraswathi, R. Potentiometric sensing of heavy metal ions using a novel zeolite Y membrane. *Electroanalysis* **18**, 2297–2304 (2006).

39. Hamlaoui, M. L., Kherrat, R., Marrakchi, M., Jaffrezic-Renault, N. & Walcarius, A. Development of an ammonium ISFET sensor with a polymeric membrane including zeolite. *Mater. Sci. Eng. C* **21**, 25–28 (2002).

40. Hamlaoui, M. L., Reybier, K., Marrakchi, M., Jaffrezic-Renault, N., Martelet, C., Kherrat, R. & Walcarius, A. Development of a urea biosensor based on a polymeric membrane including zeolite. *Anal. Chim. Acta* **466**, 39–45 (2002).

41. King, A. J., Lillie, G. C., Cheung, V. W. Y., Holmes, S. M. & Dryfe, R. A. W. Potentiometry in aqueous solutions using zeolite films. *Analyst* **129**, 157–160 (2004).

42. Arvand-Barmchi, M., Mousavi, M. F., Zanjanchi, M. A. & Shamsipur, M. A PTEV-based zeolite membrane potentiometric sensor for cesium ion. *Sensors Actuators, B Chem.* **96**, 560–564 (2003).

43. Arvand, M., Moghimi, M. & Bagherinia, M. A. Zeolite-modified sol-gel electrode as an electrochemical sensor for potentiometric determination of cesium ions in water samples. *Anal. Lett.* **42**, 393–408 (2009).

44. Giahi, M., Aghaie, H., Arvand, M. & Hejri, A. M. Application of a zeolite-poly(vinyl chloride) electrode to potentiometric studies of alkali metal ions. *Russ. J. Electrochem.* **41**, 1290–1295 (2005).

45. Al-Ani, A., Darton, R. J., Sneddon, S. & Zholobenko, V. Nanostructured Zeolites: The Introduction of Intracrystalline Mesoporosity in Basic Faujasite-type Catalysts. *ACS Appl. Nano Mater.* **1**, 310–318 (2017).

46. Zholobenko, V., Freitas, C., Jendrlin, M., Bazin, P., Travert, A. & Thibault-Starzyk, F. Probing the acid sites of zeolites with pyridine: Quantitative AGIR measurements of the molar absorption coefficients. *J. Catal.* **385**, 52–60 (2020).

47. Jendrlin, M., Khumngern, S., Numnuam, A., Thavarungkul, P., Kanatharana, P., Kirsanov, D., Zholobenko, V. L., Mendecki, L. & Radu, A. Ion sensing pencil: Draw your own sensor. *Sensors Actuators, B Chem.* **337**, 129751 (2021).

48. Wang, Q., Gao, Q., Gao, X. & Nie, F. Angle Principal Component Analysis. in *Angle Principal Component Analysis* 2936–2942 (2017).

49. Wold, S., Sjöström, M. & Eriksson, L. PLS-regression: A basic tool of chemometrics. in *Chemometrics and Intelligent Laboratory Systems* vol. 58 109–130 (Elsevier, 2001).

50. Treacy, M. M. J. & Higgins, J. B. Collection of Simulated XRD Powder Patterns for Zeolites Fifth (5th) Revised Edition. *Collect. Simulated XRD Powder Patterns Zeolites Fifth Revis. Ed.* (2007) doi:10.1016/B978-0-444-53067-7.X5470-7.

51. Baerlocher, C., Mccusker, L. B. & Olson, D. H. *Atlas of Zeolite Framework types*. (Elsevier, 2007).

52. Zholobenko, V. L., Dwyer, J., Zhang, R., Chapple, A. P., Rhodes, N. P. & Stuart, J. A. Structural transitions in zeolite P An in situ FTIR study. *J. Chem. Soc. Faraday Trans.* **94**, 1779–1781 (1998).

53. Kelemen, G. & Schön, G. Ionic conductivity in dehydrated zeolites. *J. Mater. Sci.* **27**, 6036–6040 (1992).

54. Ajayi, O. A., Adefila, S. S. & Ityokumbul, M. T. Organic template free synthesis of ZSM11 from kaolinite clay. *Niger. J. Technol.* **36**, 444 (2017).

Chapter 6

Conclusions and future work recommendations

6.1 Conclusions

The main objective of this study has been preparation, characterisation and performance evaluation of zeolite-based sensors. Zeolites have been utilised for the detection of gaseous environmental pollutants using FTIR spectroscopy and for the potentiometric detection of cations in water solutions.

Environmental monitoring of pollutants, such as NO_x and CO_x, which can be facilitated by a range of gas sensors, is of considerable fundamental and practical importance. Sensors containing NaX, NaY, MOR, FER, BEA-12, BEA-19, ZSM-5, Sn-BEA and dealuminated BEA zeolites have been prepared and extensively characterised by IR, DR UV-VIS and NMR spectroscopy, XRD, TGA and N_2 adsorption-desorption. To obtain an environmental CO sensor, copper was introduced into zeolites by ion exchange and impregnation methods. The latter method allowed much higher Cu-loadings and was therefore utilised for screening potential sensors. Even though the Cu^+ yields were lower than the ion-exchanged counterpart, the total number of available Cu^+ species was higher. Sensors were then exposed to CO (1 mbar in vacuo). All the samples showed response to CO in the 2200-2100 cm^{-1} region. Zeolites MOR and BEA-19 demonstrated the highest sensitivities and Cu^+/Cu ratios due to their channel network and intermediate Si/Al ratio. Therefore, these samples were chosen for further applicability experiments, but since the water adsorption presented a significant problem to sensor performance of Cu-containing MOR sample, more a hydrophobic zeolite Sn-BEA was impregnated by $Cu(NO_3)_2$ solution and chosen in an attempt to optimise the CO sensor.

Furthermore, the non-Cu-impregnated Sn-BEA was also utilised as a gas sensor. The Sn-BEA material has demonstrated a nearly defect-free structure with high hydrophobicity and sub-micron particle size. Sn-BEA and DeAl-BEA have been utilised as IR-based gas sensors at room temperature, and their performance has been evaluated for the response to CO, CO_2, NO

and NO_2 in the presence of water vapours. Sn-BEA displayed a selective response to NO_2, while DeAl-BEA to both CO_2 and NO_2. The collected data demonstrate the potential of zeolite BEA based sensors to determine the current concentration of the analyte gas and the maximum concentration during a certain period.

Apart from the gas sensors, for the first time, the concept of ion sensing pencil (ISP) was demonstrated. The pencil's lead carries chemical sensing functionality and it is constructed by compression of graphite and zeolite, while the clutch was prepared by 3D printing. The ISP was used to draw a chemical sensor by simple abrasion onto a hydrophobic surface. The ISP can be stored at home, used immediately off-the-shelf without any conditioning prior to measurements. Its simple preparation, handling, and measuring protocols enabled the possibility of integration into large scale sensor networks or to be offered to the general public using readout devices already present at many homes. The chemical functionality of ISP was demonstrated by producing 14 ISPs prepared by compression of graphite and one of 14 different zeolites individually in 60:40 wt.%. These ISPs were then used to draw electrodes which were characterized in analogy to ion-selective electrodes. The ISP-drawn electrodes were utilised as a multi-sensor array for the determination of water quality in a model sample, which is the first reported case of using zeolite-based electrodes in multisystem arrays, followed by the demonstration of their potential to be used by non-trained personnel.

The work presented in the last chapter was focused on a systematic analysis of the structure – performance relationship using chemometric techniques, which can be applied to sensor arrays with varying response patterns. A set of thirteen synthetic and three natural zeolites was characterised by IR spectroscopy, SEM, TEM, EDX, XRD, TGA and N_2 adsorption-desorption. The obtained information on zeolite physical and chemical properties was related to potentiometric sensitivity of zeolite-modified electrodes in aqueous solutions of Na^+, K^+, NH_4^+, Ca^{2+} and Mg^{2+} using PCA and PLS modelling. Thus, it was demonstrated how structural

and physical properties impact the performance of zeolite-modified potentiometric sensors. In addition to steric factors, e.g. zeolite pore size, the important characteristics governing the sensor performance are the Si/Al ratio and the presence of specific extraframework cations. K^+ and Na^+ showed a strong effect on the potentiometric sensitivity towards Ca^{2+}. The level of precision achieved by the PLS models indicates that semi-quantitative predictions are feasible.

Overall, this work demonstrates the potential applications of zeolites in different types of sensors. Both gas and potentiometric sensors, as well as their precursors, have been extensively characterised. For the first time, Cu-impregnated zeolites have been utilised as room temperature CO sensors. Also, a common selective catalyst Sn-containing BEA was used as a sensor, both as-made and Cu-impregnated. The new design of zeolite-modified electrodes has been established and the biggest set of zeolites framework types utilised in potentiometric measurements. The work has also elucidated a structure-performance relationship and therefore the used chemometric techniques should become a standard method of data evaluation in all types of zeolite-modified electrodes.

6.2 Future work recommendations

6.2.1 Environment pollutant gas sensors

- Following the work presented in chapters 2 and 3, the main goals in future work on both the Cu-containing and Sn-BEA sensors should include identifying the limits of detection to determine the working concentration range. Moreover, considering that sensors would not be disposable, the maximum exposure time, reusability (number of reactivation cycles) and response repeatability should be further studied. The sample regeneration method should be established, either by using reducing gases (H_2, N_2H_4)

or high-temperature activation in vacuo. Furthermore, sensor responses and application as NDIR sensors should be evaluated.

- For Cu-containing zeolite CO sensors specifically, the important goal would be the optimisation of the copper introduction methods to maximise the Cu^{+} content, which is crucial for the sensing mechanism. Also, the introduction of other metal cations may enable sensing of other gases of interest (e.g. Ag^{+} for NO_x and Zn^{2+}, Pt^{2+} for acetone sensing).
- Preparation of nanosized Sn-BEA particles that would enable better coating and thus film consistency. Additionally, the zeolites with other atoms incorporated in the framework should be used (e.g. Zr, Ti, Hf, Mo) and their respective content in the BEA framework could be further optimised to improve the overall sensitivity.

6.2.2 Ion-sensitive pencil

- Based on the work presented in chapter 4, the local community (e.g. Staffordshire) should be engaged to conduct ISP-based Citizen Science projects. The CS projects should be inspiring and entertaining for the public while collecting a substantial amount of meaningful data for the scientists. For example, ISPs could be used as a science-popularisation tool in secondary schools, where groups of students would be given a task to draw a set of electrodes and use it to measure local water samples (e.g. wells, streams, lakes). This would be beneficial for raising awareness of the importance of natural sciences, pollution monitoring and environment preservation. At the same time, the data collected using a range of different zeolite-containing electrodes should yield a big data set that would further improve the robustness of the existing model.
- ISP-drawn electrodes should be studied using other electrochemical techniques. Bearing in mind the advances in the design of readout devices (miniaturisation, smartphone compatibility), electrochemical characterisation of portable setups should

no longer be limited to only potentiometry. Also, the multi-technique approach should be used to help with the elucidation of the ISP-drawn electrode response mechanism. For ISP-drawn electrodes to be used as long-term sensors, the water diffusion and ion transfer through the graphite-zeolite matrix should be better understood. It was observed that after the prolonged water exposure there is a signal drift and a decrease in response slope. Two hypotheses should be tested, either there is a leak of cations from the zeolite to the solution or both the cations and anions enter the zeolite-graphite matrix. To elucidate this phenomenon, electrochemical impedance spectroscopy (EIS) could be used. EIS provides information on electrode resistivity, which should decrease as both the cation and the anion enter the matrix.

- Following the work in chapter 5, the optimisation of the multi-sensor array performance should be conducted by a collection of ISP calibration data for more zeolite framework types and increasing the list of relevant physical and chemical parameters. This should enable the improvement in the prediction models and potential array composition specific for other viable applications (e.g. plant nutrients monitoring in precision agriculture). For example, if the Ca^{2+} ions are going to be monitored, the multisensor array should consist of more K-containing zeolites.

Chapter 7 Appendix

7.1 List of Figures

7.2 List of Tables

7.3 Reference samples XRD patterns

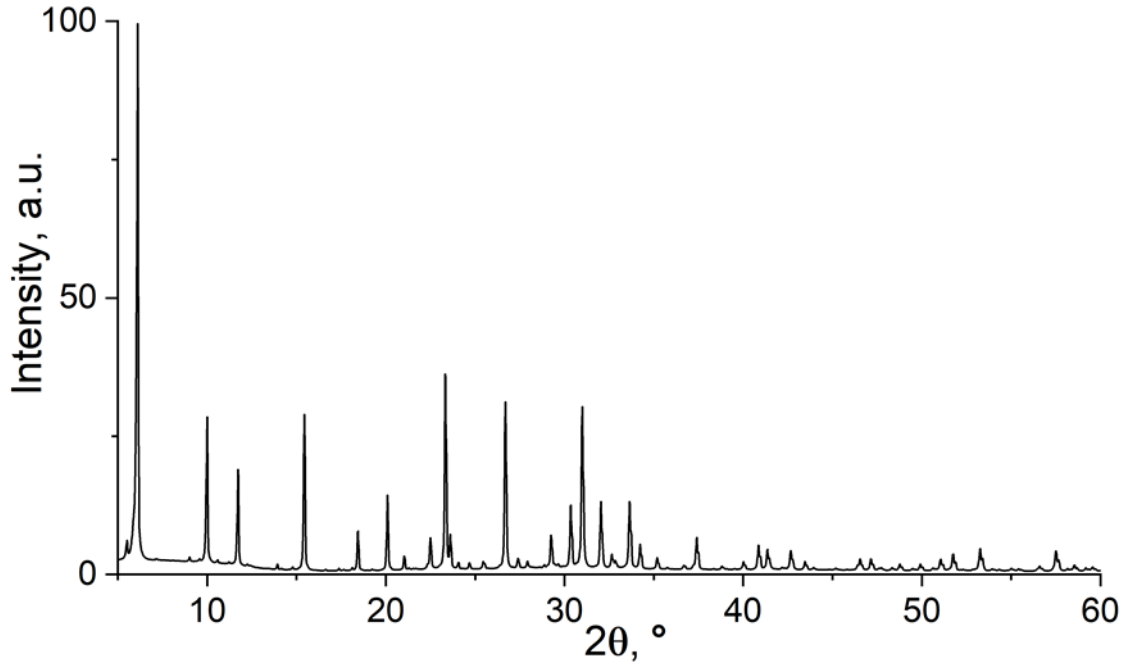

Figure 7.1. XRD pattern of NaX.

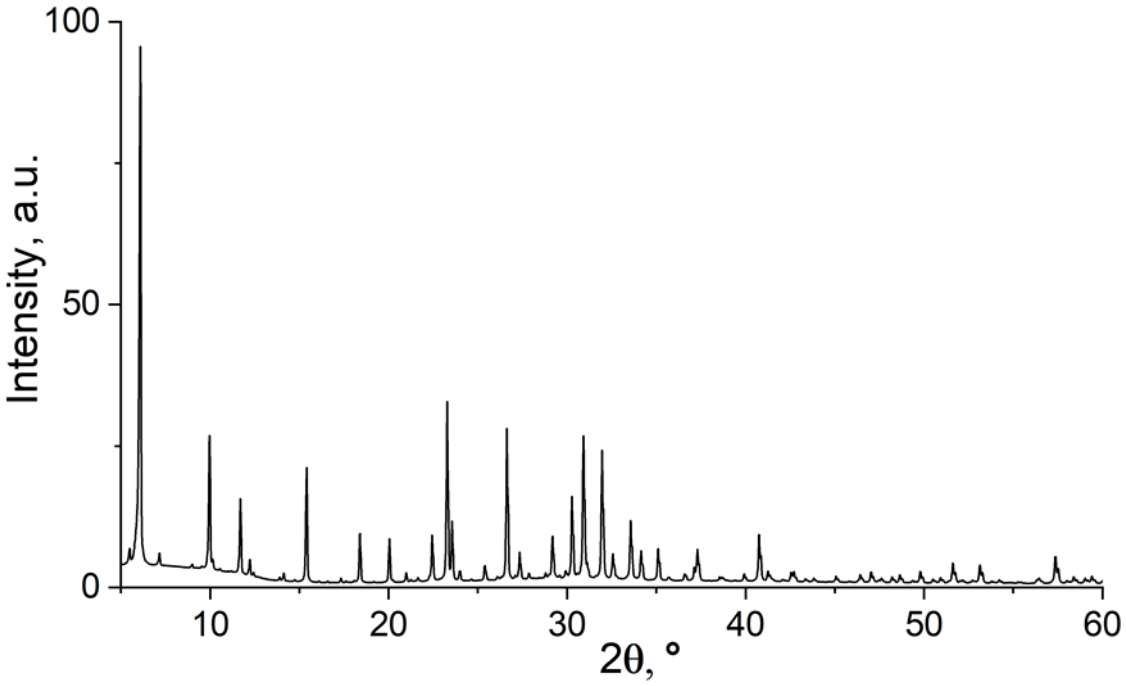

Figure 7.2. XRD pattern of KX.

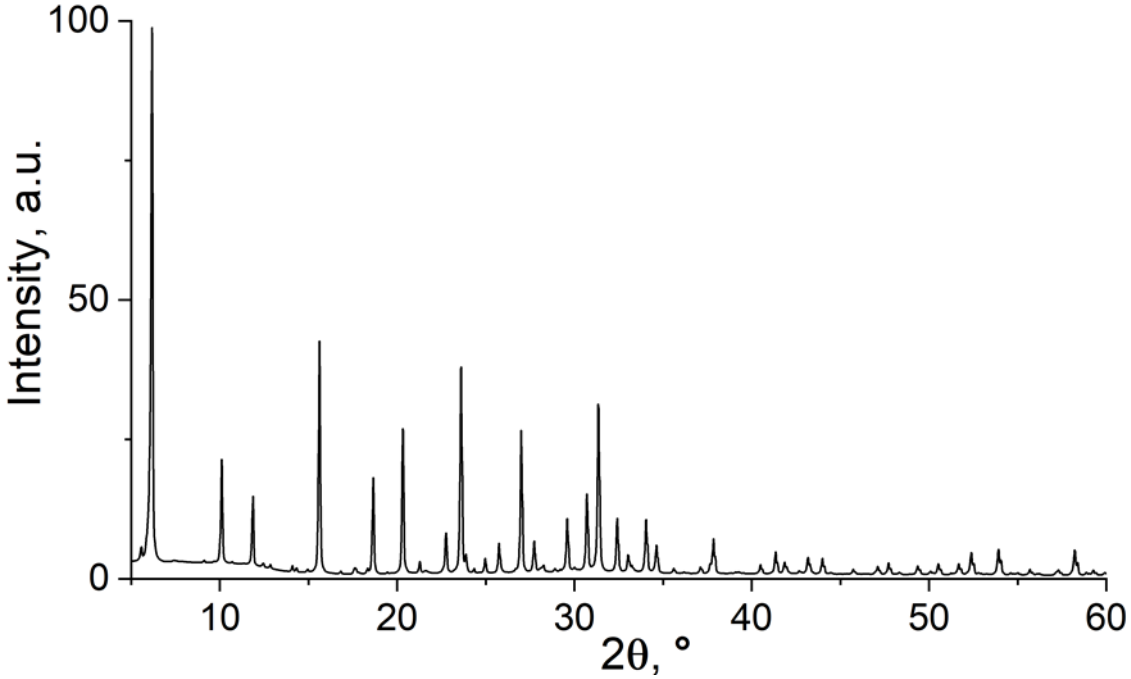

Figure 7.3. XRD pattern of NaY.

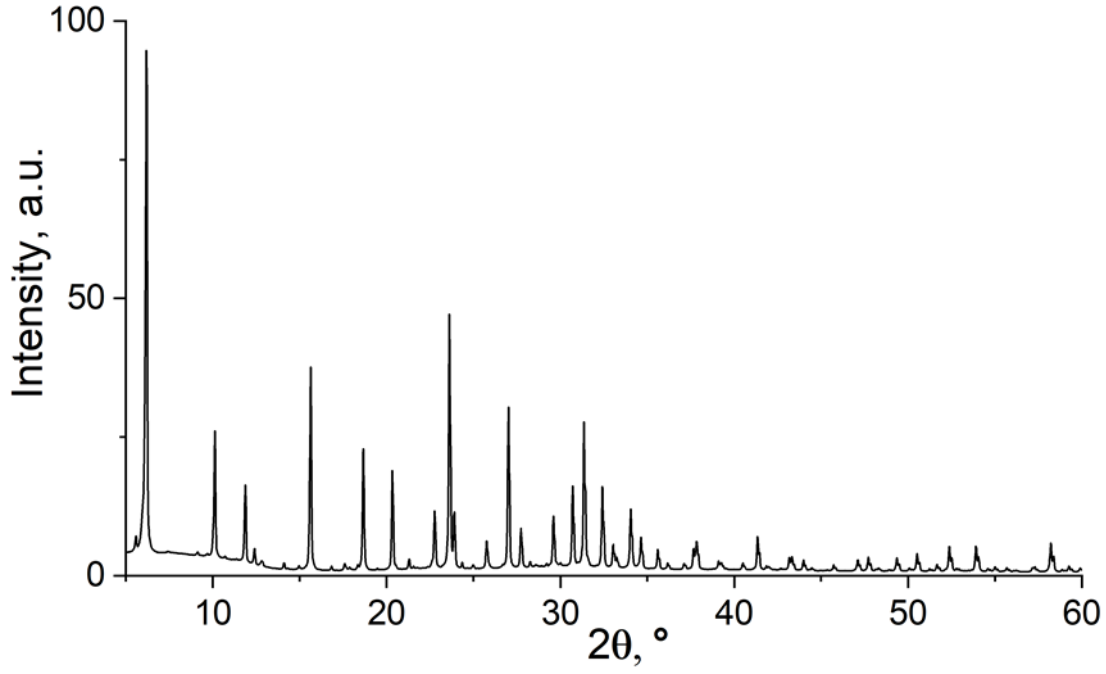

Figure 7.4. XRD pattern of KY.

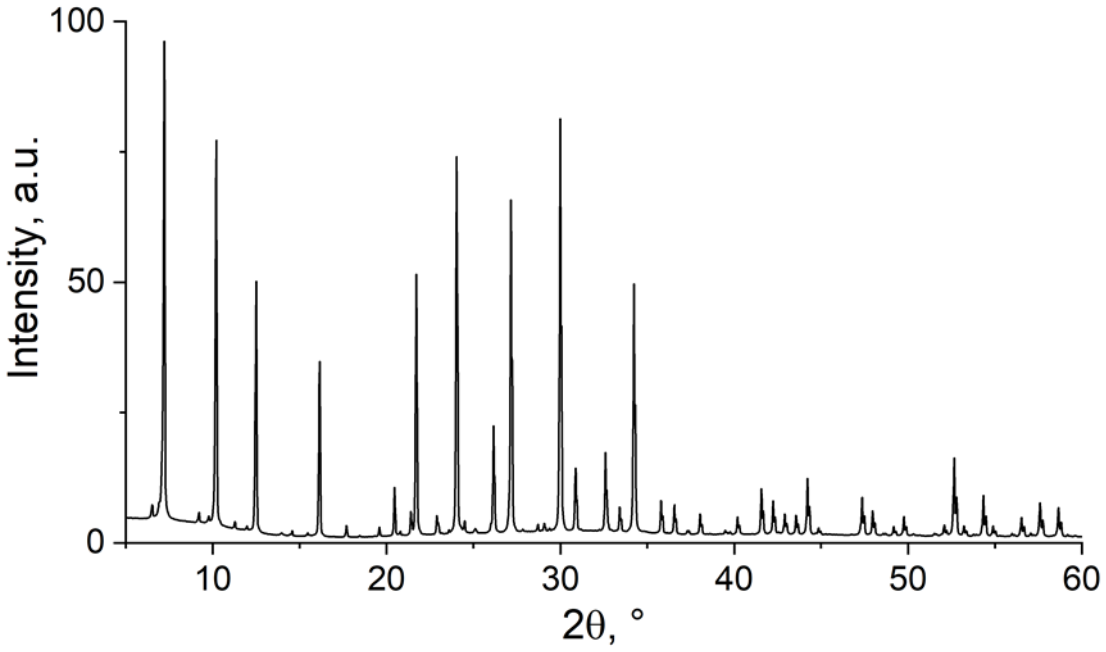

Figure 7.5. XRD pattern of NaA.

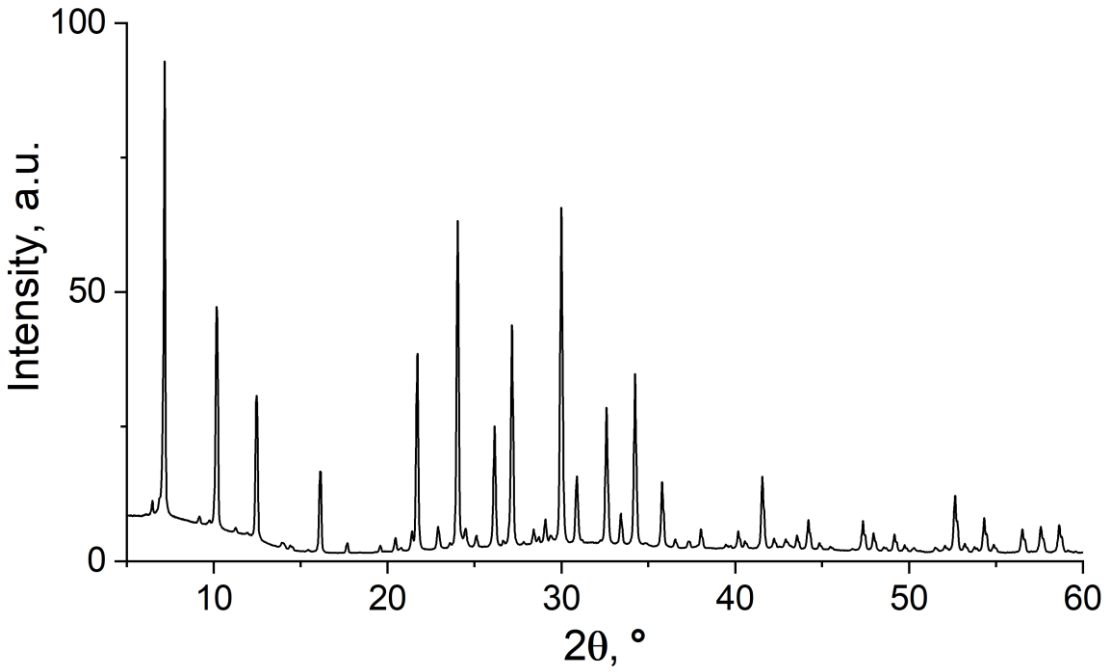

Figure 7.6. XRD pattern of KA.

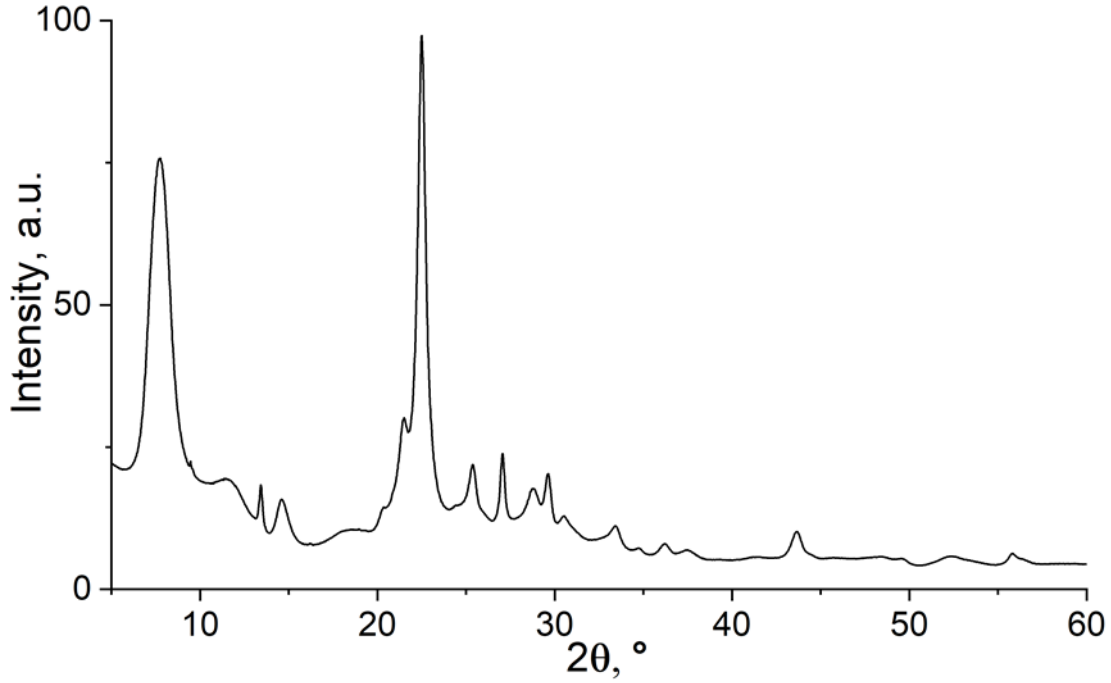

Figure 7.7. XRD pattern of BEA 12.

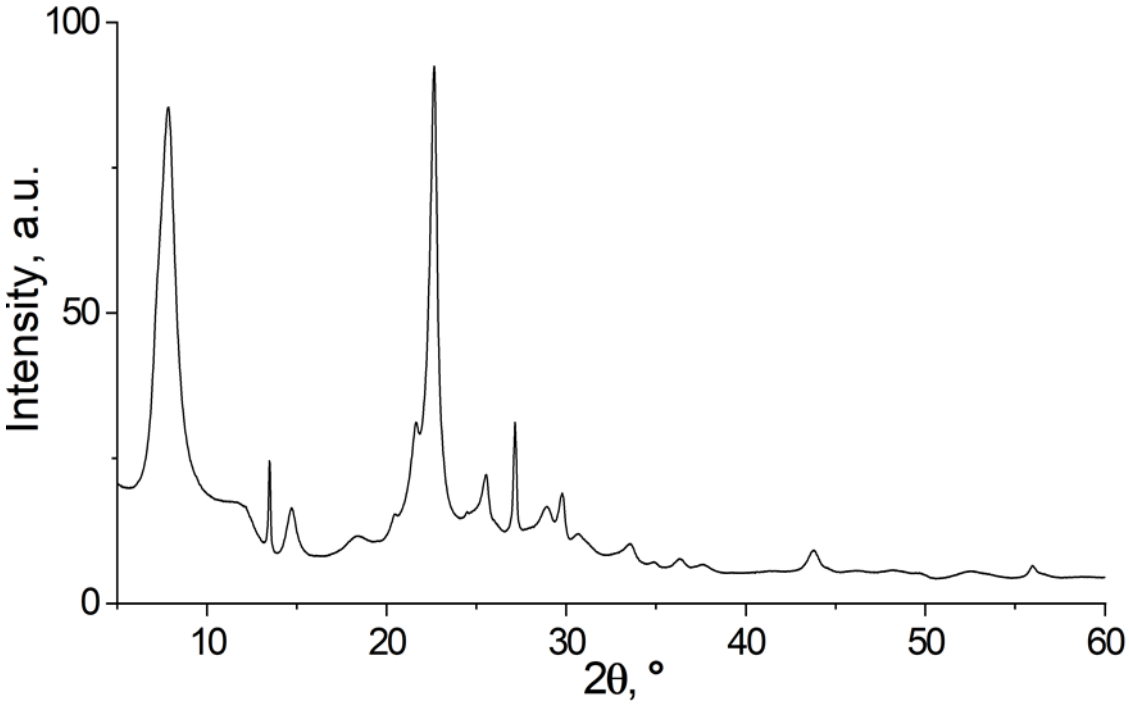

Figure 7.8. XRD pattern of BEA 19.

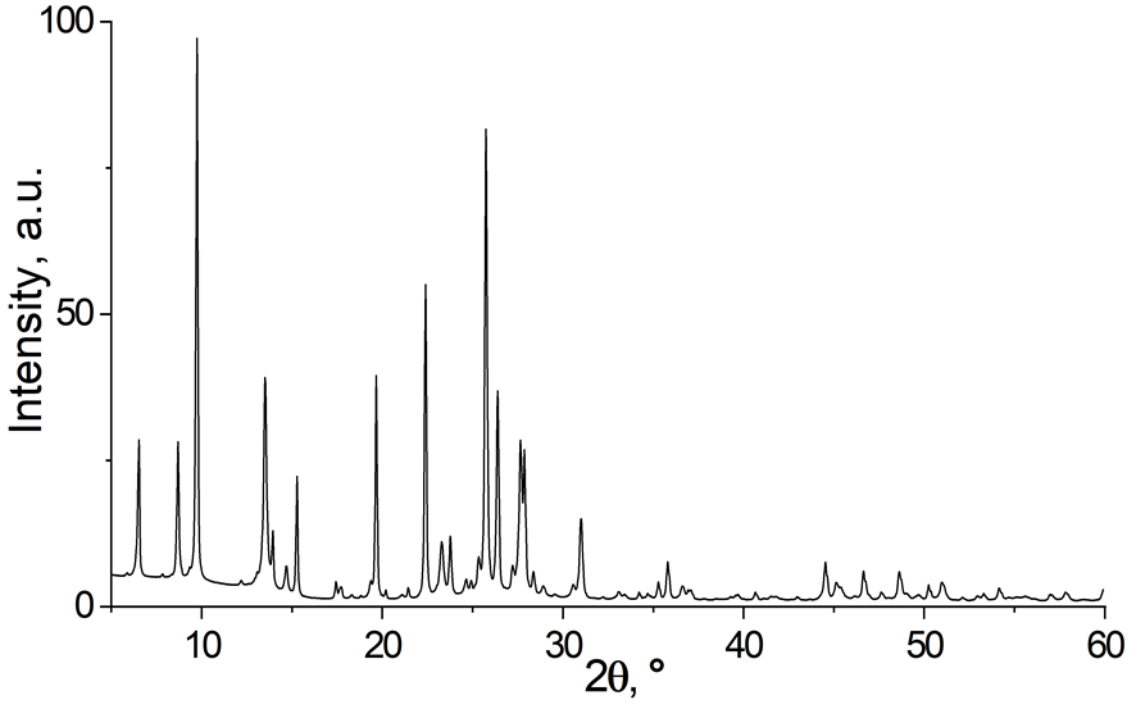

Figure 7.9. XRD pattern of MOR.

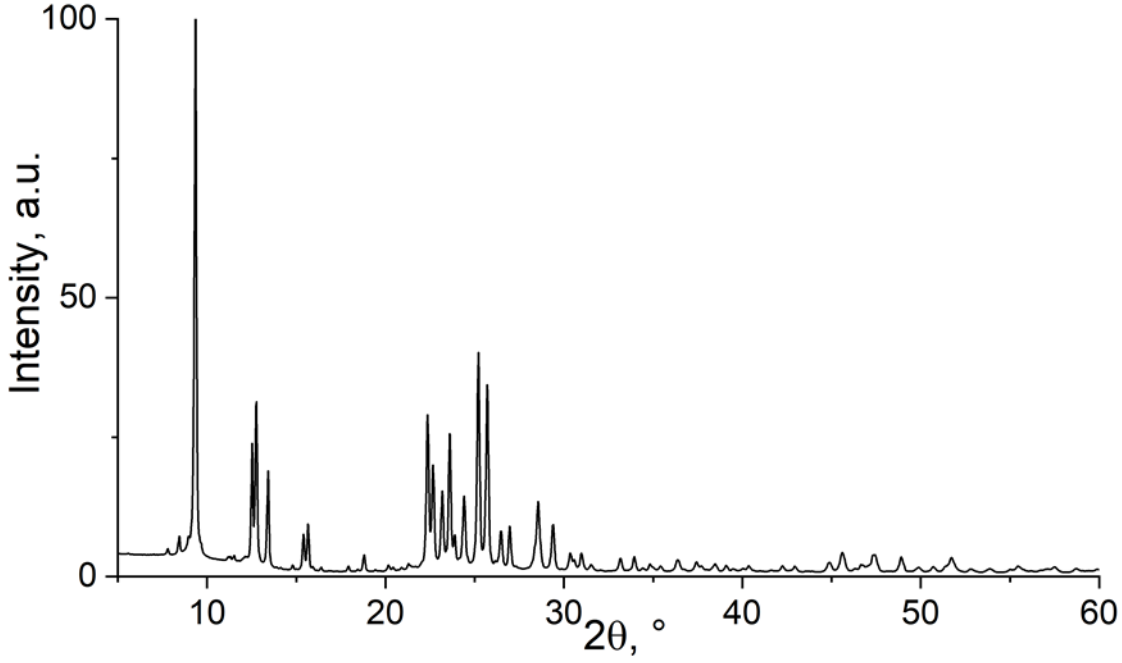

Figure 7.10. XRD pattern of FER.

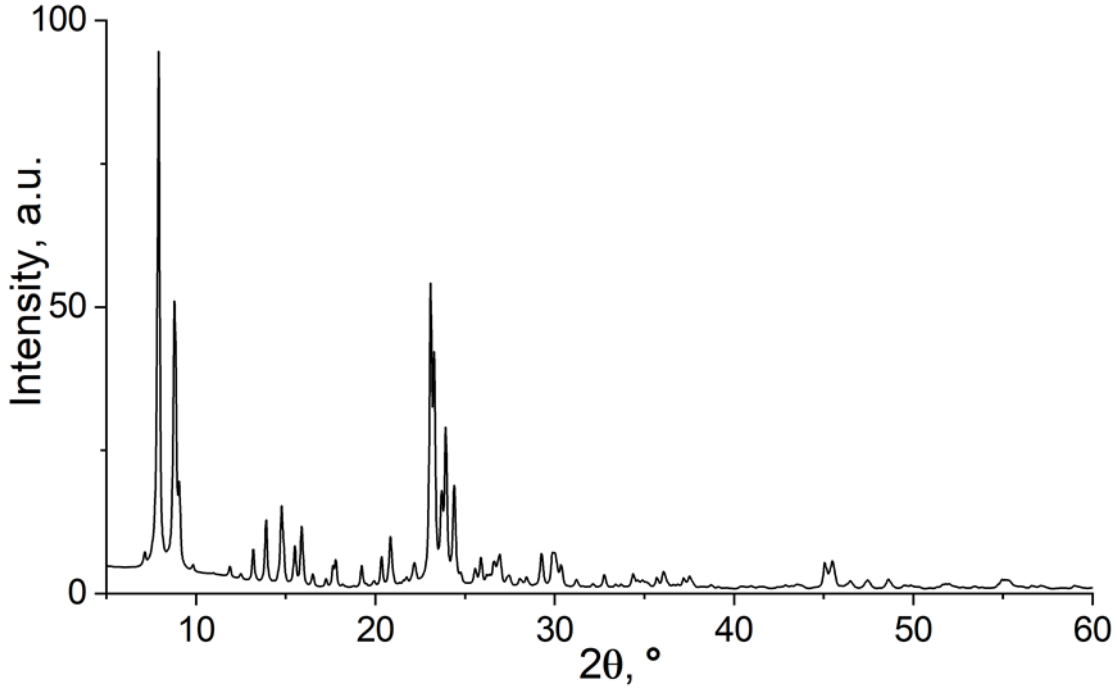

Figure 7.11. XRD pattern of ZSM-5.

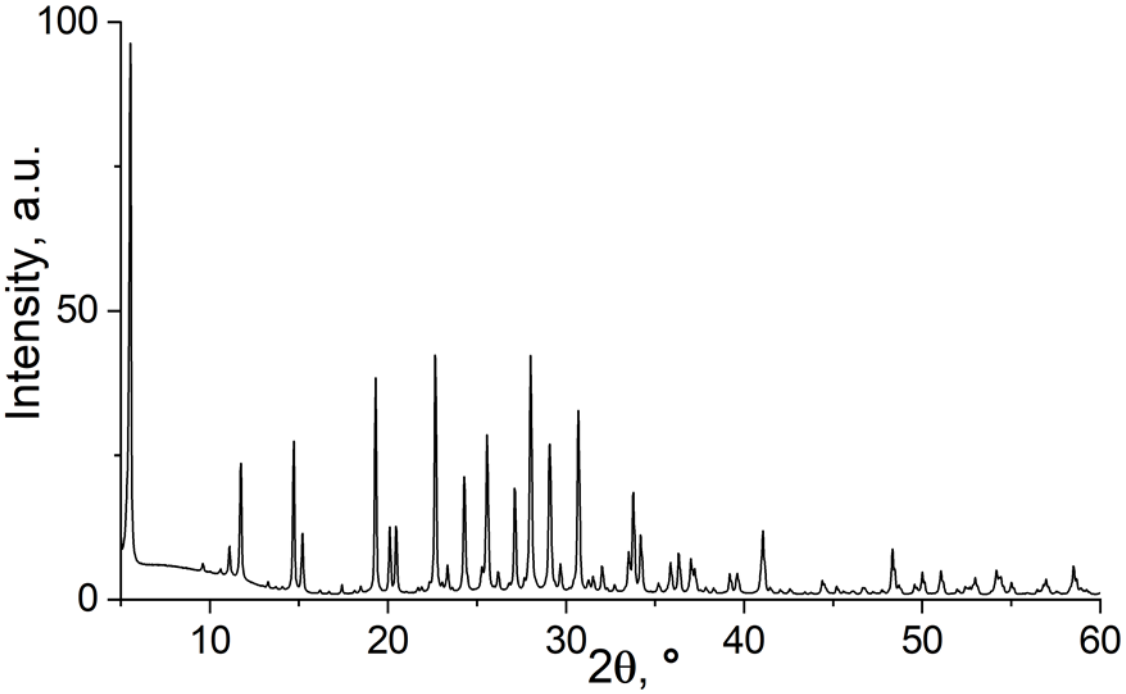

Figure 7.12. XRD pattern of K-LTL.

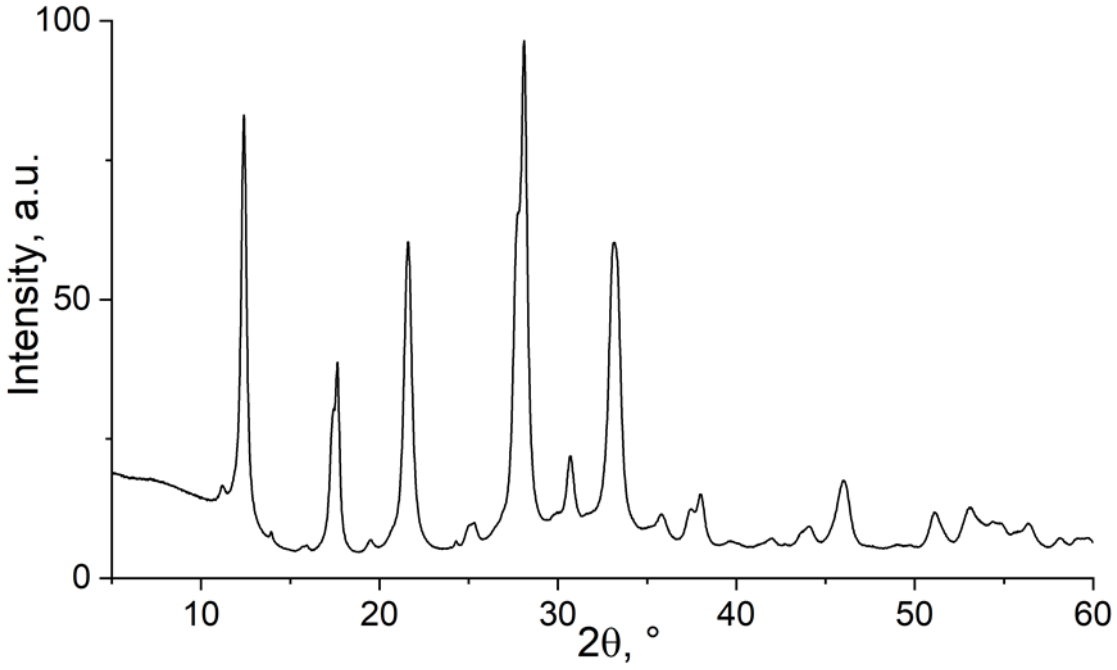

Figure 7.13. XRD pattern of MAP.

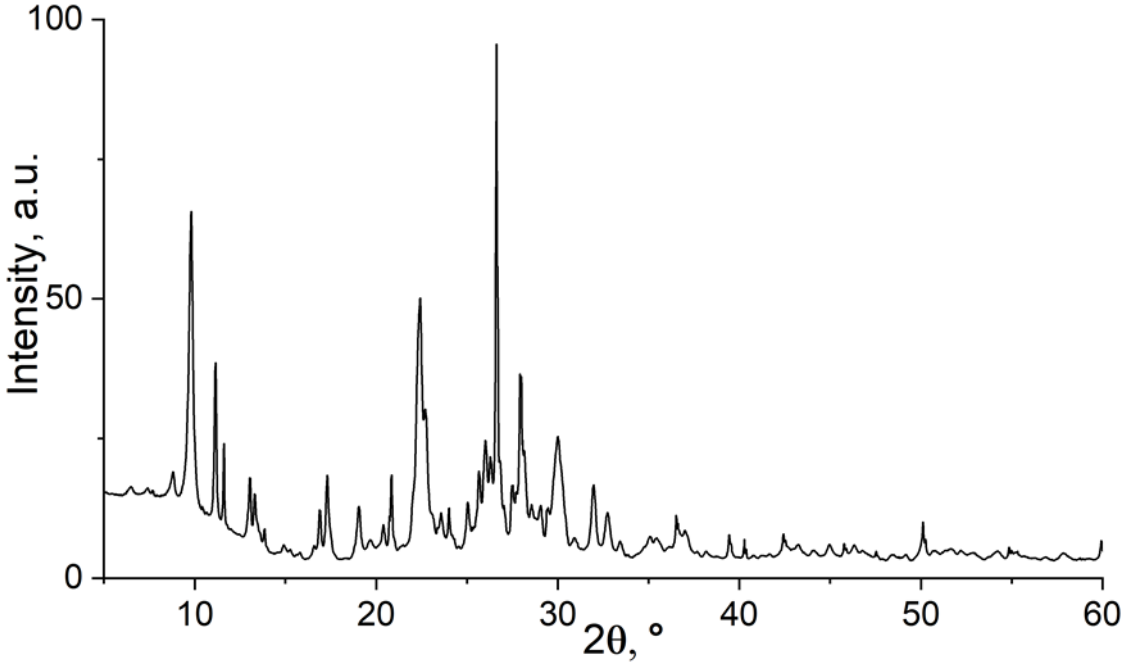

Figure 7.14. XRD pattern of HEU-A.

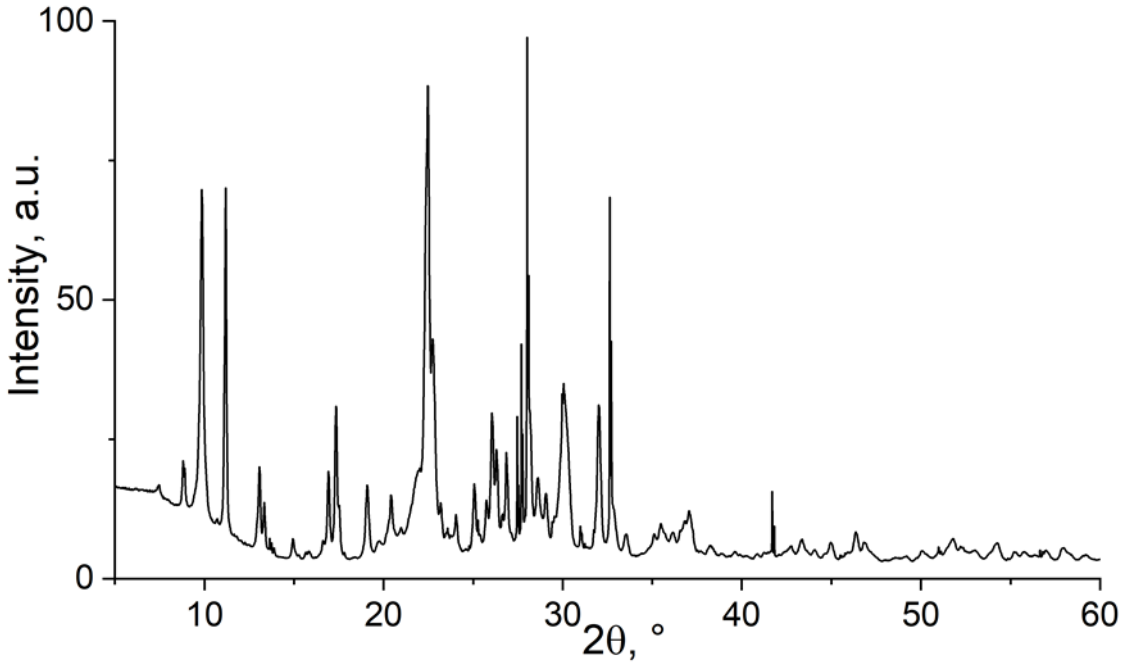

Figure 7.15. XRD pattern of HEU-B.

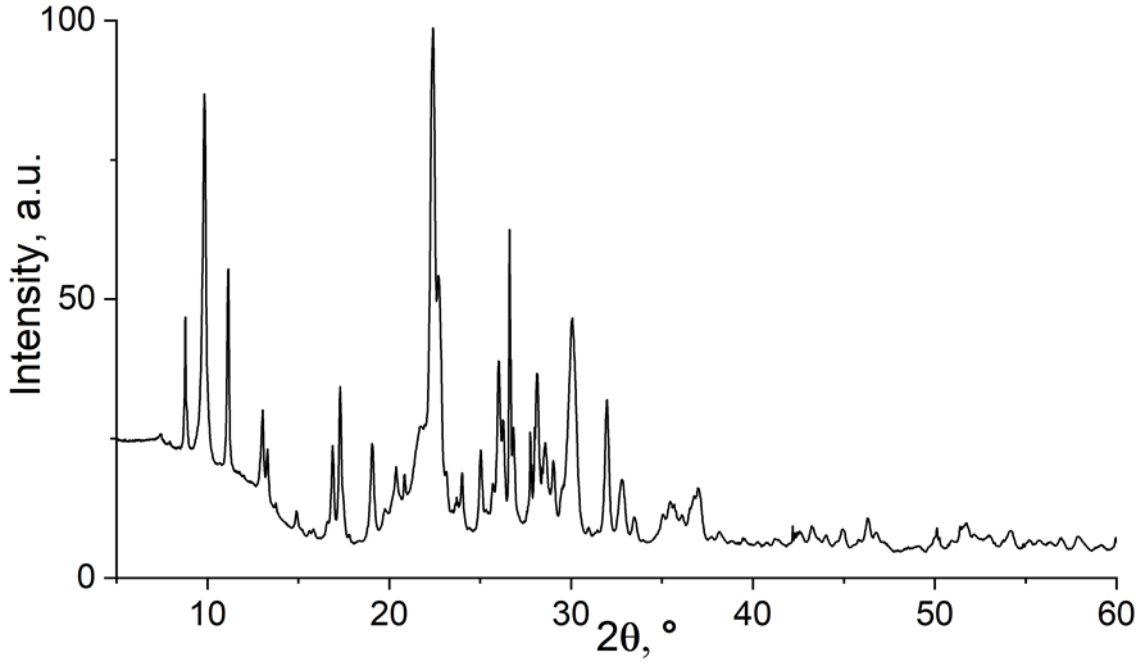

Figure 7.16. XRD pattern of HEU-C.

7.4 FTIR spectra

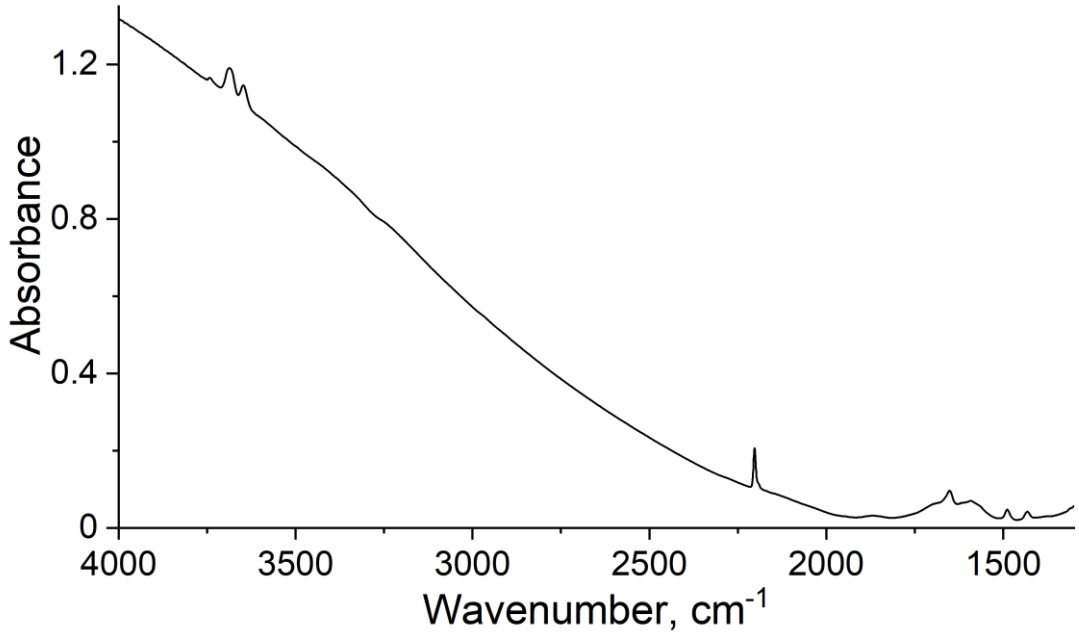

Figure 7.17. FTIR spectrum of NaX.

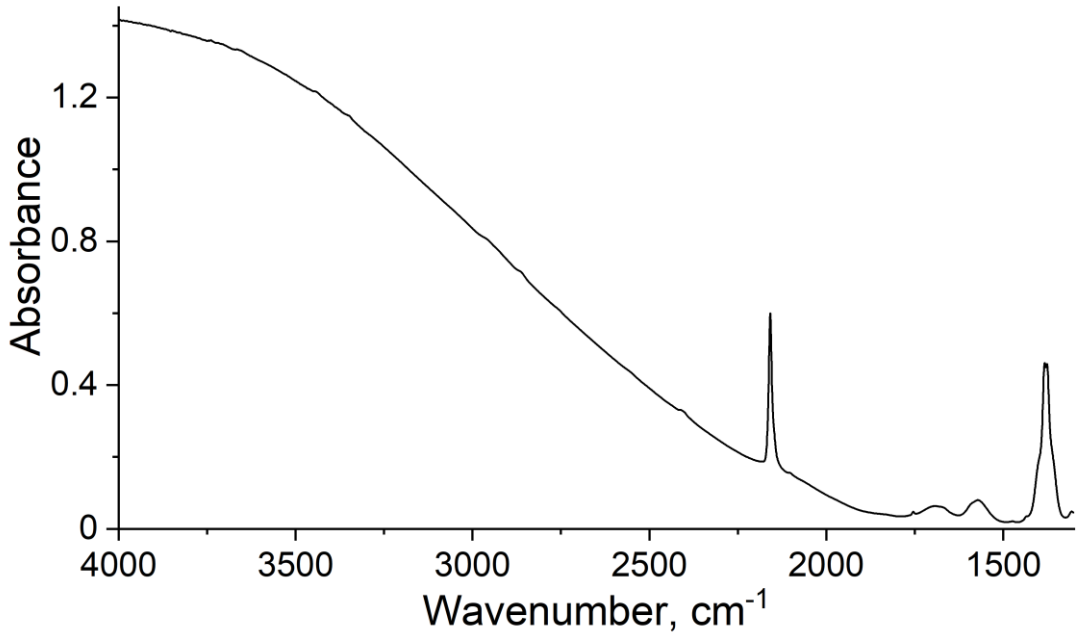

Figure 7.18. FTIR spectrum of KX.

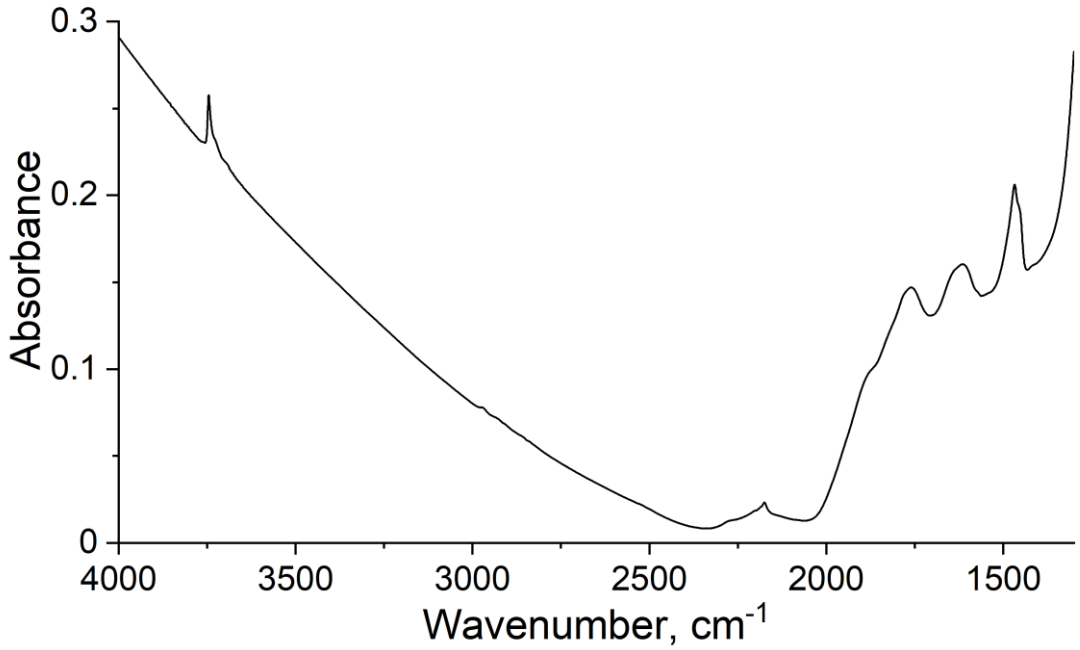

Figure 7.19. FTIR spectrum of NaY.

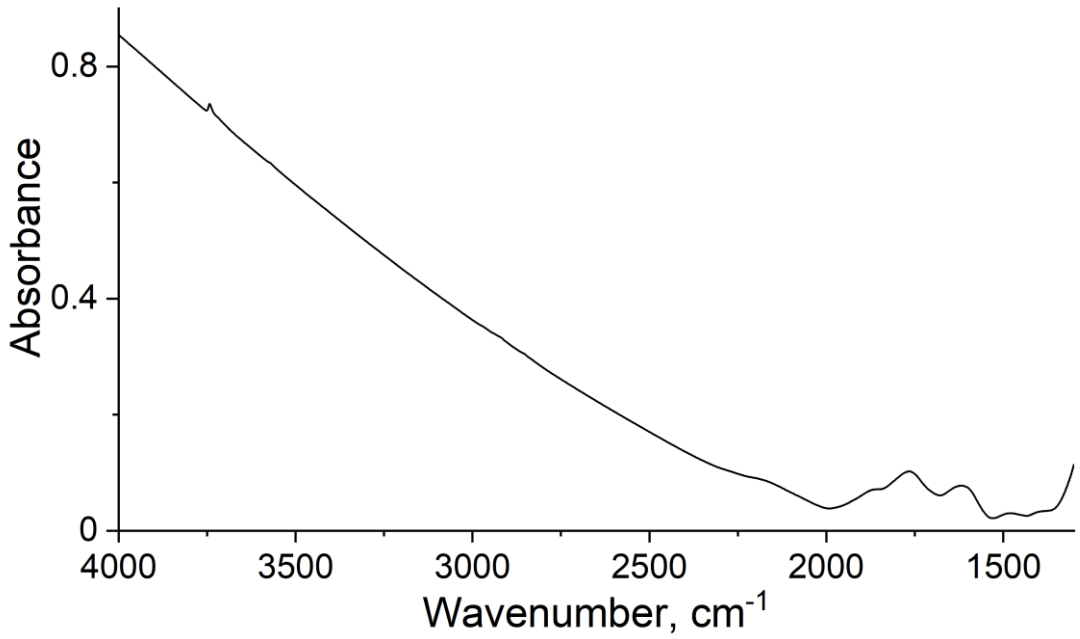

Figure 7.20. FTIR spectrum of KY.

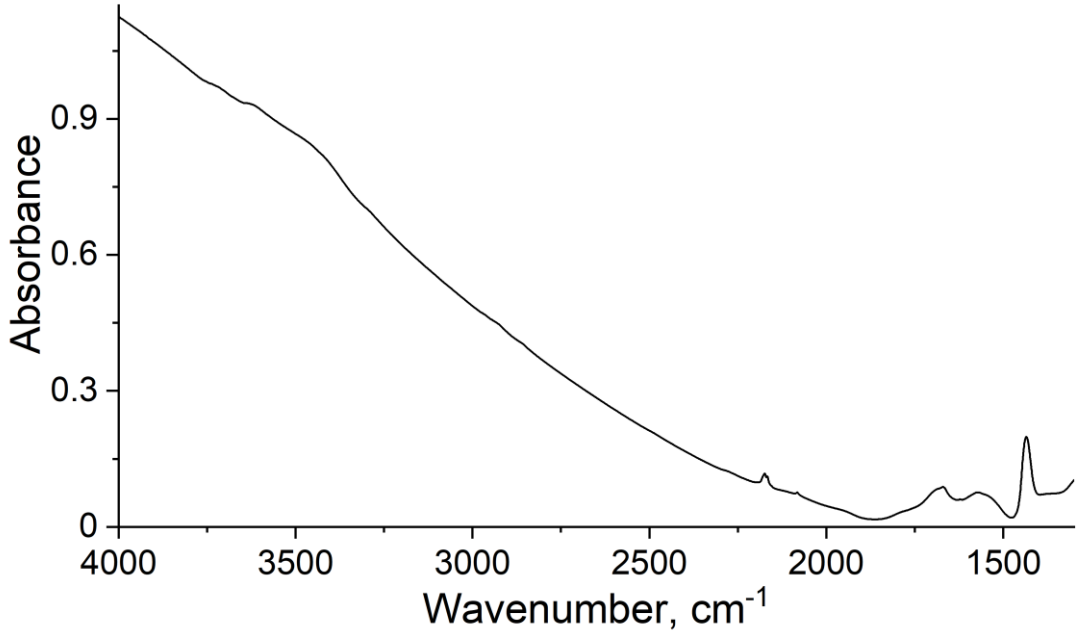

Figure 7.21. FTIR spectrum of NaA.

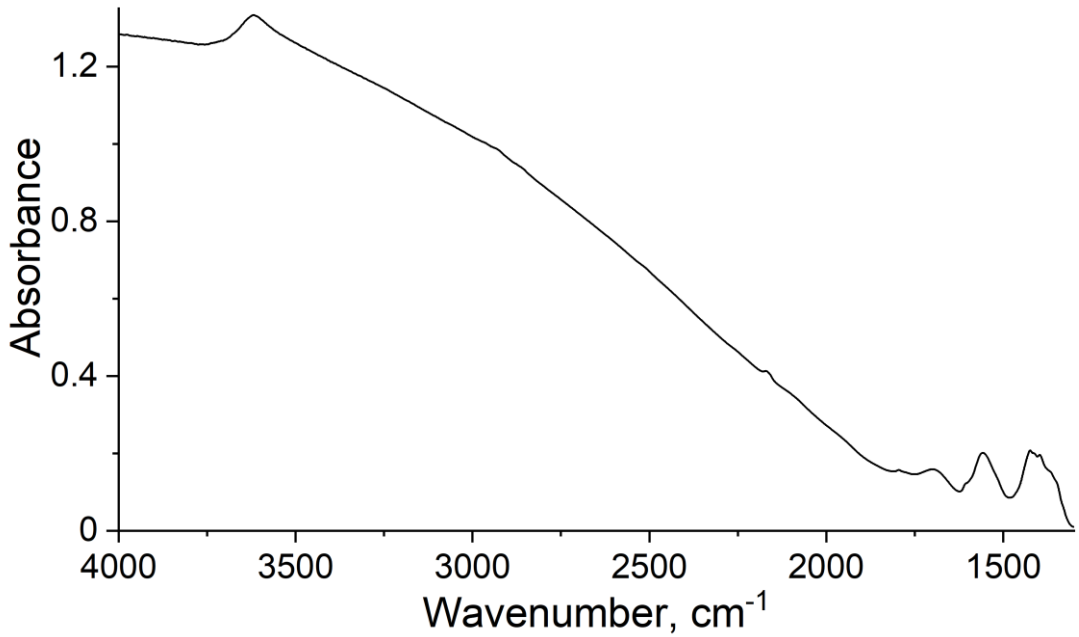

Figure 7.22. FTIR spectrum of KA.

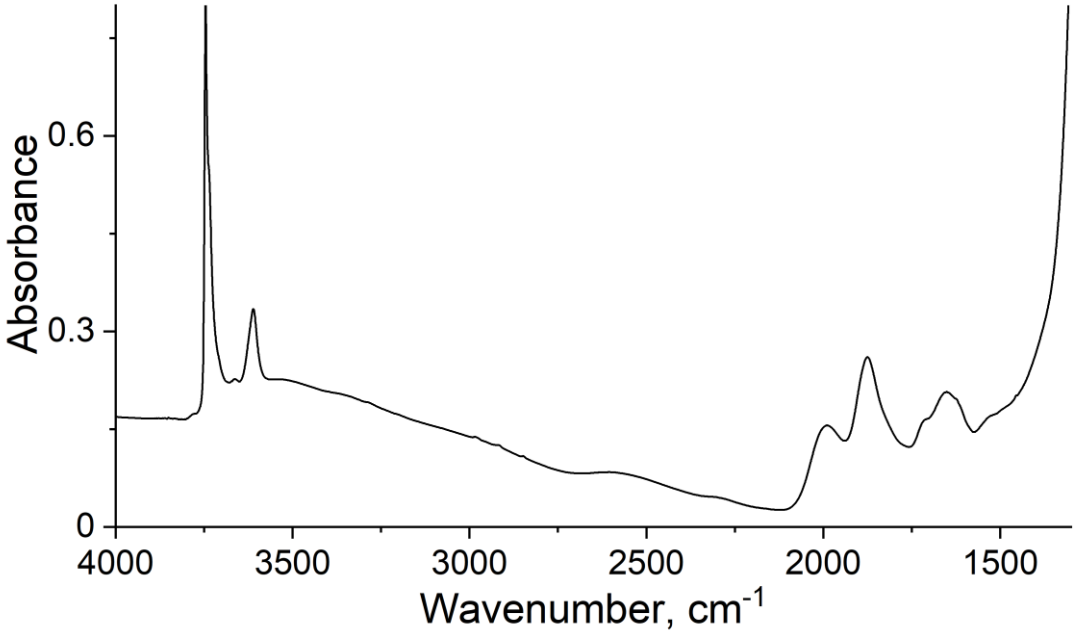

Figure 7.23. FTIR spectrum of BEA-12.

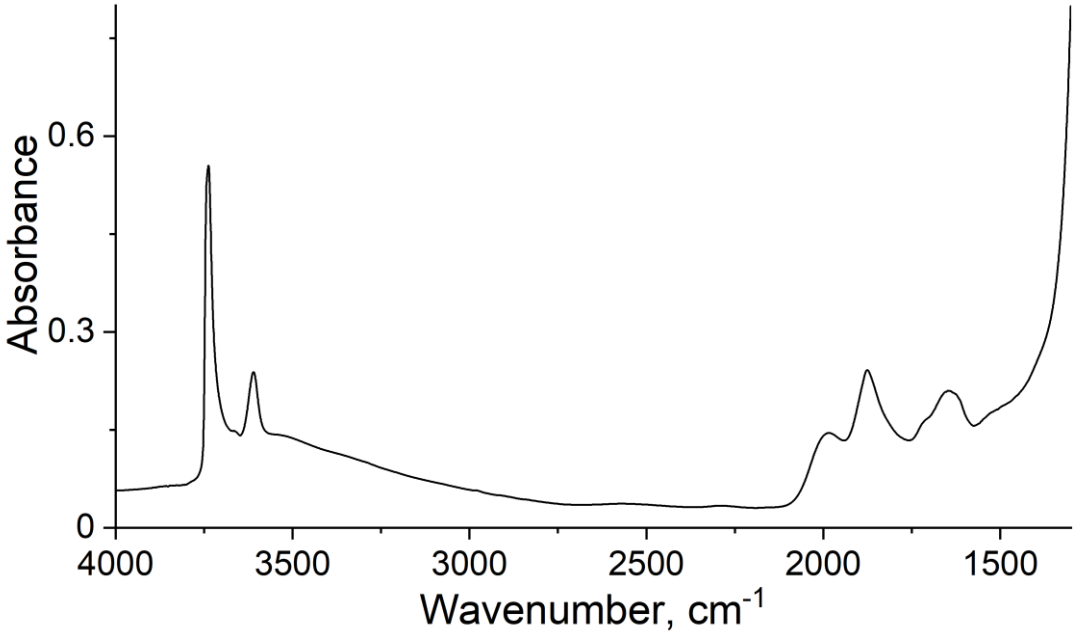

Figure 7.24. FTIR spectrum of BEA-19.

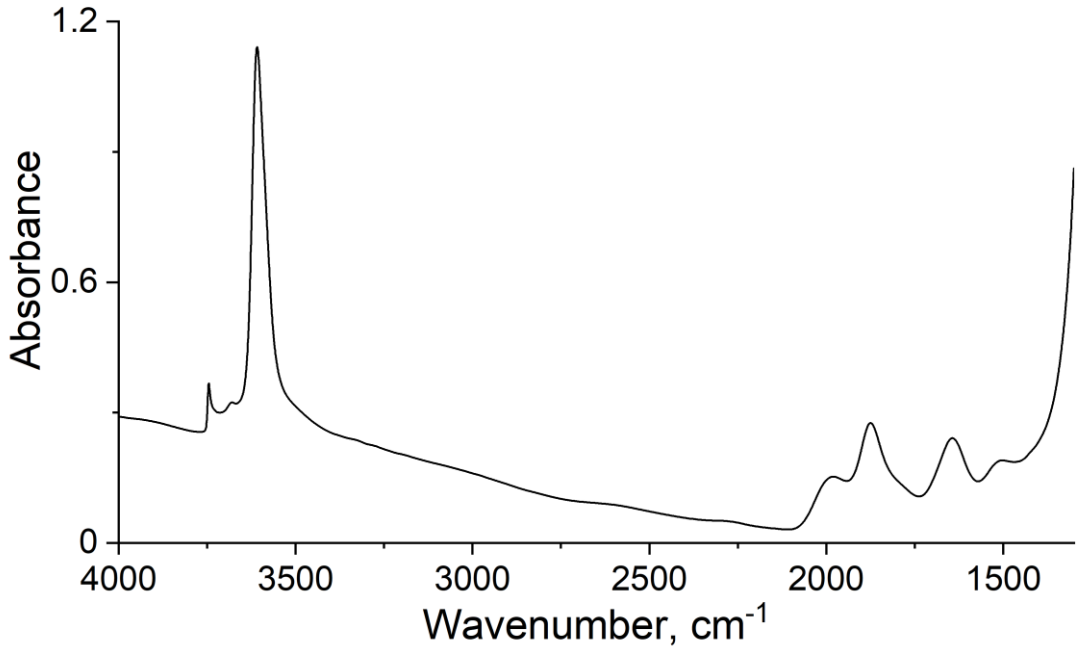

Figure 7.25. FTIR spectrum of MOR.

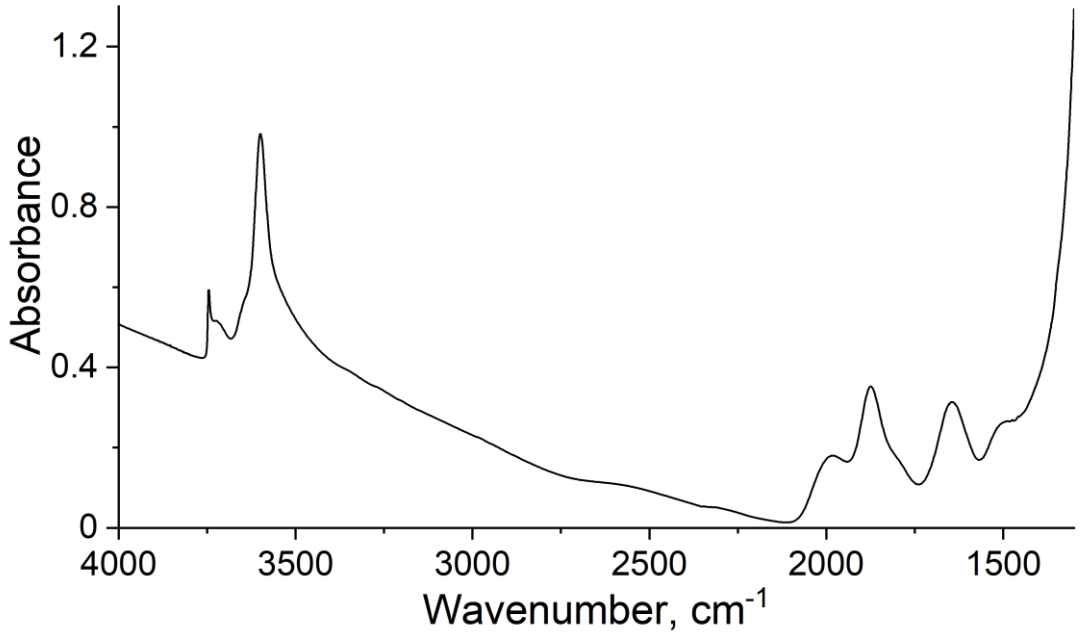

Figure 7.26. FTIR spectrum of FER.

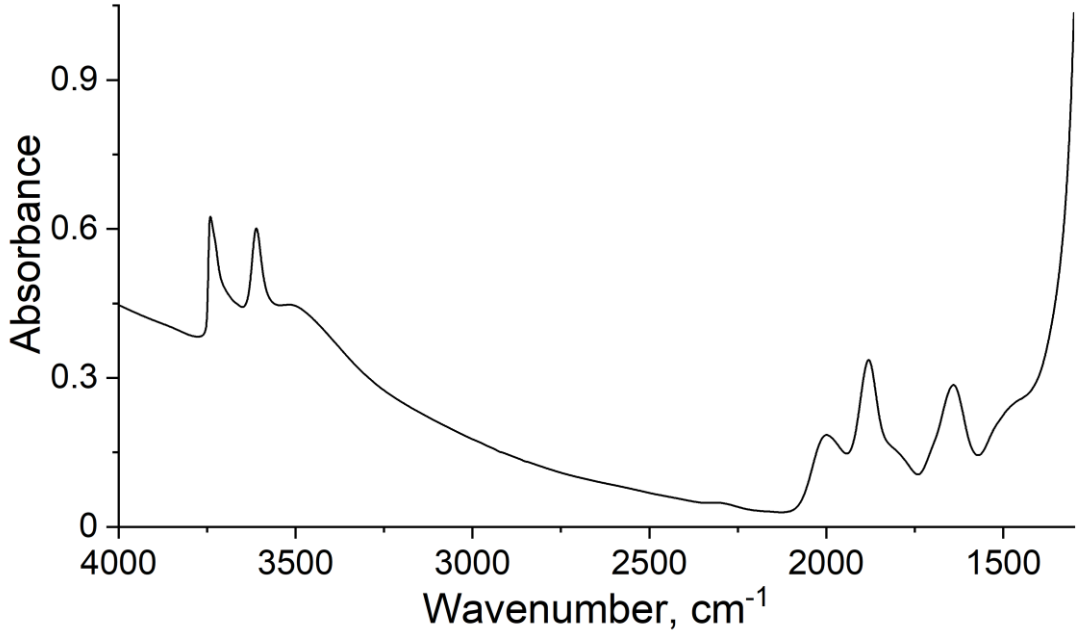

Figure 7.27. FTIR spectrum of ZSM-5.

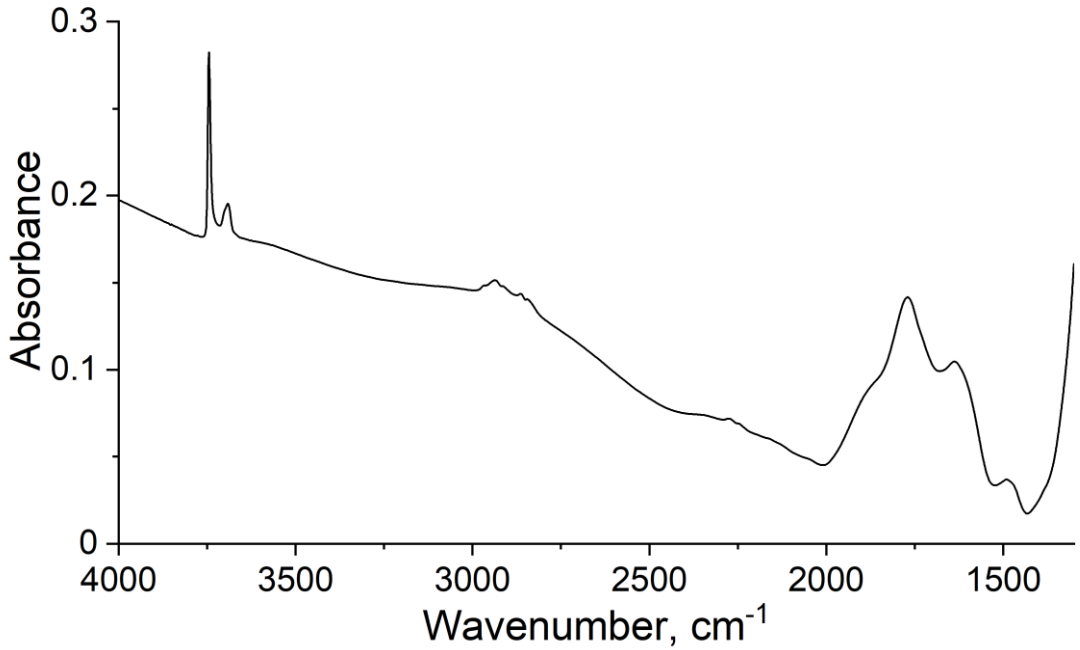

Figure 7.28. FTIR spectrum of K-LTL.

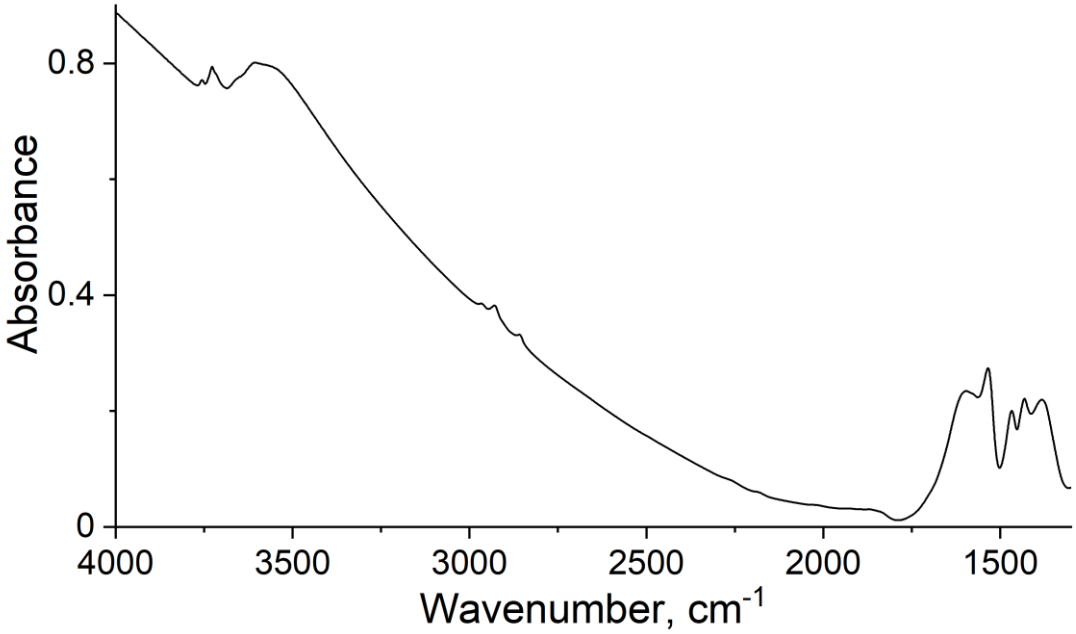

Figure 7.29. FTIR spectrum of MAP.

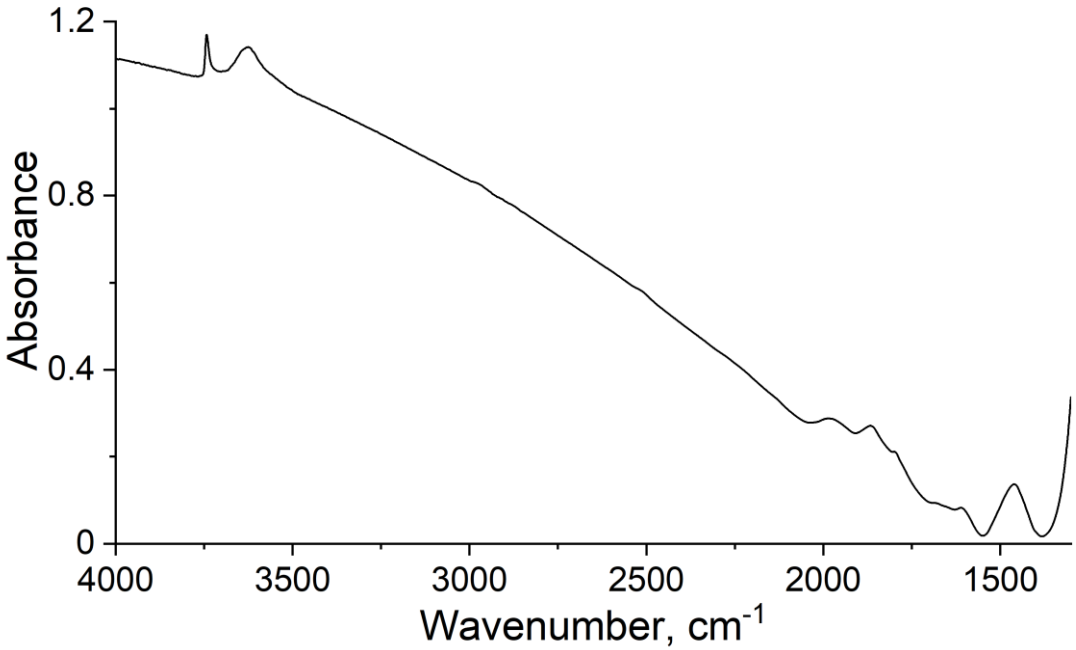

Figure 7.30. FTIR spectrum of HEU-A.

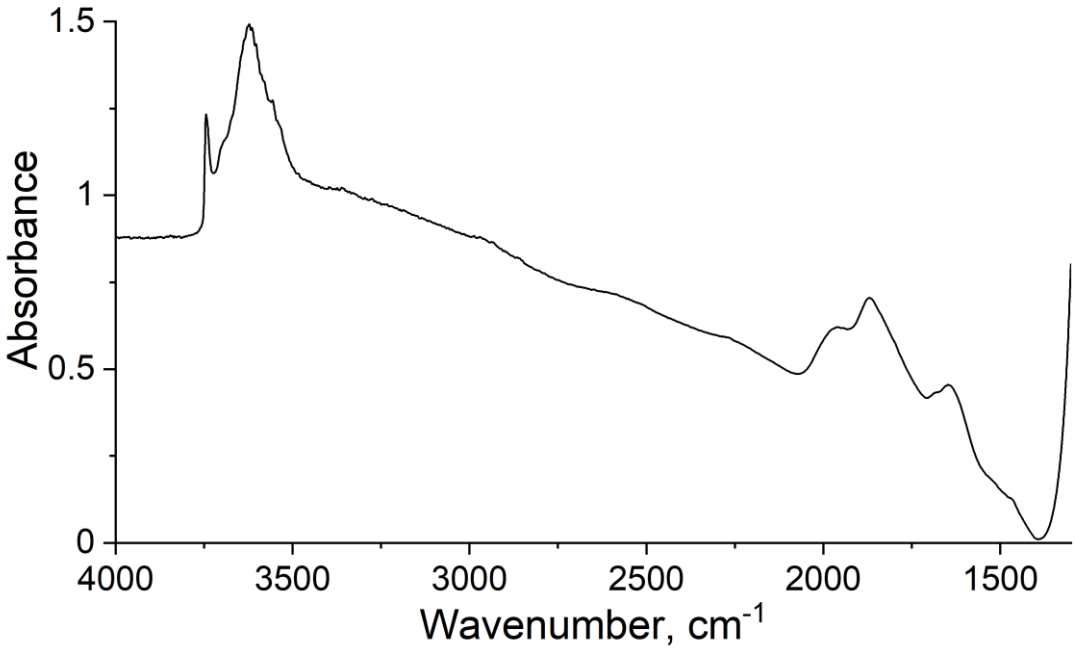

Figure 7.31. FTIR spectrum of HEU-B.

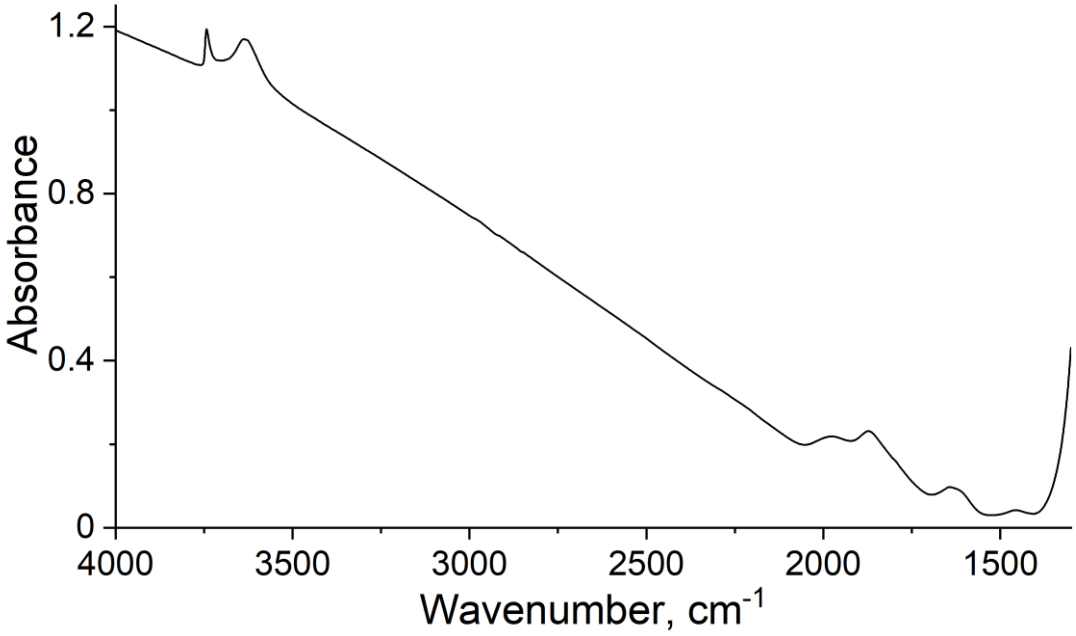

Figure 7.32. FTIR spectrum of HEU-C.

7.5 TGA curves

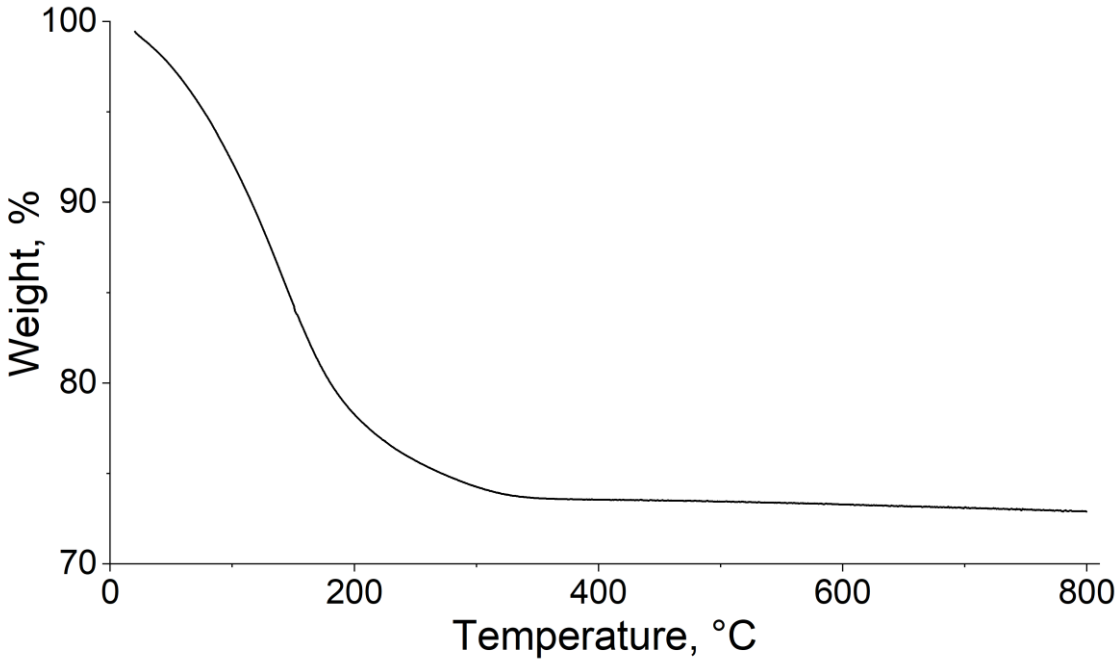

Figure 7.33. TGA curve of NaX.

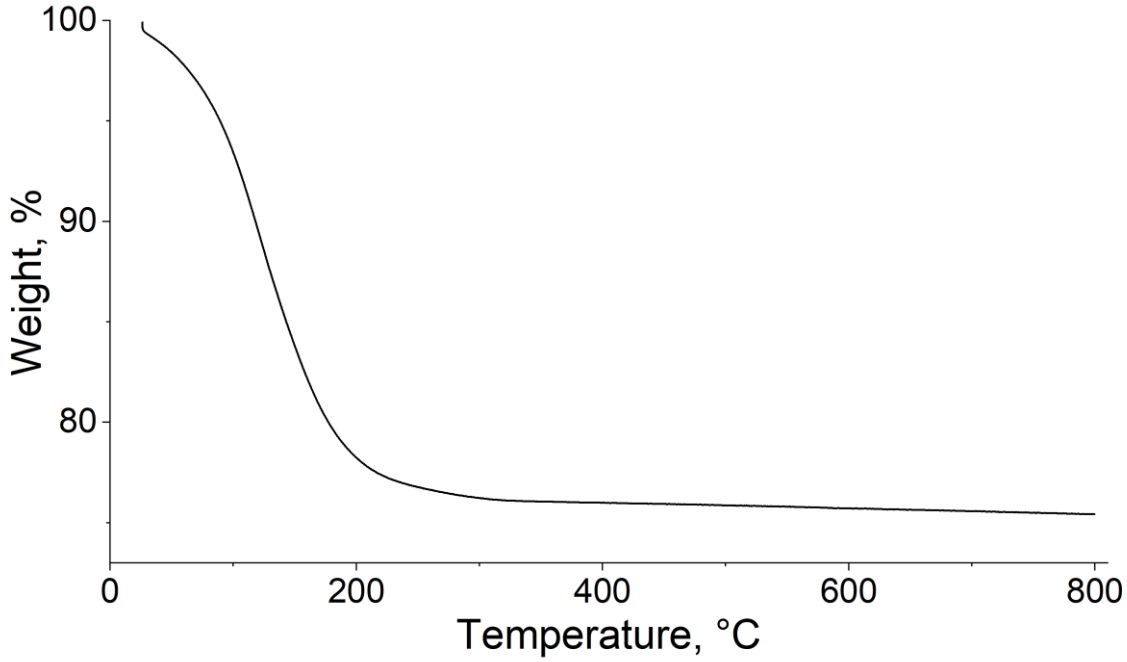

Figure 7.34. TGA curve of NaY.

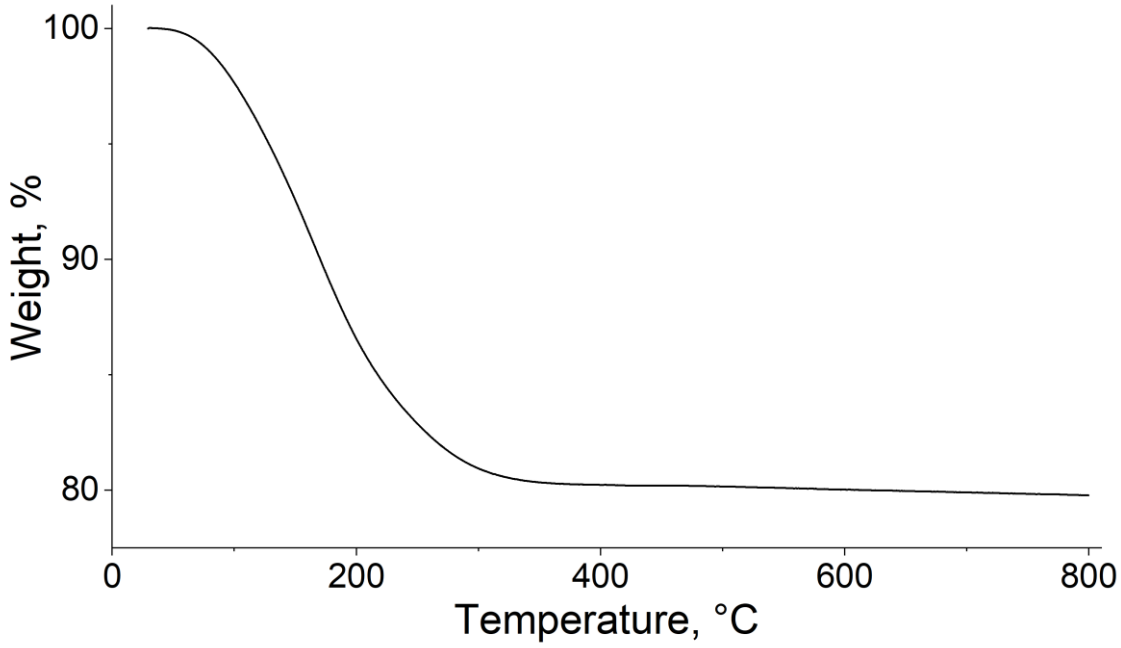

Figure 7.35. TGA curve of KX.

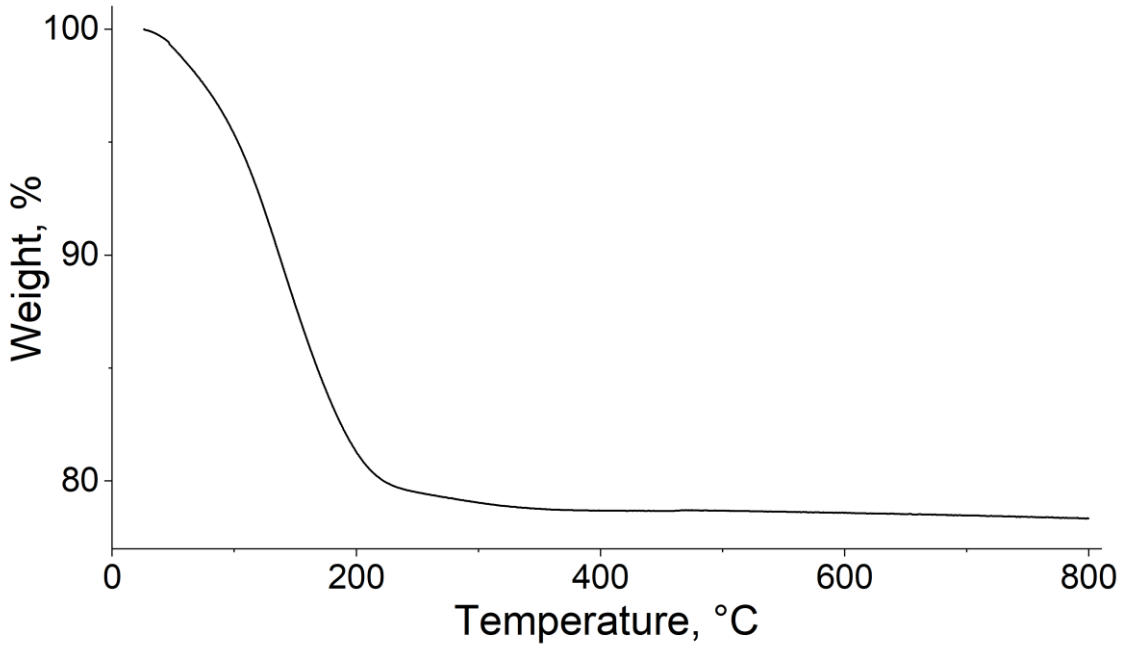

Figure 7.36. TGA curve of KY.

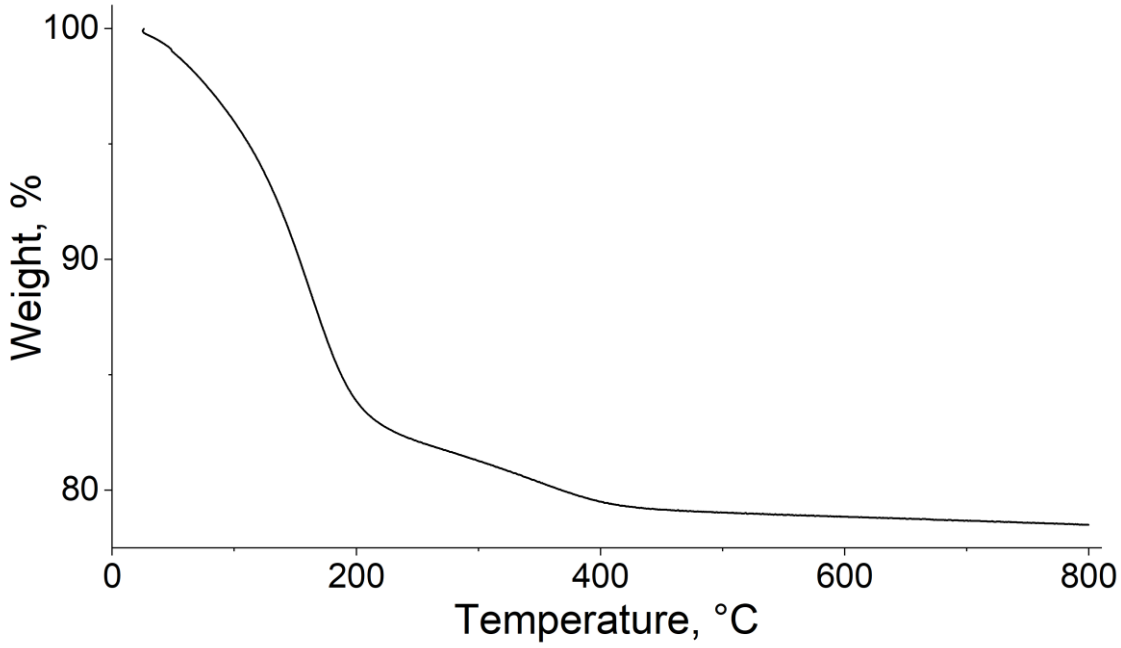

Figure 7.37. TGA curve of NaA.

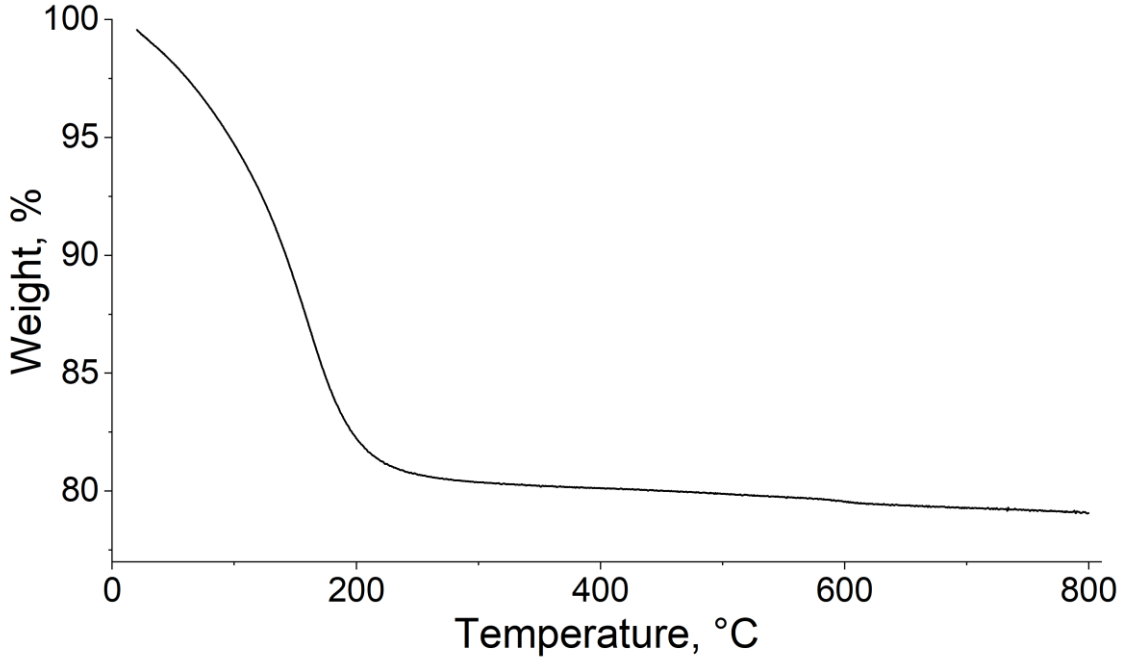

Figure 7.38. TGA curve of KA.

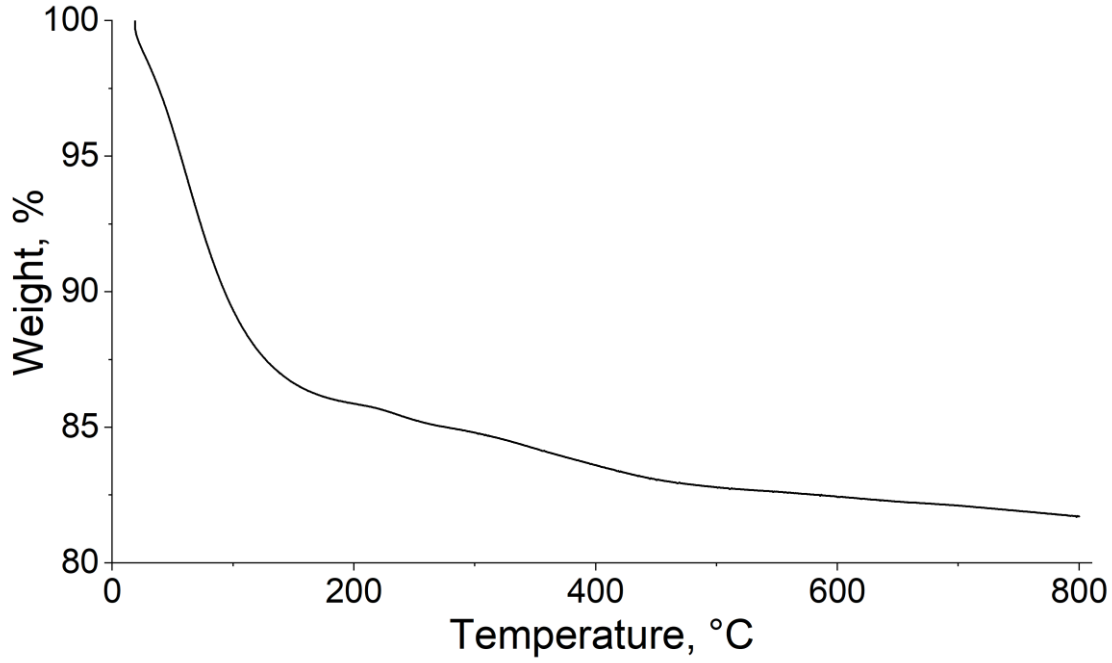

Figure 7.39. TGA curve of BEA-12.

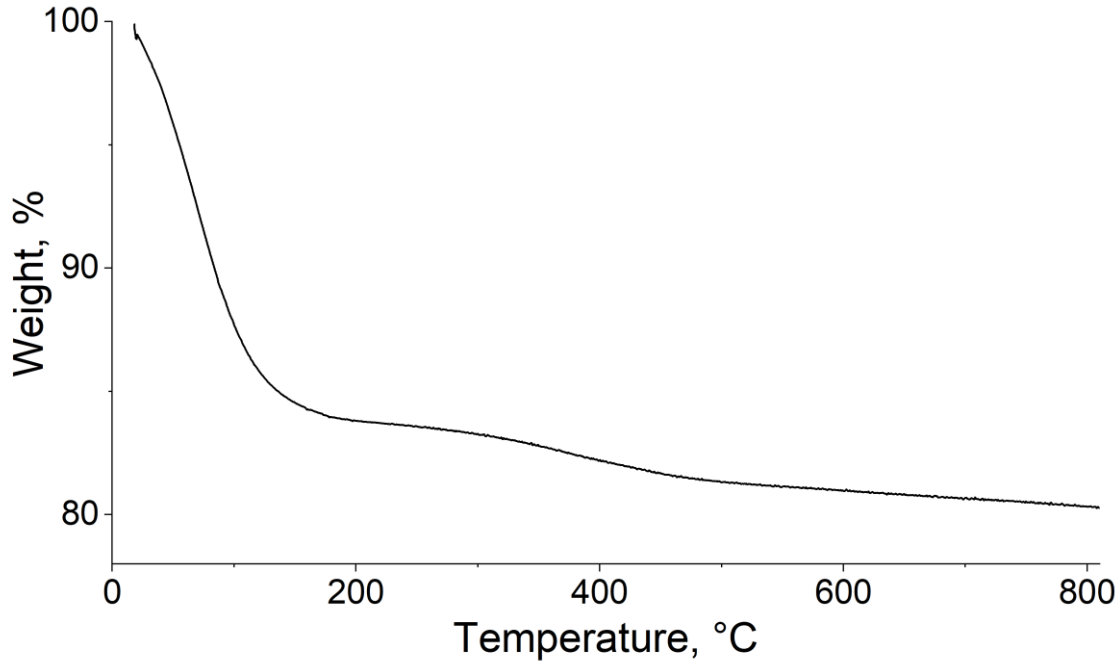

Figure 7.40. TGA curve of BEA-19.

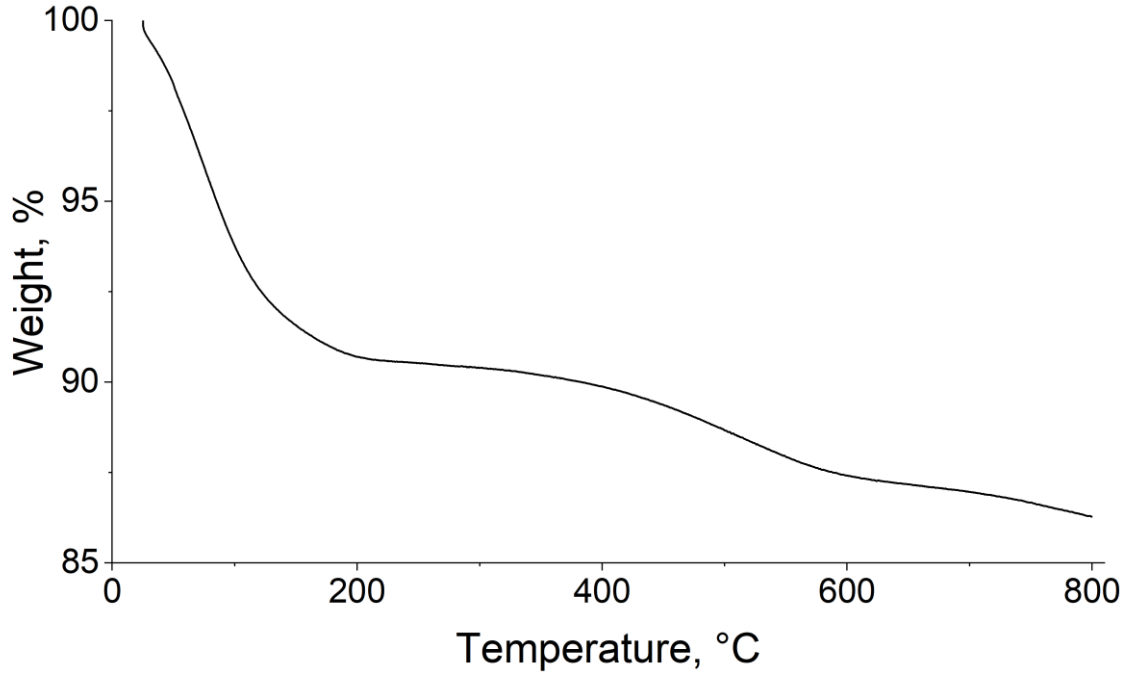

Figure 7.41. TGA curve of MOR.

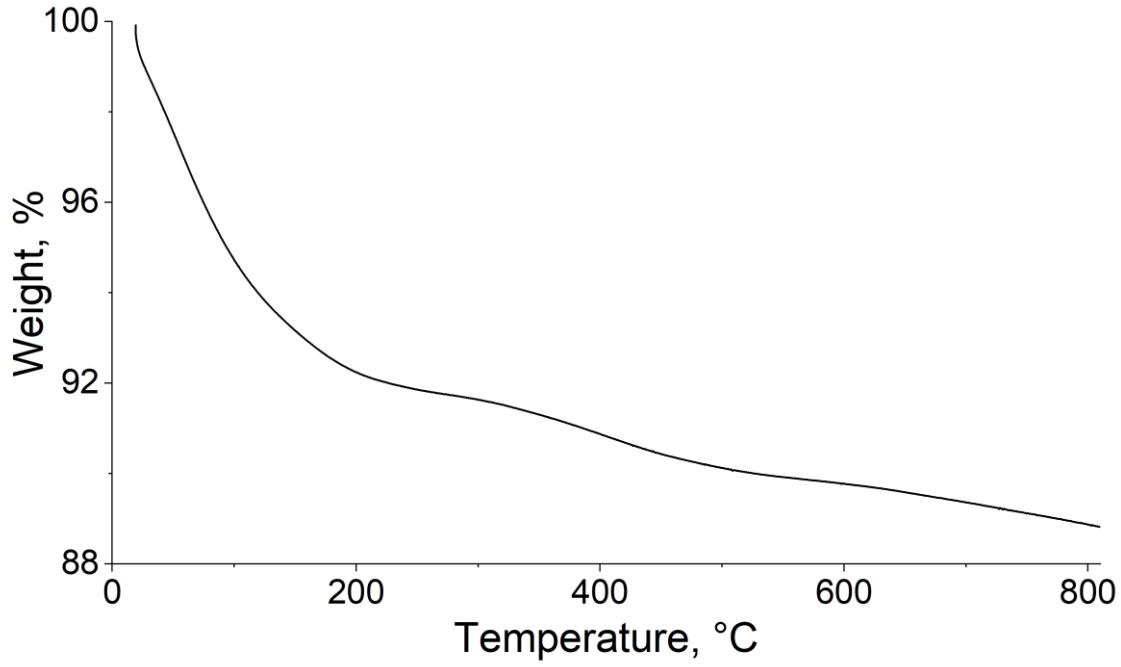

Figure 7.42. TGA curve of FER.

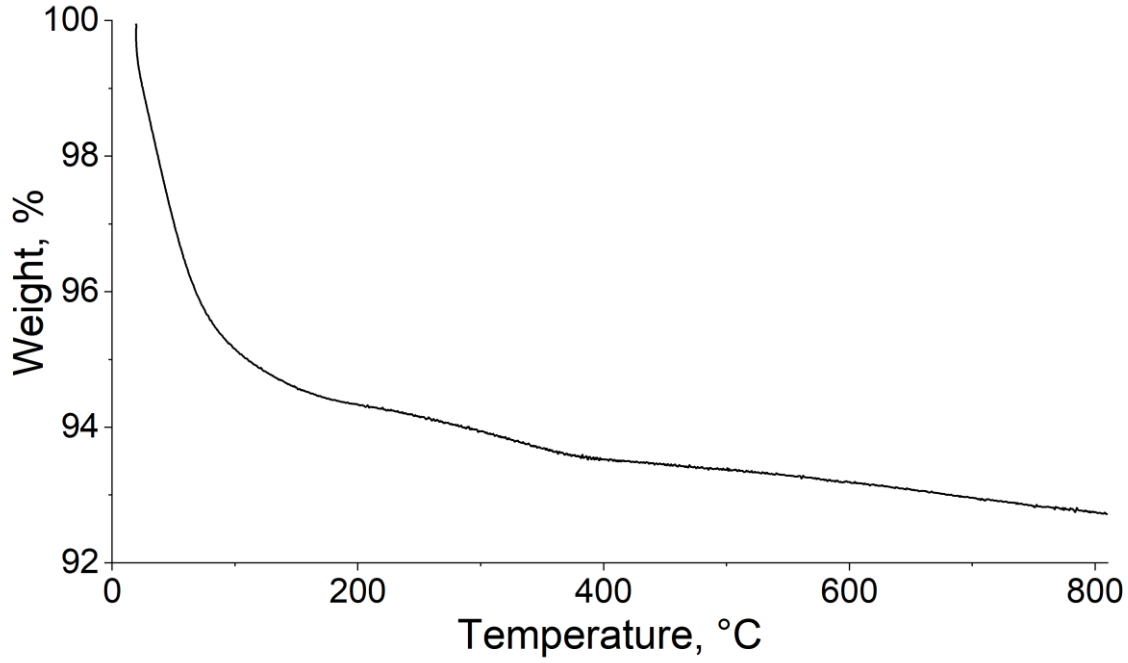

Figure 7.43. TGA curve of ZSM-5.

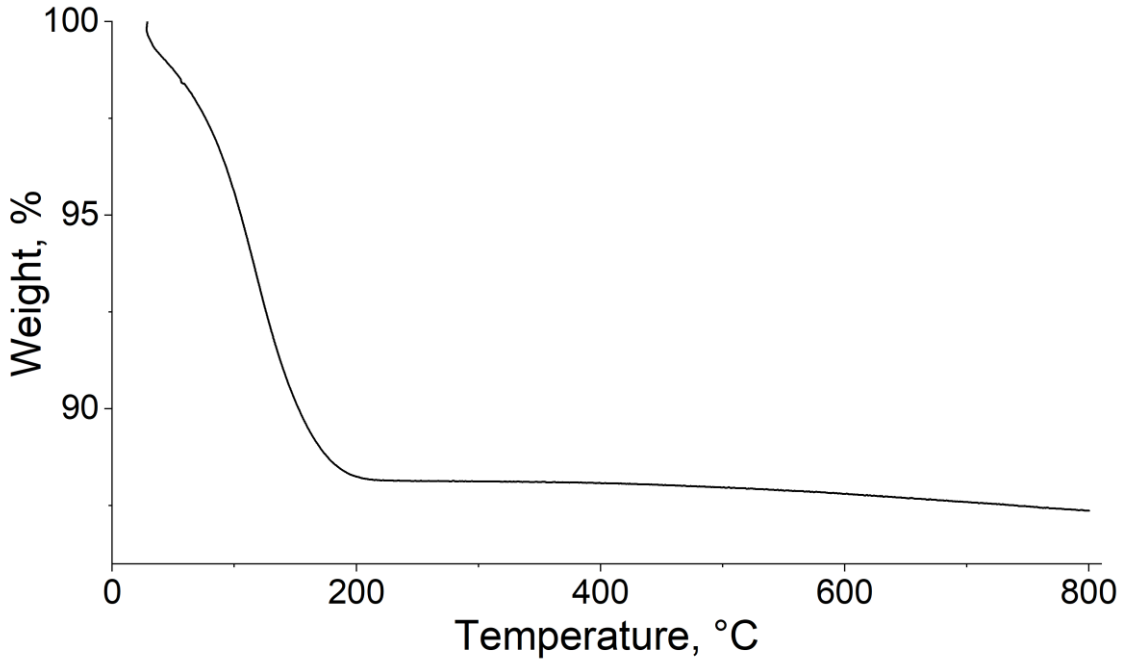

Figure 7.44. TGA curve of K-LTL.

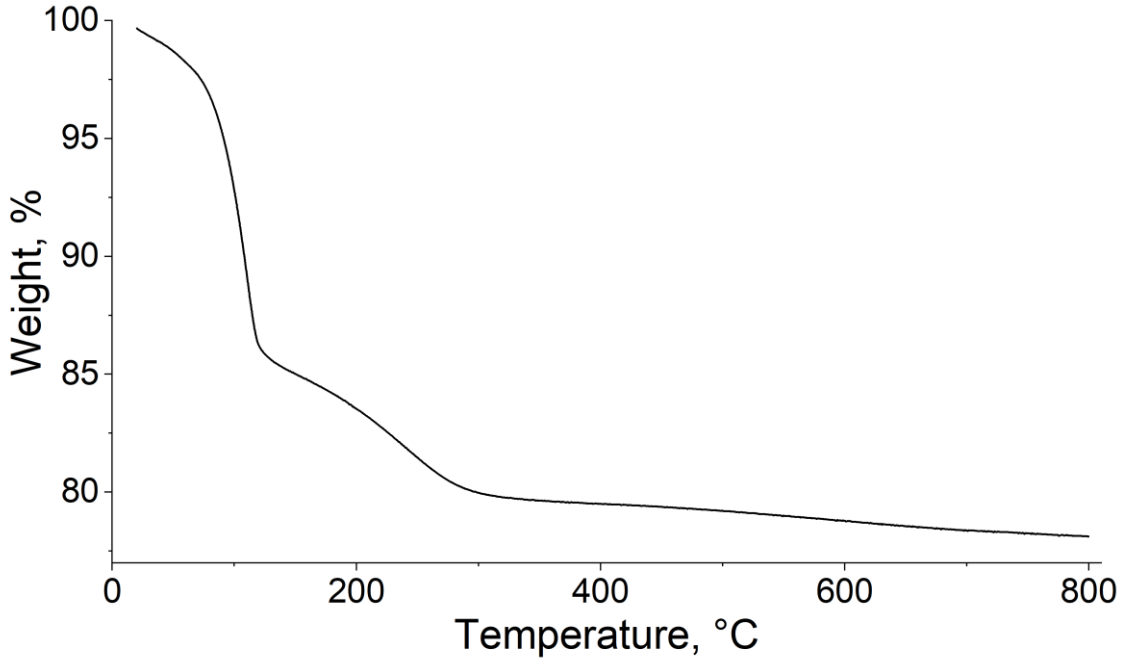

Figure 7.45. TGA curve of Na-MAP.

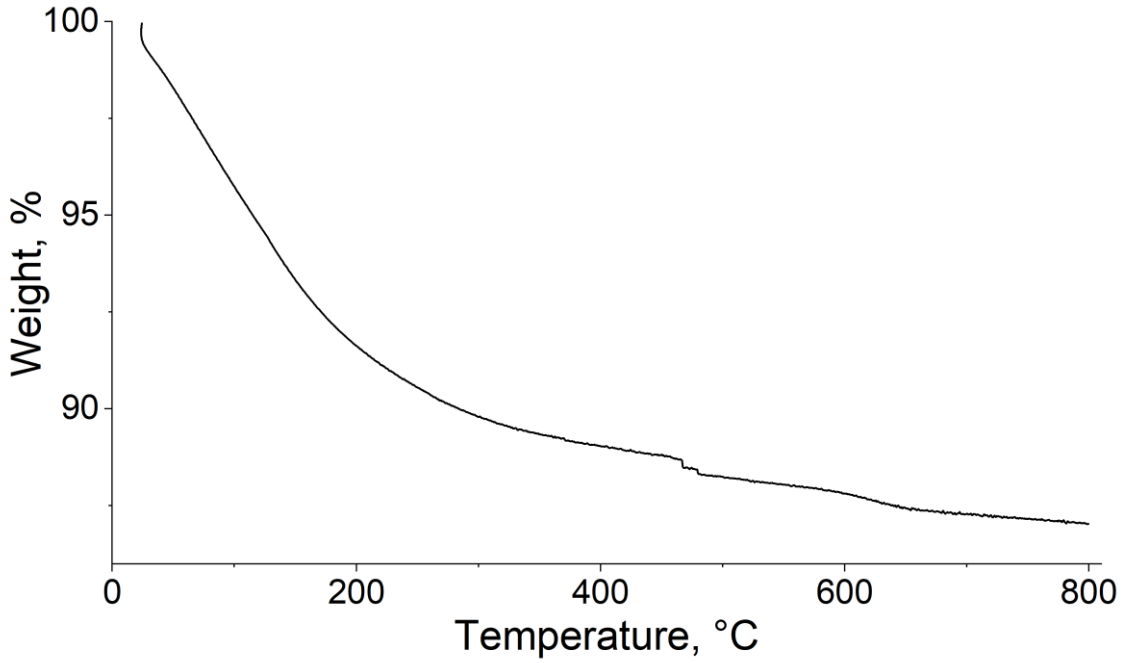

Figure 7.46. TGA curve of HEU-A.

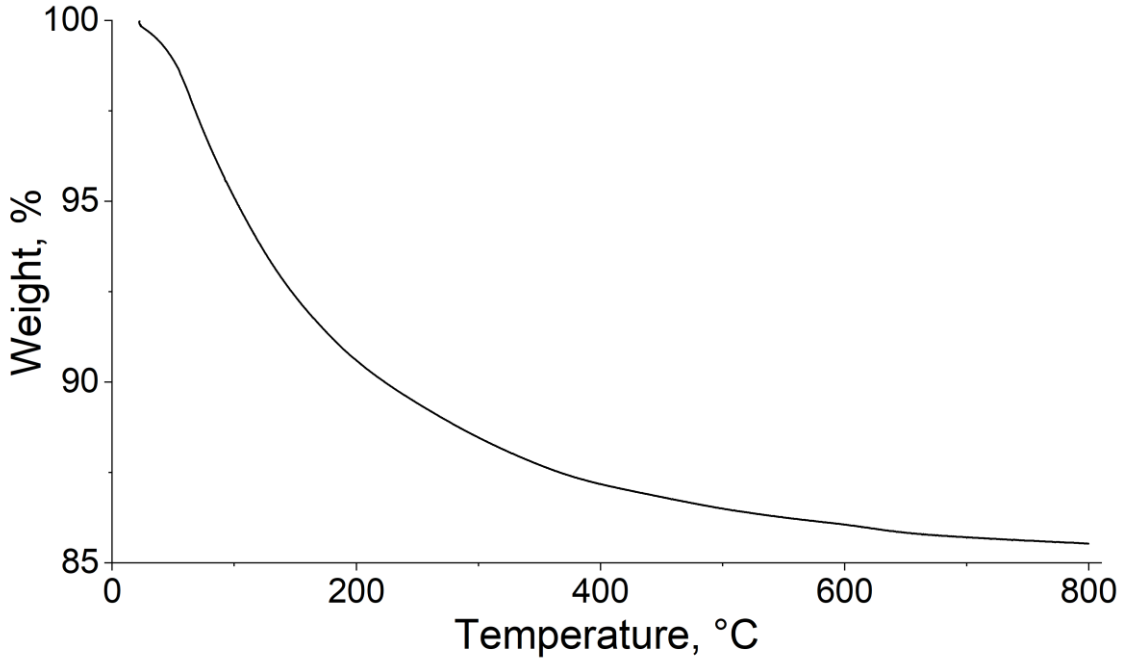

Figure 7.47. TGA curve of HEU-B.

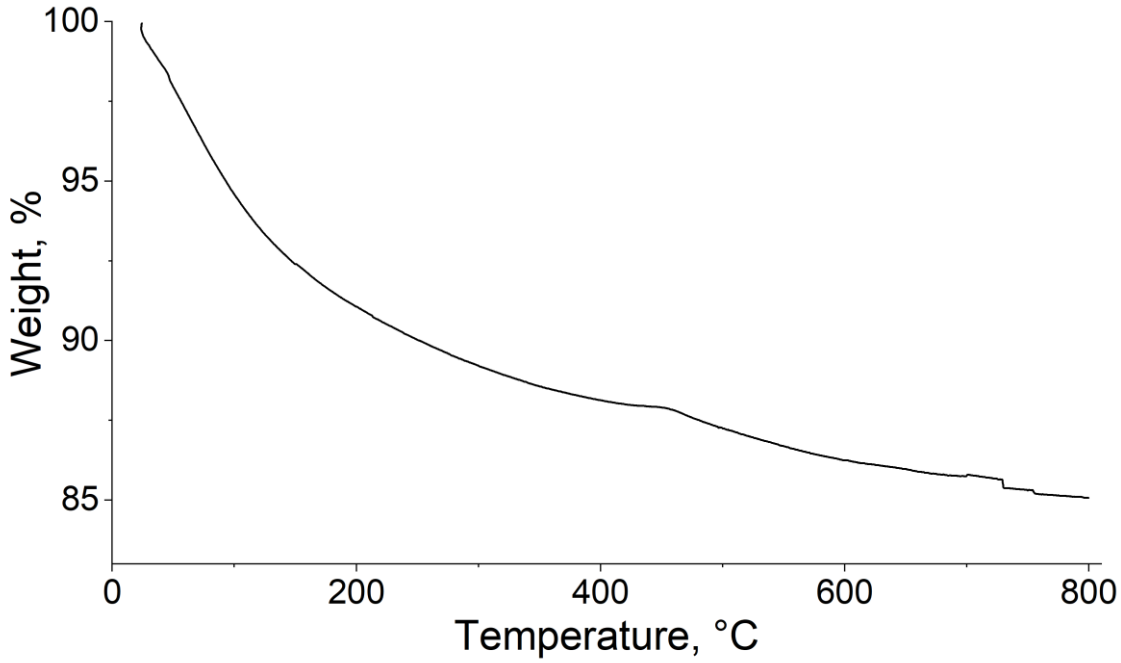

Figure 7.48. TGA curve of HEU-C.

Table 7.1. TGA weight loss data of reference samples at 200 °C and 400 °C.

Zeolite	Weight loss at 200 °C, %	Weight loss at 400 °C, %
NaX	21.74	26.45
KX	13.44	19.78
NaY	21.77	24.01
KY	18.72	21.31
NaA	16.14	20.5
KA	17.77	19.88
MOR	9.3	10.12
FER	7.76	9.14
BEA 12	14.13	16.4
BEA 19	16.2	17.79
ZSM-5	5.67	6.48
LTL	11.75	11.92
MAP	16.47	20.5
HEU-A	8.37	10.97
HEU-B	9.4	12.83
HEU-C	8.94	11.88

7.6 N_2 adsorption-desorption isotherms

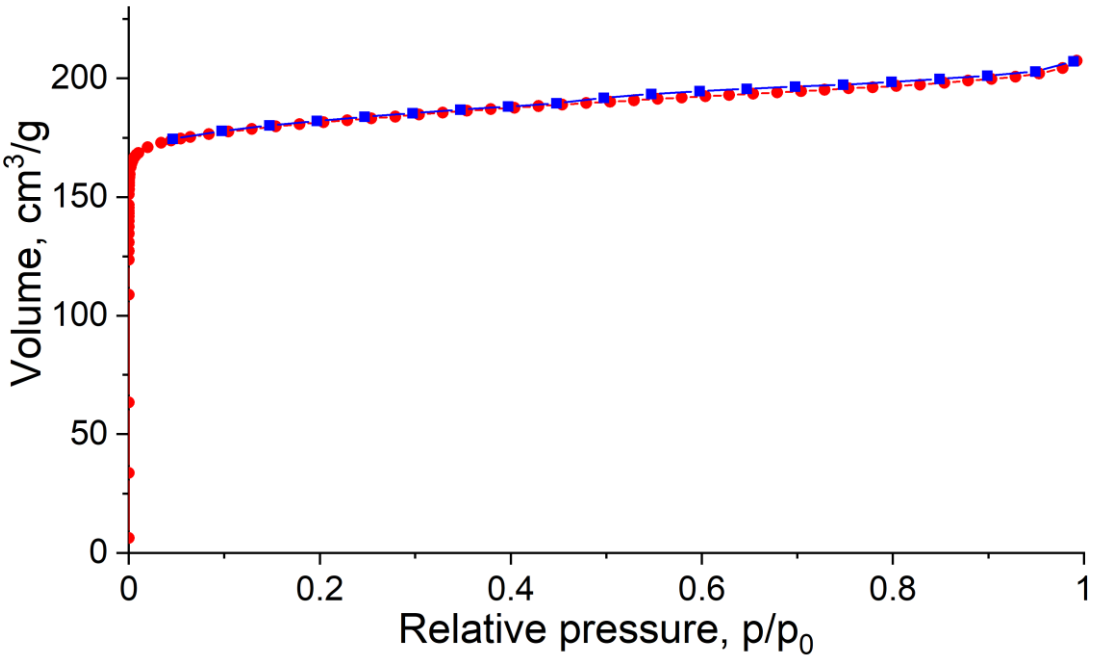

Figure 7.49. N_2 adsorption-desorption isotherm of NaX.

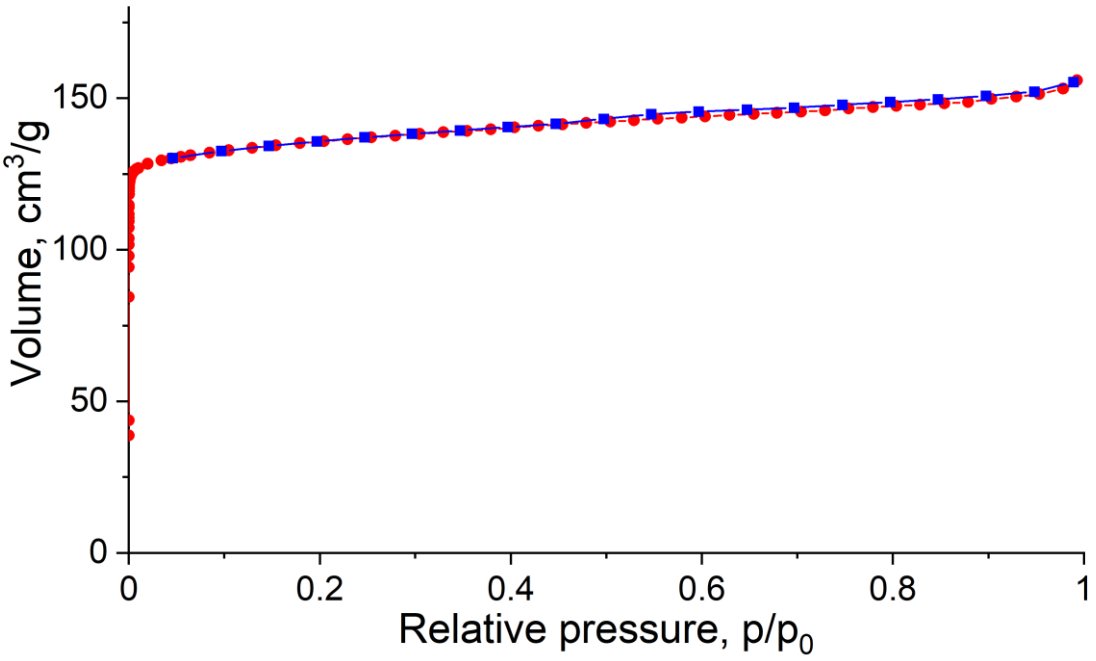

Figure 7.50. N_2 adsorption-desorption isotherm of KX.

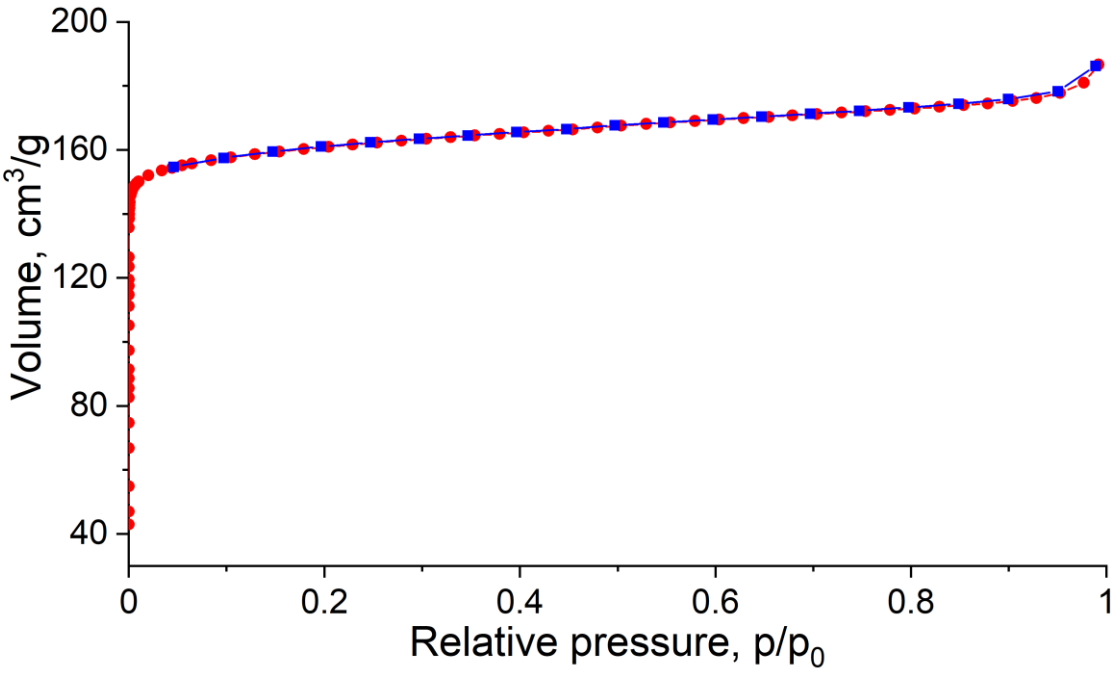

Figure 7.51. N_2 adsorption-desorption isotherm of NaY.

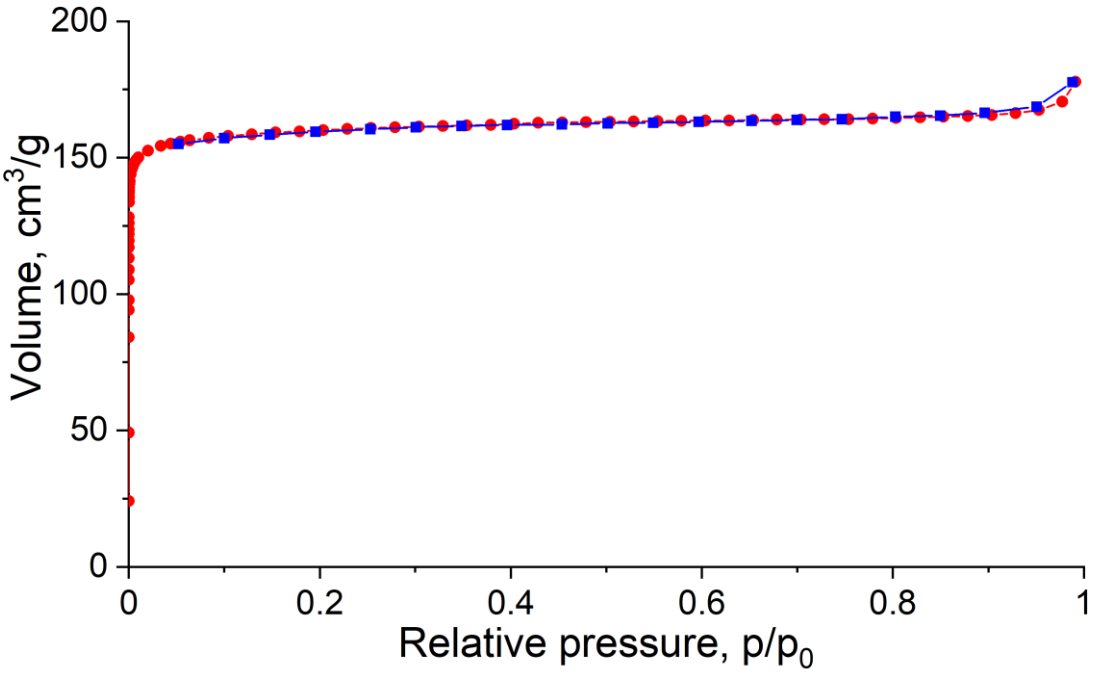

Figure 7.52. N_2 adsorption-desorption isotherm of KY.

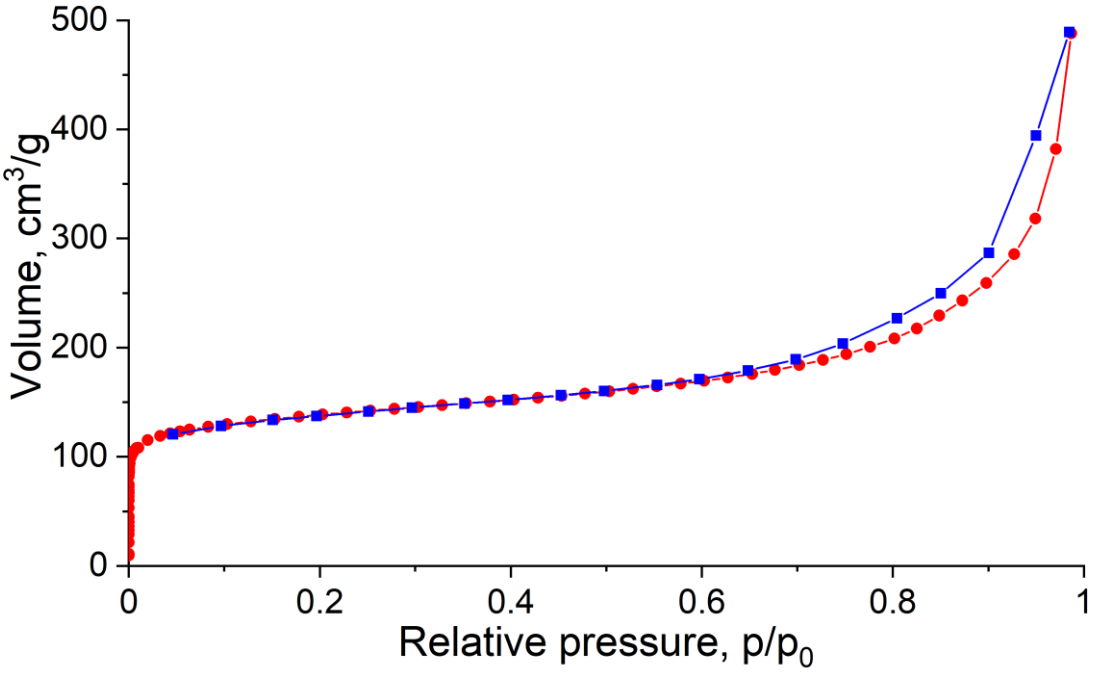

Figure 7.53. N_2 adsorption-desorption isotherm of BEA-12.

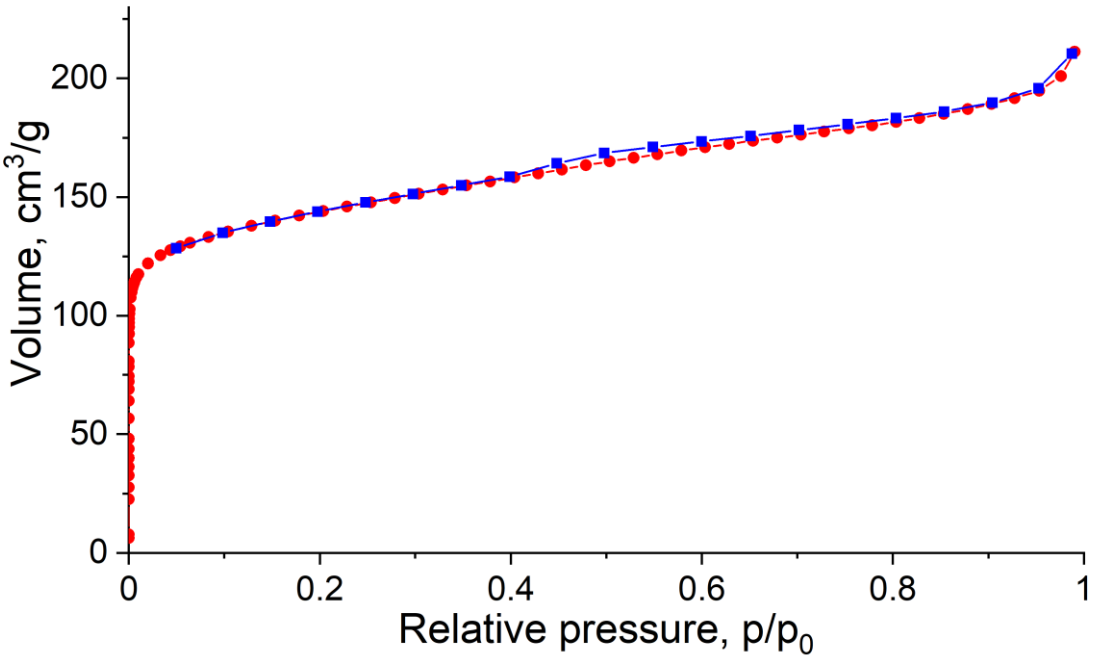

Figure 7.54. N_2 adsorption-desorption isotherm of BEA-19.

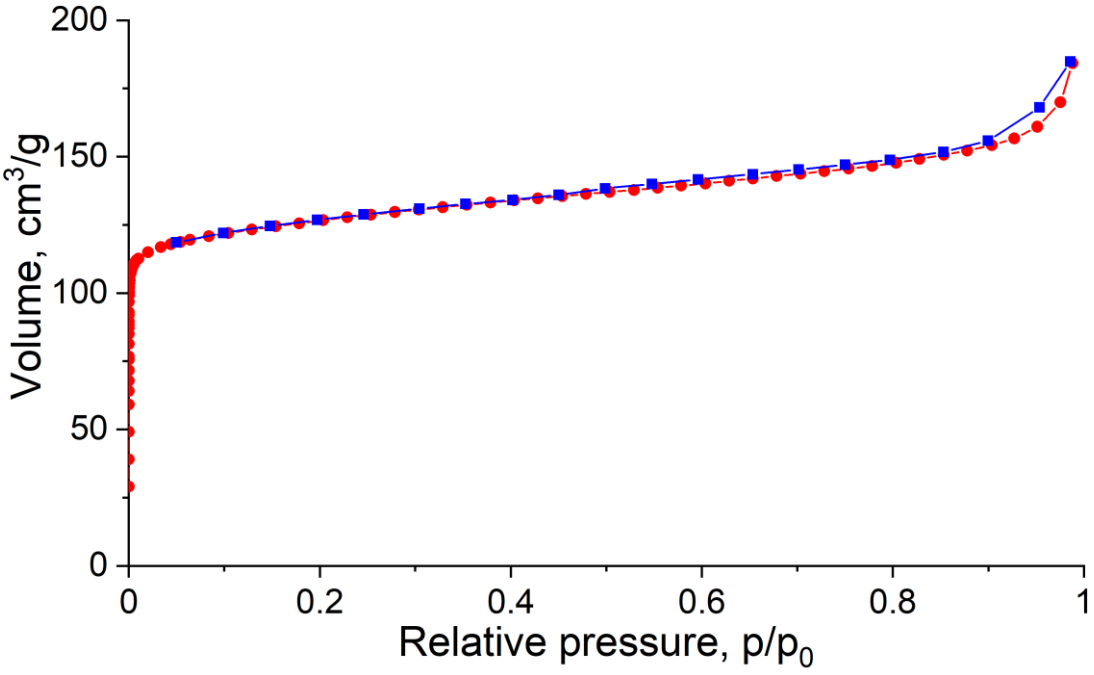

Figure 7.55. N_2 adsorption-desorption isotherm of NH_4-MOR.

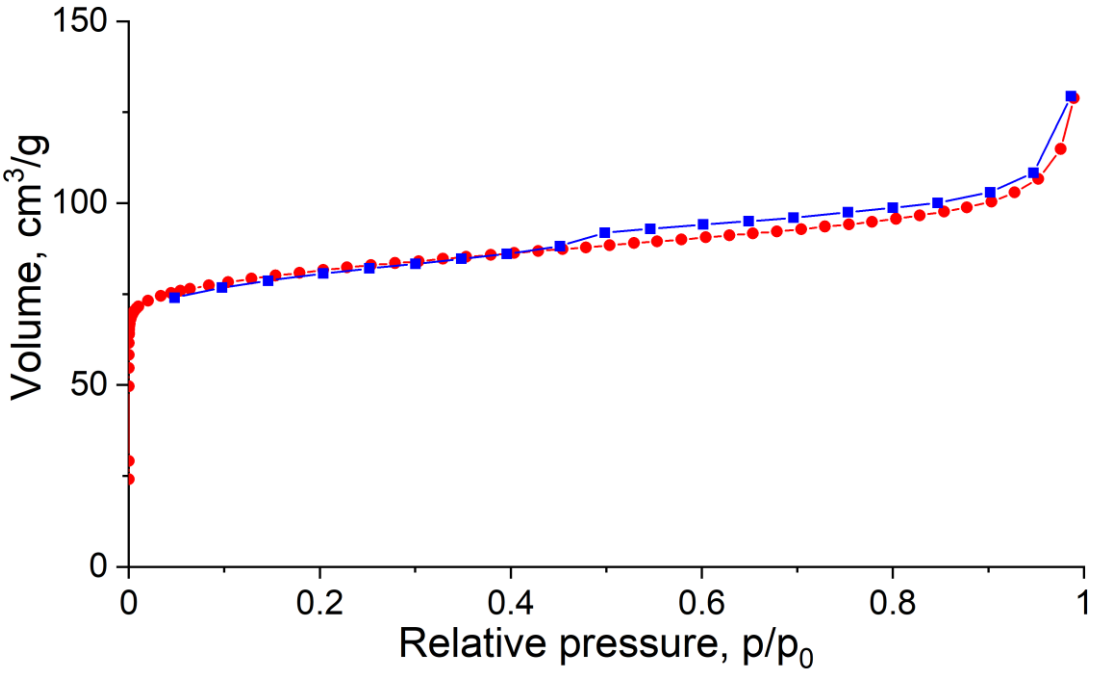

Figure 7.56. N_2 adsorption-desorption isotherm of FER.

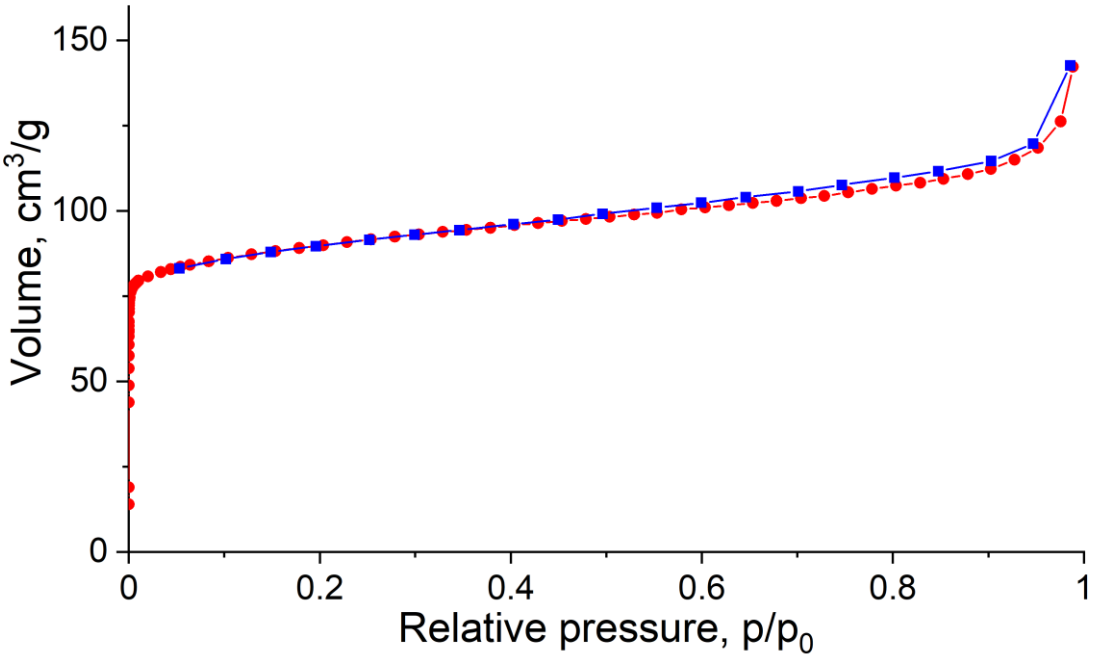

Figure 7.57. N_2 adsorption-desorption isotherm of K-LTL.

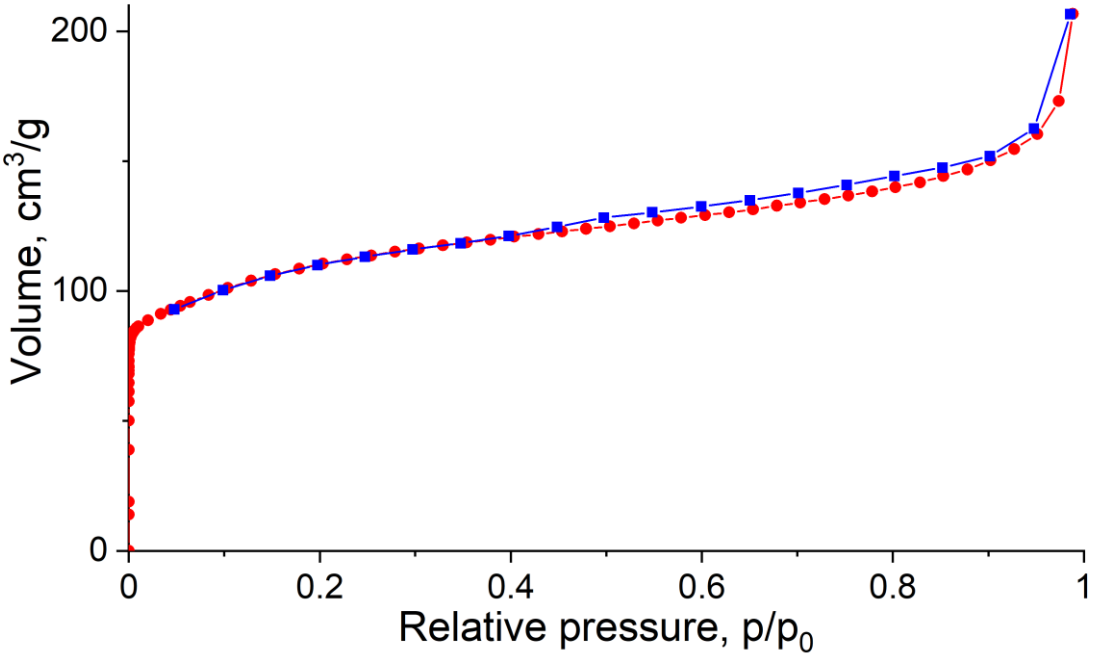

Figure 7.58. N_2 adsorption-desorption isotherm of ZSM-5.

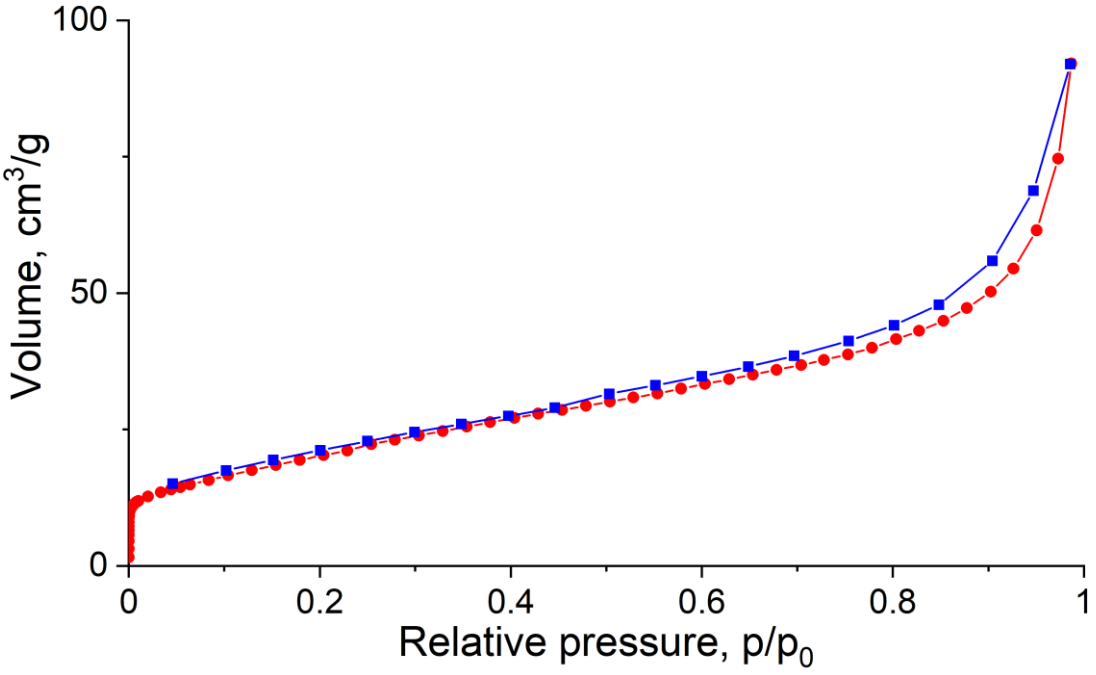

Figure 7.59. N_2 adsorption-desorption isotherm of HEU-A.

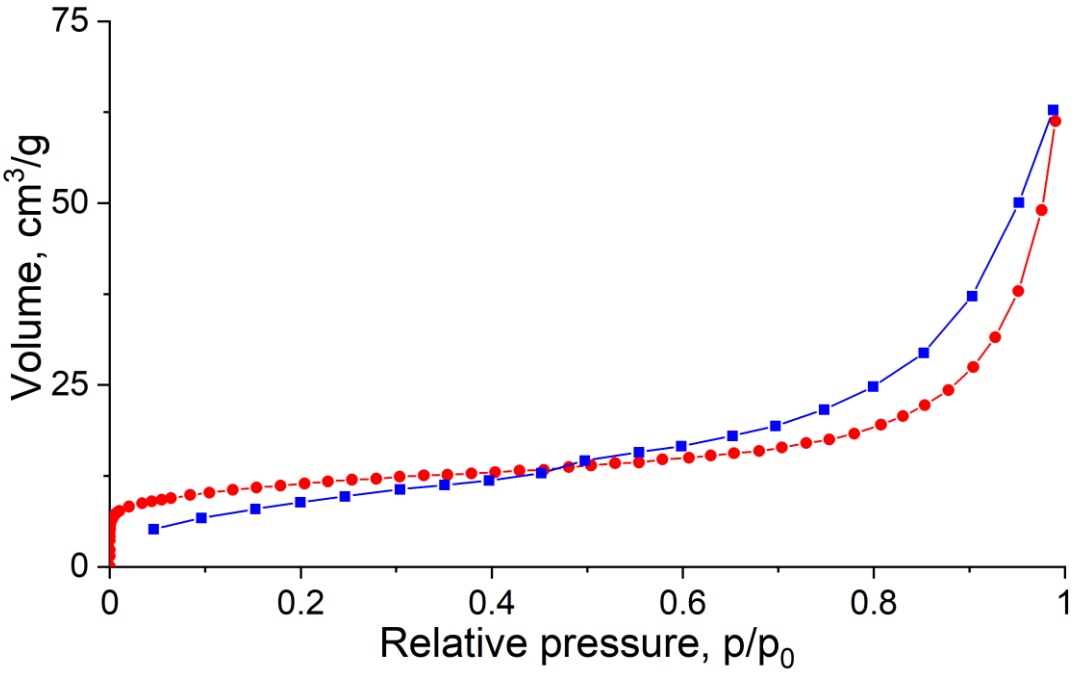

Figure 7.60. N_2 adsorption-desorption isotherm of HEU-B.

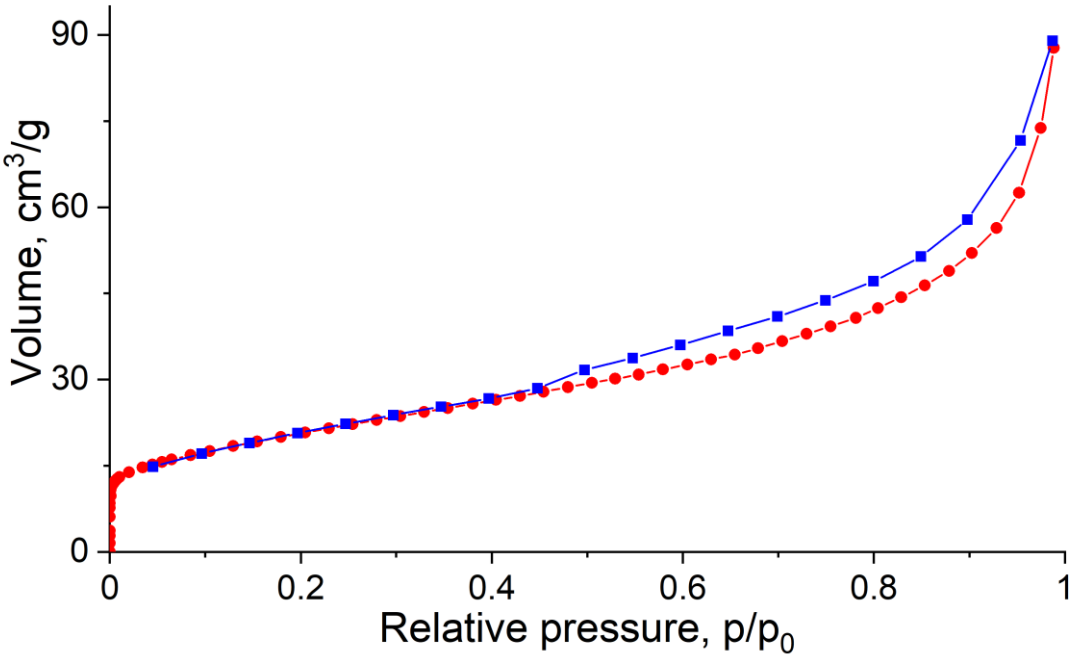

Figure 7.61. N_2 adsorption-desorption isotherm of HEU-C.

Table 7.2. N_2 adsorption-desorption data of the reference samples, *calculated by DFT.

Zeolite	BET area, m^2/g	$V_{0.95}$, cm^3/g	V_{micro}, cm^3/g*	V_t, cm^3/g*	V_{meso}, cm^3/g*
NaX	732	0.313	0.286	0.328	0.042
KX	548	0.235	0.210	0.241	0.031
NaY	650	0.277	0.256	0.284	0.028
KY	655	0.260	0.249	0.260	0.011
MOR	494	0.249	0.176	0.245	0.069
FER	315	0.165	0.113	0.165	0.052
BEA 12	517	0.506	0.139	0.436	0.297
BEA 19	537	0.302	0.160	0.284	0.124
ZSM-5	399	0.249	0.125	0.238	0.113
LTL	346	0.184	0.123	0.180	0.057
HEU-A	77	0.095	0.006	0.080	0.074
HEU-B	41	0.059	0.007	0.046	0.039
HEU-C	74	0.097	0.007	0.083	0.076

7.7 SEM-EDX data

Table 7.3. SEM-EDX data of the reference samples.

Zeolite	Si/Al	Na/Al	K/Al	Mg/Al	Ca/Al	Fe/Al
NaX	1.5	0.7	-	-	-	-
KX	1.2	0.3	0.6	-	-	-
NaY	2.6	1.0	-	-	-	-
KY	2.5	0.2	0.7	-	-	-
NaA	1.0	1.0	-	-	-	-
KA	1.0	0.6	0.4	-	-	-
MOR	9.6	-	-	-	-	-
FER	10.1	-	-	-	-	-
BEA 12	12.7	-	-	-	-	-
BEA 19	19.0	-	-	-	-	-
ZSM-5	37.8	-	-	-	-	-
LTL	3.4	-	1.0	-	-	-
MAP	1.0	1.0	-	-	-	-
HEU-A*	4.6	0.5	0.2	0.1	0.2	-
HEU-B*	5.5	-	0.3	0.2	0.2	0.1
HEU-C*	5.1	0.1	0.3	-	0.2	0.1

7.8 Supplementary FTIR spectra for Chapter 3

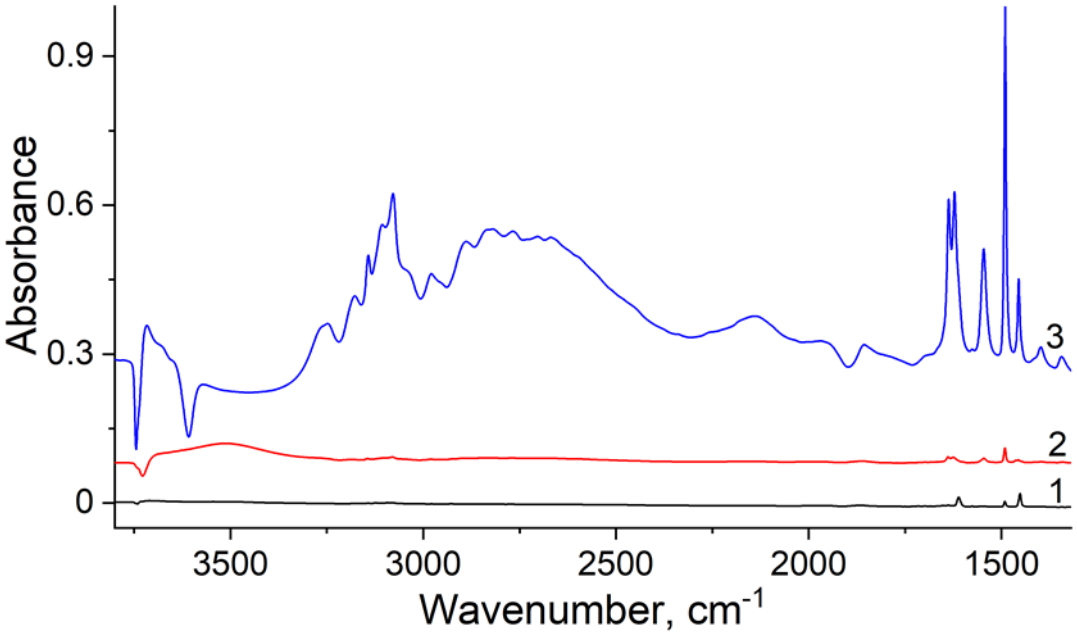

Figure 7.62. Difference FTIR spectra of Sn-BEA (1), DeAl-BEA (2) and BEA-19 (3) following pyridine adsorption.

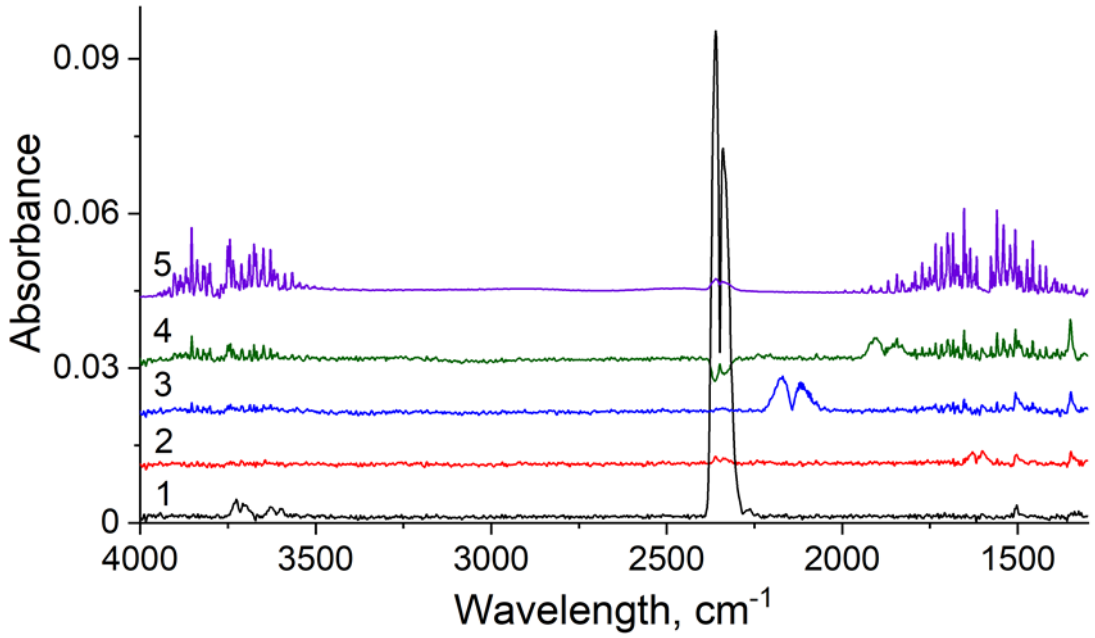

Figure 7.63. FTIR spectra of the selected exhaust-fume gases, 5000 ppm of CO_2 (1), 1000 ppm of NO_2 (2), 5000 ppm of CO (3), 5000 ppm of NO (4), water vapour (5).

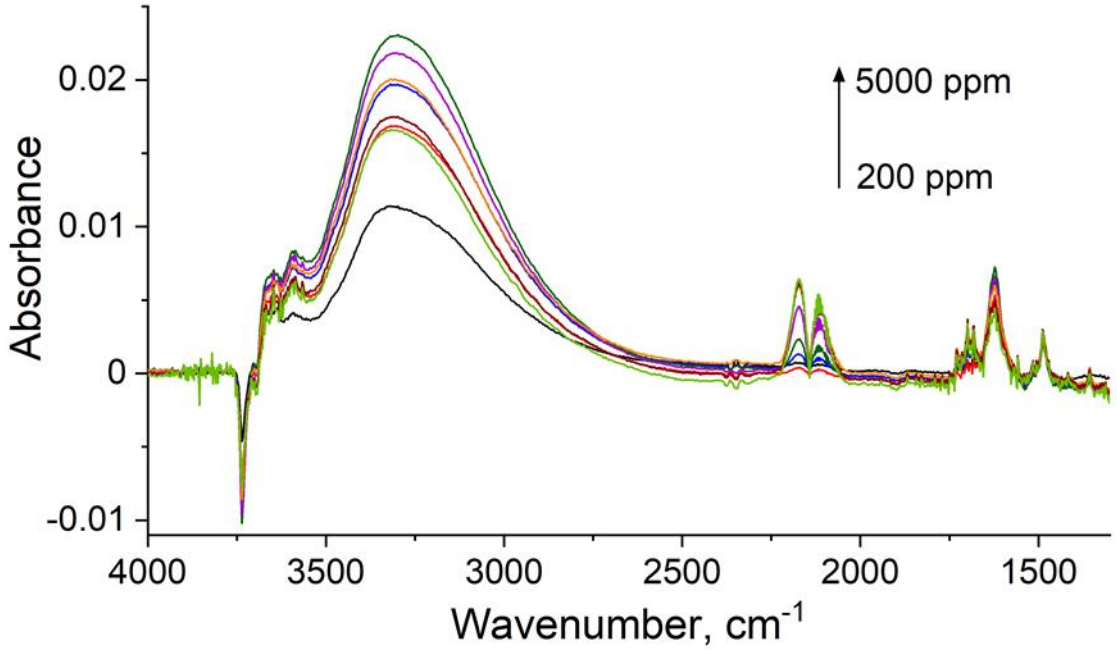

Figure 7.64. Difference FTIR spectra of CO adsorbed on Sn-BEA, 200 ppm (black), 400 ppm, 800 ppm, 1600 ppm, 3200 ppm, 4000 ppm, 4500 ppm, 5000 ppm.

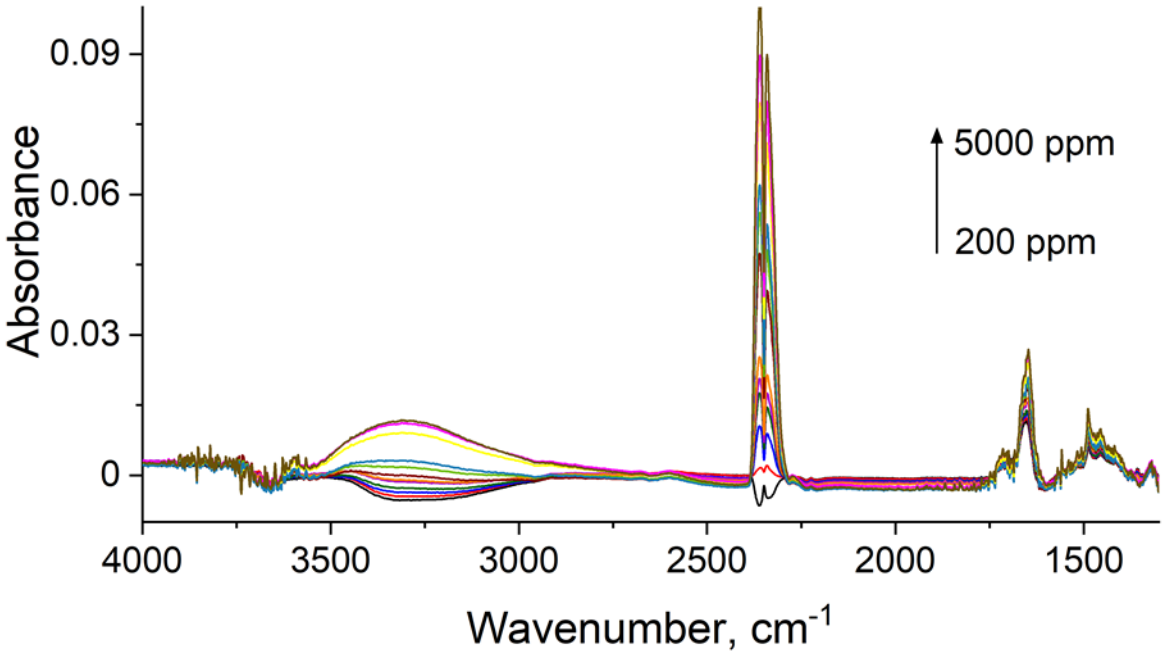

Figure 7.65. Difference FTIR spectra of CO_2 adsorbed on Sn-BEA, 200 ppm (black), 200-1000 ppm increments of 200 ppm, 1000-5000 ppm increments of 500 ppm.

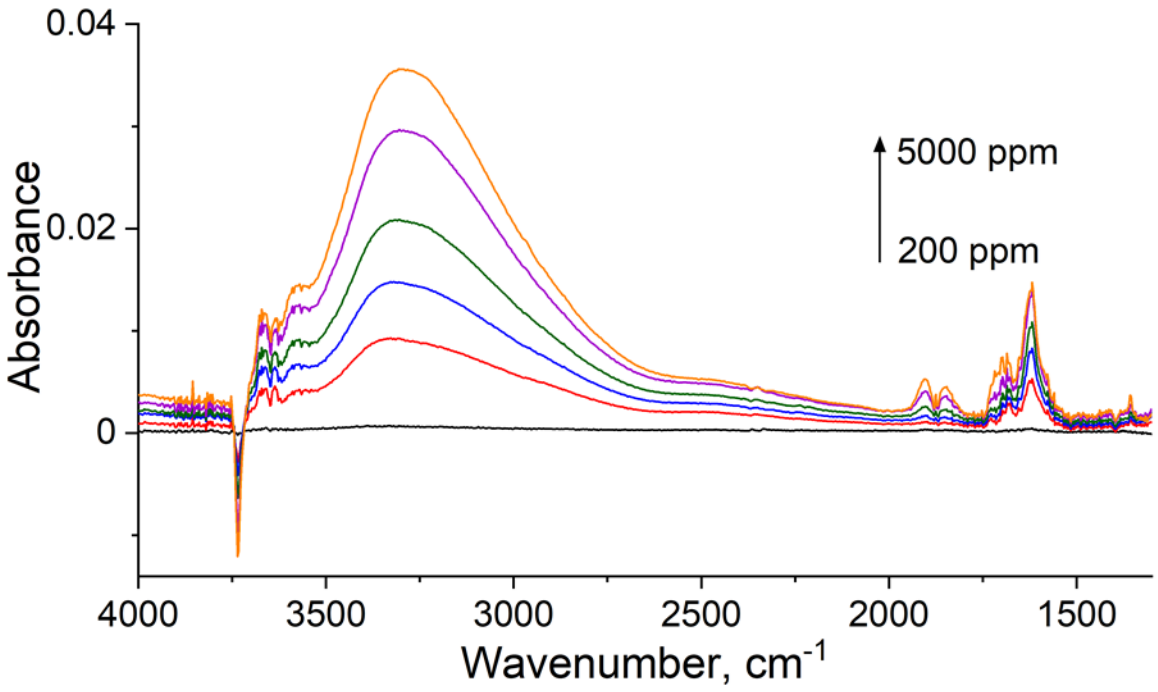

Figure 7.66. Difference FTIR spectra of NO adsorbed on Sn-BEA, 200 ppm (black), 400 ppm, 800 ppm, 1600 ppm, 3200 ppm, 5000 ppm.

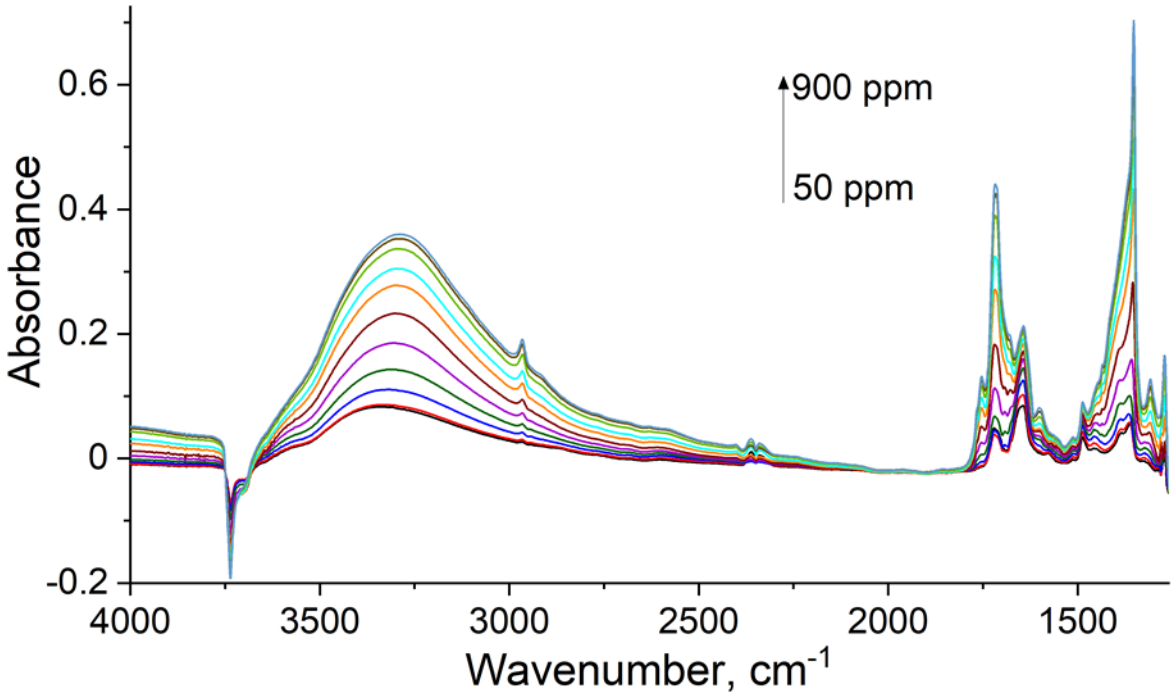

Figure 7.67. Difference FTIR spectra of NO_2 adsorbed on Sn-BEA, 50 ppm (black), 100-900 ppm increments of 100 ppm.

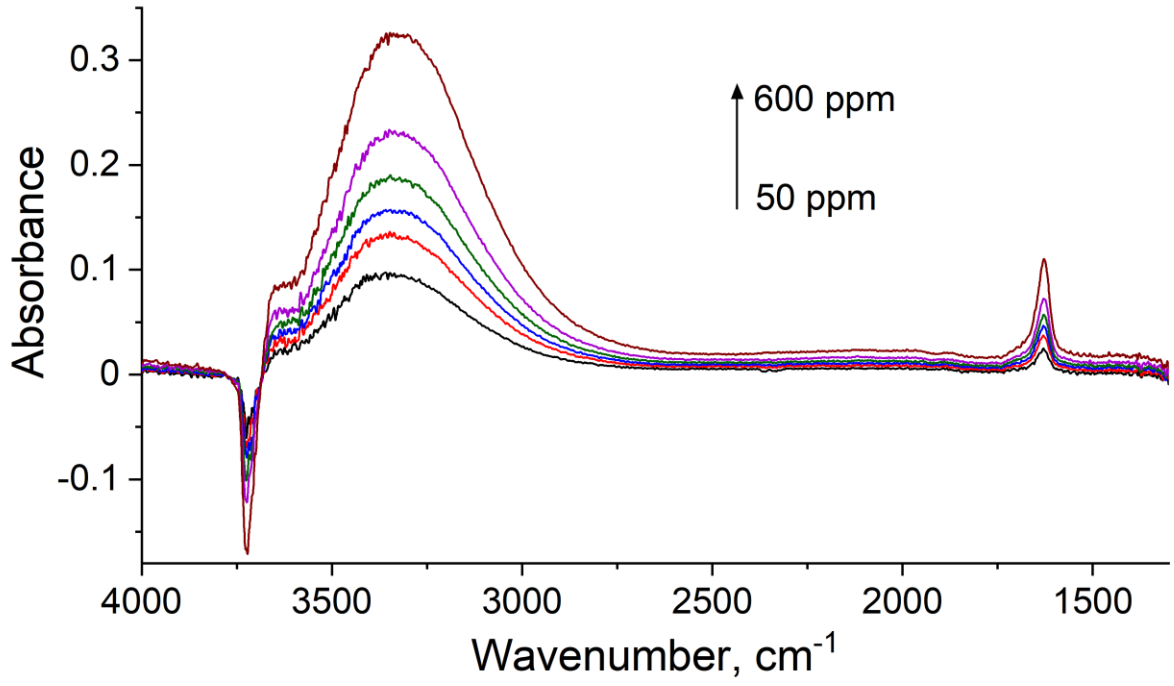

Figure 7.68. Difference FTIR spectra of CO adsorbed on DeAl-BEA, 50 ppm (black), 100 ppm, 200 ppm, 300 ppm, 400 ppm, 600 ppm.

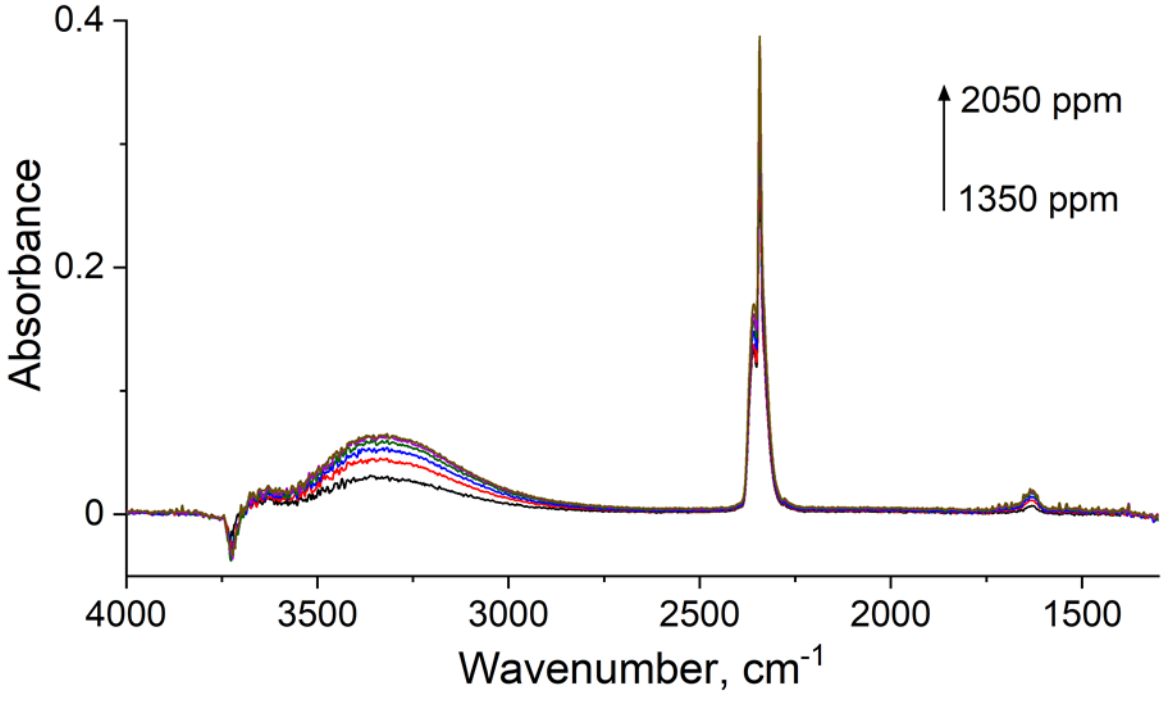

Figure 7.69. Difference FTIR spectra of CO_2 adsorbed on DeAl-BEA, 1350 ppm (black), increments of 150 ppm.

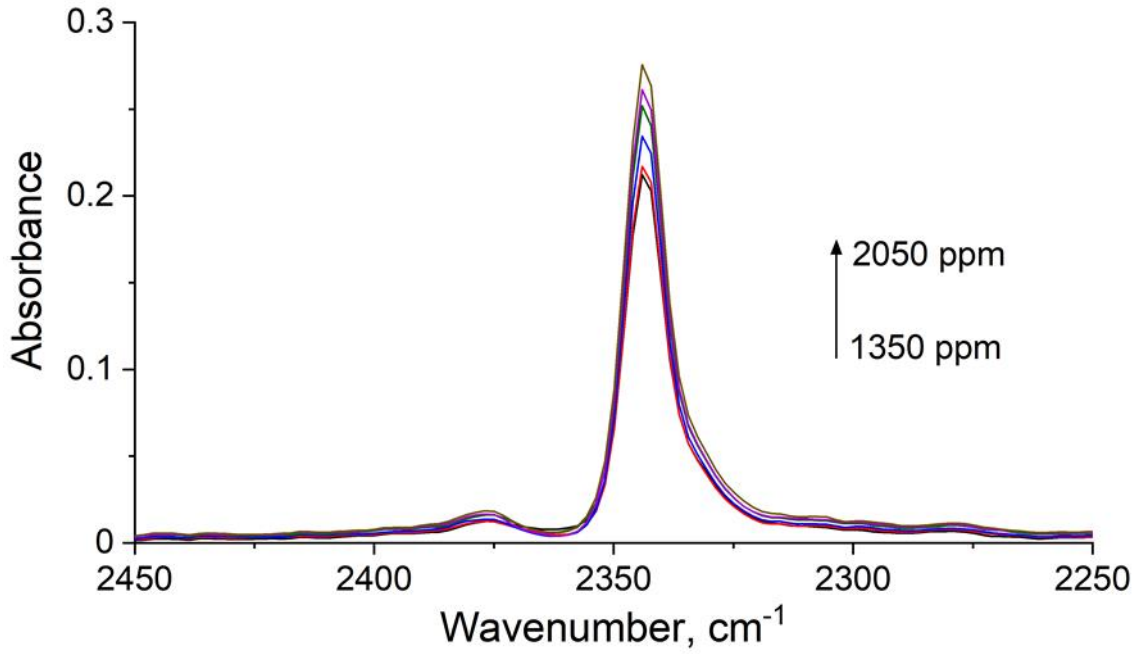

Figure 7.70. Difference FTIR spectra of CO_2 adsorbed on DeAl-BEA, zoomed in the 2450-2240 cm^{-1} region, 1350 ppm (black), increments of 150 ppm, CO_2 gas phase spectrum subtracted.

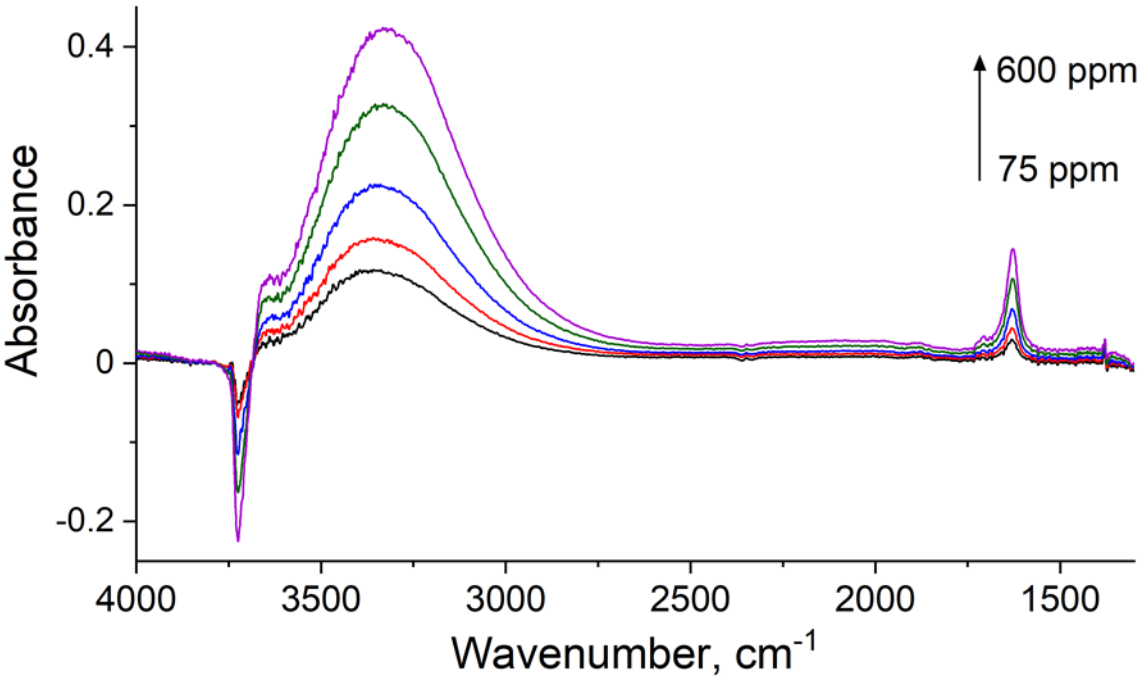

Figure 7.71. Difference FTIR spectra of NO adsorbed on DeAl-BEA, 75 ppm (black), 100 ppm, 200 ppm, 400 ppm, 600 ppm.

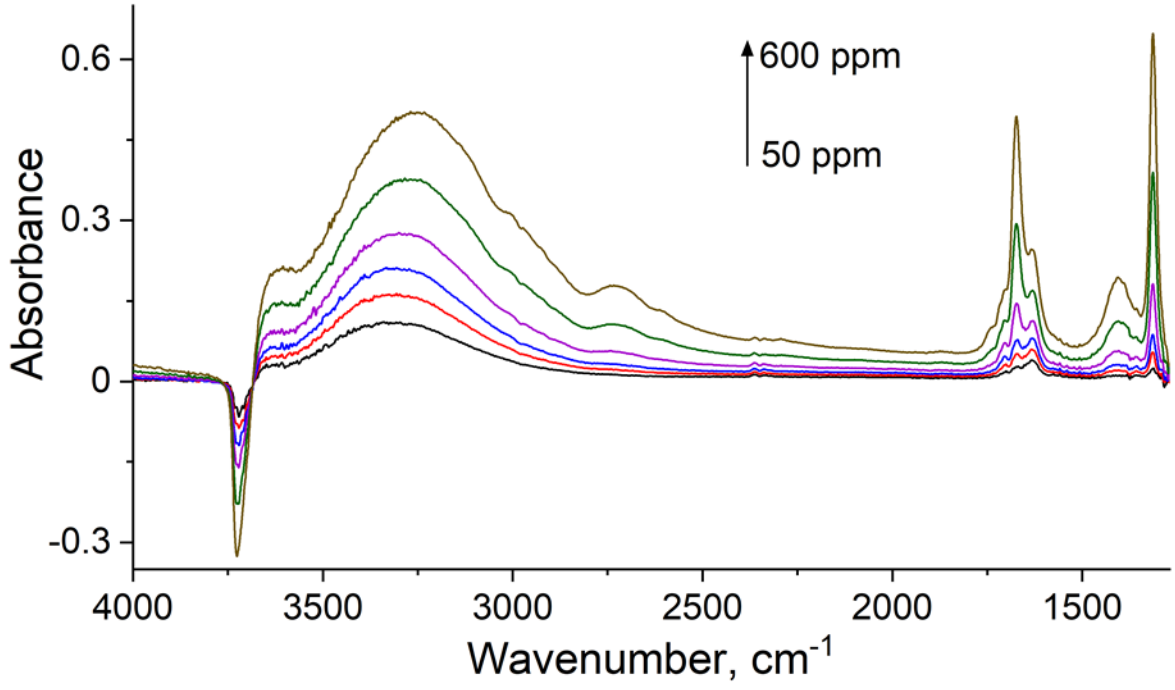

Figure 7.72. Difference FTIR spectra of NO_2 adsorbed on DeAl-BEA, 50 ppm (black), 75 ppm, 100 ppm, 200 ppm, 400 ppm, 600 ppm.

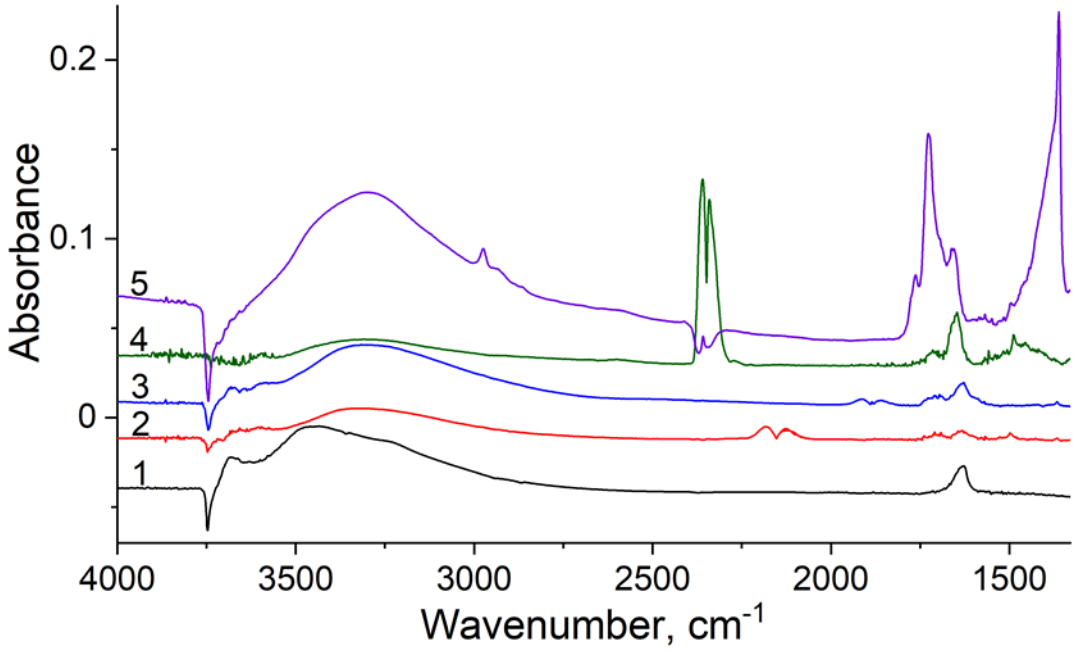

Figure 7.73. Difference FTIR spectra of 5000 ppm of H_2O (1), 5000 ppm of CO (2), 5000 ppm of NO (3), 5000 ppm of CO_2 (4) and 900 ppm of NO_2 (5) adsorbed on Sn-BEA, all the spectra are offset and spectrum 1 is multiplied by a factor of 0.1 for clarity.

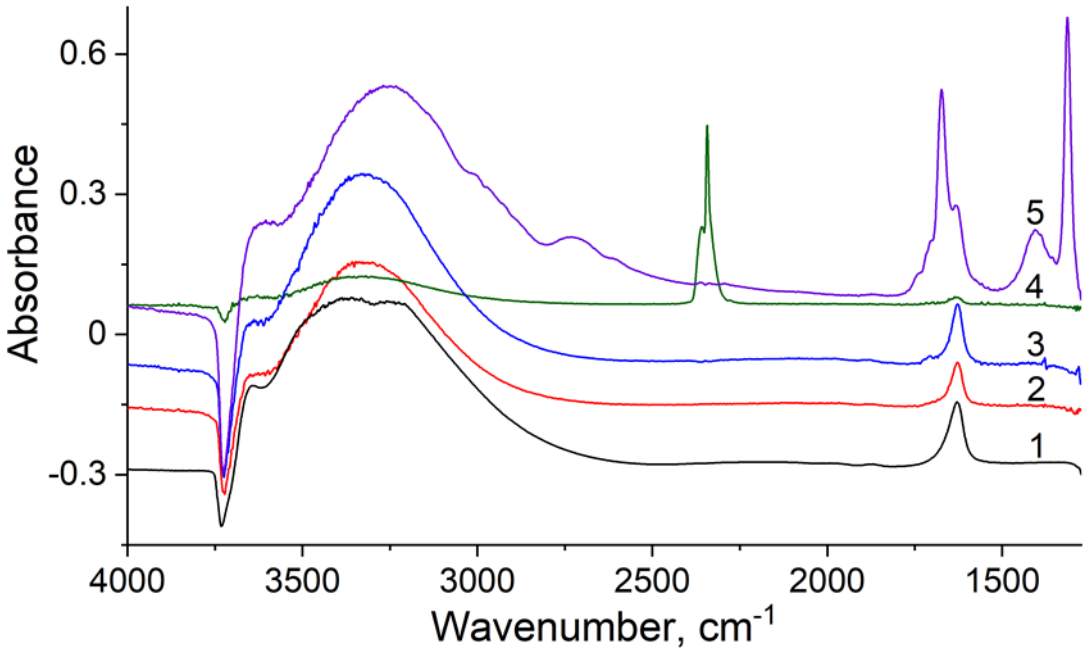

Figure 7.74. Difference FTIR spectra of 5000 ppm of H_2O (1), 600 ppm of CO (2), 600 ppm of NO (3), 2050 ppm of CO_2 (4) and 600 ppm of NO_2 (5) adsorbed on DeAl-BEA, all the spectra are offset and spectrum 1 is multiplied by a factor of 0.1 for clarity.

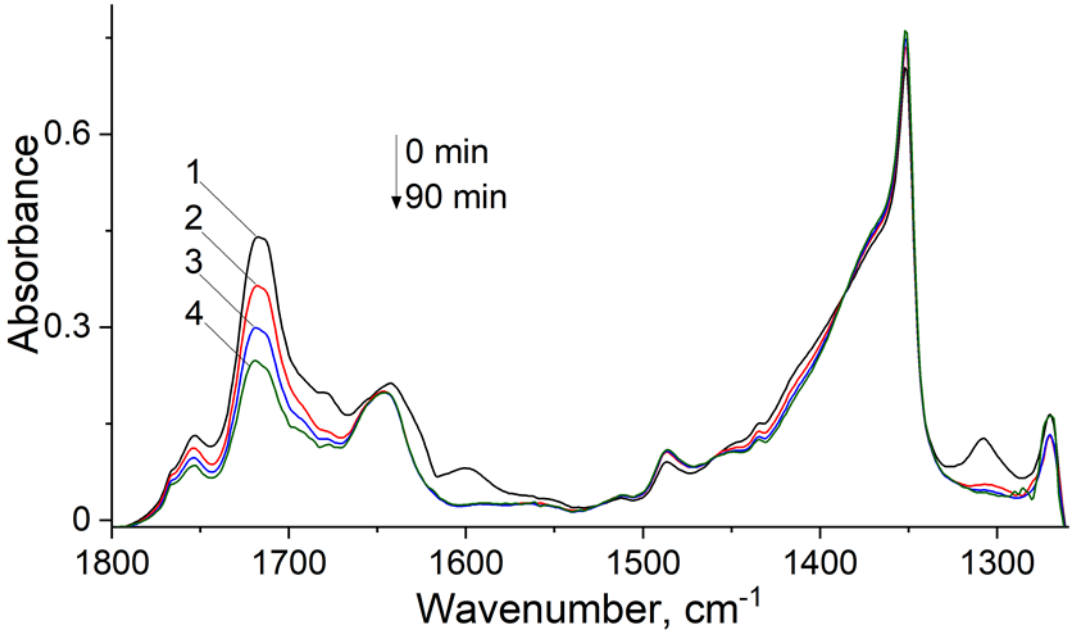

Figure 7.75. Difference FTIR spectra of 900 ppm of NO_2 adsorbed on Sn-BEA (1), followed by desorption at room temperature for 30 min (2), 60 min (3) and 90 min (4).